Development of high-throughput technologies for the study of drug-membrane interactions

---

Claire Elizabeth Stanley

Department of Chemistry

Imperial College London

A Thesis Submitted for a Degree of Doctor of Philosophy

Oct 2011

I, Claire Elizabeth Stanley, declare that all the material presented in this thesis is my own work except where noted.

For Mum, Dad, Paul & Adam

Abstract

Understanding how drug molecules interact with our body and what effects they may induce as a result is of fundamental concern to the pharmaceutical industry. Crucially we want to use this knowledge to our advantage during the drug discovery process in order to manipulate a drug's efficacy *in vivo* - therefore the development of new technologies, able to effectively screen numerous desirable drug-membrane interactions, is of key importance.

The first half of this thesis details the development of a vesicle leakage assay, as a means to assess the effect of cationic amphiphilic drugs (CADs) on model lipid membranes. Having demonstrated the reproducibility of the assay, the assay was transferred into a microfluidic format where water-in-oil droplet systems act as individual experimental vessels. As such, it has been demonstrated that the use of fluorescence lifetime techniques can provide a way in which to translate this assay into a high-throughput format.

The second part of the thesis is concerned with using droplet interface bilayers (DIBs) as a means to probe the effect of exogenous species upon a single lipid bilayer, as opposed to bulk vesicle populations. Several advantages exist for using such a system, including for example the ease with which one is able to control the composition of the aqueous compartments on either side of the bilayer and to form asymmetric bilayers. An assay, involving the use of pH gradients, is detailed, where proof-of-concept experiments illustrate that pH sensitive dyes could be used to report the extent to which lipid bilayers are

perturbed by drug molecules for example. Furthermore, a novel automated approach has been developed, offering advantages over the manual manipulation of lipid-containing droplets for DIB formation, where a microfluidic approach is used for their generation in high-throughput. Consequently, this approach enables the formation of multiple DIBs, where the composition may be differed and the droplet dimensions controlled, enabling the formation of DIB networks that can be arranged in either two- or three-dimensions.

Acknowledgements

This thesis could not have been produced without the help and support of many people over the last four years. I would therefore like to convey my gratitude to everyone who has contributed to this [long!] journey.

First and foremost unconditional thanks must be given to each of my supervisors for their advice and guidance throughout the course of this project. I would like to thank Oscar Ces for his constant enthusiasm and knowledge in the area of biophysics, Andrew deMello for his invaluable expertise in the field of microfluidics and Tony Gee for his experiences brought to the project from an industrial point of view. I would also like to thank the EPSRC and GSK for funding this PhD and the Society of the Chemical Industry for the prestigious scholarship awarded to me during my second year at Imperial.

I would especially like to thank and acknowledge Xize Niu, Katherine Elvira, Tom Robinson and Monpichar Srisa-Art for their advice and collaboration with respect to the microfluidic and droplet interface bilayer work presented in this thesis. It has been a pleasure working with each of you and much fun! Thank you also to Nick Brooks, Annela Seddon, Christina Turner and Gemma Shearman for teaching me about various lipid-related "stuff" and Marie Kirsten, Duncan Casey, Andre Studer, Kalypso Charalambous and Dave Miller for always lending a helping hand.

Thank you also to each member of the membrane biophysics, non-specific binding and deMello / Edel research groups for their contributions during group meetings.

Special thanks to all fellow "5th floorers" – past and present – for the many discussions, friendship and, of course, constant flow of tea, biscuits and super strong coffee! Thank you to Natalia Goehring, Dora Tang, Arwen Tyler, Jessica Knott, and Hanna Barriga for their friendship and support over the last few years. I would especially like to thank Natalia for rekindling my love of drawing and for the constant laughter she brings into every day.

Most importantly, thank you to Adam for his support, love and friendship over the last nine years and to my amazing Mum and Dad for their continual encouragement, love and unconditional support.

Table of Contents

ABSTRACT.....i

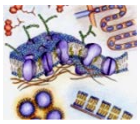
ACKNOWLEDGEMENTS.....iii

TABLE OF CONTENTS.....v

LIST OF FIGURES.....xiv

LIST OF TABLES.....xxiv

ABBREVIATIONS.....xxvii



CHAPTER 1: Introduction

1.1 OVERVIEW.....2

1.2 CELL MEMBRANES AND THEIR BIOPHYSICAL PROPERTIES.....3

1.2.1 Structure and function of biological membranes.....3

1.2.1.1 Membrane lipids.....4

1.2.1.2 Asymmetrical lipid distribution in cell membranes.....8

1.2.1.3 Proteins.....9

1.2.2 Membrane biophysics.....10

1.2.2.1 Lipid mesophases.....10

1.2.2.2 Membrane curvature and curvature elasticity (g_c).....11

1.2.2.3 Lateral stress and spontaneous mean curvature.....12

1.2.2.4 Stored curvature elastic stress.....14

1.3 DRUG-MEMBRANE INTERACTIONS....16
1.3.1 Passive transport....17
1.3.2 Active transport....18
1.3.3 Drug translocation via membrane degradation....20

1.4 HIGH-THROUGHPUT TECHNOLOGIES FOR THE STUDY OF DRUG-MEMBRANE INTERACTIONS....22
1.4.1 Microfluidics....22
1.4.1.1 Introduction....22
1.4.1.2 Laminar flow in microfluidic systems....24
1.4.1.3 Segmented flows....25
1.4.1.4 Methods for forming microfluidic droplets....26
1.4.1.5 Droplet manipulation....29
1.4.1.6 Microfluidic technologies amenable for investigating drug-membrane interactions....31
1.4.2 Supported lipid bilayers....35
1.4.2.1 Formation of supported lipid bilayers....36
1.4.2.2 Patterning supported lipid bilayers....39
1.4.2.3 Production of composition arrays....49
1.4.2.4 Problems associated with the SLB technique....51
1.4.3 Droplet interface bilayers (DIBs)....53
1.4.3.1 Definition....53
1.4.3.2 Advantages of the DIB system....55
1.4.3.3 High throughput lipid bilayer formation....57

1.5 CONCLUDING REMARKS AND THESIS AIM....62



CHAPTER 2: Development of carboxyfluorescein leakage assay for the study of drug-membrane interactions

2.1 OVERVIEW.....65

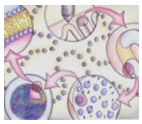
2.2 INTRODUCTION.....65
2.2.1 Properties of carboxyfluorescein.....65
2.2.2 Carboxyfluorescein in liposomes.....68
2.2.3 Summary and chapter aims.....69

2.3 MATERIALS AND METHODS.....70
2.3.1 Materials.....70
2.3.1.1 Vesicle preparation.....70
2.3.1.2 Dye and buffer solutions.....70
2.3.1.3 Drugs.....71
2.3.1.4 Gel filtration column.....71
2.3.2 Methods.....71
2.3.2.1 Encapsulation of carboxyfluorescein.....71
2.3.2.2 Exclusion of external dye by gel filtration.....74
2.3.2.3 Column calibration.....75
2.3.2.4 Efflux measurements.....75
2.3.2.5 Critical micelle concentration (CMC) measurements.....76

2.4 RESULTS AND DISCUSSION.....80
2.4.1 Assay development.....80
2.4.1.1 Assay format.....80
2.4.1.2 Calibration of column.....83
2.4.1.3 Control measurements.....85
2.4.2 Reproducibility of assay: investigations with chlorpromazine, WAY and imipramine.....88

2.4.3 Dependency of efflux rate on DOPE content..... 95
2.4.3.1 Calibration of column using vesicles comprised of DOPC : DOPE..... 96
2.4.3.2 Control for CF vs DOPC : DOPE samples.....97
2.4.3.3 Results for DOPC : DOPE samples..... 98

2.5 CHAPTER SUMMARY.....102



CHAPTER 3: Translation of carboxyfluorescein leakage assay into a microfluidic format

3.1 OVERVIEW.....104

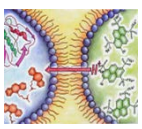
3.2 INTRODUCTION..... 104
3.2.1 Droplet microfluidics.....104
3.2.2 Fluorescence lifetime measurements.....105
3.2.3 Summary and chapter aims.....108

3.3 MATERIALS AND METHODS.....109
3.3.1 Materials.....109
3.3.1.1 Dye and buffer solutions..... 109
3.3.1.2 Photomasks.....109
3.3.1.3 Soft-lithography and substrate materials.....109
3.3.1.4 Performing measurements in microfluidic devices..... 110
3.3.1.5 Carboxyfluorescein leakage assay.....110
3.3.2 Methods..... 111
3.3.2.1 Dye and buffer preparation.....111
3.3.2.2 Creation of photomask..... 111
3.3.2.3 PDMS preparation.....112

3.3.2.4 Procedure for microfluidic device assembly.....113
3.3.2.5 Carboxyfluorescein leakage assay.....117
3.3.2.6 Fluorescence intensity measurements in a microfluidic format.....118
3.3.2.7 Fluorescence lifetime measurements in bulk.....118
3.3.2.8 Fluorescence lifetime measurements in a microfluidic format.....119
3.3.2.9 Data analysis of lifetime measurements.....121

3.4 RESULTS AND DISCUSSION.....123
3.4.1 Fluorescence intensity measurements.....123
3.4.2 Fluorescence lifetime experiments.....126
3.4.2.1 Carboxyfluorescein calibration experiment performed in a cuvette format.....127
3.4.2.2 Carboxyfluorescein leakage assay performed using imipramine in a cuvette format.....130
3.4.2.3 Carboxyfluorescein calibration experiment performed using a microfluidic format.....133
3.4.2.4 Carboxyfluorescein leakage assay, performed using imipramine in a microfluidic format.....135
3.4.2.5 Comparison of the leakage data gained in the cuvette and microfluidic formats.....143
3.4.2.6 Problems associated with the microfluidic format.....145

3.5 CHAPTER SUMMARY.....147



CHAPTER 4: Droplet interface bilayers (DIBs) for probing drug-membrane interactions

4.1 OVERVIEW.....149

4.2 INTRODUCTION 149
4.2.1 Liposomes versus artificial planar bilayers 149
4.2.2 Traditional methods for forming artificial planar bilayers 150
4.2.3 Droplet interface bilayers 152
4.2.4 Summary and chapter aims 155

4.3 MATERIALS AND METHODS 157
4.3.1 Materials 157
4.3.1.1 Lipids 157
4.3.1.2 Dye and buffer solutions 157
4.3.1.3 DIB formation 158
4.3.1.4 Interfacial tension measurements 158
4.3.2 Methods 158
4.3.2.1 Vesicle preparation 158
4.3.2.2 DIB formation 159
4.3.2.3 Leakage experiments 159
4.3.2.4 Control experiments 159
4.3.2.5 Pyranine fluorescence spectra 160
4.3.2.6 Imaging 160
4.3.2.7 Image analysis 163
4.3.2.8 Interfacial tension (IFT) measurements 164
4.3.3 Movie 164
4.3.3.1 Movie 4.1: 'Formation of droplet interface bilayer (DIB)' 164

4.4 RESULTS AND DISCUSSION 165
4.4.1 Formation of droplet interface bilayers (DIBs) 165
4.4.1.1 Open channel format for DIB formation 165
4.4.1.2 DIB formation with different lipids: DPhPC versus DOPC 168
4.4.2 Proof-of-concept DIB leakage experiments 171
4.4.2.1 Carboxyfluorescein 172

4.4.2.2 Properties of pyranine....176
4.4.2.3 DIB leakage assay with pyranine....180
4.4.2.4 Limitations of method....187

4.5 CHAPTER SUMMARY....189



CHAPTER 5: A microfluidic approach for high-throughput droplet interface bilayer (DIB) formation

5.1 OVERVIEW....191

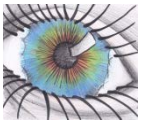
5.2 INTRODUCTION....191
5.2.1 Use of mechanical pumping for bilayer formation....191
5.2.2 Formation of DIB networks....193
5.2.3 Electrical methods....194
5.2.4 High-throughput approaches....196
5.2.5 Summary and chapter aims....198

5.3 MATERIALS AND METHODS....198
5.3.1 Materials....199
5.3.1.1 Lipids....199
5.3.1.2 DIB formation....199
5.3.1.3 Devices....199
5.3.2 Methods....200
5.3.2.1 Vesicle preparation....200
5.3.2.2 Device fabrication....200
5.3.2.3 Water-in-oil droplet formation....202
5.3.2.4 Fluorescence leakage experiments....204
5.3.2.5 Control experiments....205

5.3.2.6 Imaging.....205
5.3.3 Movies.....206
5.3.3.1 Movie 5.1: 'Small droplets filling the chamber in device 4'.....206
5.3.3.2 Movie 5.2: 'Large droplets filling the chamber in device 4'.....207
5.3.3.3 Movie 5.3: 'Formation of large droplet DIB network in device 4'.....208
5.3.3.4 Movie 5.4: "Formation of DIBs with DOPC using device 4'.....209

5.4 RESULTS AND DISCUSSION..... 209
5.4.1 Preliminary investigations using first generation devices.....210
5.4.1.1 Device designs.....210
5.4.1.2 First observation of stable DIB formation on-chip.....215
5.4.2 Second generation of devices.....216
5.4.2.1 Device design..... 216
5.4.2.2 High-throughput DIB formation.....218
5.4.2.3 Control of droplet size.....220
5.4.2.4 Asymmetric droplet systems..... 223

5.5 CHAPTER SUMMARY.....226



CHAPTER 6: Future Directions

6.1 OVERVIEW…… 229

6.2 CHAPTERS 2 AND 3……..…. 229

6.2.1 Critique of chapters 2 and 3……..... 229
6.2.2 Non-specific binding (NSB) in positron emission tomography (PET)…… 231

6.3 CHAPTERS 4 AND 5……..... 232
6.3.1 Expansion of droplet interface bilayer (DIB) system for use with additional lipids…….. 232
6.3.1.1 DLPC observations…… 233
6.3.1.2 Cholesterol…… 235
6.3.2 Expansion of automated approach for DIB formation……...236

APPENDIX 1..... 237
APPENDIX 2..... 239
APPENDIX 3..... 242
APPENDIX 4..... 244
APPENDIX 5..... 245
APPENDIX 6..... 246
APPENDIX 7..... 247
APPENDIX 8..... 248
APPENDIX 9..... 249
APPENDIX 10..... 250
APPENDIX 11..... 251
APPENDIX 12..... 253
APPENDIX 13..... 255
APPENDIX 14..... 256

BIBLIOGRAPHY..... 258

List of Figures

CHAPTER 1

Figure 1.1: The cell membrane....3

Figure 1.2: Prime chemical motifs of glycerophospholipids....6

Figure 1.3: Chemical structure of sphingolipids.... 7

Figure 1.4: The principle radii of curvature, R_1 and R_2 for a given surface.... 11

Figure 1.5: Lateral pressure profile of a lipid bilayer....13

Figure 1.6: The spontaneous mean curvature (H_0) exhibited by Type 0, I and II....14

Figure 1.7: Curvature elastic stress (CES).... 15

Figure 1.8: Passive transport.... 18

Figure 1.9: Active transport....19

Figure 1.10: Diagram illustrating the mechanistic implications of membrane degradation....21

Figure 1.11: An example of a microfluidic device....23

Figure 1.12: Laminar and turbulent flow....25

Figure 1.13: Continuous versus segmented flow.... 26

Figure 1.14: T-junction technique for the formation of microdroplets in a planar chip format (i.e. segmented flow)....27

Figure 1.15: Flow focusing technique for the formation of microdroplets in a planar chip format (i.e. segmented flow).....28

Figure 1.16: Operations that can be performed on droplets after having been generated.....30

Figure 1.17: High-throughput formation of monodisperse, unilamellar GUVs using microfluidics.....32

Figure 1.18: Development of "lung-on-a-chip" devices.....34

Figure 1.19: Supported lipid bilayer.....35

Figure 1.20: Approaches used to deposit fluid phospholipid bilayers upon a substrate.....36

Figure 1.21: Diagram illustrating the various mechanisms of vesicle rupture to yield SLB formation.....38

Figure 1.22: Diagrams illustrating the "blotting" and "stamping" techniques developed by Hovis and Boxer to create patterned, supported lipid bilayers.....41

Figure 1.23: Protein stamping and caulking for patterned SLB formation.....43

Figure 1.24: Polymer lift-off technique for the formation of patterned SLBs.....44

Figure 1.25: Aluminium lift-off technique for patterned SLB formation.....46

Figure 1.26: Patterned SLB formation via lipid polymerisation.....47

Figure 1.27: Hydrogel stamping for the creation of patterned supported lipid bilayers.....49

Figure 1.28: Methods for forming supported lipid bilayer composition arrays..... 51

Figure 1.29: Droplet Interface Bilayer (DIB) definition..... 54

Figure 1.30: Asymmetric droplet interface bilayer (aDIB) formation and the formation of droplet interface bilayer networks.....56

Figure 1.31: The falling drop method for high-throughput lipid bilayer formation..... 58

Figure 1.32: Black lipid membrane (BLM) approach for high-throughput lipid bilayer formation..... 60

Figure 1.33: Hanging droplet screening chip using droplet interface bilayers (DIBs).....61

CHAPTER 2

Figure 2.1: Molecular structure and excitation / emission spectra of 5(6)-carboxyfluorescein..... 66

Figure 2.2: Fluorescence properties of carboxyfluorescein (CF)..... 67

Figure 2.3: Visualisation of carboxyfluorescein (CF) release from liposomes contained within a cuvette and viewed under an ultraviolet (UV) lamp..... 69

Figure 2.4: Illustration of the steps involved in producing CF-encapsulated vesicles.....73

Figure 2.5: Separation of free carboxyfluorescein (CF) dye from CF-containing vesicles via the principle of size exclusion..... 74

Figure 2.6: Apparatus used to conduct interfacial surface tension (IFT) measurements..... 77

Figure 2.7: Determining equilibrium values for the interfacial surface tension (IFT_{eq})..... 78

Figure 2.8: Determination of the critical micelle concentration (CMC)..... 79

Figure 2.9: Assay format..... 81

Figure 2.10: Carboxyfluorescein (CF) calibration curve..... 82

Figure 2.11: Column calibration..... 84

Figure 2.12: Control measurements.....87

Figure 2.13: Effects of three drugs (three repeats for each) on the efflux of carboxyfluorescein from DOPC vesicles (buffer only).....88

Figure 2.14: The chemical motifs of imipramine, chlorpromazine and WAY.....89

Figure 2.15: Dependency of carboxyfluorescein (CF) leakage upon the introduction of chlorpromazine, WAY and imipramine.....91

Figure 2.16: Comparison of the leakage data for chlorpromazine, WAY and imipramine with the data gained from interfacial surface tension measurements..... 93

Figure 2.17: Calibration of column 2.....97

Figure 2.18: Control investigating the effect of introducing DOPE into a DOPC bilayer upon the final fluorescence intensity..... 98

Figure 2.19: Effect of introducing DOPE, into DOPC bilayers, upon the rate of carboxyfluorescein leakage..... 99

Figure 2.20: Chemical motifs of DOPC and DOPE..... 101

CHAPTER 3

Figure 3.1: A typical plot of intensity versus time gained during a fluorescence lifetime experiment..... 106

Figure 3.2: Principle of time-correlated single-photon counting (TCSPC) used to extract information about the fluorescence lifetime.....107

Figure 3.3: Software used to create photomask designs..... 112

Figure 3.4: Processes involved in PDMS chip manufacture, using photolithography techniques..... 114

Figure 3.5: Microfluidic chip assembly 1..... 116

Figure 3.6: Interfacing of the microfluidic chip with syringes.....117

Figure 3.7: Device configuration for droplet formation..... 121

Figure 3.8: Screen dump of the software package, SPC Image, used to analyse the fluorescence lifetime data.....122

Figure 3.9: Carboxyfluorescein calibration curve gained using intensity measurements in a microfluidic format..... 123

Figure 3.10: The various control measurements conducted to ascertain which parameters, if any, may explain the shifted calibration curve.....125

Figure 3.11: Summary of findings conducted using intensity measurements in a microfluidic format ("on-chip") and compared to the measurements conducted on the fluorescence spectrophotometer..... 126

Figure 3.12: Carboxyfluorescein calibration experiment performed in a cuvette format (fluorescence lifetime)..... 127

Figure 3.13: Carboxyfluorescein leakage assay performed using imipramine in a cuvette format (fluorescence lifetime data).....131

Figure 3.14: Fluorescence lifetime calibration measurements conducted in a microfluidic format and compared to experiments conducted in a bulk format / literature values.....134

Figure 3.15: Optimisation of the flow conditions in a microfluidic device for performing the carboxyfluorescein leakage assay.....136

Figure 3.16: Comparison of the relative initial rates of change in the fluorescence lifetime and intensity measurements when 0.8 and 1.6 mM imipramine is introduced to carboxyfluorescein-containing vesicles.....139

Figure 3.17: Predicted lifetime values based on the theoretical concentration of carboxyfluorescein present in the interior regions of the vesicles after leakage induced by the presence of 0.8 and 1.6 mM imipramine.....142

Figure 3.18: Comparison of leakage data gained in the cuvette and microfluidic formats.....144

Figure 3.19: Static droplets adsorbed to the channel in a microfluidic device..... 146

CHAPTER 4

Figure 4.1: Montal-Mueller method for the formation of artificial planar membranes.....152

Figure 4.2: Droplet Interface Bilayer (DIB) formation.....153

Figure 4.3: Methods for forming droplet interface bilayers (DIBs), including asymmetric DIBs.....155

Figure 4.4: Experimental set-up for DIB experiments using manual manipulation.....161

Figure 4.5: Screen dump of the ImageJ software used for analysing fluorescence microscopy images.....163

Figure 4.6: Stills from Movie 4.1: 'Formation of droplet interface bilayer (DIB)'.....165

Figure 4.7: Experimental evidence for the formation of droplet interface bilayers (DIBs).....167

Figure 4.8: DPhPC and DOPC for DIB formation.....168

Figure 4.9: Interfacial surface tension measurements of DOPC and DPhPC.....170

Figure 4.10: Principle of DIB-leakage experiments.....172

Figure 4.11: Carboxyfluorescein as a pH sensor for use in leakage experiments across DIBs.....173

Figure 4.12: Evidence for carboxyfluorescein leakage into the oil phase..... 175

Figure 4.13: Chemical structure of pyranine, 8-hydroxypyrene-1,3,6-trisulfonic acid (trisodium salt).....176

Figure 4.14: Fluorescence properties of pyranine solutions..... 177

Figure 4.15: The dependence of pyranine fluorescence properties upon its concentration and pH in water..... 178

Figure 4.16: Collated excitation spectra for serially diluted 1 mM pyranine stocks (in water) and in the presence of acidic and alkaline conditions..... 179

Figure 4.17: First attempt at performing a DIB leakage assay, using a 60 μM aqueous pyranine solution (solution 4.11, pH 5.5, section 4.3.1.2).....181

Figure 4.18: Dependency of excitation spectra on sample pH for 60 μM pyranine-containing solutions, plus control experiment.....183

Figure 4.19: Observed relationships between the ratio of pyranine fluorescence intensity and time for different DIB systems (including control).....185

CHAPTER 5

Figure 5.1: Devices for forming artificial lipid bilayers using microfluidics.....192

Figure 5.2: Droplet interface bilayer networks and their application.....194

Figure 5.3: EWOD for DIB formation..... 195

Figure 5.4: Current methods for using planar lipid bilayers in high-throughput screens.....197

Figure 5.5: Method of device assembly.....201

Figure 5.6: First generation device used during preliminary investigations (devices 1-3)..... 201

Figure 5.7: Schematic of the second generation device (device 4)..... 202

Figure 5.8: Water-in-oil droplet formation using an auto-sampler.....203

Figure 5.9: Format of the fluorescein leakage assay.....204

Figure 5.10: Stills from Movie 5.1: 'Small droplets filling the chamber in device 4'..... 207

Figure 5.11: Stills from Movie 5.2: 'Large droplets filling the chamber in device 4'..... 208

Figure 5.12: Stills from Movie 5.3: 'Formation of large droplet DIB network in device 4'.....208

Figure 5.13: Stills from Movie 5.4: 'Formation of DIBs with DOPC using device 4'..... 209

Figure 5.14: Device 1.....211

Figure 5.15: Device 2.....212

Figure 5.16: Observations of potential on-chip DIB formation..... 213

Figure 5.17: Device 3.....214

Figure 5.18: First observation of stable DIB formation on-chip.....216

Figure 5.19: Device 4 for high-throughput droplet interface bilayer (DIB) formation.....217

Figure 5.20: Size variation of water-in-oil droplets..... 218

Figure 5.21: Examples of droplet interface bilayer (DIB) formed in high-throughput.....219

Figure 5.22: Ability to tune droplet size, hence controlling droplet interface bilayer (DIB) contact area and the number of DIBs each droplet participates in..... 221

Figure 5.23: Potential packing arrangements of droplets participating in DIBs..... 222

Figure 5.24: Asymmetric DIB (aDIB) formation and fluorescein leakage assay showing successful DIB formation with DOPC.....224

Figure 5.25: Results of fluorescein control experiments.....225

Figure 5.26: Formation of higher order a-DIBs.....226

CHAPTER 6

Figure 6.1: Dosing system……..230

Figure 6.2: Effects of DLPC in hexadecane……...…… 234

APPENDICES

Figure A1.1: Column calibration.....237

Figure A2.1: Experimental efflux data fitted to an exponential decay model.....240

Figure A2.2: Control data confirming drug-dye interaction……..... 241

Figure A3.1: Column calibration 2..... 242

Figure A4.1: Efflux of carboxyfluorescein from vesicle lumens upon the addition of chlorpromazine; dependence on mole percent of DOPE in a DOPC bilayer..... 244

Figure A5.1: Efflux of carboxyfluorescein from vesicle lumens upon the addition of WAY; dependence on mole percent of DOPE in a DOPC bilayer..... 245

Figure A6.1: Efflux of carboxyfluorescein from vesicle lumens upon the addition of imipramine; dependence on mole percent of DOPE in a DOPC bilayer..... 246

Figure A7.1: The fluorescence lifetime gained for each of the ten solutions of carboxyfluorescein, present at different concentrations, based on the data provided in table A7.1..... 247

Figure A8.1: The change in fluorescence lifetime over time upon addition of imipramine to a DOPC vesicular solution (1.6 and 0.1 mM respectively, final concentrations), based on the data provided in table A8.1.....248

Figure A9.1: The change in fluorescence lifetime over time, based on the data provided in table A9.1 (above), of carboxyfluorescein-containing vesicles suspended in solution (DOPC, 0.1 mM see chapter 3, section 3.3.2.5) i.e. where no drug, solely buffer has been introduced.....249

Figure A10.1: The fluorescence lifetime gained for each of the ten solutions of carboxyfluorescein, present at different concentrations, based on the data provided in table A10.1.....250

Figure A11.1: The change in fluorescence lifetime over time upon addition of imipramine solutions (1.6 and 0.8 mM, final concentration) to a DOPC vesicular solution (0.1 mM, final concentration), based on the data provided in table A11.1.....251

Figure A12.1: The change in fluorescence intensity over time upon addition of imipramine solutions (1.6 and 0.8 mM, final concentration) to a DOPC vesicular solution (0.1 mM, final concentration).....253

Figure A13.1: Bright field images of droplets 1-6.....255

Figure A14.1: Droplets 1 and 2.....256

Figure A14.2: Droplets 3 and 4.....256

Figure A14.3: Droplets 5 and 6.....257

Figure A14.4: Control droplets.....257

List of Tables

CHAPTER 3

Table 3.1: The ten samples of carboxyfluorescein used to construct the calibration curves.....119

Table 3.2: The effect of propylene glycol on lifetimes of concentrated carboxyfluorescein..... 129

Table 3.3: Summary of results regarding the optimisation of the aqueous (Aq_1 and Aq_2) and oil flow rates in the microfluidic device, used to perform the carboxyfluorescein leakage assay..... 137

Table 3.4: Theoretical concentration of carboxyfluorescein present in the interior and exterior regions of the vesicles after varying amounts of leakage.....142

CHAPTER 4

Table 4.1: Summary of the advantages that the droplet interface bilayer system has over conventional methods for artificial planar bilayer formation.....154

Table 4.2: Melting points of different solvents, including hexadecane.....166

APPENDICES

Table A1.1: Column calibration data 1A..... 237

Table A1.2: Column calibration data 1B..... 238

Table A2.1: Table collating the different parameters associated with an exponential decay fit of the efflux data displayed in figure A2.1.....240

Table A3.1: Column calibration data 2A.....242

Table A3.2: Column calibration data 2B.....243

Table A7.1: Single exponential fit to carboxyfluorescein calibration data (in bulk), thus yielding the corresponding fluorescence lifetime (τ_1) and χ^2 values.....247

Table A8.1: Single exponential fit to data gained during the carboxyfluorescein leakage assay, performed using imipramine (in bulk), thus yielding the corresponding fluorescence lifetime (τ_1) and χ^2 values.....248

Table A9.1: Double exponential fit to control data, where the fluorescence lifetime of carboxyfluorescein-containing vesicles (DOPC, 0.1 mM see chapter 3, section 3.3.2.5) in solution is measured at various intervals during the time course of the experiment.....249

Table A10.1: Single exponential fit to carboxyfluorescein calibration data (in a microfluidic format), thus yielding the corresponding fluorescence lifetime (τ_1).....
250

Table A11.1: Single exponential fit to the data gained when carboxyfluorescein leakage is induced by imipramine in a microfluidic format.....251

Table A11.2: Linear regression associated with the data displayed in figure A11.1.....252

Table A11.3: Linear regression associated with the data displayed in figure A11.1.....252

Table A12.1: Fitted exponential decay associated with the data displayed in figure A12.1.....253

Table A12.2: Fitted exponential decay associated with the data displayed in figure A12.1.....254

Table A13.1: Properties of droplets 1-6.....255

Abbreviations

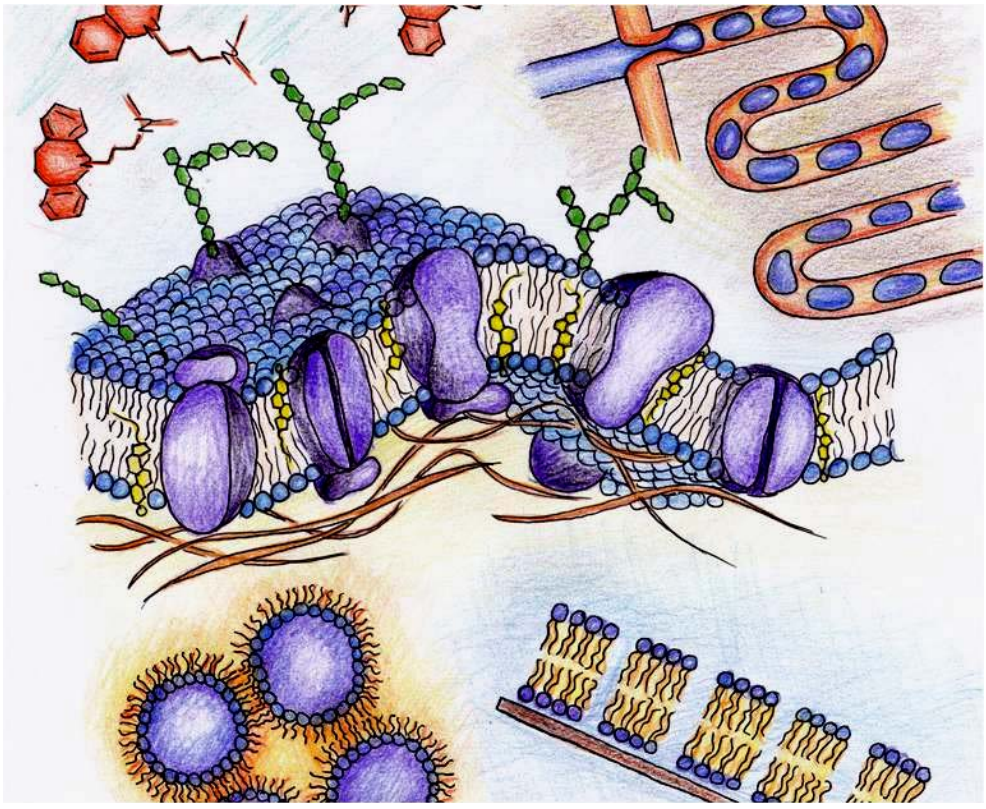
aDIB	Asymmetric droplet interface bilayers
ATP	Adenosine triphosphate
BLM	Black lipid membrane
CAD	Cationic amphiphilic drug
CCT	CTP:phosphocholine cytidylyltransferase
CES	Curvature elastic stress
CF	Carboxyfluorescein
CMC	Critical micelle concentration
DEP	Dielectrophoresis
DIB	Droplet interface bilayer
diynePC	Diacetylene phospholipid
DLPC	1,2-didodecanoyl-sn-glycero-3-phosphocholine
DNA	Deoxyribonucleic acid
DOPC	1,2-dioleoyl-*sn*-glycerolphosphatidylcholine
DOPE	1,2-dioleoyl-*sn*-glycerolphosphatidylethanolamine
DPhPC	1,2-diphytanoyl-sn-glycero-3-phosphocholine
EWOD	Electrowetting on dielectric
FCC	Face-centred cubic
FLIM	Fluorescence lifetime microscopy
FM	Fluorescence microscopy
FRAP	Fluorescence recovery after photobleaching
GUV	Giant unilamellar vesicle
HCP	Hexagonal close-packed
HEPES	4-(2-hydroxyethyl)piperazine-1-ethanesulfonic acid
IFT	Interfacial surface tension
IFT_{eq}	Equilibrium value of the IFT

IPA	Isopropyl alcohol
LPC	1-oleoyl-2-hydroxy-sn-glycero-3-phosphocholine / Lyso-phosphatidylcholine
LUV	Large unilamellar vesicles
μCP	Microcontact printing
MDR1	Multidrug resistant protein
NBD PE	Nitrobenzoxadiazol head group labelled phosphatidylethanolamine
NMR	Nuclear magnetic resonance spectroscopy
NSB	Non-specific binding
OA	Oleic acid
PC	Phosphatidylcholine
PCR	Polymerase chain reaction
PDMS	Poly(dimethylsiloxane)
PE	Phosphatidylethanolamine
PEB	Post exposure bake
PET	Positron emission tomography
PI	Phosphatidylinositol
PMMA	Poly(methyl methacrylate)
PMT	Photomultiplier tube
PS	Phosphatidylserine
PTFE	Polytetrafluoroethylene
QCM-D	Quartz crystal microbalance with dissipation monitoring
Rh PE	1,2-dioleoyl-sn-glycero-3-phosphoethanolamine-N-(lissamine rhodamine B sulfonyl) (ammonium salt)
RIE	Reactive ion etching
ROI	Regions of interest
SAXS	Small angle X-ray scattering
SDS	Sodium dodecyl sulphate
SGLT	Sodium-coupled glucose transporters
SLB	Supported lipid bilayer
SML	Sterol-modified phospholipid

sulfo-SMCC	Sulfosuccinimidyl-4-(N-maleimidomethyl)cyclohexane-1-carboxylate
SUV	Small unilamellar vesicle
TCEP	Tris(2-carboxyethyl)phosphine hydrochloride
TCSPC	Time-correlated single-photon counting
TR DHPE	N-(Texas Red sulfonyl)-1,2-dihexandecanoyl-sn-glycero-3-phosphoethanolamine
TX-100	Triton X-100
UV	Ultraviolet

Chapter 1

Introduction



"The process of scientific discovery is, in effect, a continual flight from wonder."

Albert Einstein

1.1 OVERVIEW

The answer to the following question is fundamental in understanding the rationale behind the work detailed in this thesis:

"*Why do we wish to develop high-throughput technologies for the study of drug-membrane interactions?*"

Cell membranes are an elementary feature present in every cell of our body, acting as a barrier that separates the intra- and intercellular milieux. In order for a drug molecule to reach its site of action, it must pass many membranes. Therefore understanding how drug molecules interact with lipid membranes is crucial, if further insights into the factors affecting their translocation are to be gained. In the past, cell membranes were thought to fulfil merely a structural role, however lipids in cell membranes are now viewed as more than just simple building blocks, aiding the choreography of cellular tasks and influencing protein function.[1]

It is therefore unsurprising that a wide variety of platforms are being developed for the formation of artificial lipid bilayers. Cell membranes are crucial to living organisms and so it is important to develop platforms, where studies of a biophysical nature can be conducted to probe questions on lipid (and protein) function.[2] Biophysical assays that are able probe drug-membrane interactions in high-throughput will enable a picture to be formed, containing increasing levels of complexity using a bottom up approach.

This chapter provides an overview of cell membranes, where their structure and function, as well as biophysical properties, are discussed. The interactions of drug molecules with lipid membranes are considered, as too are the current technologies available for studying the interactions of small molecules with membranes in artificial systems.

1.2 CELL MEMBRANES: AN OVERVIEW

1.2.1 Structure and function of biological membranes

Cell membranes are ubiquitous in living organisms and are composed primarily of a bilayer containing amphiphilic lipids[3-6] and sterols,[7-9] encompassing proteins (integral and peripheral), carbohydrates and a cytoskeletol network, as illustrated in figure 1.1. It serves to act not only as a means to compartmentalise and regulate the intracellular environment, segregating its contents from the outside milieu, but to perform and choreograph multiple fundamental tasks via sophisticated mechanisms.[10-13] Many of the intricacies involved in these mechanisms, including the emergence of dynamic coupling between lipids and proteins,[5,11] have only recently become better understood. For example, recent years have witnessed a large amount of debate and controversy within the literature surrounding the existence of *lipid rafts in vivo*,

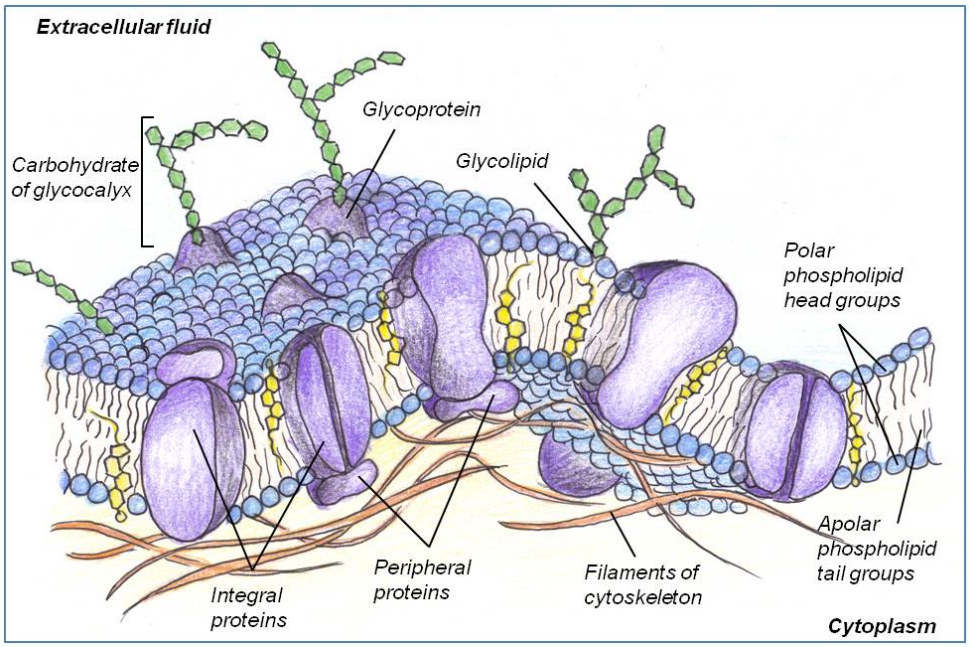


Figure 1.1: **The cell membrane.** Key features include the lipid bilayer, which possesses embedded proteins and intracellular cytoskeletol filaments.

or more pertinently *microdomains*,[14-16] and their ability to confine protein binding[17-19] thus facilitating processes such as signal transduction.[20,21] This is one example demonstrating how the interaction of proteins with membranes, and vice versa, is an extremely complicated and challenging feat.

In 1972, Singer and Nicolson expressed a revolutionary concept describing the dynamic structure of a cell membrane – The Fluid Mosaic Model.[22] This was the first model to portray biomembranes as random "two-dimensional solutions of orientated globular proteins and lipids",[22] which has since been revised.[23,24] It was suggested that the lipids must exist in a bilayer motif, with the hydrophilic (polar) head groups orientated towards the aqueous environment, the hydrophobic (apolar) tails groups orientated towards one another and the proteins spanning part (peripheral proteins) or all (integral proteins) of the membrane, in order to meet the thermodynamic requirements imposed by these amphiphiles (see figure 1.1). This enables the hydrophobic and hydrophilic portions of both the lipid and protein moieties to favourably arrange, such that their interaction with water is minimised or maximised (i.e. to fulfil the hydrophobic[25] effect). The rationale behind Singer and Nicolson's approach thus superseded previously reported models of membrane structure.[26]

1.2.1.1 Membrane lipids

Phospholipids are major constituents of cellular membranes, being amphiphilic in nature.[27] There exists a vast diversity in the chemical structure of phospholipids, owing to the presence of numerous permutations of 'head' and 'tail' assemblages; in fact, the eukaryotic cell generates more than 1000 lipid species.[28,29] This melange is required in order to govern the numerous operations carried out at the molecular level *in vivo*.[30]

There are four main classes of phospholipids present within living systems, specifically glycerophospholipids, lysophospholipids, sphingolipids and plasmologens.[7] Figures 1.2 and 1.3 illustrate the chemical nature of these lipids.

It has been postulated by van Meer *et al.*,[29] that the mammalian membrane is comprised of glycerolipids, sphingolipids and sterols – another important component of cellular membranes – in the following mole percent ratios: 65 : 10 : 25 mol % respectively. Interestingly, they also provide an estimate as to the relative abundances of phospholipids and sterols in the membranes of various cell organelles, such as the plasma membrane, endoplasmic reticulum and golgi – the plasma membrane is expected to be the most relevant cellular membrane to the studies conducted in this thesis. Information concerning the identification and quantification of all lipids and their interacting moieties in mammalian cells is of great importance, for example with respect to furthering our understanding of lipid-based disease mechanisms, and forms a current focus of lipidomics.

A class of enzymes known collectively as the phospholipases, of which there are four families (A_1, A_2, C and D),[31-36] act to cleave phospholipids at specific sites. For example, lysophospholipids are generated as a result of phospholipase A_2 catalytically cleaving the *sn*-2 fatty acyl bond of phospholipids (with the corresponding fatty acid also being generated).[31]

The general motif of glycerophospholipids includes: i) a lipophilic backbone attached to glycerol via the *sn*-1 and -2 positions,[3,4] and ii) a polar head group linked to the glycerol moiety via a phosphate group (figure 1.2). If phosphatidic acid is esterified at *sn*-1 and -2 an array of phosphatidyl (or diacylglycerol) lipids are produced, including phosphatidylcholine (PC), phosphatidylethanolamine (PE), phosphatidylserine (PS) and phosphatidylinositol (PI) (figure 1.2),[5] most of which are found in varying compositions in different cell types.[6] Numerous chain lengths can be incorporated at the -1 and -2 positions (a shorter chain length, i.e. C_{16}-C_{18}, is normally found in the *sn*-1 position). The most abundant mammalian lipid is phosphatidylcholine (PC),[5] with phosphatidylethanolamine (PE) being the second most abundant.[28,37] Alkylacylglycerols are produced when alcohols are incorporated at the *sn*-1 position, resulting in the production

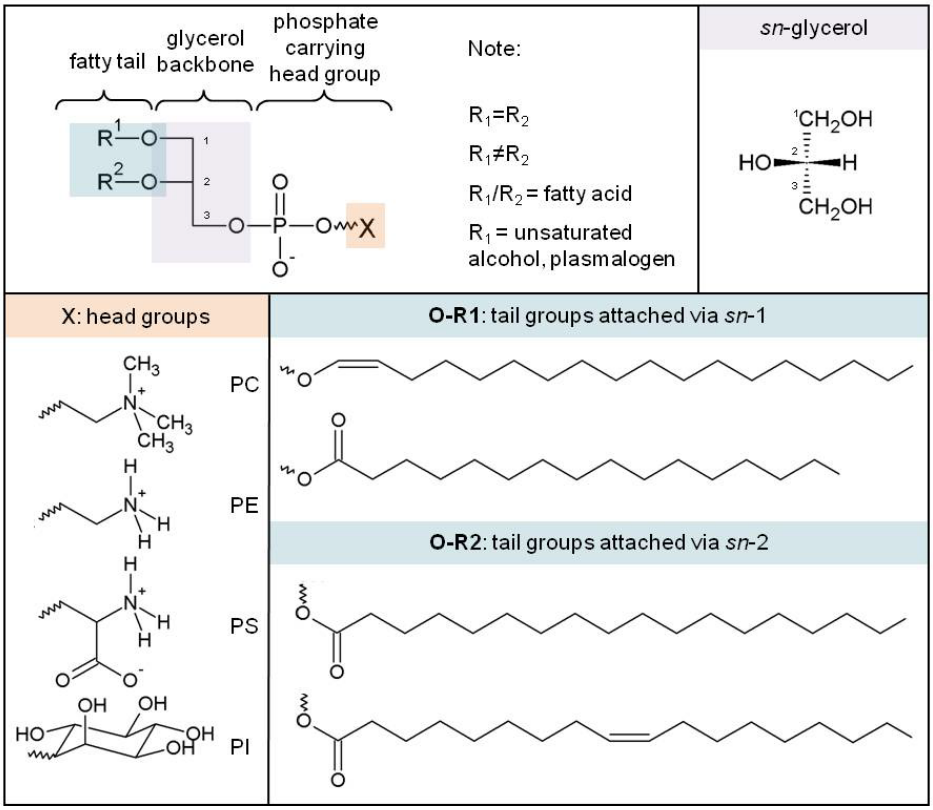


Figure 1.2: **Prime chemical motifs of glycerophospholipids.** The generic structure of a glycerophospholipid is displayed, which consists primarily of a glycerol backbone, to which fatty tails and a phosphate carrying head group are attached.

of an ether as opposed to an ester bonded unit. Alternatively, if an unsaturated alcohol is introduced at this position, a sub-class of the glycerolipids known as plasmalogens (alkenylacylglycerols) are formed.[5] Various fatty acids incorporating *cis* double bonds may also be present at *sn*-2.

Sphingolipids are a class of phospholipids that contain a sphingoid base, normally sphingosine, attached to a fatty acid (via an amide bond) and a phosphate-carrying headgroup.[5] Figure 1.3 illustrates the chemical nature of the sphingolipids. Phosphocholine derived sphingolipids (sphingomyelin) and phytosphingosine (possessing an additional OH on C_4 of sphinganine) are the most frequently found sphingolipids in nature.[3] Other derivatives do exist including galactosylceramide, glucosylceramide and lactosylceramide.

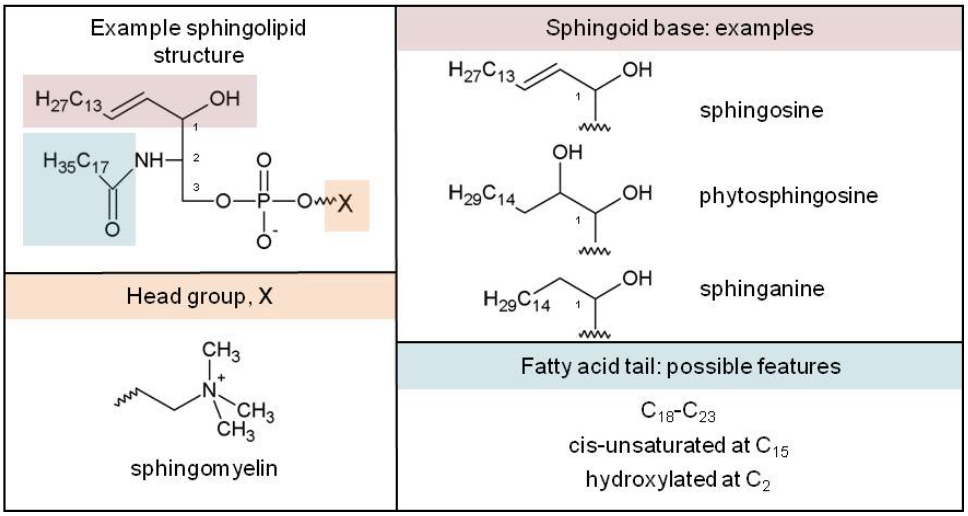


Figure 1.3: **Chemical structure of sphingolipids.** The generic structure of a sphingolipid is displayed, which consists primarily of a glycerol backbone, to which a sphingoid base, fatty tail and a phosphate carrying head group are attached.

The biophysical properties of sphingolipids are inherently different to those of glycerolipids. In particular, the 2-amide and 3-hydroxyl groups, present in the interfacial region of sphingolipids, function as both hydrogen bond donors and acceptors, whereas glycerolipids only have hydrogen bond-accepting properties in the analogous interfacial region.[38] This property enables sphingolipids to self-associate with one another and results in the formation of more tightly packed lipid membranes that can be up to 30 % thicker than glycerolipids.[38] Additionally, the presence of a very long amide-linked chain, which leads to chain asymmetry, has been found to produce unusual phase behaviour, including interdigitated phases.[39]

Sterols, another important class of molecules found in eukaryotic cell membranes, are much more hydrophobic than phospholipids and their rigid structure allows them to associate between the chains of adjacent lipid molecules in the bilayer.[7] Being enriched in the plasma membrane, sterols acts to reduce the permeability of the membrane to small molecules due to the close packing of the lipids.[29]

Furthermore, sterols, such as cholesterol, play a crucial role in the membrane as phase moderators. Sphingolipids possess much higher melting temperatures than glycerolipids (generally above physiological temperatures),[38] which could result in the formation of solid gel phase regions. Cholesterol has been found to bind preferentially to sphingolipids and therefore acts to fluidise the membrane by disrupting the long range chain order and increasing the molecular motion. The chain melting temperatures of the lipids used in this investigation have all been below room temperature, thus the temperature at which the investigations in this thesis have been conducted does not raise cause for concern.

1.2.1.2 Asymmetrical lipid distribution in cell membranes

The asymmetric distribution of phospholipids between the two monolayers of biological membrane was first recognised by Bretscher more than 30 years ago.[40] The existence of asymmetrically distributed phospholipids within the lipid bilayer is of great importance, as displayed by the prevalent expression in eukaryotic and bacterial systems (though the presence of asymmetry in the latter case is less certain, most likely attributed to challenging experimental procedures). Boon and Smith[41] cite numerous examples present in the literature detailing possible consequences with regard to loss of asymmetry: interruption of signal transduction pathways,[42] induction of apoptosis[43] and the regulation of hemostasis and thrombosis[44] are a few examples illustrating the need for efficient maintenance of asymmetry across the plasma membrane.

In order for lipid asymmetry to occur and consequently be maintained, a process must exist whereby the lipids have the ability to move from the outer leaflet of the lipid bilayer to the inner and vice versa. This translocation, or 'flip-flop',[45] is greatly dependent on the nature of the lipid head groups (such as the size and charge), possessing a half-life of hours to days.[46] The rate of translocation however is significantly enhanced by the presence of a specialised set of proteins.

Aminophospholipid translocases ('flippases') specifically aid the stereospecific[47] movement of aminophospholipids from the outer to the inner lipid monolayer,[44] displaying a high degree of head-group selectivity. Conversely, 'floppases' aid the translocation of both choline- and aminophospholipids in the opposing direction to flippases;[48] both proteins require the expenditure of cellular energy (i.e. they are both adenosine triphosphate (ATP) dependent). The third variety of membrane translocases, known as 'scramblases', act to scramble phospholipids in both the 'flip' and 'flop' directions thus destroying lipid asymmetry[41] and has been found to be calcium dependant.[49]

In addition to this hypothesis, a second theory regarding the origins of lipid asymmetry also exists. This believes that the cytoskeleton proteins interact with and influence the positioning of the inner leaflet lipids. It appears that there is evidence present in the literature both for and against this latter hypothesis, as detailed by Boon and Smith;[41] although in hindsight a degree of both hypotheses may exist in reality.

1.2.1.3 Proteins

As previously mentioned both integral (*transmembrane*) and peripheral (*receptor*) proteins are key constituents of the cell membrane and are amphiphilic in nature. The former often traverse the lipid bilayer as a single α-helix, a β-barrel or multiple α-helices, acting as transporters of specific molecules (e.g. anions) or signals through the cell membrane.[7] The latter may only be half embedded into the lipid bilayer or alternatively anchored to the membrane in a number of ways, performing tasks of recognition.[27]

With respect to the drug development process, membrane proteins are important as they constitute the vast majority of drug target receptors. A great body of research is aimed at implementing lipidic bicontinuous liquid crystals to crystallise proteins,[50] thus enabling one to gain an understanding of the molecular arrangements of their intrinsic tertiary and quaternary structures. Drug molecules can then be designed to specifically target the site of action.

However, other factors need to be taken into consideration, including the drugs' ability to traverse biomembranes (such as the blood brain barrier,[51,52] in the case of drugs targeting the brain and central nervous system). For example, our understanding of a drug's interaction with biomembranes may help to elucidate which parameters may influence the degree of non-specific binding observed *in vivo*, thus targeting protein receptors with an increased efficacy.[53-55]

1.2.2 Membrane biophysics

The physical properties of biomembranes play a crucial role with respect to the regulation of cellular process. For example, the incorporation of certain types of lipid molecules can affect the activity of membrane proteins.[56] Hence the particular composition of lipids present in the bilayer is non-trivial – the physical properties of biomembranes are discussed herein.

1.2.2.1 Lipid mesophases

Membrane lipid bilayers are biological examples of amphiphilic aggregates forming *lyotropic* liquid crystal mesophases *in vivo*, their formation driven by the hydrophobic effect (see section 1.2.1).[25] The fluid lamellar phase, L_{α}, is represented by a one-dimensional stacking of the lipid bilayers in an aqueous environment, which is the fundamental foundation of all biological membranes.[57] Over the years, researchers have studied various lipid-water model systems and established that several lipid mesophases can form in the presence of water, including the inverse hexagonal and inverse biocontinuous cubic phases.[58,59]

It is thought that non-lamellar lipid mesophases aid processes such as membrane fusion during exocytosis and interbilayer connections; it is postulated that the inverse hexagonal and micellar phases aid various steps in the fusion of two lamellar bilayer membranes,[60-63] which illustrates how cell

membrane function can depend upon the ability of biomembranes to adopt and negotiate various liquid crystalline mesophases.

The total free energy of these lipid mesophases is dictated by three major factors, specifically: (i) the bending energy per unit area (or curvature elasticity, g_c), (ii) the packing of the hydrocarbon chains (g_p) and (iii) the interaction term (a combination of hydration and electrostatic forces, g_{inter}).[53,64] The total free energy can therefore be described as the sum of these components, as indicated by equation 1.1:

$$g_{total} = g_c + g_p + g_{inter} \qquad \text{Equation 1.1}$$

1.2.2.2 Membrane curvature and curvature elasticity (g_c)

The curvature of a membrane can be expressed mathematically, and aims to characterise a two-dimensional membrane that exists in three-dimensional space.[65,66] The two principle curvatures, denoted c_1 and c_2, are required in order to provide a descriptive analysis of the curvature of a membrane and are equal to the inverse of their principle radii of curvature, R_1 and R_2 respectively (see figure 1.4).[67]

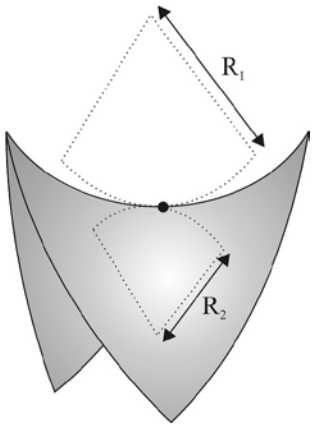


Figure 1.4: **The principle radii of curvature, R_1 and R_2 for a given surface.** The principle curvatures, c_1 and c_2, can be gained by taking the inverse of R_1 and R_2 respectively. The principle curvatures enable a descriptive analysis of the curvature of a surface to be made. Image reproduced from Seddon *et al.*[53]

The mean and Gaussian curvatures for a membrane can therefore be defined, as indicated by equations 1.2 and 1.3 respectively:[65]

$$H = \frac{1}{2}(c_1 + c_2) \qquad \text{Equation 1.2}$$

$$K = c_1 \times c_2 \qquad \text{Equation 1.3}$$

In order to assess the curvature elasticity per unit area of a lipid bilayer, the bilayer is first approximated to a single sheet of infinitesimal thickness. The deformation of this sheet will have an associated energy cost, which will be dependent on the changes in the mean and Gaussian curvatures.[53] The 'Helfrich ansatz' (equation 1.4) describes the curvature elastic energy per unit area for a membrane, which includes terms associated with the energy cost per unit area of changing the mean and Gaussian curvatures (the bending modulus, κ, and Gaussian modulus, κ_G respectively). The term, H_0, describes the spontaneous mean curvature when the surface is relaxed.

$$g_c = 2\kappa(H - H_0)^2 + \kappa_G \times K \qquad \text{Equation 1.4}$$

1.2.2.3 Lateral stress and spontaneous mean curvature

The concept of *lateral stress* aims to give an indication as to the forces acting upon an amphiphile in the plane parallel to the membrane, thus providing a more complete understanding of their tendency to produce curvature. The distribution of lateral stresses will ultimately dictate the spontaneous mean curvature (H_0): the induction of positive and negative spontaneous mean curvatures can be attributed to the non-uniform distribution of lateral stresses present at different depths within the membrane.[1,67] Factors including electrostatic repulsions between head groups, hydrogen bonding and steric repulsions need to be taken into account in order to generate a good understanding of the forces acting upon and between lipids in lipid membranes. Figure 1.5 illustrates an example of a lateral pressure profile used to describe the attractive and repulsive pressures acting upon an amphiphile (π)

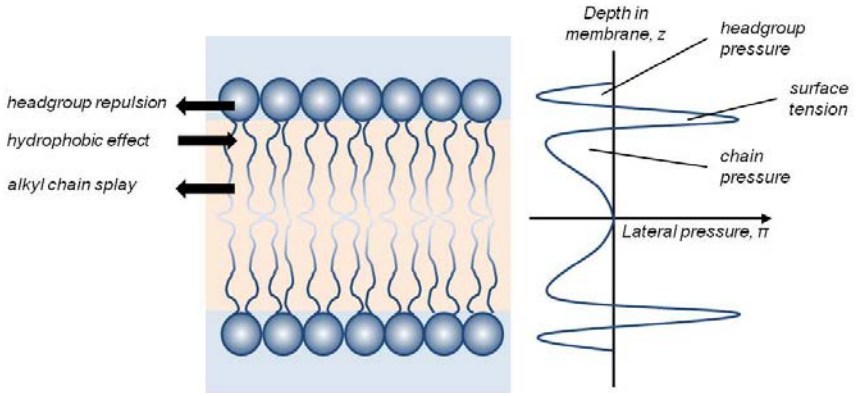


Figure 1.5: **Lateral pressure profile of a lipid bilayer**. The various lateral forces acting upon two lipid monolayers (i.e. a bilayer) at different depths in the membrane are detailed, as well as a lateral pressure profile demonstrating the attractive and repulsive forces present across the two monolayers. Diagram is based on the paper by Ces and Mulet.[67]

in a membrane at differing depths (*z*). Importantly, this profile will vary depending on the nature of the amphiphiles included in the membrane. In order for a monolayer to reach a state of equilibrium, there must be no net pressure acting upon the membrane, hence the following equation holds:

$$\int \pi(z).dz = 0 \qquad \text{Equation 1.5}$$

Depending on the spontaneous mean curvature exhibited by a particular lipid aggregation in aqueous conditions, the lipid may be classed as Type 0, I or II. Type I (e.g. lysophospholipids)[68] and Type II (e.g. 1,2-dioleoyl-*sn*-glycerolphophatidylethanolamine, DOPE) lipids are known collectively as '*non-bilayer*' lipids, typically forming micellar and inverse hexagonal phases in water respectively (see figure 1.6 for illustration).[63,67] Lipid aggregates formed form Type I and II lipids curve '*away from*' or '*towards*' the water interface respectively. This is a direct consequence of the lateral pressures acting upon the monolayer: Type I lipids exert a greater pressure in the head region than the tail region, with the converse argument being true for Type II lipids.[69] Type 0 lipids possess a spontaneous mean curvature that is approximately zero, owing to the exertion of approximately equal pressures in the head and tail regions, and are termed '*bilayer*' lipids (see figure 1.6).

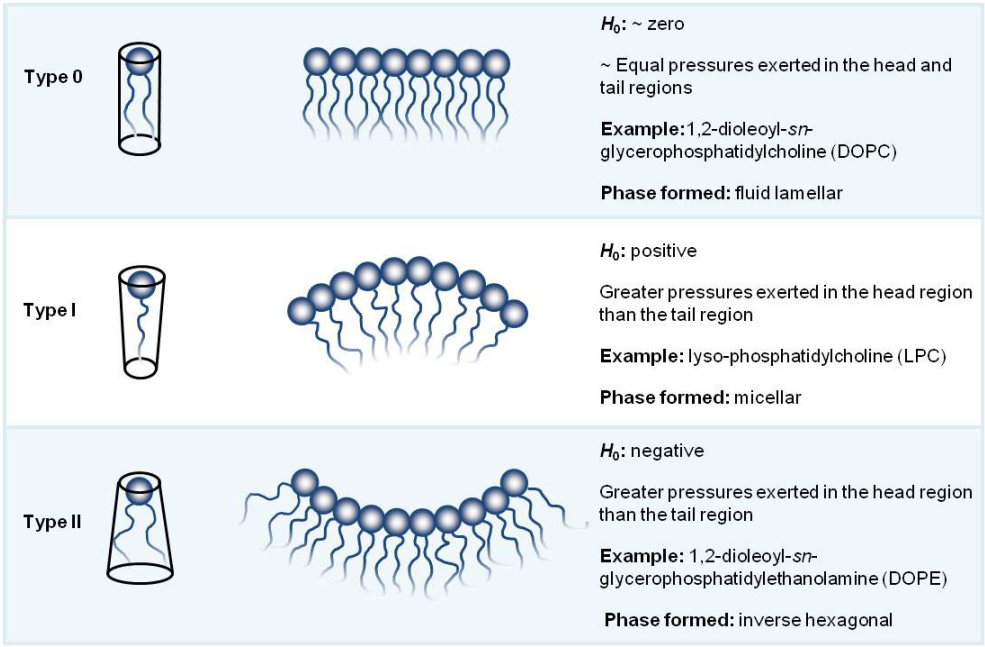


Figure 1.6: **The spontaneous mean curvature (H_0) exhibited by Type 0, I and II lipid aggregates.** This diagram illustrates the arrangement of lipid aggregates (monolayers) when composed of Type 0, I and II species and the spontaneous mean curvature they adopt. Diagram is based on the paper by Ces and Mulet.[67]

The torque tension, τ, stored in a monolayer is described by the first moment of the lateral pressure profile (equation 1.6) and is non-zero.[1] This is indicative of torque stored in a monolayer due to an imbalance of lateral stresses.[1,67]

$$\tau = \int -z.\pi(z).dz \neq 0 \qquad \text{Equation 1.6}$$

The torque that is stored within a monolayer is referred to as the stored curvature elastic stress.

1.2.2.4 Stored curvature elastic stress

Biomembranes generally exhibit fluid lamellar behaviour, yet are composed of many types of lipid. A packing frustration will inevitably ensue, as each monolayer ideally wishes to adopt its spontaneous mean curvature. This frustration is known as the *stored curvature elastic stress*.[67,70] Figure 1.7 explains this physical phenomenon pictorially.

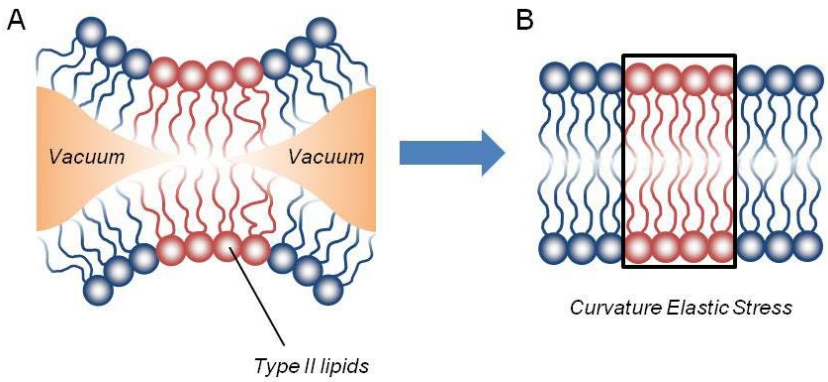


Figure 1.7: **Curvature elastic stress (CES).** (A) Schematic illustrating two monolayers that have adopted their relaxed curvature (theoretical situation). The presence of Type II lipids induces a negative spontaneous mean curvature. (B) The situation in A is energetically unfavourable, as a vacuum would form or the oily chains would be exposed to water. Hence the two monolayers couple back-to-back in order to fulfil the hydrophobic effect. The bilayer possess stored curvature elastic stress as a result (b). Image based on reference [67].

Situation 'A' represents the two monolayers exhibiting their preferred spontaneous mean curvatures. However, the generation of a vacuum and the need to maintain back to back coupling of the monolayers result in the situation presented in 'b'; the ideal situation 'a' is energetically unachievable.

There are many examples present in the literature where forces residing in the bilayer can influence biological processes.[70,71] For example, the degree of curvature elastic stress stored within a membrane is important with respect to the maintenance of lipid homeostasis. The enzyme CTP:phosphocholine cytidylyltransferase (CCT) is regulated as a result of a feedback mechanism which senses the change in stored curvature elastic stress present in a membrane.[1] This highlights the importance of phospholipids, functioning as cooperative entities and not mere structural building blocks.

1.3 DRUG-MEMBRANE INTERACTIONS

As discussed in section 1.2.1, the lipid bilayer of cell membranes regulates the passage of molecules into and out of the cell. It is important to consider the mechanisms by which drug molecules can cross biological membranes. Hence this section provides an overview of the various modes of drug translocation, including passive and active transport.

The drug molecules that have been tested in this thesis comprise one of the largest groups of drug molecules in the pharmaceutical industry – cationic amphiphilic drugs (CADs) – and specifically target the central nervous system. Their amphiphilic nature enables them to intercalate and therefore interact with biological membranes. The chemical composition of CADs facilitates this process; the presence of a secondary / tertiary nitrogen, their flat, planar, amphiphilic structures and low molecular weights – qualities closely related to Lipinski's "rule of 5"[72] – enables fast and efficient coupling to the membrane.

Investigations in this thesis have utilised a subset of a group of drug molecules, specifically chlorpromazine, imipramine and WAY, which have very good specific binding ratios *in vivo* and well defined physiochemical properties.[73] These drugs have to reach their targets in the brain after translocation across many membranes. Their pharmacological targets include D_2-dopamine and 5-HT_2 serotonin receptors and malfunctions of such systems have been closely linked to several disorders, including Parkinson's disease, Huntingdon's chorea, progressive supranuclear palsy (PSP), dystonia, tardive dyskinesia, schizophrenia and depression.[74]

The drug-membrane investigations described in this thesis are fundamental studies, as the results of concentration-dependent experiments (Chapters 2 and 3) do not intend to make physiological assertions. Rather they demonstrate that the novel technologies being developed in this thesis are suitable for investigating CAD-membrane interactions and drug translocation. The study of CAD-membrane interactions is of particular importance as little is known

about the molecular basis of non-specific binding of CAD molecules *in vivo*. Further understanding of this phenomenon will enable more accurate *in vitro* models to be developed, therefore reducing the *in vitro-in vivo* divide and better aiding the drug discovery process.

1.3.1 Passive transport

Passive transport refers to the mechanisms by which molecules are transported across biological membranes *without* the expenditure of cellular energy. The simplest mode of entry into a cell membrane is via simple diffusion, where the molecule to be transported travels down a concentration gradient from a region of high to low concentration (see figure 1.8). Small, hydrophobic molecules, such as oxygen and carbon dioxide, will rapidly traverse lipid bilayers. Small, uncharged polar molecules (water and urea for example) will permeate lipid bilayers to a lesser extent. Large, uncharged polar molecules (e.g. glucose) and those carrying a charge (e.g. ions, cationic drug molecules) will possess lower membrane permeabilities.[7,53]

The electrical potential difference across a membrane is an additional factor that contributes to passive transport, specifically influencing the passive transport of molecules carrying a net charge across a biological membrane. Most plasma membranes possess an electrical potential difference, with the inside of the membrane being negative compared to the outside, thus favouring the passage of positively charged ions into the cell.[7] The net driving force across a membrane can be calculated by coupling contributions due to the concentration and electrical gradients, yielding the *electrochemical gradient*.[7]

Passive diffusion may also be facilitated by passive transporters, i.e. membrane proteins (section 1.2.1.2), to regulate the entry / exit of less permeable molecules. Passive transporters facilitate the transport of molecules down a concentration gradient. Transport is spontaneous and can occur through membrane channels (channel-mediated) or via a passive carrier-mediated transporter (carrier-mediated).[7] Figure 1.8 illustrates the aforementioned

methods of passive transport. Anti-microbial peptides can be considered as passive transporters. They act by inserting themselves into bacterial cell membranes, thus creating aqueous pores and increasing membrane permeability via channel-mediated passive transport.[75] For example, Gramicidin A forms β-barrel secondary structures upon insertion into a lipid bilayer, aiding the transport of ions and small molecules.[75]

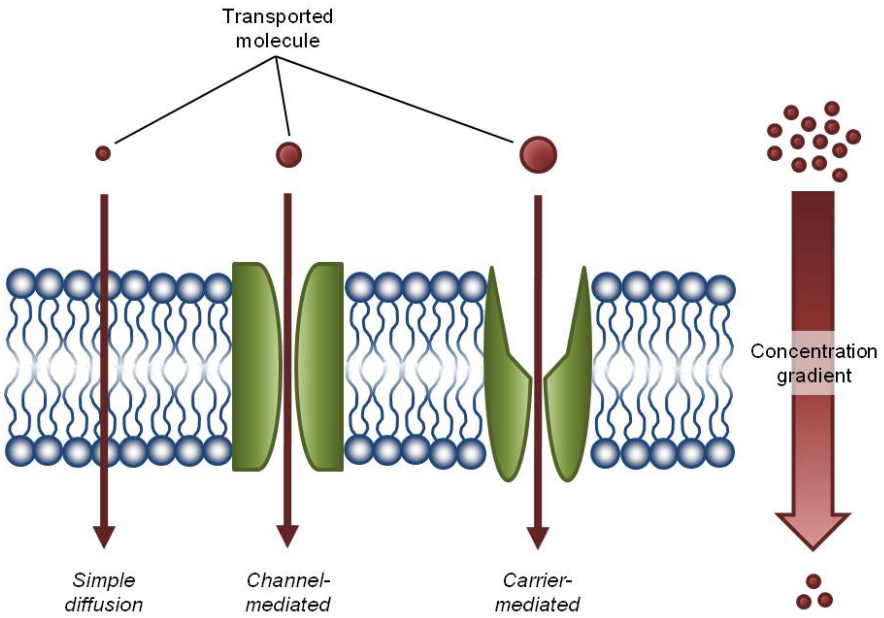


Figure 1.8: **Passive transport.** Diagram illustrating the classical modes by which molecules are transported across cell membranes in a *passive* manner. This includes simple diffusion, in addition to channel- and carrier-mediated transporters.

Carrier-mediated passive transporters interact with the molecule to be transported, binding a specific solute of interest and undergoing a series of conformational changes to transfer the molecule across a lipid bilayer.

1.3.2 Active transport

Active transporters require an expenditure of cellular energy to pump compounds *against* a concentration gradient.[7] Adenosine triphosphate (ATP)-

driven pumps use chemical energy from the hydrolysis of ATP to transport molecules against concentration gradients. This process is known as *primary* active transport and transports molecules directly across a lipid bilayer using uniporters, as illustrated in figure 1.9. The multidrug resistant protein (MDR1), also known as P-glycoprotein, is an example of an ATP-dependant active efflux pump.[76] This membrane transporter seeks to actively pump molecules, often lipophilic drugs directed for action in the brain and central nervous system, back into the blood stream.[77]

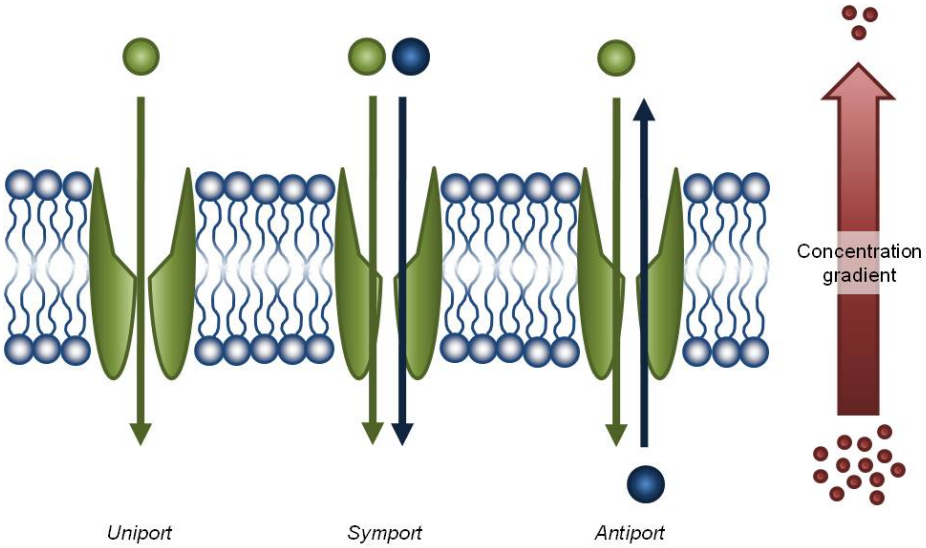


Figure 1.9: **Active transport.** Diagram illustrating the classical modes by which molecules are transported across cell membranes in an *active* manner, i.e. requiring the expenditure of cellular energy. This includes facilitated transport of molecules against a concentration gradient by uniporters, symporters and antiporters (the former is an example of primary active transport, with the latter two being examples of secondary active transport).

Secondary active transport involves the coupling of a second species to the transport of the primary species, hence providing the energy for the membrane transport. The secondary substrate may be translocated in the same direction as the primary species by symporters, such as the sodium-coupled glucose transporters (SGLTs).[78] Proteins that transport secondary species in a direction anti to the primary species are called antiporters, such as the sodium-calcium

(Na^+-Ca^{2+}) exchanger.[79] This protein drives calcium from the cell (against the concentration gradient) by using the opposing movement of sodium ions. Figure 1.9 illustrates the methods of primary and secondary active transport.

1.3.3 Drug translocation via membrane degradation

Baciu *et al.*[54] have proposed a new mechanism of drug translocation across model membranes composed of 1,2-dioleoyl-*sn*-glycero-3-phosphocholine (DOPC). In contrast to both passive and active translocation (sections 1.3.1 and 1.3.2) this mechanism displays a degradative component. Cationic amphiphilic drugs (CADs) have been found to *chemically* degrade model membranes in a catalytic manner to form water soluble micelles carrying drug molecules via an acid catalysed ester hydrolysis.

Experimental studies have investigated the degradation of model DOPC membranes by CADs (haloperidol and spiperone) in a physiological buffer using several techniques, including: small angle X-ray scattering (SAXS), nuclear magnetic resonance spectroscopy (NMR) and fluorescence microscopy (FM). In summary, experimental data gained from both SAXS and NMR experiments, employing mixtures of buffer, CAD and phospholipid, indicate the presence of the degradation products 1-oleoyl-2-hydroxy-sn-glycero-3-phosphocholine (LPC) and oleic acid (OA). Addition of CADs to electroformed giant unilamellar vesicles (GUVs) visually demonstrates the degradation of phospholipid membranes to form membranous fragments.

The experimental data has therefore led to the proposal of the following mechanism for the mode of action of CADs on model membranes (depicted in figure 1.10). Initially, the CAD is incorporated into the interfacial region of the membrane (step 1), as indicated by the SAXS data (and to a certain extent the FM data). The chemical composition of CADs facilitates this process; the presence of a secondary / tertiary nitrogen, their flat, planar, amphiphilic structures and low molecular weights enables fast and efficient coupling to the

membrane. These qualities relate closely to Lipinski's "rule of 5" – a model based on structural features proposed to predict the efficiency of drug translocation (with respect to solubility and permeability).[72]

The CAD molecules redistribute between both leaflets of the membrane (step 2), subsequently resulting in an acid catalysed ester hydrolysis of DOPC to form LPC and OA (step 3). The formation of LPC and OA thus induces the desire to exhibit positive and negative curvatures respectively (section 1.2.2.3), resulting in the formation of micellar species / small vesicles carrying CAD molecules (step 4).[55] Steps 3 and 4 are substantiated by the SAXS and NMR spectroscopy data, which indicate the presence of both micellar and inverse hexagonal phases.[80] It is postulated that these micelles are then able to fuse into further membranous species, where the process is repeated.

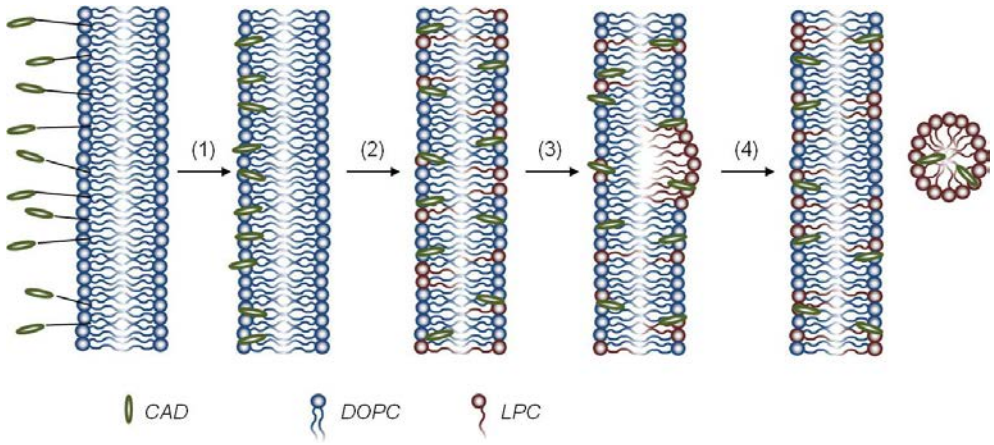


Figure 1.10: **Diagram illustrating the mechanistic implications of membrane degradation.** Drug molecules are incorporated into the interfacial region of the membrane (step 1) and redistribute between both leaflets of the membrane (step 2). This results in an acid catalysed ester hydrolysis of DOPC to form the degradation products LPC and OA (step 3). Consequently, micellar species / small vesicles are formed that carry drug molecules (step 4). Images reproduced from paper by Sebai *et al.*[54]

1.4 HIGH-THROUGHPUT TECHNOLOGIES FOR THE STUDY OF DRUG-MEMBRANE INTERACTIONS

Within the scope of this thesis, the careful manipulation of fluids on the microscale (i.e. microfluidics) and droplet interface bilayer (DIB) technologies provide platforms upon which the interaction of pharmaceutical agents with model lipid membranes may be investigated. It is the further use of microfluidic technologies, coupled with the interfacing of DIB technologies with microfluidic systems, which will lead to the aspiration of producing high-throughput drug-membrane assays, a premise which is at present highly desirable in relation to the pharmaceutical industry. Herein, the major technologies that are currently available for the study of drug-membrane interactions in a high-throughput format are reviewed, including microfluidic, supported lipid bilayer and DIB technologies.

1.4.1 Microfluidics

1.4.1.1 Introduction

Over the last two decades microfluidic manipulation of fluids on the micro-scale (i.e. 10^{-9} to 10^{-18} litres) has become highly desirable in the biological, chemical and medical sciences.[81-92] Development of microfluidic technologies has continued, owing to the desirable features that are afforded with system miniaturisation. For example, microfluidic technologies enable small fluid volumes to be manipulated with ease, are associated with low production costs, yield reduced instrumental footprints owing to their small size, afford enhanced analytical performances and enable thousands of samples to be sampled per second.[93] Droplet-based microfluidics offers further advantages, as discrete and monodisperse experimental compartments are afforded.[94] Therefore the opportunity to perform quantitative analyses on single molecules and cells is presented, as is the opportunity to perform large numbers of

experiments. Furthermore, high-throughput analysis of systems in *parallel* have emerged as a direct consequence, enabling DNA analysis and the possibility for pharmaceutical screening and drug discovery to be conducted on a single microfluidic chip.[95,96] Figure 1.11 illustrates an example of a microfluidic device.[88,97]

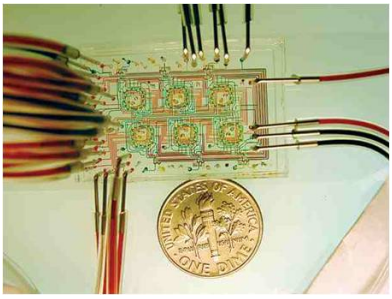


Figure 1.11: **An example of a microfluidic device.** The device has been photographed next to a one dime coin in order to provide an indication of its relative size. Image reproduced from the papers by Balagaddé *et al.*[97] and Whitesides *et al.*[88]

Microfluidic devices are typically made from poly(dimethylsiloxane) (PDMS). PDMS is often used as it has many desirable characteristics. These include the following:

(i) It is a low cost material;[85]

(ii) It is gas permeable and therefore oxygen can be supplied to cells contained within PDMS devices, for example;[98]

(iii) It can successfully translate features, with a resolution of less than 100 nm;[99]

(iv) It is optically transparent between 240-1100 nm;[99]

(v) It is chemically inert and nontoxic;[99,100]

(vi) It can be bonded reversibly and irreversibly to glass and PDMS substrates (irreversible bonding is achieved by subjecting the PDMS to an air or oxygen plasma);[101-103]

(vii) It can be deformed easily and reversibly, as it is an elastomeric material, therefore enabling valves and pumps to be incorporated into device designs.[104,105]

1.4.1.2 Laminar flow in microfluidic systems

Within microfluidic systems, the underlying physics is quite different to that on the macroscale. Devices on the micro-scale exhibit primarily laminar flow qualities, controlled diffusion and high surface area / volume ratios.[106] The distinction between turbulent and laminar flow can be characterised by use of the Reynold's number, R_e, which defines the ratio of inertial to viscous forces. Equation 1.7 is used to calculate the Reynold's number, which is dependent upon the following parameters: the fluid density (ϱ), velocity (υ), viscosity (μ) and the hydraulic diameter (D_h).[106,107]

$$R_e = \frac{\rho v D_h}{\mu} \qquad \text{Equation 1.7}$$

Importantly, when R_e < 2300, viscous forces will dominate and the transition from turbulent to laminar flow will occur. Figure 1.12 A and B illustrate examples of systems dominated by laminar (R_e < 2300) and turbulent (R_e > 2300) flow regimes respectively.[106,108] Laminar flow is often advantageous, as multiple streams flowing parallel to one another will not mix in a turbulent fashion, hence inter-stream mixing will only occur by controlled diffusion. Droplet generators often use multiple laminar streams to vary the composition of the aqueous phase in a controlled manner, meaning that the contents of each discrete droplet produced is controlled and flexibility is afforded by the microfluidic platform. The combination of multiple laminar flows in this manner, however, may appear detrimental, as mixing can only occur slowly via

diffusive transport. The introduction of snake-like channels ensures that rapid mixing ensues by chaotic advection.[109]

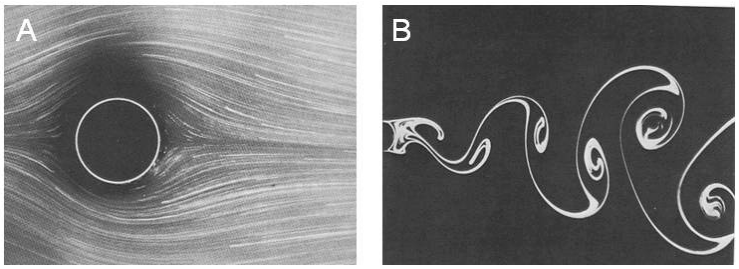


Figure 1.12: **Laminar and turbulent flow.** The diagrams illustrate examples of systems dominated by: (A) laminar (R_e < 2300) and (B) turbulent flow regimes (R_e > 2300).[110]

1.4.1.3 Segmented flows

Rather than flowing fluids through microfluidic channels using a single-phase, continuous format, a segmented flow is often adopted in order to eliminate problems associated with dispersion of the reaction mixture.[111-113] Figure 1.13 A illustrates the occurrence of this spreading effect. Segmented flow is achieved by creating discrete microdroplets that are carried by an immiscible "carrier fluid" through a microchannel. Each droplet acts as an individual experimental vessel, with the interaction of each discrete droplet with the walls of the microchannel being minimised, hence reducing loss of reagents and cross-contamination. Figure 1.13 A and B illustrate the differences between continuous and segmented flow microfluidics.

Droplet formation is also advantageous as it enables rapid, efficient and reproducible mixing to occur inside each microdroplet.[111] Furthermore, as thousands of droplets may be produced per second using this technique, it also means that large data sets can be collected therefore enabling more sophisticated statistical analyses to be performed.

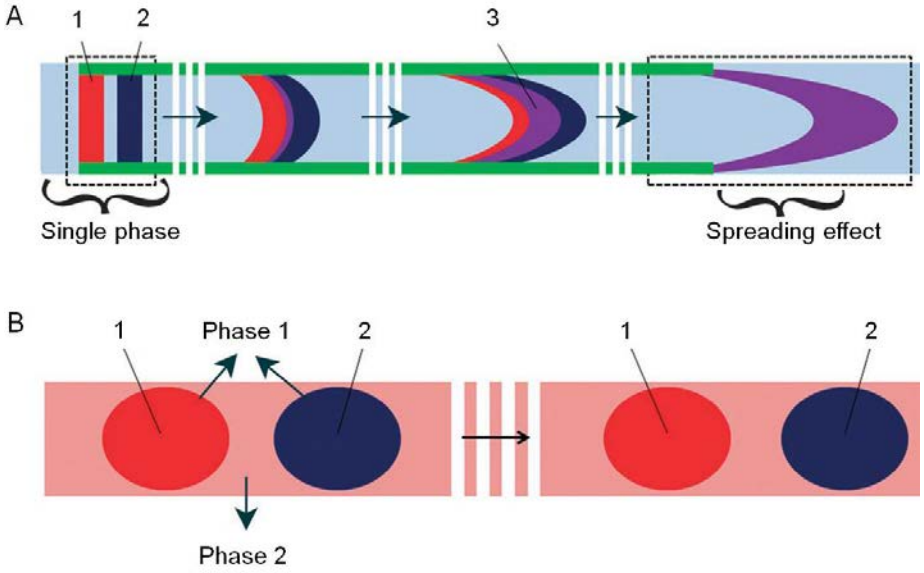


Figure 1.13: **Continuous versus segmented flow.** (A) Continuous flow format, comprised of reagents carried in a miscible phase (i.e. a single phase). It can be observed that the two reagents (1 and 2) suffer from Taylor dispersion (see the box labelled "spreading effect"), consequently mixing and forming a new compound (3). Additionally, the channel edges become spoiled by both reagents, resulting in cross-contamination as well as loss of reagent (represented by the green lines). (B) Segmented flow format, comprised of discrete microdroplets carried in an immiscible phase (i.e. two phases). As microdroplets are discrete reaction vessels they do not suffer from Taylor dispersion nor is cross-contamination / loss of reagent to the microchannel an issue. Image reproduced from the paper by Casadevall i Solvas *et al.*[112]

1.4.1.4 Methods for forming microfluidic droplets

This section will consider the formation of *water-in-oil* droplets only, as this is the format most relevant to this thesis. Other types of droplet systems can be created, for example oil-in-water and gas-liquid dispersions.[114]

It should be noted that the first realisation of segmented flow was achieved using a capillary flow.[112,115] However, the major methods used to generate water-in-oil droplet formation in a planar chip format include: (i) T-junction[113,116,117] and (ii) flow focusing.[118]

Figure 1.14 A illustrates the T-junction method.[113,116,117] The name originates from the fact that oil and aqueous streams are brought into contact with one another at a "T" junction. Depending on the delicate balance between the oil and aqueous flow rates, the two phases will meet and the aqueous phase segmented. Consequently, water-in-oil droplets are formed. Importantly, surfactant molecules are incorporated into in the oil stream (carrier fluid) to stabilise the oil-aqueous interface and hence prevent the droplets from coalescing.

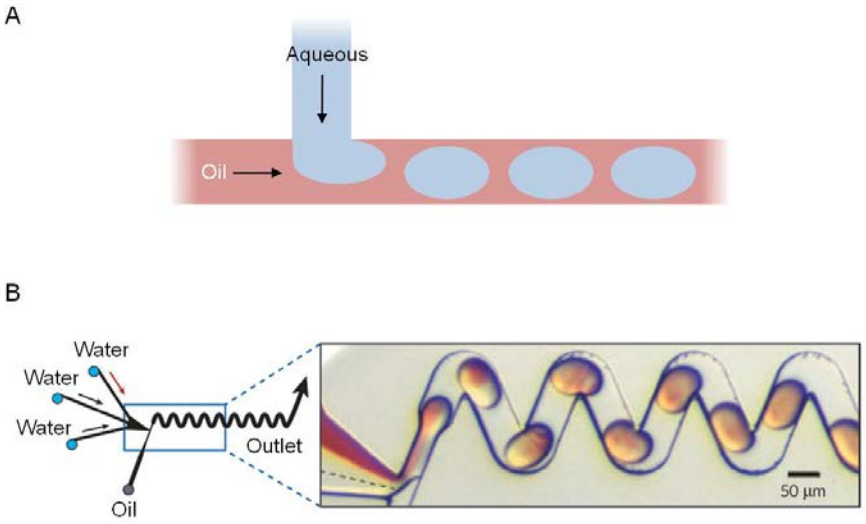


Figure 1.14: **T-junction technique for the formation of microdroplets in a planar chip format (i.e. segmented flow).** (A) A generic representation of the set up, where channels, carrying oil and aqueous streams, meet at a "T" junction. At this point the aqueous flow can be segmented. (B) An example of a microfluidic device possessing a T-junction for droplet formation. Several aqueous streams can be focussed onto the oil stream by making use of laminar flow. Winding, snake-like channels are incorporated to aid mixing of the droplet contents. This image has been reproduced by the paper by Bringer *et al.*[119]

More than one aqueous stream can be brought into contact with the oil carrier fluid if desired, as illustrated in figure 1.14 B. Here the properties of laminar flow have been exploited to control the composition of the aqueous input. Often snake-like channels are incorporated into the channel design shortly

after the point at which droplet formation occurs to aid mixing of the droplet contents via chaotic advection. The device displayed in figure 1.14 B illustrates an example of the mixing process.

The second method that can be used to create a segmented aqueous flow of water-in-oil droplets is the flow focusing technique.[118] The basic principle behind this technique is illustrated by figure 1.15 A. Three microchannels (labelled 1-3, figure 1.15 A) convene at a central point in the device. Fluids flowing through these microchannels, towards the meeting point, then exit

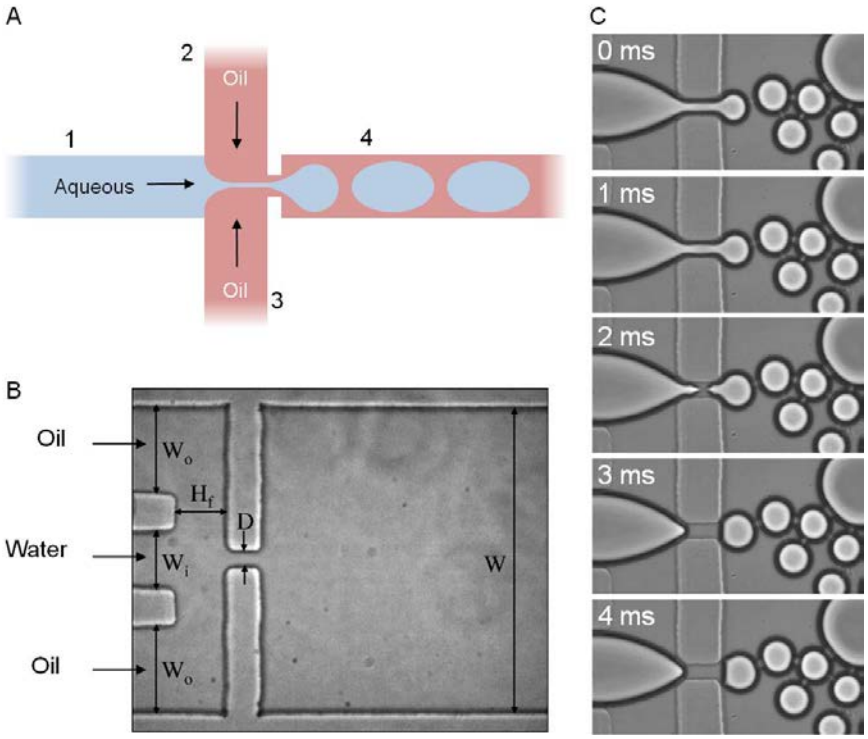


Figure 1.15: **Flow focusing technique for the formation of microdroplets in a planar chip format (i.e. segmented flow).** (A) Schematic illustrating the general setup that is required in order to form a segmented flow using the flow-focusing technique. (B) An example of a real microfluidic chip that is designed to enable droplet formation using the flow focusing technique. (C) A series of images illustrating the formation of a single droplet using the device detailed in B. Images B and C have been reproduced by the paper by Anna *et al.*[118]

through an orifice into a fourth microchannel (labelled 4 in figure 1.15). Specifically, two oil streams (denoted by 2 and 3 in figure 1.15 A) flow towards the central point, i.e. in opposing directions to one another. These are used to 'focus' a third stream – the aqueous stream (denoted by 1 in figure 1.15 A) – that meets two oil streams flowing through channels 2 and 3 (figure 1.15 A). As a result, the focussed aqueous stream flows through the orifice and into channel 4 (figure 1.15 A), where the aqueous stream is segmented and forms discrete microdroplets (again under optimum conditions). Figure 1.15 B illustrates a real example of a microfluidic chip that utilises the flow focusing technique for droplet generation: the three channels, that are to contain the oil and water streams, are denoted and the central point, where the trajectories of each flow meet, can be viewed. Figure 1.15 C provides a series of successive images, illustrating how a single droplet is formed using the flow focusing technique (using the device depicted in figure 1.15 B).

1.4.1.5 Droplet manipulation

After having generated a series of microdroplets, either by using the T-junction or flow focusing techniques in a planar chip format, there may be other operations that the researcher may wish to perform. The following operations are currently available and can be used to manipulate droplets, forming the extremely handy droplet "tool kit":

(i) Droplet merging. Either "active" processes (such as electrocoalescence, see figure 1.16 A)[120] or passive processes (see figure 1.16 B)[121] can be used to control the fusion of droplets. The passive process cleverly uses strategic variations in channel geometry to control fluid flow and hence droplet merging;

(ii) Droplet splitting.[122] As a result of introducing droplets to a T-junction (figure 1.16 C), droplets can be broken up in a passive manner. It can be

observed from figure 1.16 C that each initial plug is subsequently split up into eight smaller droplets.

(iii) Droplet storage. Droplets may be stored for a period of time in delay channels,[123] traps[124,125] and reservoirs,[126] as illustrated in figure 1.15 D, E and F respectively;

(iv) Droplet sorting.[127,128] Figure 1.16 G illustrates that droplets can be sorted by applying an electric field, which generates a dielectrophoretic force and attracts the droplets (1 = no electric field applied, 2 = electric field applied).

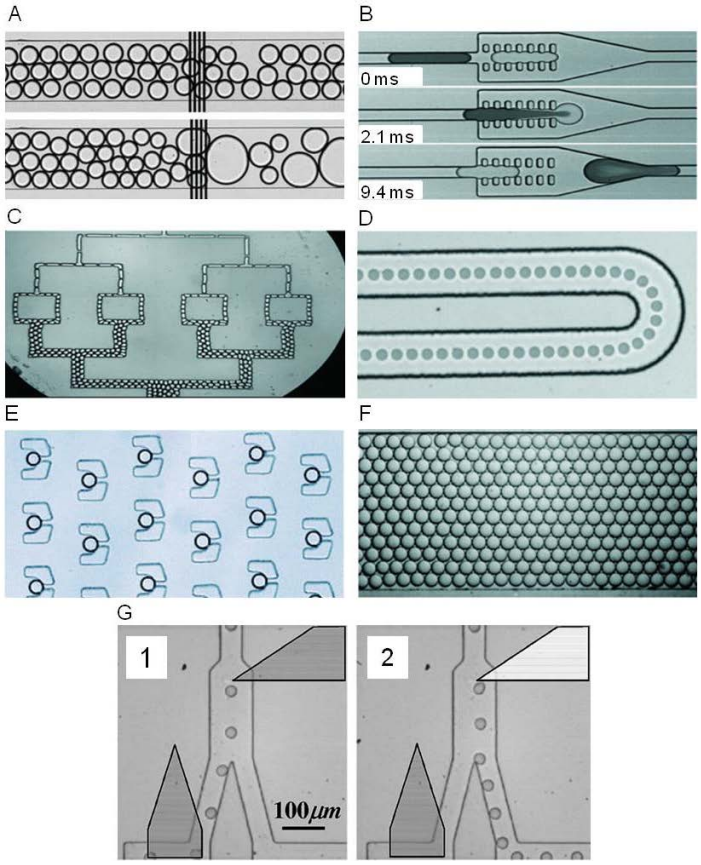


Figure 1.16: **Operations that can be performed on droplets after having been generated.** (A) Active droplet merging, e.g. by electrocoalescence.[120] (B) Passive droplet merging.[121] (C) Droplet splitting.[122] (D) Storage of droplets in microfluidic channels.[123] (E) Storage of droplets in trapping devices.[124,125] (F) Storage of droplets in reservoirs.[126] (G) Sorting of droplets, by using dielectrophoretic manipulation.[127] Images have been reproduced from the respective papers.

1.4.1.6 Microfluidic technologies amenable for investigating drug-membrane interactions

The preparation of homogenous populations of small unilamellar vesicles (SUVs, 50-200 nm in diameter) using manual methods (e.g. extrusion methods) can be achieved very easily and is a popular choice of assay format for the investigation of exogenous species upon model lipid membranes. More recently, however, there have been developments in microfluidic technology that allow the generation of SUVs using flow focusing techniques.[129,130] These techniques are advantageous as the ability to control the diameter of a monodisperse population of SUVs in a precise manner is highly desirable (for example, to investigate the effect of membrane curvature on a system).[67] Moreover, such developments will enable both SUV synthesis *and* measurement to be conducted simultaneously on a single chip, thus increasing the high-throughput capabilities of the technique. Notably, SUV assays have not been performed in a microfluidic format to date. Hence part of the work presented in this thesis has sought to demonstrate that SUV assays can be translated into a microfluidic format, as detailed in chapters 2 and 3.

Giant unilamellar vesicles (GUVs, on the order of 1-200 μm in diameter) are also popular model systems for investigating an expansive range of biological events in real time.[131,132] The formation of GUVs, however, is a much more elusive process: traditional methods for forming GUVs, which includes swelling of dried lipid films with aqueous solutions,[133,134] solvent evaporation[135] and electroformation[136,137] rarely produce sufficient numbers of vesicles in the micrometer range and do not yield monodisperse populations. Attempts have been made to use microfluidic technologies for the formation of GUVs, via the electroformation technique.[138,139] These attempts have been successful in generating a plentiful supply of GUVs in solutions of high ionic strength, which is important if physiological conditions are required and often difficult to achieve in non fluidic systems. However, the major problems associated

with each of these techniques include the inability to control the monodispersity and lamellarity of the GUVs.

Several methods exist for the formation of monodisperse populations of giant unilamellar vesicles, which include: (i) the "lipid-coated ice droplet hydration method",[140] (ii) GUV formation by inkjet printing[141,142] and (iii) GUV formation

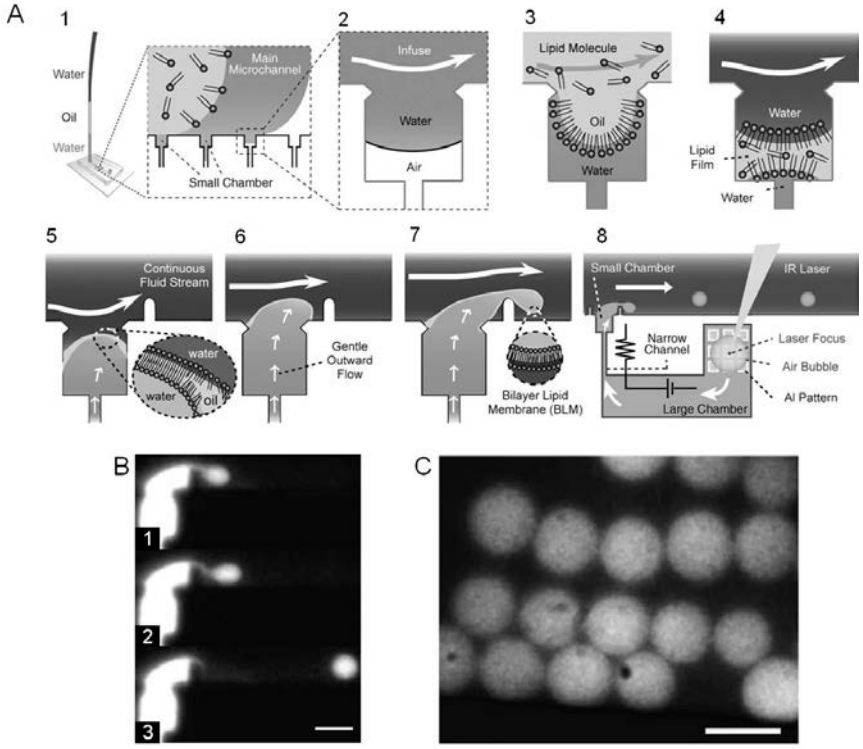


Figure 1.17: **High-throughput formation of monodisperse, unilamellar GUVs using microfluidics.** (A) The steps involved in generating a GUV. First a plug of water, followed by a plug of oil (containing lipids), followed by another plug of water are introduced into a microchannel and flow over small chambers that form T-junctions with the main channel (1) – the air is squeezed out of the small chambers during this process through the PDMS walls (2). A lipid monolayer forms at the first interface (water-oil, see 3), with a second monolayer forming at the second interface (oil-water, see 4). The fluid stream that crosses each of the T-junctions draws the lipid film out of the small chamber (5), further thinning the bilayer as it protrudes (6). A small PDMS post aids vesicle formation (7). An air bubble is generated in a large chamber (connected to the small chambers), using a laser spot, in order to aid the gentle outward flow of the protruding bilayer film (8). (B) Images 1-3 illustrate the formation of a single GUV that contains fluorescent calcein. (C) Fluorescence image of several GUVs generated using this technique. Note that the scale bars in B and C represent 20 μm. Images reproduced from Ota *et al.*[143]

using microfluidic T-junctions (figure 1.17).[143] The latter two techniques are highly advantageous, as populations of *unilamellar* GUVs can be produced (i.e. those that consist of a single-walled lipid bilayer) in a high-throughput manner. Frequencies of up to 200 Hz can be attained using these two methods,[141] though only the method by Ota *et al.*[143] uses microfluidics for GUV formation. Figure 1.17 illustrates the process that is undertaken to produce single-walled, monodisperse solutions of GUVs in high-throughput.

Importantly, microfluidic devices have also been used to investigate the permeability of drug- and other biomolecules across more complex membrane systems. For example, researchers have looked at drug permeability across the endothelium, where cells have either been trapped in microhole arrays[144] or cell cultures grown in the actual device.[145] The latter study highlights the importance of simulating experimental conditions that represent the natural environment, accounting for factors such as the shear-stress, which affects drug uptake across cardiovascular endothelial cells.[145]

More recently, researchers at Harvard University have developed a novel device, coined a "lung-on-a-chip" device.[146] The device is made from micropatterned PDMS and consists of three layers sandwiched together: a porous membrane and upper / lower layers, as illustrated in figure 1.18 A and B. Human epithelial and endothelial cells are cultured on either side of the porous membrane, which is coated with extracellular matrix, and supplied with nutrients / cells using directed microfluidic flow. In order to simulate the breathing action imposed on the cells by the action of the lung, a vacuum pump is used; importantly, the inherent elasticity of PDMS means that it is able to withstand the change in pressure and hence replicate the process of 'breathing' in an analogous manner to a lung (see figure 1.18 C). This research demonstrates that immune responses can be triggered upon the introduction of bacteria, as well as the induction of inflammation upon the introduction of toxins, and importantly suggests that such platforms can be used to screen for drug-responses and efficacy on the cellular level.[146] This research will no doubt

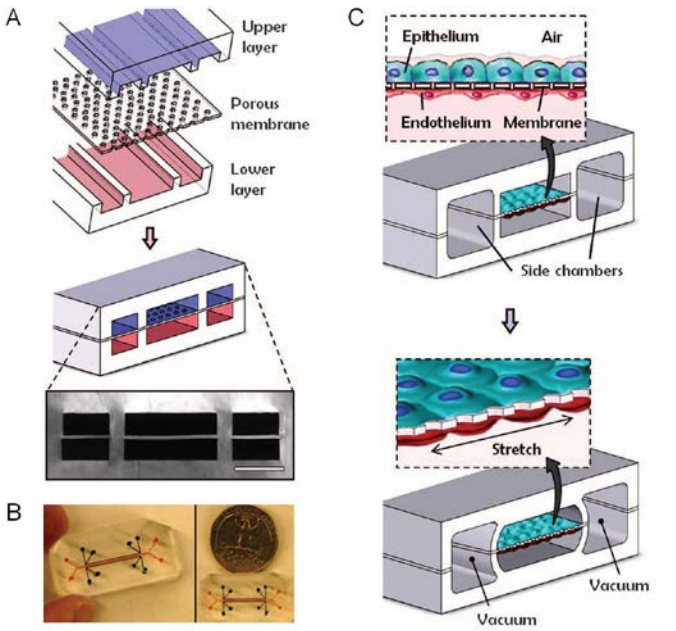


Figure 1.18: **Development of "lung-on-a-chip" devices.** (A) Here the nature of the device is illustrated, which is comprised of three PDMS layers, one of which contains micropores. The scale bar represents 200 μm. (B) Illustrates a photograph of the device. (C) These images demonstrate how the device is able to 'breath' upon the application/removal of a vacuum, thus mimicking the environment found in a lung. Epithelial cells are cultured on one side of the porous membrane and endothelial cells on the other. The images have been reproduced from Huh *et al.*[146]

lead the way in the development of more sophisticated "organ-on-a-chip" devices, resulting in advances in drug discovery.

Notably, the advent of droplet-based microfluidics has also enabled the polymerase chain reaction (PCR) to be performed in a microfluidic format, which is highly desirable to the pharmaceutical industry.[123] Ultimately, one can envisage amplifying a specific region of DNA, encoding for a specific protein of interest, coupled with the online *in vitro* expression of that protein. If one could amplify numerous mutated versions of the DNA sequence in parallel, thus inducing random mutations in the expressed protein structures, one could also screen for potential inhibitors / promoters of that protein. Droplet-based, high-throughput technologies have also played an important role in controlling

protein crystallisation, crucial for structure based drug-discovery, as well as furthering our understanding of the variables involved in the process.[147] Additionally, kinetic measurements can be easily performed using droplet technologies, which in turn can reveal important information about a drug's behaviour.[148]

In summary, this section has introduced the topic of microfluidics and has highlighted many examples of current microfluidic platforms that can be used to monitor the effect of drug-membrane interactions and are applicable to the pharmaceutical industry. The following section will consider a relatively new technology, namely supported lipid bilayers (or SLBs), which has created further opportunities for probing the interaction of various species with model membranes.[149]

1.4.2 Supported lipid bilayers (SLBs)

A supported lipid bilayer (SLB) can be defined as "a single, continuous phospholipid bilayer" that is supported on a substrate of choice,[150] such as glass,[151,152] mica,[153] titanium dioxide[154] or PDMS,[155-158] via physical interactions existing between the support and bilayer.[159] Figure 1.19 illustrates the nature of an SLB, formed by introducing a vesicle population to a solid support.

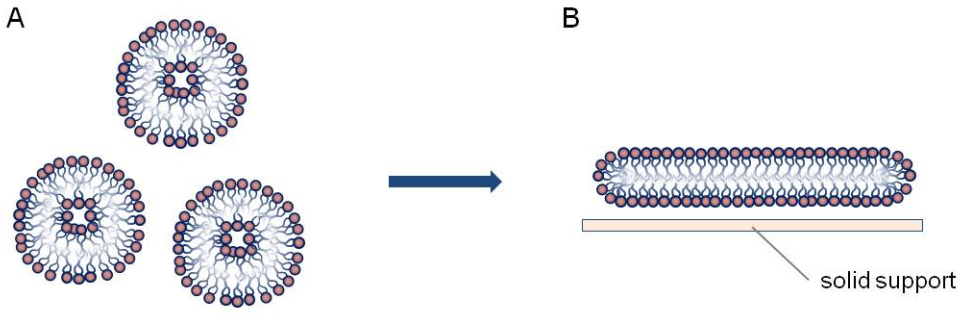


Figure 1.19: **Supported lipid bilayer.** (A) Population of vesicles. (B) Supported lipid bilayer (SLB) formed by introducing vesicles to a solid support.

SLBs have been used extensively to model biological membranes in milieux that can be manipulated and designed to suit the problem at hand; an intriguing example involves using SLBs to aid the design of biointeractive interfaces on titanium oxide, a biocompatible material often used in implant technology.[160]

1.4.2.1 Formation of supported lipid bilayers

Section 1.4.2.2 will consider solely solid-supported lipid bilayers, although a variety of surface confined membrane models exist:[161-163] polymer-cushioned lipid bilayers,[164-168] hybrid bilayers (i.e. a self-assembled monolayer coupled to a lipid monolayer),[169,170] tethered lipid bilayers,[171] freely suspended lipid bilayers[172] and supported/tethered vesicular layers[173,174] are the major examples detailed in the literature (see figure 1.20). Polymer-supported bilayers incorporate a

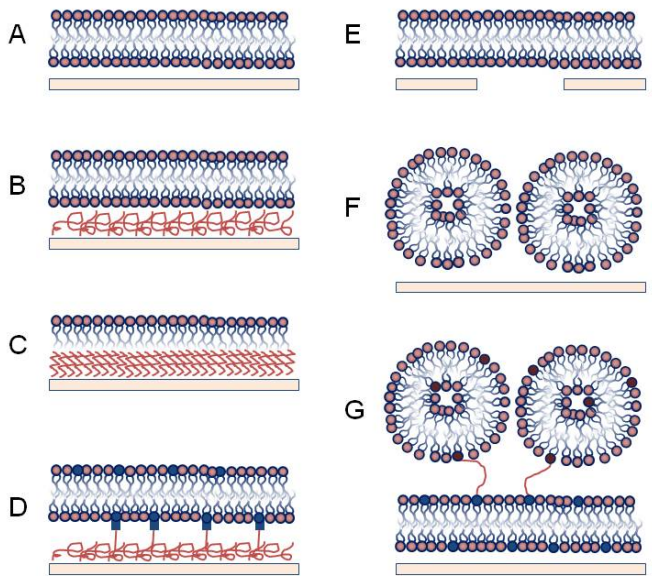


Figure 1.20: **Approaches used to deposit fluid phospholipid bilayers upon a substrate.** (A) solid-supported lipid bilayer, (B) polymer-cushioned lipid bilayer, (C) hybrid bilayer (consisting of a self-assembled monolayer and a lipid monolayer), (D) tethered lipid bilayer, (E) freely suspended lipid bilayer, (F) and (G) supported vesicular bilayers. Diagram reproduced from Richter *et al.*[161]

polymer film that is deposited onto the substrate to act as a soft cushion and functioning in an analogous manner to that of the cytoskeletal network.[175] Interestingly, Johnson *et al.*[165] have employed both solid supported and tethered egg phosphatidylcholine monolayers, incorporating the protein ponticulin, to assemble an *in vitro* actin cytoskeletal scaffold upon the supported lipid bilayer. Deposition of polymeric material onto substrates to support phospholipid bilayers is particularly advantageous if transmembrane proteins are to be reconstituted into lipid bilayers. Often proteins can become immobilised and thus denatured, as a result of unfavourable protein-substrate interactions, if solely water is the medium residing between the supported bilayer and substrate.[166]

Importantly, the lipid bilayer must retain its fluid nature after deposition onto a solid support, thus maintaining the dynamic and structural properties of a biomembrane. Typically a thin layer of water, 10-20 Å in thickness (as determined by specular reflection of neutrons),[176] resides between the substrate and bilayer, to exclude the occurrence of inhibiting interactions. Fluorescence recovery after photobleaching (FRAP) measurements are often used to assess the lateral fluidity of the deposited lipid bilayers.[177]

In 1984, Brian and McConnell instigated a method to deposit a single supported lipid bilayer upon a hydrophilic solid support; their technique involved flowing a solution of small unilamellar lipid vesicles (SUVs) over the substrate of choice.[178] The formation of an SLB is generally considered to comprise of two main steps: (i) adhesion of SUVs to the substrate followed by spontaneous rupture and (ii) coalescence of these bilayers to form the SLB.[161,179] Understanding the mechanisms of and factors influencing vesicle adsorption and rupture, to form a single continuous bilayer, has contributed largely to the advancement of SLB technologies over the last 10 years; a coherent review is afforded by Richter *et al.* and should be consulted for further information.[161] In summary, the lipid deposition pathway chosen to form SLBs is largely governed by the interplay between: (i) the bilayer and

substrate, (ii) interbilayer interactions and (iii) intrabilayer interactions. The contribution provided by each of these effects to enable successful bilayer deposition is greatly dependent upon numerous parameters, including: the nature of the substrate;[161] vesicle composition, charge, size, physical state and concentration;[180] the aqueous environment;[181] and, the presence of ions.[182,183] Quartz crystal microbalance with dissipation monitoring (QCM-D) is a powerful technique, which has enabled the determination of the lipid deposition pathways of vesicles and hence furthers the understanding of vesicle rupture mechanisms and SLB formation. For example, if the adsorbed vesicle remains intact, a high dissipation is observed. Conversely, if the adsorbed vesicle has ruptured, resulting in SLB deposition, a low dissipation is observed.[161] Figure 1.21 illustrates the various mechanisms of vesicle rupture that result in SLB formation, as determined using this method.

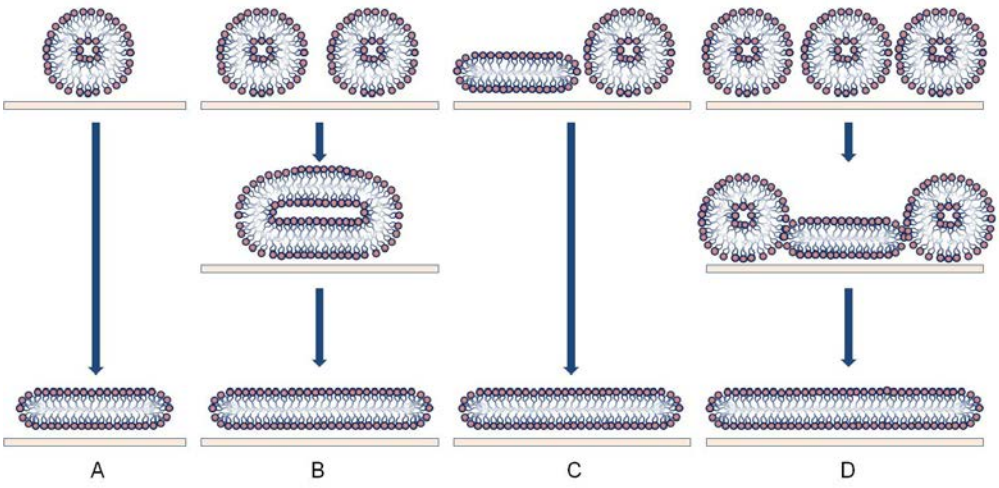


Figure 1.21: **Diagram illustrating the various mechanisms of vesicle rupture to yield SLB formation.** (A) The spontaneous rupture of alone vesicle, (B) adjacent vesicle fusion followed by vesicle rupture, (C) induced vesicle rupture by the active edge of an SLB, (D) vesicle fusion occurrence at critical vesicular coverage cooperative action. Note that the illustration is not to scale and is based on the figure detailed in the paper by Richter *et al.*[161]

Cremer and Boxer have noted that the spreading of lipid bilayers, after deposition, halts when the amount of lipid residing on a substrate is fixed.[181] This phenomenon is self-limiting, due to the highly unfavourable intermolecular interactions that phospholipid molecules would otherwise experience.[184] The lateral expansion has been found to be restricted when the lipid area exudes *ca.* 106% of its initial size (for egg phosphatidylcholine bilayers); this is termed the *self-limiting lateral expansion* of lipid bilayers[181] and proves to be an important feature with regard to the patterning of SLBs. Its application is discussed further in section 1.4.2.2.

1.4.2.2 Patterning supported lipid bilayers

It is desirable to pattern solid-supported lipid bilayers in order to create a series of regions that are distinct and separate from one another, thus enabling more than one investigation to be conducted at any one time, i.e. increasing the high-throughput capabilities associated with this technique. This has therefore led to the introduction of 'barriers', to create *corralled* regions. Lipids can diffuse laterally *within* the corralled regions, with diffusion *between* the corrals being prevented.[150] Several methods exist that enable one to incorporate barriers to lateral diffusion within the SLBs and these are reviewed herein. The majority do not require the presence of *physical* barriers to confine lateral diffusion to specific regions, exploiting the characteristic self-limited lateral expansion of lipids and eliminating the presence of unfavourable lipid-barrier interactions that are poorly understood. Methods for patterned SLB formation include the following:

(i) Mechanical scratching of glass

(ii) Blotting and stamping by microcontact printing (μCP)

(iii) Polymer lift-off technique

(iv) Aluminium lift-off technique

(v) Patterning by polymerisation

(vi) Hydrogel stamping

Mechanical scratching

Mechanical scratching of glass substrates (for example using a sharp metal rod) affords the simplest method of creating such a barrier,[150,185,186] albeit the least controllable. In this instance a topological barrier is produced that discourages the expansion of the deposited lipid bilayer.

Blotting and stamping by microcontact printing (μCP)

The process of "blotting and stamping", using microcontact printing (μCP), provides an alternative option for the creation of patterned SLBs, as illustrated by figure 1.22.[177,187-191] This methodology relies on using a pre-patterned PDMS stamp either: (i) to "blot" and hence remove specific regions of a preformed SLB or (ii) to "stamp" the SLBs attached to the pre-patterned PDMS stamp onto a fresh substrate, as illustrated by figure 1.22 A and B respectively. The latter process must be performed under aqueous conditions in order to prevent removal of the SLBs from the PDMS stamp. Alternatively, SLBs may be stamped onto clean substrates by first creating SLBs on the microscale features of patterned PDMS stamps by subjecting the oxidised stamp to a solution of small unilamellar vesicles, as illustrated in figure 1.22 C. The excess lipid is removed by shaking the stamp in the aqueous solution and the PDMS-bilayer ensemble positioned onto a clean substrate. This method is more reliable than the blotting method for SLB deposition and provides the most efficient transfer of lipid bilayer.[190]

Visualisation of the patterned SLB via the blotting and stamping method has been achieved by incorporating 1 mol % N-(Texas Red sulfonyl)-1,2-dihexandeconoyl-sn-glycero-3-phosphoethanolamine (Texas Red DHPE) into small unilamellar vesicles and monitoring the fluorescence of the fluorophore using fluorescence microscopy. Images D and E in figure 1.22 illustrate that specific regions of the SLB were successfully removed using this technique and distinct corralled regions are evident.

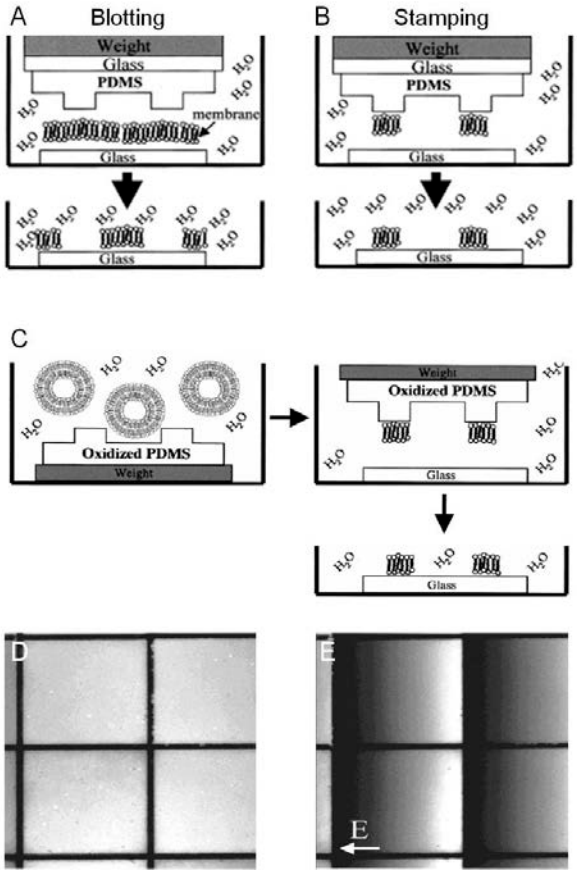


Figure 1.22: **Diagrams illustrating the "blotting" and "stamping" techniques developed by Hovis and Boxer to create patterned, supported lipid bilayers.** (A) A pre-patterned PDMS stamp is oxidised and then used to remove or "blot-out" regions of a pre formed, solid-supported SLB. (B) The PDMS stamp can also be used to transfer blotted SLBs onto a fresh glass substrate. (C) An alternative method for stamping a SLB onto a glass substrate, where the PDMS stamp is subjected to a solution of small unilamellar vesicles after oxidation followed by a rinsing stage. (D) Epifluorescent images of the solid-SLB, doped with 1 mol % N-(Texas Red sulfonyl)-1,2-dihexandeconoyl-sn-glycero-3-phosphoethanolamine (Texas Red DHPE), after blotting and (E) after application of an electric field gradient parallel to the plane of the bilayer. Diagrams have been reproduced from the paper by Hovis *et al.*[187,190]

Image E in figure 1.22 illustrates that Texas Red DHPE lipids, attracted to the anode upon the application of an electric field parallel to the plane of the bilayer (thus generating a concentration gradient), are confined to the corralled regions i.e. that the areas of lipid bilayer removed by blotting act as effective

barriers to lateral diffusion between adjacent corrals. Additionally, removal of the electric field gradient and fluorescent recovery after photobleaching (FRAP) measurements both indicate that the diffusion coefficients of the labelled lipids (1.21 μm^2 / s) are consistent with reported values in the literature under analogous conditions,[190] a feature crucial for studies on lipid membranes.

In addition to forming barriers by removing portions of the SLB via the blotting methodology, barriers to lipid lateral diffusion may be gained by stamping down barriers comprised of protein onto substrates. Kung *et al.* describe two ways in which this may be achieved.[177] Firstly, the protein barrier may be stamped onto a glass substrate using a pre-patterned PDMS stamp, in an analogous manner to what has been described previously for lipids. A solution of small unilamellar vesicles is then flowed over the stamped protein barriers and patterned SLB formation is achieved. Figure 1.23 A-C illustrates this approach.

Secondly, specific portions of the SLB may be removed by blotting, after which protein is 'caulked' into areas where lipid has been removed; protein caulking is illustrated by Figure 1.23 D-F. Figure 1.23 G and H represent false colour images of fluorescent protein (Texas Red bovine serum albumin, TR BSA, red) and lipid (labelled with 2 mol % nitrobenzoxadiazol head group labelled phosphatidylethanolamine, NBD PE) that have been transferred onto the glass substrate via the method of either protein stamping or protein caulking respectively. It can be observed that the authors have created patterned SLBs that are very uniform in nature and vary in size. A major advantage of incorporating protein into the patterned SLB design, i.e. acting as a barrier to lateral diffusion, is that cell attachment can ensue – for example, barriers comprised of fibronectin can act as a point for attachment of endothelial cells.[191]

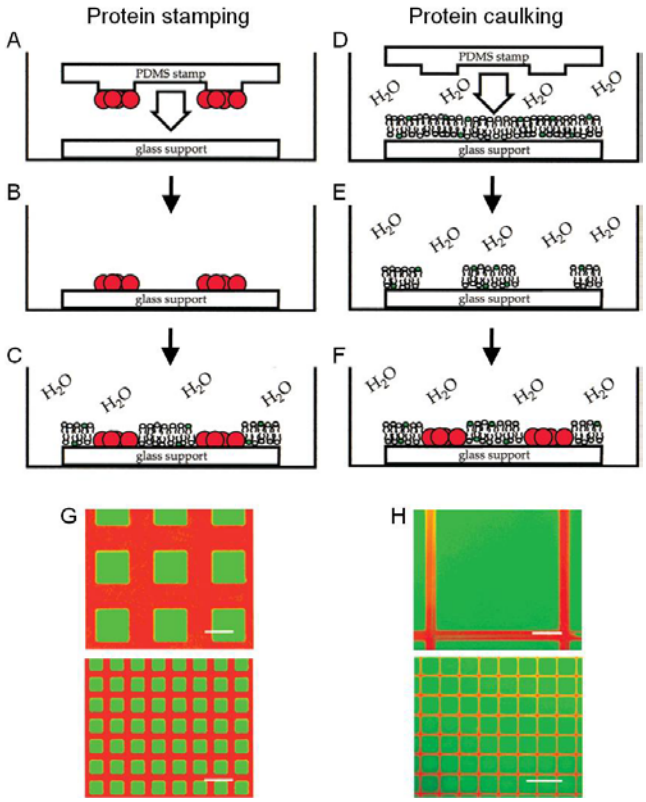


Figure 1.23: **Protein stamping and caulking for patterned SLB formation.** (A)-(C) illustrate the protein stamping method for barrier formation: (A) fluorescently labelled protein is initially attached to the PDMS stamp, (B) the protein is transferred to the glass substrate via stamping and (C) small unilamaller vesicles (doped with a fluorescent tag) are introduced to backfill the non-stamped regions. (D)-(E) represent the protein caulking method for barrier formation: (D) a patterned PDMS stamp is used to remove regions of a pre-formed SLB, (E) a patterned region now ensues where SLB has been removed and (F) protein is introduced and binds to the exposed regions of glass. (G) and (H) illustrate an example of the types of patterned SLBs that can be generated: the protein and lipid are represented by the red and green regions respectively. The scale bars in G and H represent 20 and 50 μm respectively. The illustration is based on figures in the paper by Kung *et al.*[177]

Polymer lift-off technique.

The fabrication processes involved in the polymer lift-off technique for the patterning of SLBs, developed by Orth *et al.*,[192] are detailed in figure 1.24 A. The polymer lift-off technique relies on the deposition of both photoresist and Parylene to pattern an SLB. Specifically, photoresist is deposited onto

Parylene-coated silicon substrates, after which the photoresist is patterned using photolithography and the exposed Parylene surfaces removed using reactive ion etching (RIE). The RIE step serves two purposes; firstly to remove areas of exposed Parylene, but more importantly to afford a surface that is more favourable for lipid assembly (i.e. the newly exposed silicon surface is more hydrophilic than Parylene). Small unilamellar vesicles are then delivered to the surface to form a SLB (on both the silicon substrate and Parylene). Peeling of the Parylene results in the formation of a patterned lipid bilayer. An example of the type of patterned SLBs that can be attained using this technique is displayed in figure 1.24 B.

This technique is advantageous, when compared to the stamping and blotting techniques, as sharp boundaries are produced in the patterned SLBs and many

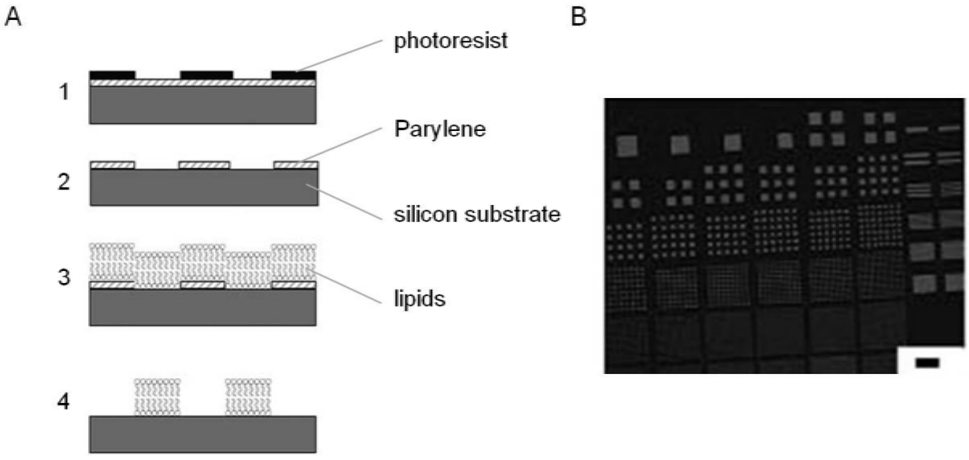


Figure 1.24: **Polymer lift-off technique for the formation of patterned SLBs**. (A) Illustration of the steps involved in the fabrication process. First the photoresist is patterned using photolithographical techniques (1), after which the exposed photoresist and Parylene are removed using developer and reactive ion etching respectively (2). Small unilamellar vesicles are then introduced to the Parylene and silicon substrate and a SLB is formed (3). Patterning of the SLB results when the Parylene sheet is stripped from the substrate (4). (B) An example of a patterned SLB gained using this technique (scale bar = 70 μm). Images are based on the paper by Orth *et al.*[192]

of the disadvantages associated with deformation of the PDMS stamps are eliminated. Moreover, this technique enables the production of higher resolution patterned SLBs, where features in the region of 1 μm have been reported. The success of the technique is largely owed to the chemical nature of Parylene, which binds weakly to the substrate in question, so is easily removed in one step, and is also chemically inert.[192]

Aluminium lift-off.

The aluminium lift-off approach utilises a layer of aluminium that is deposited onto a silicon substrate and subsequently patterned using traditional lithographical methods (photolithography or electron beam lithography), in order to produce patterned SLBs. The first stage in figure 1.25 (1) includes a side-on depiction of the patterned aluminium template. The patterned aluminium template is then treated with 3-aminopropyltriethoxysilane in dry acetone to yield amine-terminated glass, after which sulfosuccinimidyl-4-(N-maleimidomethyl)cyclohexane-1-carboxylate (sulfo-SMCC) is introduced in order to yield succinimidyl attachment to the surface amines. Monomeric fibronectin (fluorescently labelled), formed by treating fibronectin with tris(2-carboxyethyl)phosphine hydrochloride (TCEP) to reduce disulphide bonds, is covalently attached to a pre-patterned and pre-treated silicon surface to define barriers to lateral diffusion (stage 2 in figure 1.25 and the enlarged box for further details relating to the chemisty).[193] Upon dissolution of the aluminium in alkaline solution (stage 3 in figure 1.25), small unilamellar vesicles are introduced to the patterned substrate affording a patterned SLB (stage 4 in figure 1.25).

Disadvantages associated with this technique include the need for highly alkaline conditions to remove the deposited aluminium, which raises concerns relating to the biocompatibility of the covalently attached protein. Furthermore, economic considerations do not favour this technique; each

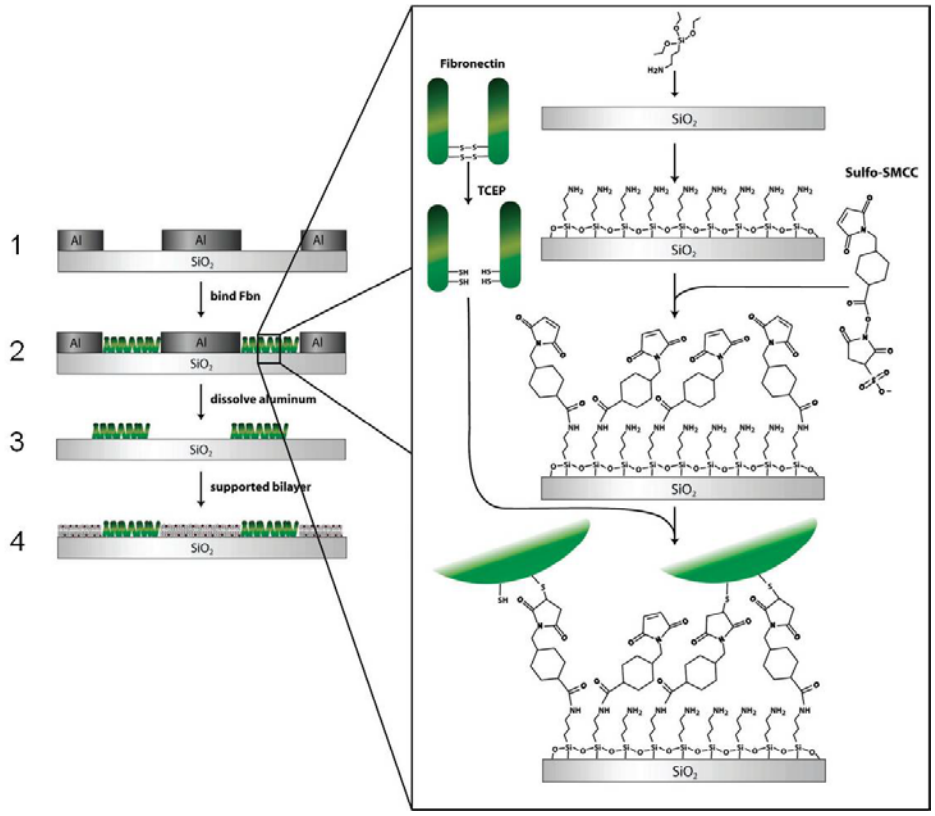


Figure 1.25: **Aluminium lift-off technique for patterned SLB formation.** Stages 1-4 illustrate the steps involved in patterning a SLB using this methodology, specifically: (1) patterning of the aluminium coated silicon using lithographical techniques, (2) introduction of protein barriers by covalent attachment of fibronectin chemically treated silicon (see the enlarged box for details of the chemistry), (3) chemical "lift-off" of the deposited aluminium and (4) formation of patterned SLBs by the introduction of small unilamellar vesicles. Image reproduced from the paper by Jackson *et al.*[193]

patterned SLB may only be used once. However, high-quality patterns can be produced relatively quickly using this technique.

Patterning by polymerisation

Patterning by polymerisation utilises phospholipids that are able to polymerise upon the introduction of light as barriers to lipid diffusion between corrals. In the example described by Okazaki *et al.*,[194] a bilayer comprised of diacetylene phospholipid (diynePC) are assembled onto solid supports (stage 1 in figure

1.26) and polymerised using photolithographical methods (stages 2 and 3 in figure 1.26). The non-polymerised material can then be removed using sodium dodecyl sulphate (SDS) solution (stage 4 in figure 1.26). A solution of small unilamellar vesicles can then be introduced to the pre-patterned substrate, where rupture and SLB formation results, as illustrated in stage 5 of figure 1.26.

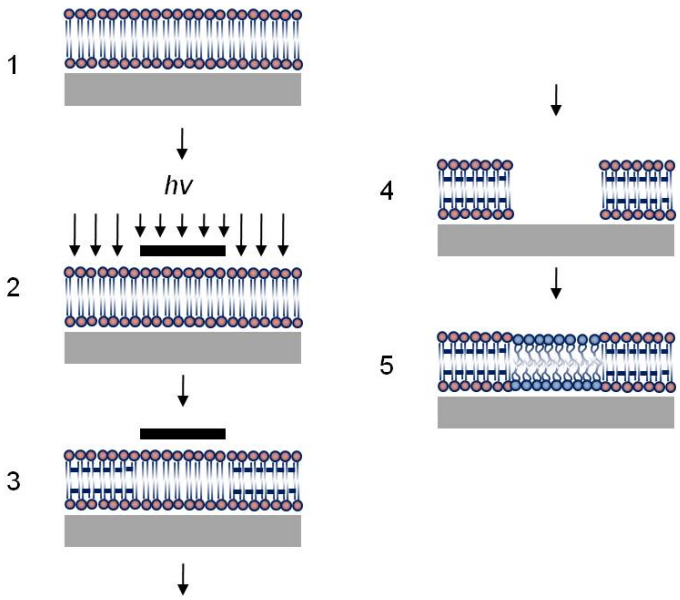


Figure 1.26: **Patterned SLB formation via lipid polymerisation.** Diacetylene phospholipid (diynePC) bilayer are assembled onto a solid support (stage 1) and specific regions polymerised by using a photo mask to direct UV light (stages 2 & 3). The regions that are not polymerised are removed (stage 4) and the exposed regions backfilled with a solution of small unilamellar vesicles (stage 5). The diagram is based on the paper by Okazaki *et al.*[194]

One advantage associated with this technique is that hybrid patterned bilayers remove the existence of energetically unfavourable environments, i.e. the 'edges' of the supported lipid bilayer. The process of SLB formation was found to be enhanced using this process. Therefore regions that may possess anomalous characteristics, when compared to the bulk SLB, are removed, such

as regions possessing heightened levels of membrane curvature. This allows experiments of a biophysical nature to be conducted upon lipid bilayers that are more 'controlled' in biophysical terms.

Hydrogel stamping.

Madj and Mayer have developed a very effective technique for the deposition of patterned SLBs, which contrasts largely to those discussed hitherto.[195,196] They have demonstrated that stamps comprised of hydrogel, specifically high-gel strength agarose (4 % w/v), inked with solutions of small unilamellar vesicles enable a patterned SLB to be printed onto a substrate ca. 100 times without the need for re-inking. Figure 1.27 illustrates the stages required to produce patterned supported bilayers using the hydrogel stamping technique.

Specifically, a PDMS cast is produced (stage 1 in figure 1.27 A) and the hydrogel then poured on top of this cast and allowed to set (stage 2 in figure 1.27 A). After the hydrogel has set, it may then be peeled away from the PDMS cast (stage 3 in figure 1.27 A). Vesicle solutions may then be administered to the raised features ("posts") of the agarose gel, which over a short period of time are taken up by the gel (figure 1.27 B). The pore size, determined by the agarose gel, allows liposomes to diffuse throughout the stamp. As the stamp comes into contact with the substrate, liposomes at the stamp-substrate interface are thought to fuse to form an SLB in a similar manner to that of vesicular fusion from solution (figure 1.27 C).[196]

With respect to determining the reproducibility of SLB deposition, FRAP experiments have revealed that diffusion coefficients for the 6^{th} and 100^{th} stamped array are consistent to within 5 % of each other. The mean fluorescent intensity reduced by only ca. 10 % from the 6^{th} to the 100^{th} array, a feature which is very desirable for bilayer deposition and suggests that reproducibility of this method is amenable for high-throughput capabilities in the future. Furthermore, Madj and Mayer have demonstrated the applicability

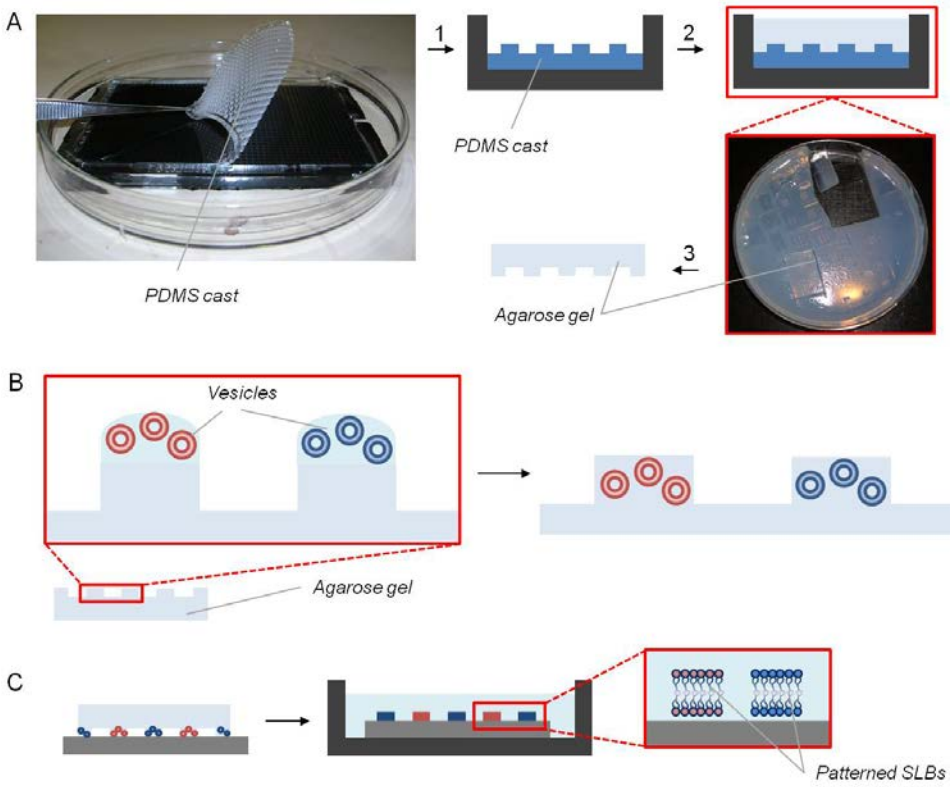


Figure 1.27: **Hydrogel stamping for the creation of patterned supported lipid bilayers.** (A) Initially a PDMS cast is produced (stage 1), after which a solution of high-strength agarose gel is poured on top of the PDMS cast and allowed to set (stage 2). Once the hydrogel has set, it may be peeled away from the cast (stage 3). (B) The agarose gel is then doped with vesicle solution and allowed to absorb the solutions. (C) The loaded agarose stamp is then placed into contact with a substrate, which is then transferred into an aqueous environment. Patterned supported lipid bilayers result. Images in the figure are based on the information provided by Madj and Mayer (Supporting Information).[196]

of such a technique to biophysical studies, where they have conducted investigations probing both drug- and protein-membrane interactions.

1.4.2.3 Production of composition arrays

The previous section has reviewed the various methods that are available to produce patterned supported lipid bilayers. This is extremely important if numerous experiments are required to be conducted in parallel (i.e. to increase the number of experimental repeats) and in high-throughput (i.e. in order to increase the speed with which a great volume of data is collected). However, in

order to conduct high-throughput investigations of a biophysical nature, it is desirable to create single arrays that vary in lipid composition. Madj and Mayer touched upon the ability of their hydrogel stamping technique for producing composition arrays; however, the approach described is not high-throughput in nature as each post on the hydrogel has to be individually addressed by manual pipetting. However robotic technologies could be viewed as a way in which to bridge this gap, as Castellana and Cremer have envisaged as a result of the investigations that they have conducted.[197,198] Specifically, they state that although spatially addressing each experimental area is slow, it enables the lipid composition in each unit to be controlled more rigorously.

The main methods detailed in the literature that enable the creation of patterned SLB *composition* arrays in high-throughput include the following:

(i) Controlled mixing and surface capture,[199] a technique that utilises microcontact printing (to form barriers) interfaced with microfluidics to produce lipid composition arrays. Laminar flow is used in order to ensure that mixing and surface capture is controlled (see figure 1.28 A for further information);

(ii) Stamping by microcontact printing,[190] where the PDMS stamp is designed such that it is able to print areas of SLB that vary in size and where the unstamped regions may then be 'backfilled' using a second vesicle solution to create composition arrays (see figure 1.28 B for further information);

(iii) Spatially selective manipulation by laminar flow,[200] where lipid in a SLB can be 'stripped' and then 'replaced' using laminar flow (see figure 1.28 C for further information); and finally,

(iv) Scanning probe lithography,[201] where a pre-patterned substrate is doped with small unilamellar vesicles and the resulting SLB then patterned using the 'tip' of a scanning probe for composition array formation (see figure 1.28 D).

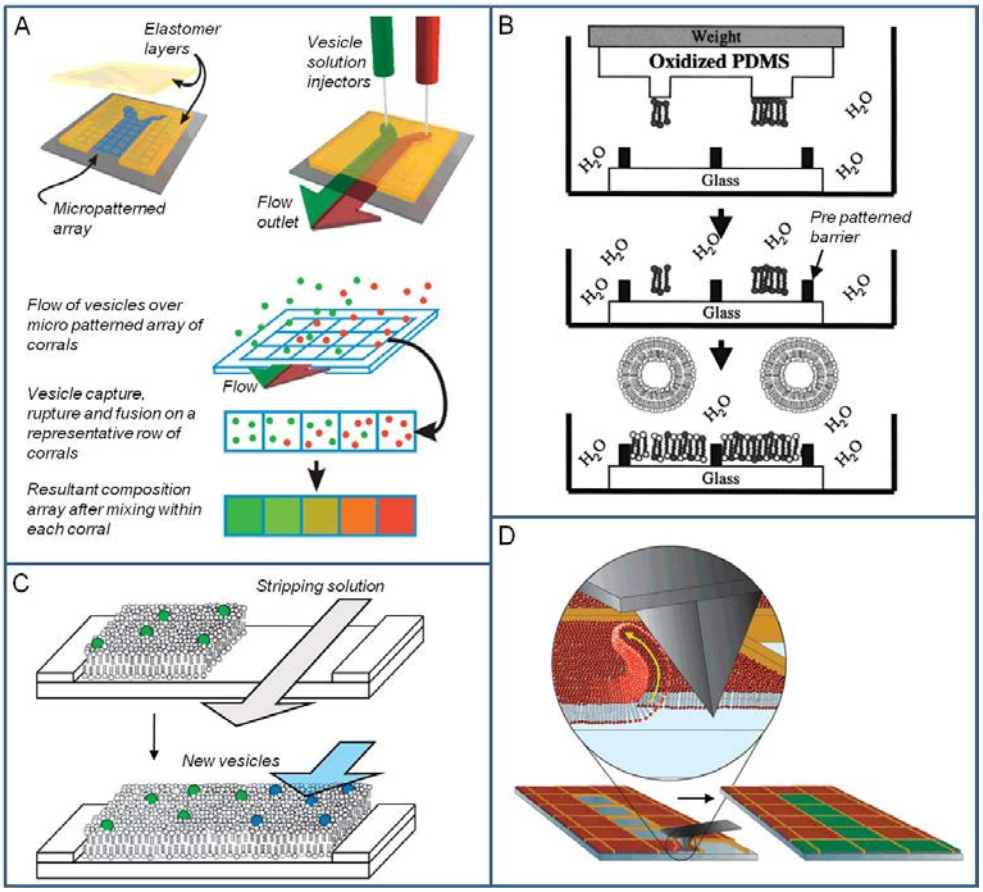


Figure 1.28: **Methods for forming supported lipid bilayer composition arrays.** (A) Controlled mixing and surface capture. This method relies on using laminar flow to create lipid composition arrays.[199] (B) Stamping by microcontact printing. Oxidised PDMS stamps, pre patterned using photolithographic methods and subjected to vesicle suspensions, are able to print SLBs of different areas onto substrates. The unstamped regions can then be 'backfilled' with a different vesicle suspension.[190] (C) Spatially selective manipulation by laminar flow. Here a laminar stream containing a stripping solution is scanning across the desired section of SLB to be removed. A second batch of new vesicles is then introduced to enable composition array formation.[200] (D) Scanning probe lithography. In this instance the tip of a scanning probe is used to remove specific regions of deposited SLB – new vesicles can be introduced thereafter.[201] Images are reproduced from the references provided.

1.4.2.4 Problems associated with the SLB technique

Having personally attempted to deposit supported lipid bilayers onto solid supports, using the microcontact printing technique, it can be confirmed the process can be extremely difficult to master. First of all, it was found that the

quality of printing was particularly poor when using a PDMS stamp, which was attributed to the deformation of the PDMS upon the application of pressure. Hovis *et al.* noted that the predicted thickness of the grid lines after 106 % lateral self expansion of the remaining bilayer was not achieved, which they attribute to the deformation of the PDMS stamp.[187] Secondly, sophisticated stamping devices are required in order to print complex composition arrays. Thirdly, as the technique requires a single SLB to be transferred under aqueous conditions, and within a time period dictated by the oxidised PDMS stamp, the transferral process has to be conducted relatively quickly and is therefore difficult to execute. Furthermore, it is felt that the transferral of a single supported lipid bilayer is extremely difficult to achieve, owing to the fact that there will always be an excess of small unilamellar vesicles present in the aqueous solution (unless a flow system can be implemented where washing stages take place). Even still, it is felt that the deposition of a single supported bilayer is far from trivial. Hower, Hovis *et al.*[190] feel that both leaflets of the lipid bilayer are removed during the blotting process, when assessing the fluorescence intensities of the blotted regions. They also indicate that in order to enhance transfer efficiencies using microcontact printing, the following guidelines should be followed, in order to gain transfer efficiencies of greater than 80 %:

(i) Use extruded vesicles and cleaned / baked glass substrates within three days of preparation;

(ii) Use a buffer solution (e.g. 10 mM Tris, 100 mM NaCl, pH 8) as opposed to Millipore water;

(iii) Design the pattern to be printed in a grid-like system containing large corralled regions separated by small barriers;

(iv) Use Sylgard 182 (instead of 184) for PDMS stamp manufacture; and,

(v) Complete the printing procedure in less than 15 s.

In conclusion, it is felt that this technique is not the easiest to grasp and would require several years for a lab to set up the process successfully. In general, a major limitation of the SLB methodology surrounds the fact that the lipid bilayers are *supported*. Therefore controversies persist, with opinions suggesting that substrate-membrane interactions may impact upon the physical nature of the bilayer, even if polymer-cushioned SLBs are utilised. Furthermore, as the distance between the SLB and substrate is so small, i.e. on the order of 10 Å (as detailed in section 1.4.2.1), the ability to manipulate this water volume is virtually impossible. Additionally, it is believed no published articles exist, surrounding the formation of asymmetric bilayers using the SLB technique to date, which coupled with the difficulties associated with mastering the technique do not suggest that it is the most suitable approach to build upon. A methodology that has recently taken hold in the scientific world is associated with droplet interface bilayers (DIBs), which addresses and overcomes each of the aforementioned problems.

1.4.3 Droplet interface bilayers

Droplet Interface Bilayers (DIBs) are a new and emerging technology that have surfaced as a major alternative to traditional methods for creating single lipid bilayers for probing the interaction of drug molecules and proteins with artificial lipid membranes. 2006 saw the emergence of the very first droplet interface bilayer, developed concomitantly by the labs of Takeuchi[202] and Bayley.[203]

1.4.3.1 Definition

The term, "Droplet Interface Bilayer", relates to the formation of a lipid *bilayer*, as a result of forming an *interface* between two aqueous *droplets* in an oil

environment. Importantly, the aqueous droplets contain surfactant molecules in order to stabilise the oil-aqueous interface, hence ensuring that the water droplets do not merge. Each droplet is therefore surrounded by a surfactant monolayer. The surfactant of choice in this instance is a biological amphiphile, i.e. a phospholipid, and the interface that forms between two aqueous droplets is a lipid bilayer. Figure 1.29 illustrates how droplet interface bilayers are formed.

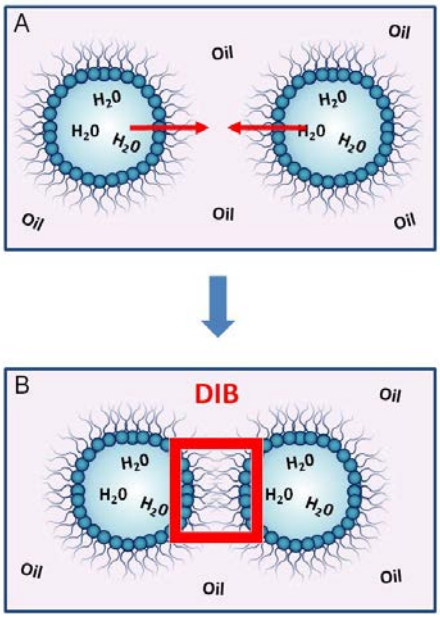


Figure 1.29: **Droplet Interface Bilayer (DIB) definition.** (A) Two aqueous droplets, whose interfaces are stabilised using surfactant molecules (i.e. amphiphilic phospholipids), are submersed in an oil environment. As a result, lipid monolayers reside at the droplets' oil-aqueous interface. (B) Upon bringing the two droplets into contact with one another, a droplet interface bilayer is formed.

DIBs can be formed by incorporating the lipid into either the oil or aqueous phase (as they are amphiphilic molecules), termed the "lipid-out" and "lipid-in" approaches respectively. However the latter method is often favoured, where extruded vesicle suspensions are utilised, as this reduces lipid consumption and generally results in faster DIB production.[204]

1.4.3.2 Advantages of the DIB system

The major advantage of the DIB system, over other technologies such as supported lipid bilayers (as discussed in section 1.4.2) for example, is that it is extremely easy to implement. All that is required to successfully make a droplet interface bilayer is the following: some oil, water, lipid and a chamber to hold the sample in. The technique is extremely quick to pick up and within a few hours the researcher can observe the formation of their first DIB. This process is fascinating, whereby the "zipping-up" of two monolayers to form a single lipid bilayer can be observed in real time using a microscope. It is felt that the ease with which DIB formation can be achieved will appeal to many researchers in the fields of biophysics and biochemistry, and as such, will prevail to become a major technology for research conducted within these disciplines. Hence this is one of the reasons why the latter part of this thesis concentrates on the development of DIB technologies.

Other factors that make this method very advantageous include: the stability of the platform once formed and the nature of the aqueous compartments that are created during DIB formation. When a DIB is formed, it possesses a lifetime that exists on the order of days to weeks. This is highly desirable and contrasts largely to classical techniques of artificial bilayer formation, such as the Montal-Mueller method for example, where only very fragile lipid membranes can be created and are stable for up to an hour at best. Unlike the supported lipid bilayer method, the aqueous compartments that are present on either side of a lipid membrane created using the DIB methodology may be manipulated with ease. This is extremely advantageous, providing the researcher with the option to tune the aqueous composition on either side of the lipid bilayer.

Further advantages of the DIB technology include the ability to form asymmetric droplet interface bilayers (aDIBs)[205] with ease, thus producing a

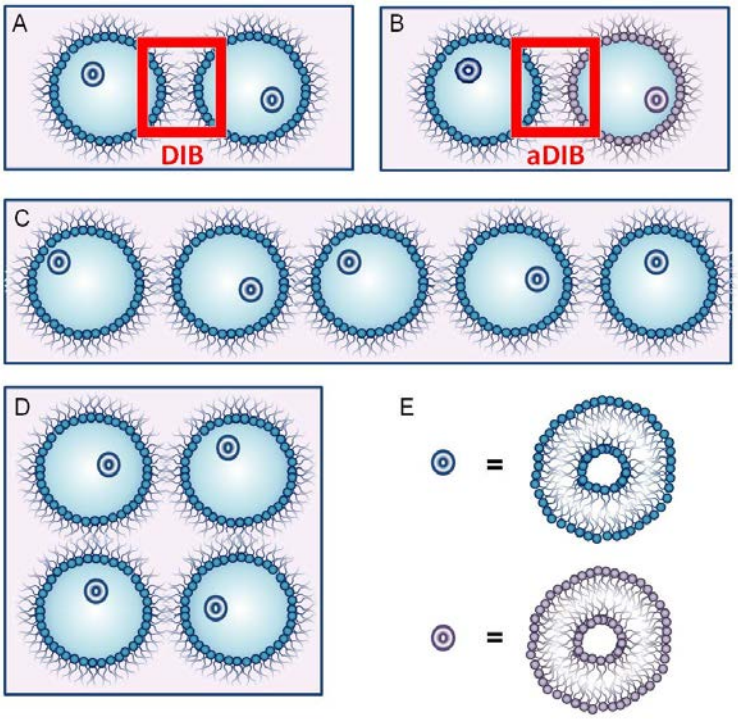


Figure 1.30: **Asymmetric droplet interface bilayer (aDIB) formation and the formation of droplet interface bilayer networks.** (A) Illustration of a droplet interface bilayer, formed with the lipid in the aqueous phase initially (as vesicles). Here, the lipid composition on either side of the bilayer is the same. (B) Formation of an asymmetric droplet interface bilayer (aDIB). Different lipid compositions are used to form the vesicle populations in each droplet. (C) A linear sequence of droplets that forms a DIB network possessing multiple DIBs. (D) An example of a more advanced DIB network, where each droplets forms two DIBs with its neighbours. (E) A key to indicate that the small doughnut-shaped features represent small unilamellar vesicles.

system that has the potential to mimic nature more closely. Figure 1.30 A and B illustrate how asymmetric DIBs differ from the most basic of DIB systems. In order to create an asymmetric DIB, a second vesicle suspension has to be extruded that is comprised of an alternative lipid composition (c.f. the first vesicle suspension). A droplet from each of two different vesicle suspensions is then pipetted into an oil environment – after a period of time the two droplets are brought into contact with one another resulting in the formation of an asymmetric DIB.

It can also be observed that the concept of DIBs can be extended to produce DIB networks that contain more than one DIB, as established by Holden *et al.* and Hwang *et al.*[203,206] Figure 1.30 C and D illustrate how linear sequences of DIBs, as well as more complicated DIB arrangements, can be achieved. The ability to form more than one bilayer per experimental unit will enable advanced systems to be explored.

1.4.3.3 High throughput lipid bilayer formation

To date, there has been very little development with respect to techniques that are able to produce lipid bilayers, or DIBs, in a high-throughput, automated manner. This is most probably because the suspension of lipid bilayers can be challenging and that the concept of DIBs has only been established very recently. However there are now a few examples present in the literature that describe methods able to conduct experiments across several lipid bilayers, with the major application of these methods having been to monitor transmembrane ion channel currents. This includes the following methods:

(i) Falling drop method

(ii) Black lipid membrane (BLM) approach

(iii) Hanging droplet screening chip using droplet interface bilayers (DIBs)

Falling drop method

The falling drop method[207,208] relies on using gravity to deposit a small droplet (containing lipid vesicles, and hence possessing a lipid monolayer at the droplet interface) onto a monolayer-containing surface, where a lipid bilayer is formed in a horizontal plane. Figure 1.31 A and B illustrate how the falling drop process works and the scale of assay that may be achieved when using a liquid-handling robot respectively.

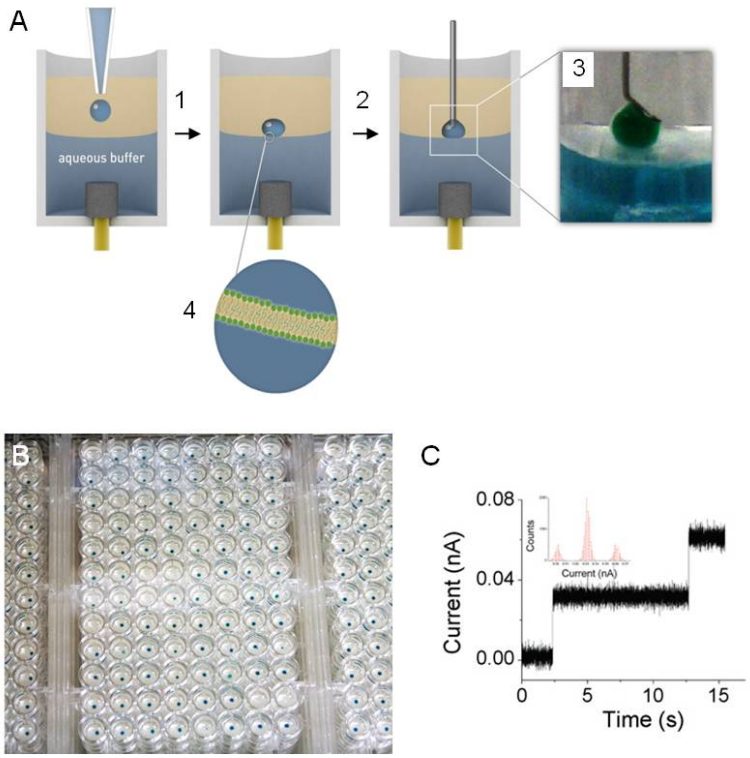


Figure 1.31: **The falling drop method for high-throughput lipid bilayer formation.** (A) Illustration of how the falling drop method works. An aqueous, lipid-containing droplet is deposited into a well and falls on top of a lipid monolayer, formed at the interface between an aqueous and oil phase (stage 1). A second electrode may then be incorporated into the droplet to enable electrical measurements to be conducted (stage 2). Image 3 illustrates a photograph of the electrode incorporated into the droplet and image 4 illustrates where DIB formation occurs. (B) The capability of performing high-throughput measurements using this method is demonstrated, where droplets have been dispensed into 96-well plates. (C) An example of the type of experiment that may be conducted; here, the incorporation of alpha hemolysin pores into the membrane has been investigated. Images reproduced from Poulos *et al.*[207]

Figure 1.31 C illustrates the type of measurement that may be conducted using this setup; specifically, the incorporation of alpha-hemolysin pores into 1,2-diphytanoyl-sn-glycero-3-phosphocholine (DPhPC) bilayers has been investigated.

Although this has been an important development, with respect to initiating research into the high-throughput capabilities of artificial lipid bilayer systems,

there are still limitations in the methodology. For example a major limitation of this technique is due to the orientation of the lipid bilayer – the fact that the bilayer is orientated in the horizontal plane means that the lifetime of the bilayer is far reduced when compared to those assembled in the vertical plane.[207] This is thought to be due to the effect of gravity acting upon the dispensed droplet. Additionally, this technique does not enable more advanced experiments to be conducted, perhaps those concerned with cooperativity, i.e. where more than one bilayer is required.

Black lipid membrane (BLM) approach

This method utilises black lipid membranes, i.e. membranes that are suspended across apertures, as opposed to bilayers interfaces that are formed between *droplets*.[209-211] Figure 1.32 A illustrates a device that can be used to create numerous lipid bilayers, which are suspended across apertures present in a Parylene sheet. Microfluidic channels are used to deliver both lipid and buffer solution for lipid bilayer assembly via an inlet to the bottom channel. The device possesses nine recording wells (see image 2 in figure 1.32 A); electrodes are placed in each of the recording wells, as well as a common electrode that is placed in the bottom channel, in order to measure membrane current. Image 3 in figure 1.32 A illustrates an image taken on a scanning electron microscope (SEM) of the microfabricated apertures present in the Parylene sheet (situated in each recording well).

A disadvantage associated with this technique is associated with the complexity of the device. The microfabrication procedures, which are required in order to pattern the Parylene sheet, are depicted in figure 1.32 B. Therefore, specialist technologies and clean rooms will be required in order to pattern the Parylene. Secondly, the device design is quite complicated, as can be observed from figure 1.32 C. Here it is apparent that several layers are required in order to assemble the device. Therefore, great care will be required during device construction to ensure proper alignment and good sealing.

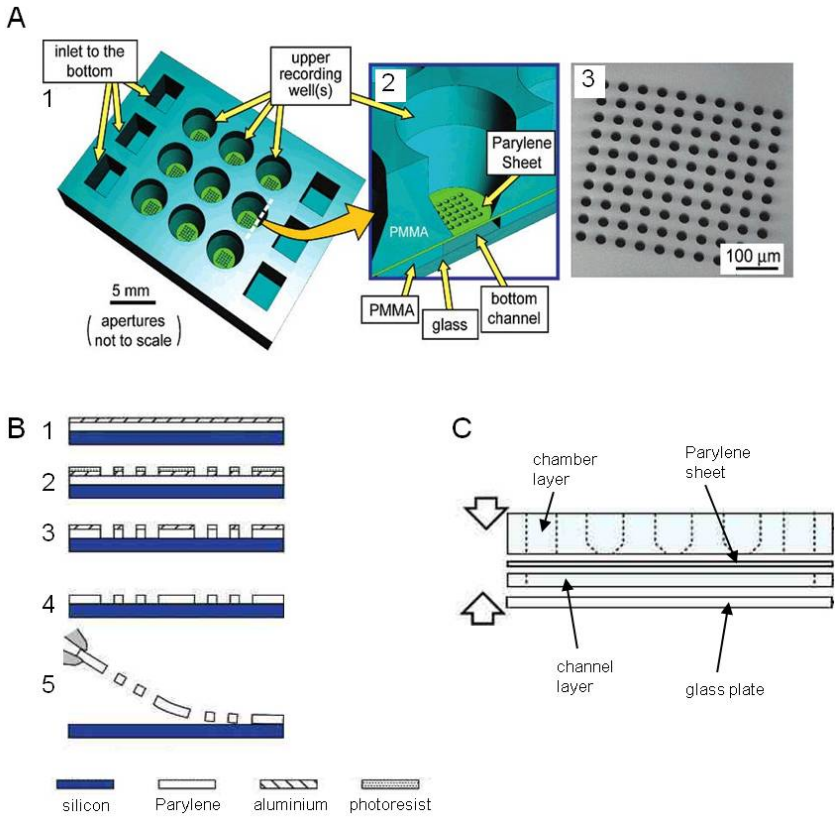


Figure 1.32: **Black lipid membrane (BLM) approach for high-throughput lipid bilayer formation.** (A) Device design used to create numerous lipid bilayers suspended across apertures fabricated in a Parylene sheet (1). An enlarged image of a single upper recording well is displayed in 2. Image 3 represents an image of the patterned Parylene sheet, taken on a scanning electron microscope (SEM). (B) Steps involved in the microfabrication of the Parylene sheet. First, Parylene and aluminium are deposited onto a silicon substrate (1). The aluminium is patterned using photolithographic procedures (2). An oxygen plasma is then used to etch the Parylene, using the aluminium as a mask (3). The residual aluminium is then removed (4) and the Parylene substrate peeled off (5). (C) Here the various layers used in order to construct the device are detailed. Images reproduced from the paper by Le Pioufle *et al.*[209]

Hanging droplet screening chip using droplet interface bilayers (DIBs)

Syeda *et al.*[212] have recently developed an approach in order to probe the effect of a number of drug molecules as potential blockers of the pore, α-hemolysin. This technique utilises a droplet suspended from a Ag/AgCl electrode that is

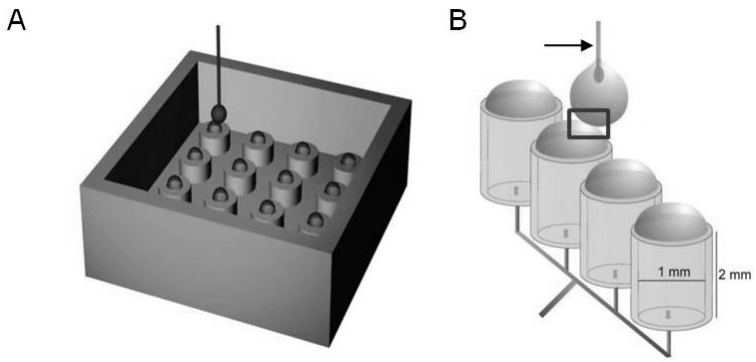


Figure 1.33: **Hanging droplet screening chip using droplet interface bilayers (DIBs).** (A) An illustration of the 16-well assay plate for investigating the potential blocking ability of drugs molecules on the pore, α-hemolysin. 16 wells that contain lipid and the drug of interest are submersed in an oil environment in order to enable monolayer formation at the oil-aqueous interface. (B) Enlarged image that depicts four wells and the formation of a DIB between the suspended droplet and well (each of which are coated with a lipid monolayer at the oil-aqueous interface). Incorporation of electrodes into the chip design enables electrical measurements to be conducted. Images are reproduced from the paper by Syeda *et al.*[212]

also mobile. They have produced a 16-well assay plate, which contains 16 wells filled with lipid as well as the drug to be tested (and a pure lipid-buffer well to act a control), as illustrated in figure 1.33 A. The 16-well assay plate is then filled with oil, which thus enables lipid monolayers to form at the oil-aqueous interface of each well after a period of time. The droplet that is suspended from the electrode contains the pore of interest (cleverly synthesised *in situ*), and can be brought into contact with a well manually. A DIB is formed as a result (see figure 1.33 B), with the pores then incorporating themselves into the bilayer - an electrical measurement recorded. The suspended droplet is then disconnected from the well and connected to the next – the process is repeated until an electrical measurement for each of the wells has been taken.

In addition to issues that may surface due to contamination of the chip, for example, if the assay design is expanded to enable more than 16 units per assay to be investigated, this technique, as with the others detailed in this section, is

limited by the fact that the format is only able to afford one lipid bilayer per experimental unit, hence limiting its application to more advanced situations.

1.5 CONCLUDING REMARKS AND THESIS AIM

In summary, it is extremely important to further our understanding of how small molecules interact with lipid membranes. We yearn to learn more, as it is imperative to discover how drug molecules interact with our body at the molecular level – often little consideration is given to drug-lipid interactions within the pharmaceutical industry, for example. The major aim of this thesis has therefore been to develop new technologies, able to be used in screening drug-membrane interactions.

Artificial membranes have long been employed as a means to investigate the effect of exogenous species (such as proteins) on lipid membranes. Carboxyfluorescein leakage assays in particular have been effective in revealing how such species perturb the membrane and consequently influence the efflux kinetics. Chapter 2 details the steps taken to develop a carboxyfluorescein leakage assay for the study of drug-membrane interactions, where the reproducibility of the assay and the effect of lipid composition on the rate of carboxyfluorescein leakage are investigated. Chapter 3 builds on the work detailed in chapter 2, demonstrating that the carboxyfluorescein leakage assay can be performed in a microfluidic format and hence offers the possibility to rapidly screen drug- and protein-membrane interactions in high-throughput.

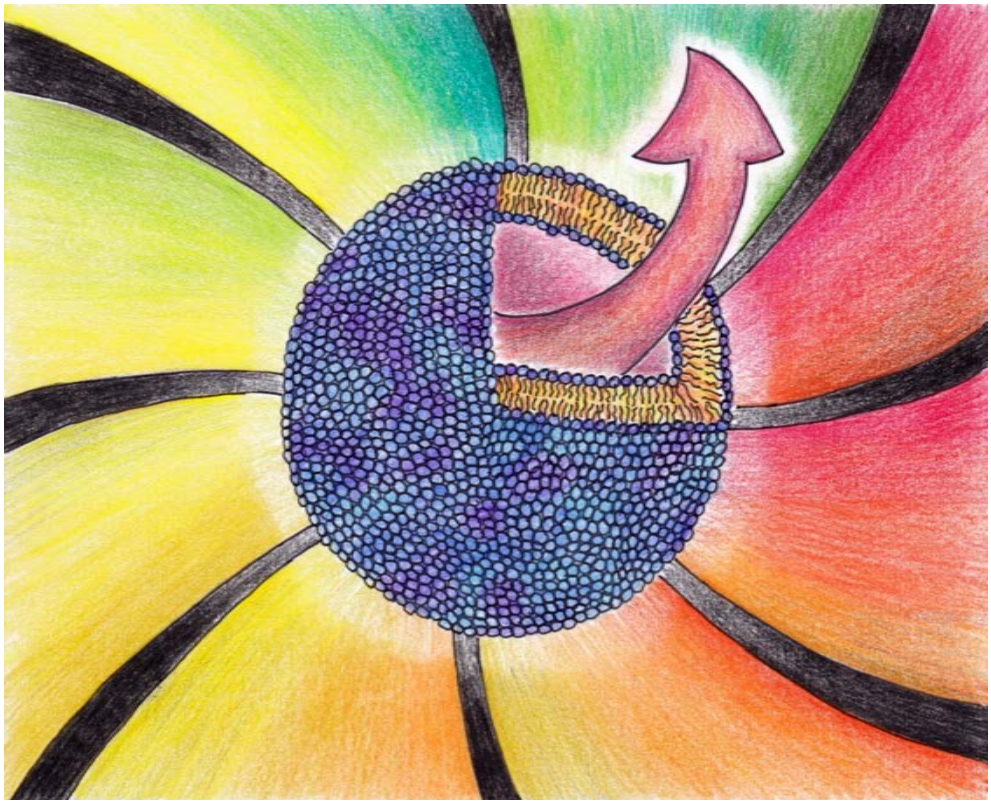
As discussed in section 1.4.3, DIBs are an extremely advantageous platform for probing the interaction of small molecules upon artificial membranes. Upon reviewing the literature, it is apparent that only a handful of examples have exploited the high-throughput aspect of DIB technologies. Opportunities therefore exist to produce platforms for the generation and manipulation and droplets in a high-throughput and automated fashion.

Chapter 4 demonstrates that DIB formation is easily reproduced using the lipid 1,2-diphytanoyl-sn-glycero-3-phosphocholine (DPhPC) and details the successful formation of DIBs comprised of the more biologically relevant lipid, 1,2-dioleoyl-sn-glycero-3-phosphocholine (DOPC) for the first time. Furthermore, a proof-of-concept leakage assay across DIBs, that uses pH gradients to potentially assess drug-membrane interactions, has been detailed. The problems associated with the manual manipulation of droplets have also been highlighted, hence justifying the need for an approach able to form DIBs reliably and in a uniform manner.

Chapter 5 presents work that has been published recently in Chemical Communications,[213] detailing the development of a microfluidic approach for the formation of DIB networks in a high-throughput and controlled manner. An automated system has been set up, where the size of water-in-oil droplets participating in DIB formation is uniform and tuneable. Additionally the ability to form three dimensional DIB networks, where droplets are able to fill predefined structures of any desired shape or size, and the possibility for asymmetric DIB formation has been demonstrated.

Chapter 2

A carboxyfluorescein leakage assay for the study of drug-membrane interactions



"If we knew what it was we were doing, it would not be called research, would it?"

Albert Einstein

2.1 OVERVIEW

Drug discovery is often focussed largely around investigating the interaction of pharmaceutically active agents, i.e. small drug molecules, with the target protein(s) of interest. However, little consideration is given to the interaction of such molecules with the fabric of our cell membranes – lipids. Often they are viewed merely to possess structural qualities, acting in passive manner, whereas it is now apparent that their function is more significant.[214,215]

Artificial membranes have long been employed as a means to investigate the effect of exogenous species (such as proteins) on lipid membranes. Carboxyfluorescein (CF) leakage assays in particular have been effective in revealing how such species perturb the membrane and consequently influence the efflux kinetics. This chapter details the steps taken to develop a CF leakage assay for the study of drug-membrane interactions, where the reproducibility of the assay and the effect of lipid composition on the rate of CF leakage are investigated.

2.2 INTRODUCTION

2.2.1 Properties of carboxyfluorescein

CF, a derivative of the well known fluorescein family, is a molecule that exhibits an unusual fluorescence behaviour. Its structure differs to that of fluorescein due to the possession of an extra carboxyl group, situated at either the 5- or 6-position, as displayed in figure 2.1 A. This feature is advantageous, reducing the ability of CF molecules to partition into hydrophobic environments by up to three orders of magnitude (c.f. fluorescein)[216,217] and thus resulting in enhanced retention of the molecule within vesicular species. Notably, the most soluble and highly fluorescent form of CF is the trivalent anion, in the pH range 7-11.[216]

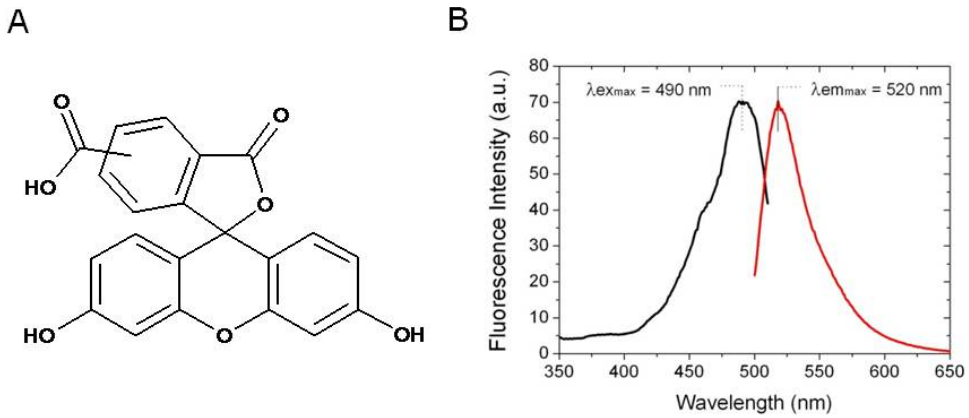
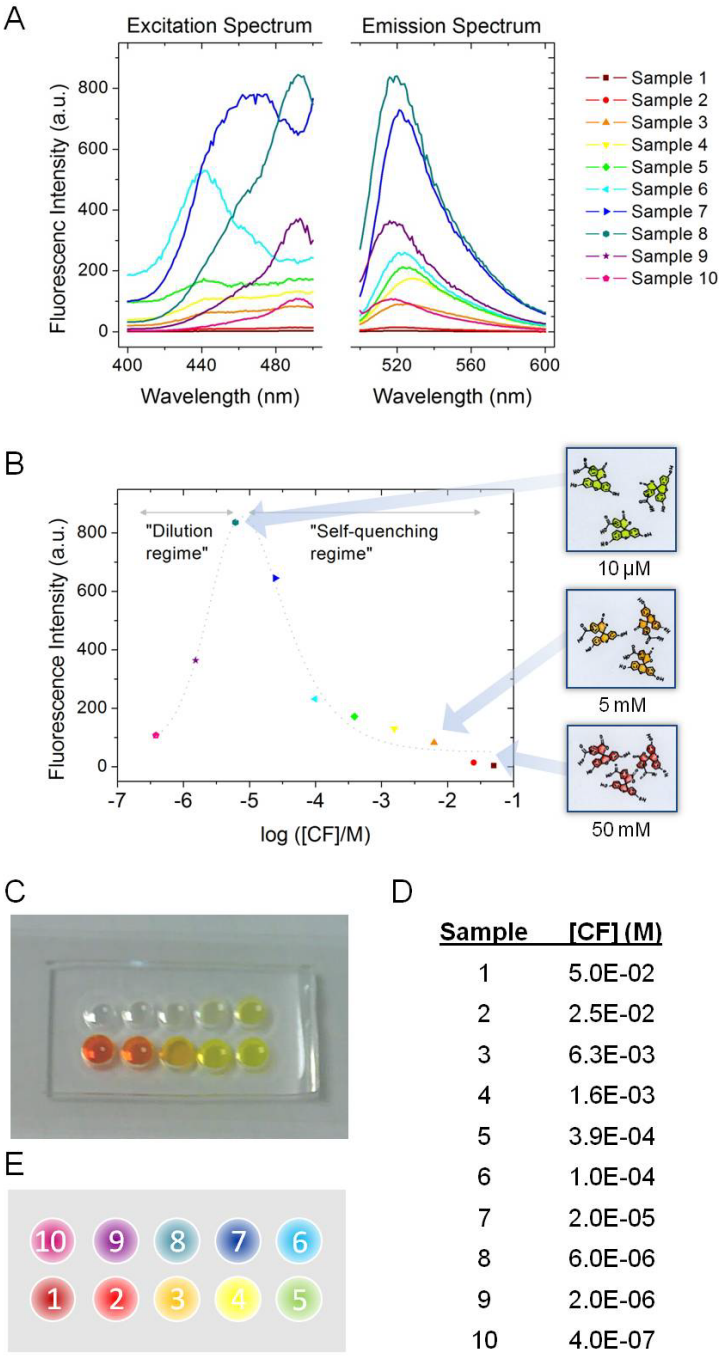


Figure 2.1: **Molecular structure and excitation / emission spectra of 5(6)-carboxyfluorescein.** (A) Illustration of the molecular structure of CF. (B) Graph showing the excitation / emission spectra of 5(6)-CF, where the maximum emission and excitation wavelengths are 490 and 520 nm respectively for a 0.2 mM CF sample.

When excited by blue light, the molecule emits green radiation; more specifically, CF has excitation and emission maxima of approximately 490 nm and 520 nm respectively as illustrated in figure 2.1 B. Moreover, at particularly high concentrations (in the region of 1-100 mM), the fluorescence emission is effectively quenched. This phenomenon, known as 'self-quenching', is believed to arise predominantly due to the formation of non-fluorescent CF-CF dimers and energy transfer between these dimers.[218]

The fluorescence spectra in figure 2.2 reveal how the fluorescence spectra of CF change with concentration. A combined plot of both excitation and emission spectra for various CF concentrations is included, in addition to a graph of the fluorescence intensity values (gained using an excitation of 516 nm) versus concentration. Upon dilution of a self-quenched sample of CF (i.e. 50 mM), an increase in the fluorescence output is observed. A maximum in the fluorescence intensity occurs at ca. 1.0E-05 M CF (see figure 2.2 B, "self-quenching regime"). Upon dilution, the fluorescence intensity decreases as illustrated in figure 2.2 B and is represented by the region labelled the "dilution regime".



Sample	[CF] (M)
1	5.0E-02
2	2.5E-02
3	6.3E-03
4	1.6E-03
5	3.9E-04
6	1.0E-04
7	2.0E-05
8	6.0E-06
9	2.0E-06
10	4.0E-07

Figure 2.2: **Fluorescence properties of carboxyfluorescein (CF).** (A) Excitation and emission spectra for different concentrations of CF in solution. (B) Graph indicating the dependence of CF fluorescence emission on concentration, constructed by taking the value attained at 516 nm for each CF concentration measured. (C) An image illustrating the nature of the samples used to construct the calibration. (D) Table indicating the concentration of the CF samples tested. (E) Key illustrating which sample, in the image displayed in C, refers to which CF concentration.

A photograph of the CF samples utilised in the serial dilution study is displayed in figure 3.2 C. The self-quenched dye is a deep red, with the sample exhibiting the greatest fluorescence output possessing a faint green / yellow colour (i.e. sample 7 in figure 2.2 C, D and E).

2.2.2 Carboxyfluorescein in liposomes

The encapsulation of fluorescent markers, such as CF, at self-quenched concentrations and within phospholipid shells has been a popular assay format over the last few decades.[219] There are numerous examples of membrane-leakage assays detailed within the literature and it appears that the main applications of such an assay seek to probe the interaction of exogenous species upon a membrane,[220-226] to monitor fusion events or to act as a vehicle to investigate intracellular delivery.[227-229] This investigation has exploited the former application in order to indirectly monitor drug-membrane interactions.

CF-containing vesicles can be prepared, where dye molecules are present within the interior region of the vesicle (i.e. contained within the vesicle lumens). Crucially, the underlying principle of this assay relies on the fact that there is little contribution to the output fluorescence intensity when the dye is spatially confined within liposomes, at self-quenched concentrations (i.e. 50 mM for the experiments conducted within this investigation). Therefore unless a distinct event takes place on or at the lipid bilayer, that is able to perturb the membrane in such a way to allow the release of dye molecules, there will be no observed change in the observed fluorescence intensity. Figure 2.3 clearly demonstrates this principle. A vesicular solution, containing 300 μM dioleoyl phosphatidylcholine and encapsulating 200 mM CF, when excited with ultraviolet (UV) does not fluoresce (see figure 2.3 A). Once the membrane disrupting detergent Triton X-100 (TX-100) is introduced into

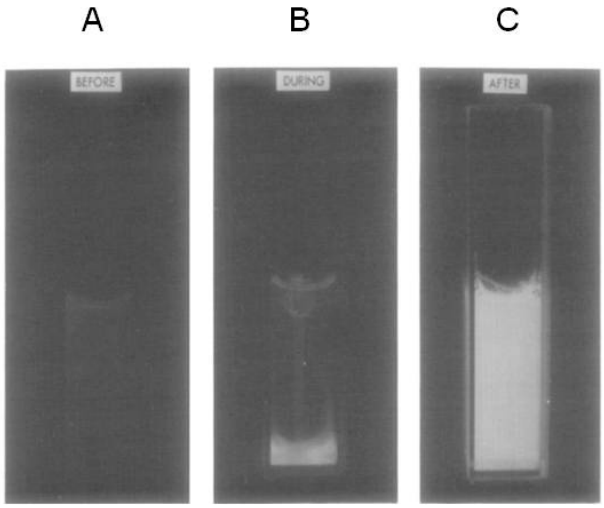


Figure 2.3: **Visualisation of carboxyfluorescein (CF) release from liposomes contained within a cuvette and viewed under an ultraviolet (UV) lamp.** (A) Vesicles containing 200 mM of encapsulated CF. (B) Partial dye release upon the addition of Triton-X 100. (C) Release of the internalised dye, resulting in a final CF concentration of ca. 70 μM and 20-fold fluorescent enhancement. Image reproduced from Weinstein *et al.*[216]

the sample, however, partial release of CF can be detected, as displayed in figure 2.3 B. Complete disruption results in release of the internalised dye into the total cuvette volume (see figure 2.3 C) – this lysis results in a final CF concentration of ca. 70 μM and a 20-fold enhancement in fluorescence intensity.[216] In summary this method can therefore distinguish between material that has been released from vesicles and that which is still retained.

2.2.3 Summary and chapter aims

As detailed in section 2.2.2, CF leakage assays have been a popular choice of assay format, where information about the effect of membrane active species may be investigated. Importantly, this exploits the fluorescence properties of CF, as discussed in section 2.2.1. In summary, the experiments detailed in this chapter aim to:

1. Indicate the steps taken to develop the CF leakage assay.
2. Investigate the reproducibility of the assay and the dependence of CF leakage, using drugs such as chlorpromazine, WAY and imipramine.
3. Investigate the dependency of efflux rate on DOPE content in a DOPC membrane.

2.3 MATERIALS AND METHODS

The following section details the materials required and methods employed in order to perform each of the experiments described in this chapter.

2.3.1 Materials

2.3.1.1 Vesicle preparation

1,2-dioleoyl-sn-glycero-3-phosphocholine (DOPC), 1,2-dioleoyl-sn-glycero-3-phosphoethanolamine (DOPE) and 1,2-dioleoyl-sn-glycero-3-phosphoethanolamine-N-(lissamine rhodamine B sulfonyl) (ammonium salt) (Rh PE) were purchased from Avanti® Polar Lipids, Inc. and used to prepare large unilamellar vesicles (LUVs). Lipids were lyophilised initially in cyclohexane (Sigma-Aldrich).

2.3.1.2 Dye and buffer solutions

The fluorescent dye 5(6)-CF (CF), Trizma® hydrochloride (TRIS-HCl), sodium chloride (NaCl) and sodium hydroxide (NaOH), all purchased from Sigma-Aldrich, were the main components of the buffers used in these experiments. An aqueous CF stock solution (internal buffer, solution 2.1), incorporating 50 mM CF, 10 mM TRIS-HCl, 10 mM NaCl and adjusted to pH 7. 4 with ca. 135 mM NaOH (to aid CF solubilisation) at room temperature, was used for vesicle formation. An elution buffer (solution 2.2) was also prepared and consisted of 10 mM TRIS-HCl, 107 mM NaCl – approximately 5 mM NaOH was required to adjust to pH 7.4 at room temperature. Solution 2.1

was covered in foil and kept in the dark at all times, and all buffers stored at 4 °C when not in use. The two solutions used are summarised as follows:

Solution 2.1:	50 mM CF, 10 mM TRIS-HCl, 10 mM NaCl, pH 7.4
Solution 2.2:	10 mM TRIS-HCl, 107 mM NaCl, pH 7.4

2.3.1.3 Drugs

The following drugs were utilised in the experiments detailed within this chapter: chlorpromazine, WAY-100635 and imipramine (all purchased from Sigma-Aldrich). Aqueous stock solutions were prepared using the elution buffer (solution 2.2, see section 2.3.1.2) and diluted to provide the desired drug concentration. All aqueous stock solutions were stored at 4 °C when not in use.

2.3.1.4 Gel filtration column

Sephadex™ G25m (GE Heathcare) is a medium suitable for the separation of molecules with a molecular weight, M_r, of greater than 30,000 g/mol from those with M_r < 1,500 g/mol and was therefore chosen to separate vesicles containing entrapped CF from free dye. The Sephadex™ G25 medium was bought pre-prepared and stored at 4 °C when not in use.

2.3.2 Methods

2.3.2.1 Encapsulation of carboxyfluorescein

Stock solutions of DOPC (25 mg / ml, 786.15 g / mol) and DOPE (25 mg / ml, 744.03 g / mol) were prepared in chloroform. Subsequently, the correct volumes were pipetted into a 10 ml round bottomed flask (for each specific experiment) to yield a final concentration of 12.5 mM in 500 µl (6.3E-06 moles). Using a stream of nitrogen, the solvent was removed gently, hence

resulting in the formation of a thin lipid film. The sample was then placed in a dessicator (under vacuum) for a minimum of one hour to ensure removal of residual solvent molecules. The lipid film was hydrated with 500 μl of the CF stock solution (solution 2.2, section 2.3.1.2) and left for 5-10 minutes, after which the sample was vortexed to ensure removal of lipid from the glass vessel. Five freeze-thaw cycles were performed with liquid nitrogen to aid the disruption of multilamellar species and the sample extruded 21 times through a polycarbonate membrane (100 nm diameter pore size) to form large unilamellar vesicles.[230] See steps A-E of figure 2.4 for an illustrative representation of this procedure.

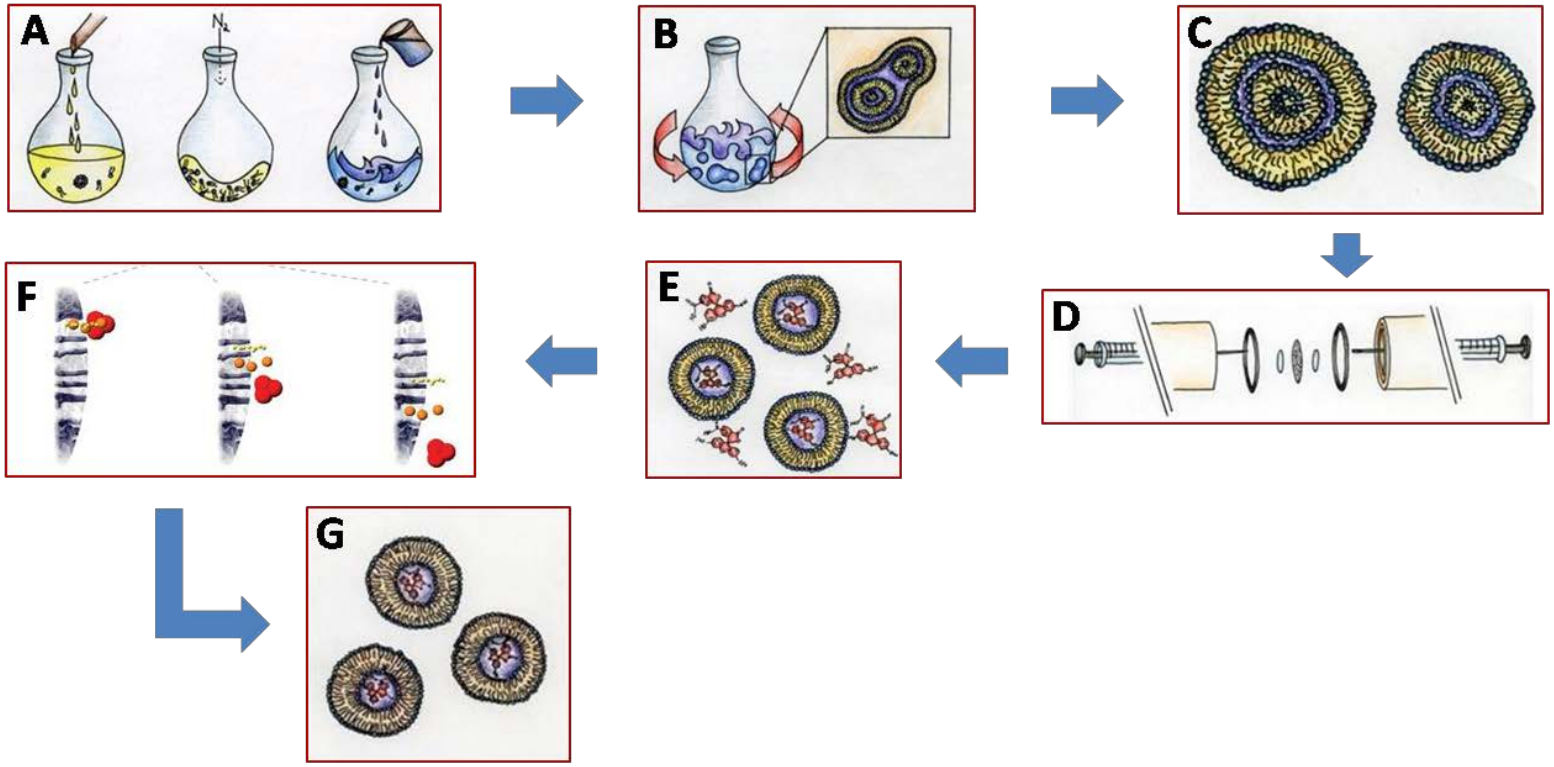


Figure 2.4: **Illustration of the steps involved in producing CF-encapsulated vesicles.** (A) A lipid film is formed by depositing the lipid of interest into a round bottom flask and removing the solvent under a stream of nitrogen, after which the film is hydrated with the CF-containing buffer. (B) The sample is then vortexed and freeze-thawed, resulting in the formation of multilamellar species (C). Extrusion of the sample through a polycarbonate membrane (D) yields unilamellar vesicles (E). The unencapsulated dye is then removed, using a Sephadex column (F, image reproduced from GE Healthcare's Gel Filtration Handbook),[231] to afford CF-encapsulated vesicles (G).

2.3.2.2 Exclusion of external dye by gel filtration

After extrusion, CF will be present in the interior and exterior milieux of the vesicles. The external dye was removed using a gel filtration column, via the principle of size exclusion.[232,233] First, the column was prepared by passing 5-10 column volumes of Milli-Q water through the gel. The column was then equilibrated with three column volumes of the elution buffer (solution 2.2). A 300 µl aliquot of the extruded vesicle sample was loaded onto the column and consequently separated from the free dye, as illustrated in figure 2.5 A and B respectively. Fresh vesicle samples were prepared for each day of experiments and the column washed with copious amounts of Milli-Q water between experiments. See steps F-G of figure 2.4 for an illustrative representation of this procedure. The collected vesicle suspension post-elution contained a lipid concentration of ca. 2 mM, which was subsequently diluted to a concentration of 0.2 mM for use in efflux measurements.

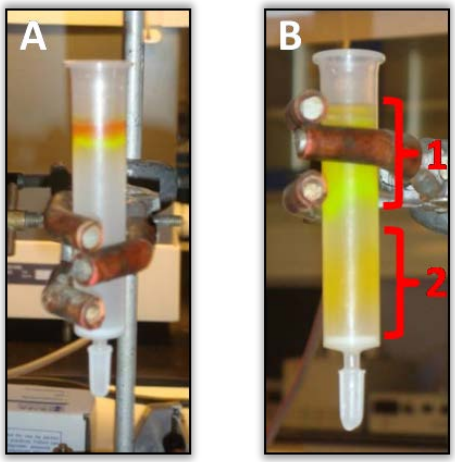


Figure 2.5: **Separation of free carboxyfluorescein (CF) dye from CF-containing vesicles via the principle of size exclusion.** (A) 300 µl of CF-encapsulated vesicles was deposited onto a Sephadex column™; one can immediately observe dilution of the free CF (depicted by yellow band). The red band represents the CF-containing vesicles. (B) Upon elution of the sample with elution buffer (solution 2.2), it is apparent that the free dye is retained within the column whereas the vesicle population clearly moves preferentially along the column (highlighted in B, by 1 and 2 respectively).

2.3.2.3 Column calibration

The Sephadex™ column, used to exclude unencapsulated dye from the CF containing vesicles, was calibrated to confirm the lipid concentration gained post elution (ca. 2 mM). Note that section 2.4.1.2 describes and discusses this in detail, as it was an important step in assay development. In order to conduct these experiments, the following lipid mixture was utilised: DOPC, doped with the lipid Rh PE (1 mg / ml, 1318.75 g / mol) in a 99.5 : 0.5 mol % ratio. Fluorescence measurements were conducted using a Cary Eclipse (Varian) Fluorescence Spectrophotometer (Varian, Inc.). All measurements involving Rh PE utilised an excitation wavelength of 557 nm, with fluorescence emission collected from 570 – 700 nm. Excitation and emission slits were both set to 5 nm, and a medium scan rate and a photomultiplier tube (PMT) detector voltage of 500 V utilised. The fluorescence experiments described within this chapter were conducted utilising Microwell plates (Microplate 96 well, Fisher Scientific Ltd), which are able to contain a total volume of 400 µl.

2.3.2.4 Efflux measurements

For all efflux measurements, conducted with CF, an excitation wavelength of 490 nm was employed. Where kinetic experiments were conducted, an emission wavelength of 516 nm was chosen. Excitation and emission slits were both set to 5 nm, and a medium scan rate and a photomultiplier tube (PMT) detector voltage of 500 V utilised.

The general format of the experiments involved introducing a 150 µl aliquot of drug solution (or buffer, for control experiments) to a 150 µl sample of dye-loaded vesicles (lipid concentration equal to 0.2 mM) residing in one of the Microplate wells. The final lipid and drug concentration are therefore half that of their initial concentrations; the lipid concentration was always maintained at 0.1 mM (final concentration) with the concentration of the exogenous species being varied. Efflux of the dye from the vesicles was then monitored by measuring the fluorescence intensity at 516 nm at specific intervals over time.

Addition of 1 % (v/v) of Triton X-100 achieved disruption of the vesicles, hence releasing entrapped dye into the total sample volume (303 µl) and enabling the final fluorescence intensity (at $t \rightarrow \infty$) to be determined. All efflux measurements were conducted at room temperature.

2.3.2.5 Critical micelle concentration (CMC) measurements

Interfacial surface tension (IFT) measurements were conducted using an Easy Drop tensiometer (Krüss), for the determination of the critical micelle concentration (CMC) for various of drug molecules. A 0.5 ml glass syringe (Hamiliton, bore inner diameter = 3.256 mm), equipped with a disposable needle (Krüss, diameter = 1.830 mm), was used to dose and hence interrogate the solution of interest. The Easy Drop tensiometer and syringe mounting stage can be viewed in figure 2.6 A and B respectively. Note, that as water-in-air IFT measurements were utilised in these experiments, it is crucial to ensure that the hanging droplet does not lose volume over time (i.e. over a measurement period of 10 minutes). Hence to maintain a constant volume, the droplet was suspended within a closed environment, i.e. a chamber, comprised of a glass cuvette (Starna Scientific Ltd., Type 3 (2 cm x 1 cm x 5 cm) and cover plate (Krüss), containing a few millilitres of buffer solution (as illustrated in figure 2.6 C).

The graphs illustrated in figure 2.6 D, E and F illustrate the effect upon the IFT, droplet area and volume in the presence and absence of a closed environment. The use of a chamber (a cuvette with a few millilitres of buffer and a cover plate) was found to prevent droplet evaporation.

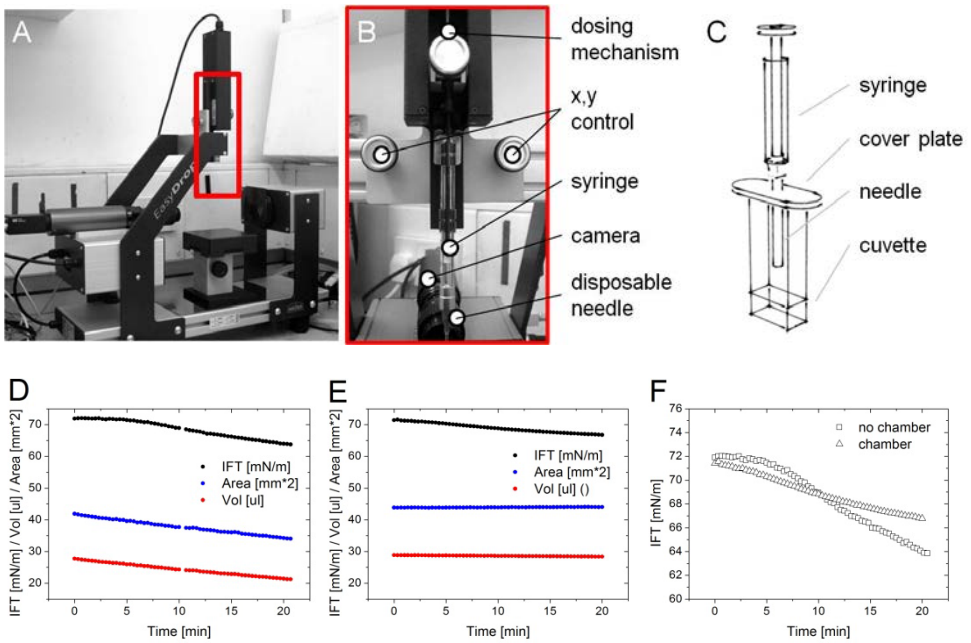


Figure 2.6: **Apparatus used to conduct interfacial surface tension (IFT) measurements.** (A) Easy Drop tensiometer; the red box indicates the location of the dosing mechanism and syringe housing. (B) An enlarged version of the motorised dosing syringe. (C) The specific experimental setup utilised; importantly, a cuvette containing a few millilitres of buffer and capped with a cover plate are used to minimise evaporation of the droplets under investigation. (D) Graph indicating the change in the IFT, area and volume of a droplet (sample is an aqueous solution of 1 mM DOPC vesicles) without the use of a chamber (i.e. cuvette and cover plate). (E) The same experiments as presented in D, but in the presence of a chamber (i.e. cuvette and cover plate). (F) Comparison of the IFT results gained in the presence and absence of a chamber.

All data were collected using the software programme "Drop Shape Analysis". Specifically, the Trackerman programme was utilised to determine an equilibrium value of the IFT (IFT_{eq}). This programme was set up to record an IFT measurement every 10 s, for a total duration of 10 minutes. After approximately 6-7 minutes the system reached equilibrium and the remaining data points were used to ascertain the IFT_{eq}. Each data point represents an average of three or more IFT_{eq}s, quoting an error equal to plus or minus one standard deviation. See figure 2.7, which illustrates the type of trace

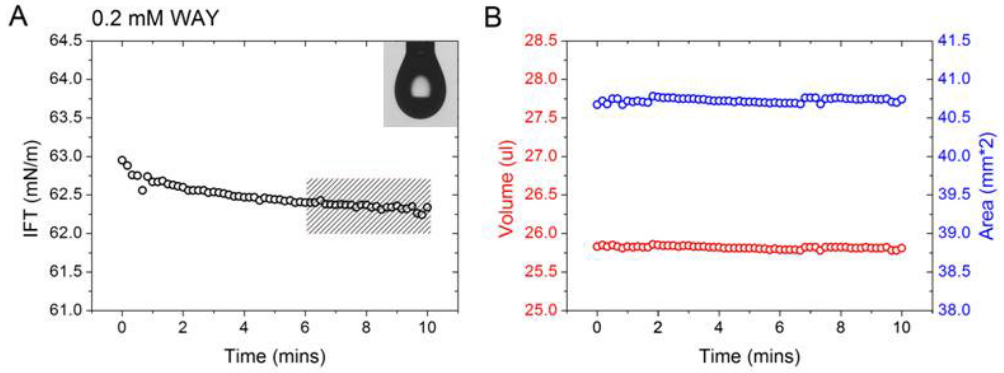


Figure 2.7: **Determining equilibrium values for the interfacial surface tension (IFT_{eq}).** (A) Example of an interfacial tension (IFT) curve gained over time using the Trackerman programme for a sample containing 0.2 mM WAY. The shaded region depicts the data used to ascertain the equilibrium value of the IFT (IFT_{eq}) for one measurement. The inset image illustrates the hanging droplet from which the measurement was gained. (B) The graph illustrates that a constant area and volume are maintained throughout the duration of the experiment.

gained from the Trackerman programme (for 0.2 mM WAY) and the region used to determine the IFT_{eq}.

In order to determine the CMC for a drug of interest, the IFT_{eq} for several drug concentrations is determined. A plot of the IFT versus concentration can then be constructed. The CMC is defined as the concentration at which further addition of drug molecules leads to the formation of more micelles (i.e. the air-water interface is saturated with drug monomers).[234] The expected relationship between IFT and drug concentration is displayed in figure 2.8. Linear extrapolation of the data contributing to (i) the decrease in the IFT (possessing a negative gradient) and (ii) the point at which the IFT no longer changes will yield a value for the CMC. All experiments were conducted at room temperature. The lights in the vicinity of the tensiometer were turned off to ensure that good contrast was gained between the drop circumference and background.

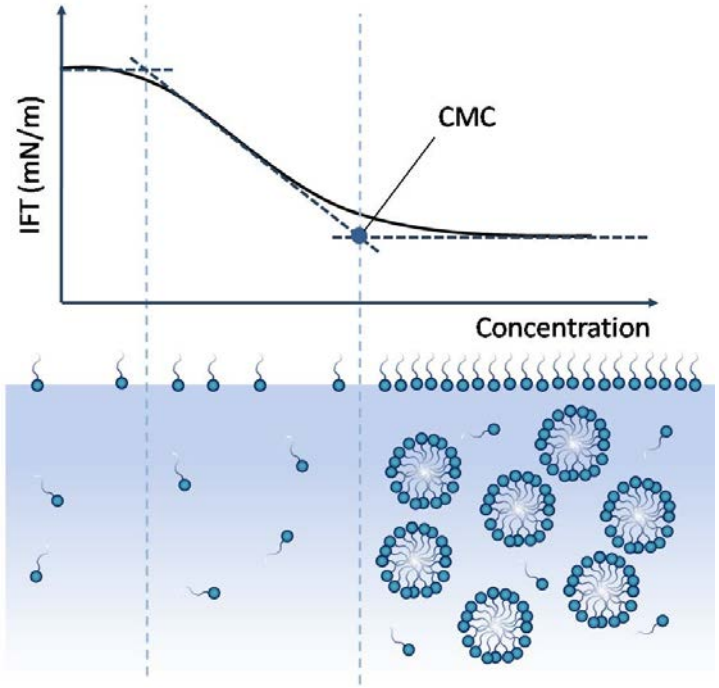


Figure 2.8: **Determination of the critical micelle concentration (CMC).** The graph illustrates the nature of a theoretical plot of the interfacial surface tension versus concentration for a surfactant (i.e. drug molecule). The data is then extrapolated to determine the CMC, as indicated on the diagram. At low surfactant concentrations, relatively few monomers reside at the air-water interface. However upon increasing the concentration of surfactant, more and more monomers incorporate themselves at the interface, thus resulting in a decrease in the interfacial surface tension (IFT). At a critical concentration, i.e. the CMC, the air-water interface becomes saturated with monomers. Further increases in the surfactant concentration thus results in the aggregation of monomers to form increased numbers of micelles.

2.4 RESULTS AND DISCUSSION

2.4.1 Assay development

The various steps involved in the development of the CF assay are detailed in this section. Specifically, the assay format is addressed, as well as the steps taken in order to calibrate the Sephadex™ column and important control measurements.

2.4.1.1 Assay format

The bulk fluorescence measurements conducted during this investigation utilised a well plate and followed a specific format, illustrated by figure 2.9. The experimental format consisted of placing 150 μl of pre-prepared vesicle sample loaded with dye into a well (figure 2.9 (i)), followed by a further 150 μl of drug or solely buffer (control) solution (figure 2.9 (ii)). The fluorescence intensity (f(t)) at 516 nm was monitored at 10 s time intervals after this addition and the system was completely disrupted with 1 % (v/v) Triton-X 100 to yield the final fluorescence intensity (f_{inf}, figure 2.9 (iii)). This information can also be represented graphically, as illustrated by the example efflux curve displayed in figure 2.9.

As CF possesses a unique fluorescence fingerprint, it means that this property can be exploited when utilising dye-leakage assays. As described previously (section 2.2.1), CF is self-quenched at very high CF concentrations, which subsides, upon dilution, to yield an increase in the fluorescence intensity (until a maximum value is reached). Hence, the experiment can be tuned such that the complete disruption of vesicles, encapsulating 50 mM CF, results in a final CF concentration that is close to this maximum output intensity (i.e. a fluorescence intensity of ca. 700 a.u. is gained, for a given set of experimental conditions, when a CF concentration of at ca. 10 μM is present, see the CF calibration curve displayed in figure 2.10).

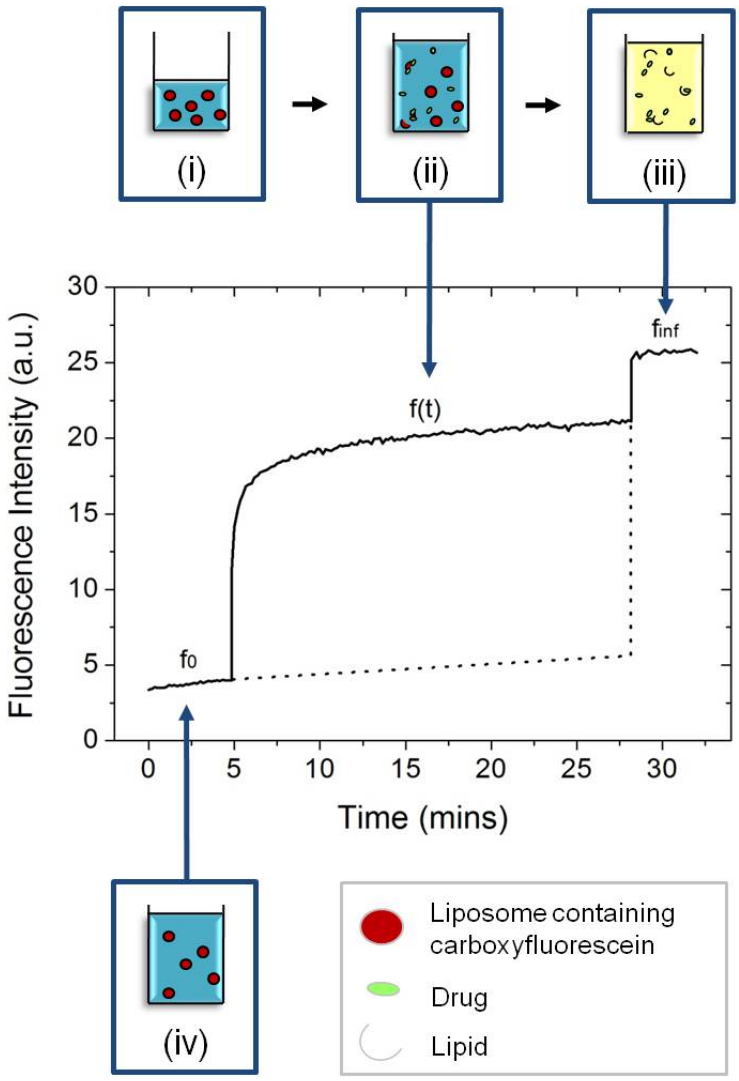


Figure 2.9: **Assay format.** Pictorial representation of the basic experimental format practised during this investigation, including a typical time-course curve monitoring the rate of efflux of self-quenched CF from encapsulated vesicles. Initially, 150 μl of the dye-loaded vesicle suspension is placed into the well (i). Upon inclusion of a membrane disrupting entity (ii), the increase in fluorescence intensity at specific time points (f(t)) can be monitored i.e. efflux of dye from vesicles. Addition of 1 % (v/v) Triton-X 100 yields the final fluorescence intensity (f_{inf}) after complete vesicle disruption (iii). Note that the initial fluorescence intensity (f_0) is gained by measuring a sample comprised of 150 μl of the dye-loaded vesicle suspension and 150 μl of buffer solution (iv).

The total volume of aqueous solution held in the well during the experiment (300 µl) is known and the approximate concentration of lipid required in order to achieve this maximum intensity (i.e. after disruption of vesicles) may therefore be calculated. Each vesicle (with a diameter taken to be 100 nm) will contain approximately 5E-04 fl of 50 mM CF. The number of vesicles can be calculated and hence the molarity of lipid required, achieving the optimum dilution.

For example, if a final concentration of ca. 10 µM CF is desired (ca. -5 on the log scale using units of mol / dm^3, see figure 2.10), which should possess a fluorescence intensity of ca. 700 a.u. according to the calibration curve, then the dilution factor going from a 50 mM to a 10 µM solution would be 5000. Therefore the total internal vesicle volume present in the system would have to encapsulate ca. 0.1 µl of 50 mM CF in order for this to be achieved.

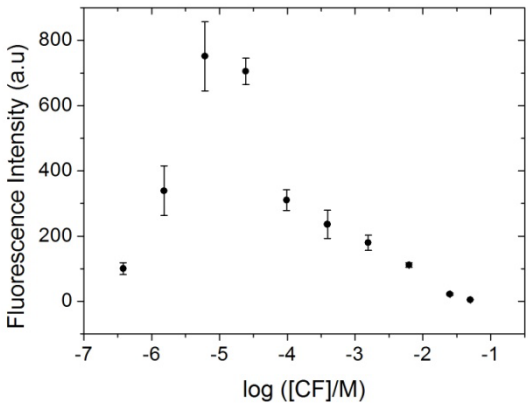


Figure 2.10: **Carboxyfluorescein (CF) calibration curve.** The dependence of fluorescence intensity (490 nm excitation, 516 nm emission) upon CF concentration is demonstrated and several repeats of the data included (error is equal to ± 1 s.d.). Ideally, 100% leakage of CF from vesicle lumens would result in a final CF concentration that yields a fluorescence value close to the fluorescence maximum.

The number of vesicles (ves) that could encapsulate 0.1 µl, calculated using a total internal vesicle volume of 5E-13 µl, is ca. 2E+11. The number of moles per vesicle, 2.5E-20 mol/ves (the value of which assumes a cross sectional area

of a lipid head group to be ca. 0.66 nm^2 [235] and a bilayer to thus contain ca. 9E-04 lipids), can be utilised to determine the moles of lipid required, 3E-08 mol, and hence molarity, 1E-04 M (0.1 mM). This lipid concentration was used in all vesicle experiments.

In order to normalise the data and therefore enable direct comparison between each experimental data set, an efflux function (see equation 2.1) can be implemented. This yields a result where $0 < E(t) > 1$ holds,[236] where E(t) is defined as follows:

$$E(t) = \frac{(f_{inf} - f(t))}{(f_{inf} - f_0)} \qquad \text{Equation 2.1}$$

f_0 = the fluorescence intensity of the sample in the absence of membrane perturbing agent

f(t) = the fluorescence intensity of the sample at a specific time point, t, after having introduced the membrane perturbing agent.

f_{inf} = the fluorescence intensity of the sample after having introduced 1 % v/v Triton-X 100

The percent of CF leakage is thus defined as:

$$\%\ CF\ \ leakage\ \ = 1 - E(t).100\% \qquad \text{Equation 2.2}$$

2.4.1.2 Calibration of column

The first step involved calibrating the Sephadex™ column, used to separate the CF-containing vesicles from the free dye, in order to determine the lipid concentration of the sample collected. Initial experiments involved preparing Sephadex™ columns by hand; however it was found that pre-packed

Sephadex™ columns afforded better reproducibility between column changes and hence less variation in the final lipid concentration collected.

The graph displayed in figure 2.11 A indicates the percentage of lipid collected in each fraction, after having eluted an extruded aliquot of 12.5 mM DOPC (300 μl), doped with RhPE (DOPC : Rh PE, 99.5 : 0.5 mol %), through the column. Each fraction was found to contain 475 μl of elutant, equivalent to five "drops". Fractions 6-9 were then combined, yielding a total lipid concentration of 2.0 ± 0.2 M (see Appendix 1). Although lipid is present in fraction 10, as observed in figure 2.11 A, this was not combined with fractions 6-9. This is because fraction 10 was found to contain the first traces of the free dye, as determined by running a 300 μl aliquot of the CF stock solution through the column.

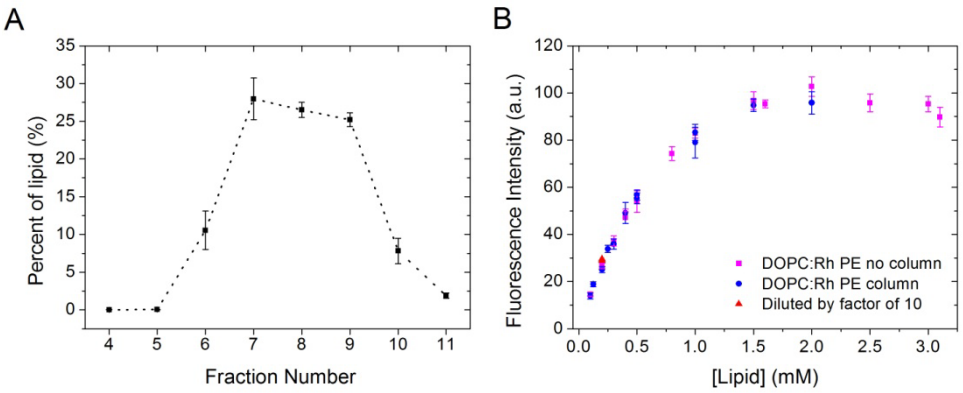


Figure 2.11: **Column calibration.** (A) Graph indicating the fractions into which the lipid, i.e. DOPC doped with Rh PE (99.5 : 0.5 mol %), is eluted. The fluorescence intensities of each fraction at 591 nm were measured and the percentage of lipid in each calculated accordingly. Fractions 6-9 were combined and used to perform efflux measurements. (B) The lipid concentration of the elutant (combined fractions 6-9) was thought to be ca. 2.0 mM. In order to confirm this, the sample was diluted to form numerous solutions of different lipid concentration (DOPC : RhPE column), and the fluorescence intensities of each compared to a vesicle sample prepared in an analogous manner, which had not been eluted through a Sephadex™ column prior to dilution (DOPC : RhPE no column). It can also be observed that a 10 fold dilution of the combined vesicle fractions, as is performed during each experiment, successfully yields a lipid concentration of 0.2 mM within error ("diluted by a factor of 10"). Errors represent ± 1 s.d. ($n > 3$).

Furthermore, the total lipid concentration of the combined fractions was confirmed by performing an examination with an external standard of known lipid concentration. First, the vesicle suspension assumed to be ca. 2 mM, i.e. the elutant comprised of the combined fractions (numbers 6-9), was diluted in order to yield numerous solutions of different lipid concentration. The fluorescence intensities of these samples (at 591 nm) were then plotted and displayed in figure 2.11 B. These data were then compared to an external standard of known concentration, where, for example, loss of lipid to the column could not have occurred. Specifically, a 12.5 mM DOPC : RhPE (99.5 : 0.5 mol %) lipid sample was extruded, diluted to form solutions of various lipid concentration and the fluorescence intensities measured. It can be observed, from figure 2.11 B, that the results from the two experiments are in good agreement with one another, i.e. they are within error, hence confirming that lipid is not lost to the column and that the lipid concentration can be taken to be ca. 2.0 mM. A dilution of the combined elutant fractions "by a factor of 10" was also included, in order to mimic the exact dilution conditions that occur during experiments. The results are displayed in figure 2.11 B and indicate that dilution falls within the remit of the external standard.

2.4.1.3 Control measurements

The control measurements relevant to all experiments have been included in this section. Those more specific to a particular experiment (such as drug-dye interactions) have been integrated within the relevant sections.

Evidence for vesicle formation and encapsulation of carboxyfluorescein

The first question one may wish to ask is what evidence can be collected to prove that these CF-encapsulating vesicles have indeed been produced and the external dye removed? A key observation that has been made certainly supports their formation. After fractions 6-9 have been collected from the column and collated (containing ca. 2.0 mM lipid and appearing red/orange in colour), the solution is then diluted to form a lipid concentration of

approximately 0.2 mM. In order to achieve this, 160 µl of the 2.0 mM lipid suspension is pipetted into 1440 µl of the elution buffer to yield a total volume of 1600 µl. Crucially, there is no change in the colour of the solution upon dilution, indicating that: (i) the external dye has been successfully removed and (ii) the vesicles maintain their form, i.e. they do not burst. Additionally, dynamic light scattering experiments have been conducted, revealing that the average diameter of the vesicle population post elution is 115 ± 4 nm.

Effects due to scattering from vesicles alone (at a concentration of 0.1 mM)

One may expect phospholipid vesicles to scatter light, being spherical entities. As these assays utilise 490 nm light to excite the samples, it is important to investigate to what extent it is dispersed. A control has been performed with solely DOPC vesicles, where the final concentration of lipid ranges from 12.5 mM to 4 µM. The data are displayed in figure 2.12 A. It can be seen that at the concentrations employed in this investigation (0.1 mM final), only a very small contribution to the fluorescence intensity will arise due to scattering in the region of interest (500-600 nm).

Assessing leakage of CF from vesicles over time

An important control includes assessing the rate of leakage of encapsulated CF from the interior of a vesicle, i.e. when the vesicles are present in buffer alone and no membrane perturbing species have been introduced. This has been assessed over 1 hour time periods, with the CF containing vesicles being used no longer than 1 hour after production. Figure 2.12 B illustrates that CF leakage from vesicles in the absence of membrane perturbing species is minimal, over a one hour time period.

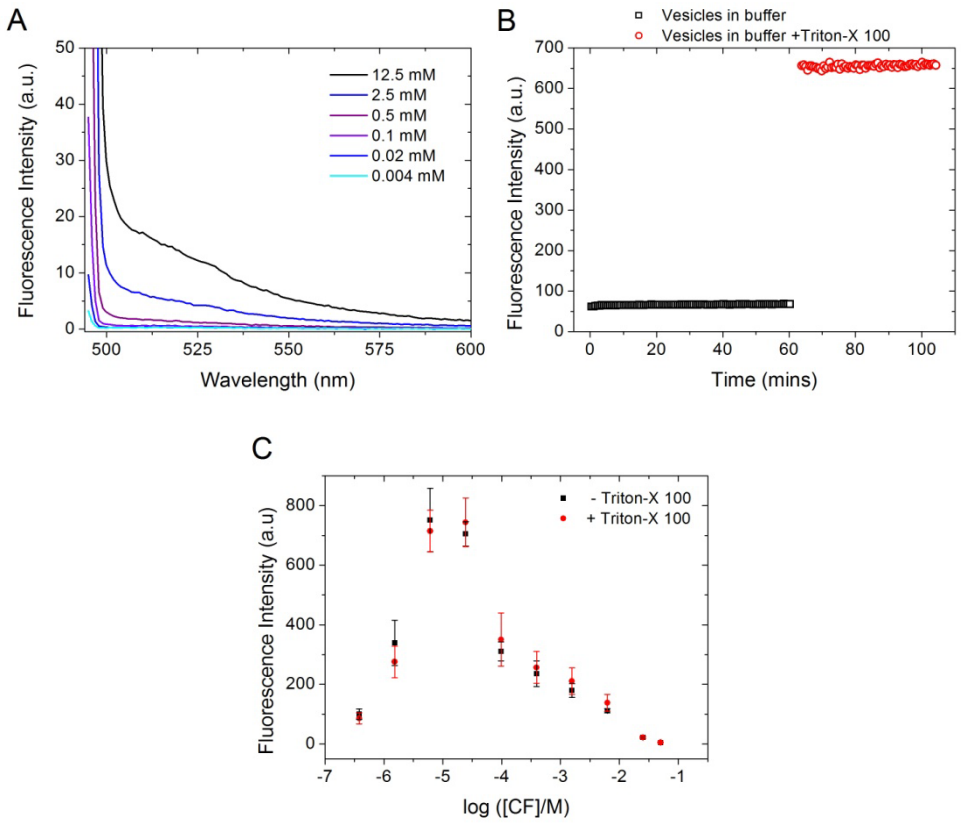


Figure 2.12: **Control measurements.** (A) Influence on the fluorescence intensity due to scattering from vesicles alone (using different lipid concentrations), where an excitation wavelength of 490 nm is employed. (B) Graph illustrating the extent of CF leakage from vesicles over a one hour time frame. It can be observed that the addition of Triton-X 100 results in the release of the internalised dye. (C) Effect of Triton-X 100 addition on the fluorescence intensity of CF over a wide concentration range.

Triton-X 100 and carboxyfluorescein control

The effect of Triton-X 100 on the fluorescence intensity of CF has also been investigated over a range of concentrations, as illustrated by the graph presented in figure 2.12 C. Within error, it can be ascertained that Triton-X 100 does not affect the final fluorescence intensity. Every attempt was made to ensure the amount of Triton-X 100 introduced was equivalent, though this was often difficult due to the viscous nature of the surfactant.

2.4.2 Reproducibility of assay: investigations with chlorpromazine, WAY and imipramine

The first experiments included investigating the reproducibility of the assay. In order to achieve this, three water soluble drugs were chosen, namely imipramine, WAY and chlorpromazine. The effect of drug concentration on the efflux of CF from vesicle lumens was investigated, the results of which are displayed in figure 2.13. Note that each repeat comprised freshly made vesicle and drug suspensions.

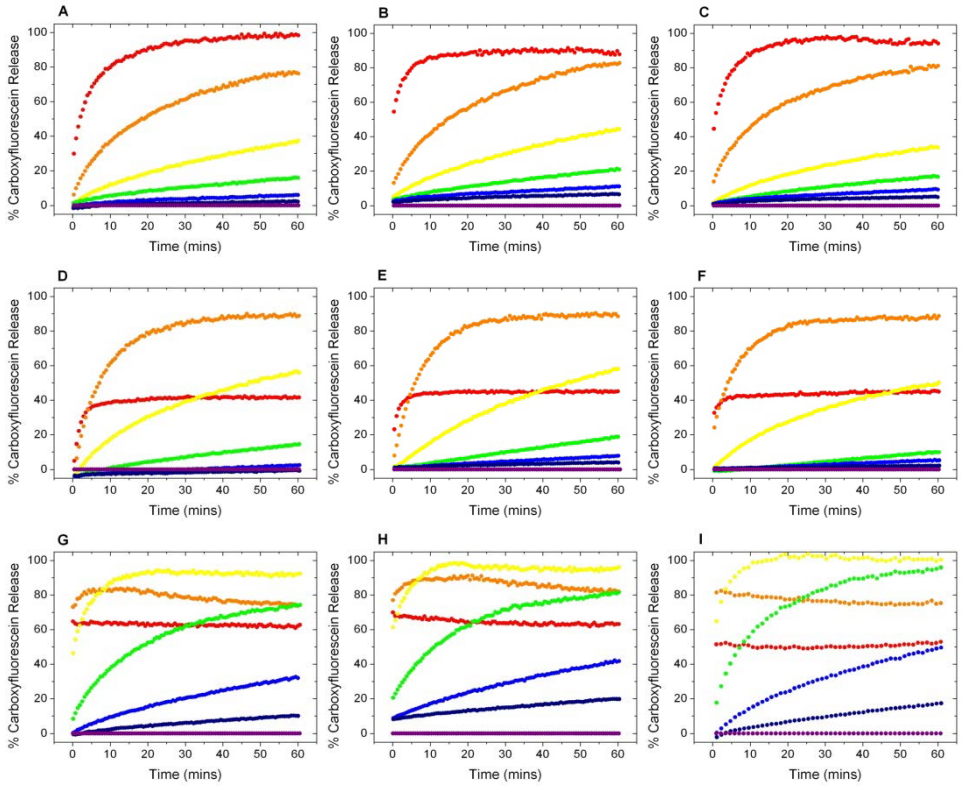


Figure 2.13: **Effects of three drugs (three repeats for each) on the efflux of carboxyfluorescein from DOPC vesicles (buffer only).** (A-C) Imipramine, (D-F) WAY, (G-I) chlorpromazine. Drug concentrations employed (final) are represented as follows: 1.6 mM (●), 0.8 mM (●), 0.4 mM (●), 0.2 mM (●), 0.1 mM (●), 0.05 mM (●), 0 mM (●).

Visual inspection of the efflux curves displayed in figure 2.13 reveals that there is a good level of reproducibility from experiment to experiment (for each drug investigated). It was important to utilise drug and vesicle suspensions that were freshly made in each instance, in order to introduce as much variation as possible into the experimental data gained. It can also be observed that efflux of CF is dependent upon the concentration of drug present. Generally speaking, the more drug molecules present per set volume, the faster the rate of CF release. In simple terms, this can be understood by considering the amount of amphiphilic drug molecules available to intercalate at the polar / apolar interface of the lipid membrane - the more drug molecules that are present, the more likely it is that they are able to incorporate themselves within the amphiphilic lipid environment. The chemical motifs of imipramine, chlorpromazine and WAY are displayed in figure 2.14 for reference.

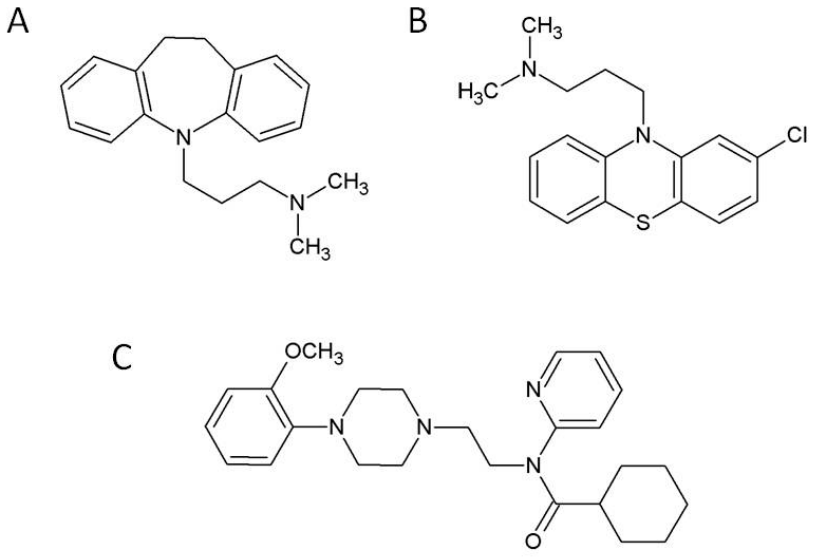


Figure 2.14: **The chemical motifs of imipramine, chlorpromazine and WAY.** (A) imipramine, (B) chlorpromazine and (C) WAY.

In order to gain quantitative information from the data presented in figure 2.13, the efflux curves were fitted using an exponential decay model to ascertain the initial rate of CF release (see Appendix 2 for further information). The dependency of the initial rate of CF release on drug concentration (with regards to chlorpromazine, WAY and imipramine) has been summarised graphically and is displayed in figure 2.15 A.

Not only can it be observed that the rate of CF release is linked to changes in drug concentration (where the final lipid concentration remains constant), the assay is able to distinguish between relative initial rates of CF release due to the introduction of different drug samples present at different concentrations in solution. For example, it can be observed from figure 2.15 A that the initial percent of CF release per minute (initial % CF release / min) is more prominent for chlorpromazine, than for WAY or imipramine and hence the ability of these drugs to induce CF release can be ranked in the following order:

chlorpromazine > WAY > imipramine

This is easily visualised if the initial % CF release / min for a specific drug concentration is monitored (e.g. 0.4 mM).

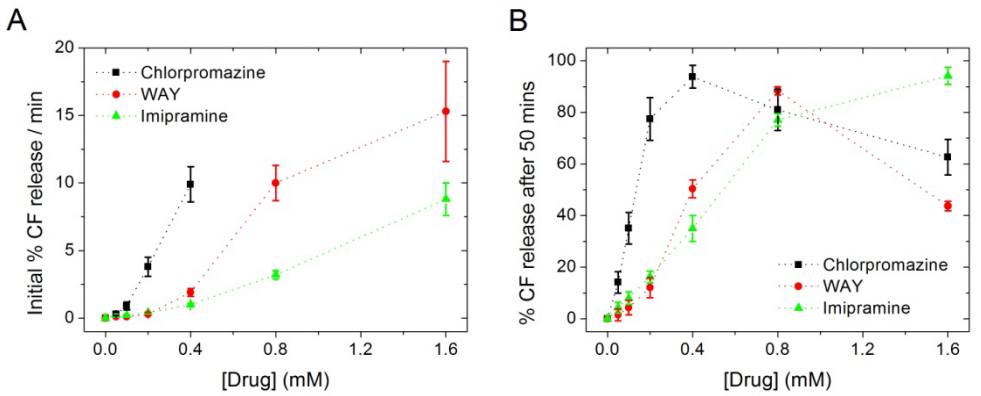


Figure 2.15: **Dependency of carboxyfluorescein (CF) leakage upon the introduction of chlorpromazine, WAY and imipramine.** (A) Dependency of the initial rate of CF release on the concentration of chlorpromazine, WAY and imipramine. (B) The percentage of CF released after 50 minutes in the presence of different concentrations of chlorpromazine, WAY and imipramine. Reported errors represent ± 1 s.d. (where n ≥ 3).

These results are consistent with those previously reported in the literature. It has been shown, using surface plasmon resonance (SPR) techniques, that chlorpromazine exerts more pronounced effects on DOPC bilayers than imipramine.[214] Chlorpromazine is thought to bind more to DOPC bilayers, compared to imipramine, due to the fact that chlorpromazine is more hydrophobic.[214,237] Hence the degree of drug interaction with the hydrophobic lipid bilayer is enhanced, causing increased levels of molecular disorganisation and resulting in increased levels of CF release. The water solubility of imipramine is twice that of WAY (50 and 25 mg / ml respectively[238,239]), which may provide one explanation as to why WAY induces a greater effect on CF leakage than imipramine.

A graph illustrating the percent of CF released from vesicle lumens, fifty minutes after introducing chlorpromazine, WAY and imipramine, has also been constructed (see figure 2.15 B). This provides information about the extent of CF released at later time points (as $t \rightarrow \infty$) with different drug concentrations. Naturally, the data displayed in figure 2.15 B mirrors the

information represented in figure 2.15 A: a higher drug concentration leads to a higher initial rate of release, which in turn will lead to a greater percent of CF release, if capturing the data at a specific time point. It can be observed that the data could be represented by a sigmoidal function, where the percent of CF released after 50 minutes begins to approach a plateau as the drug concentration is increased. However, upon looking at the traces for chlorpromazine and WAY, in figure 2.15 B, it can observed that the percent of CF released after 50 minutes appears to decrease after the introduction of certain drug concentrations (i.e. drug concentrations at the higher end of the spectrum utilised). The reason why this feature occurs is due to the presence of drug-dye interactions. More specifically, the apparent decrease in the percentage of CF released after 50 minutes observed in the presence of chlorpromazine and WAY (figure 2.13 and 2.15 B) is due to the dye interacting with drug micelles, which is a well known phenomenon.[240] Hence, the use of a dye that internalises within surfactant micelles is one way in which to determine the critical micelle concentration (CMC) for a drug.[241,242] CMC measurements have been undertaken in order to confirm this finding using a drop tensiometer (see section 2.3.2.4 for further information). The dependence of the interfacial surface tension on the concentration of chlorpromazine, WAY and imipramine has been determined, and is displayed in figure 2.16 G, H and I. The leakage data (initial percentage of CF release per minute and percentage of CF release after 50 mins) have also been included in figure 2.16 for each drug investigated.

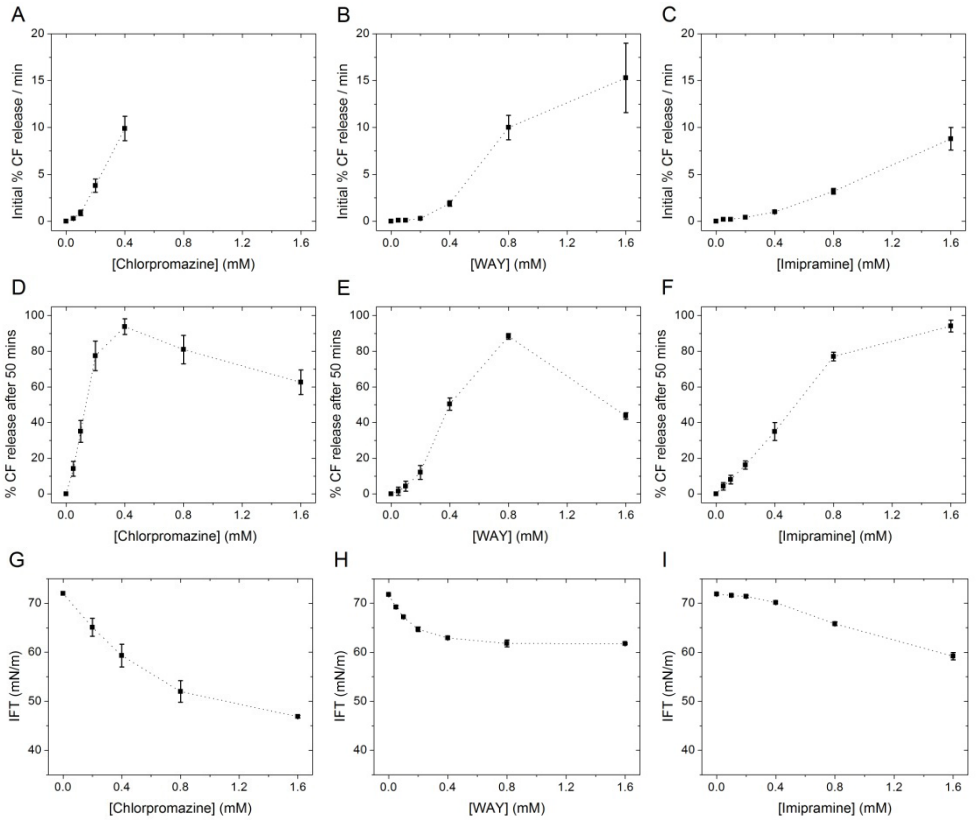


Figure 2.16: **Comparison of the leakage data for chlorpromazine, WAY and imipramine with the data gained from interfacial surface tension measurements.** (A), (B) and (C) illustrate the dependence of the initial percentage of CF release per minute upon the introduction of different concentrations of chlorpromazine, WAY and imipramine respectively. (D), (E) and (F) illustrate the dependence of the percentage of CF released after 50 minutes upon the introduction of different concentrations of chlorpromazine, WAY and imipramine respectively. (G), (H) and (I) illustrate the dependence of the interfacial surface tension (IFT) on the concentration of chlorpromazine, WAY and imipramine respectively. Reported errors represent ± 1 s.d. (where $n \geq 3$).

Inspection of the data presented in figure 2.16 H, shows that the interfacial surface tension (IFT) reaches a plateau at relatively low concentrations of WAY (i.e. at concentrations approximately equal to or greater than 0.2 M). Hence the CMC, in the case of WAY, is obtained at a relatively low concentration (ca. 0.2 mM). The CMC for chlorpromazine is much higher than for WAY. It can be observed from the plot of IFT versus concentration, in figure 2.16 G, that the reduction in the IFT from 0.8 to 1.6 mM deviates from

linearity, indicating that the CMC is fast being approached but has not yet been achieved. Imipramine has a comparatively high CMC; figure 2.16 I illustrates that a linear relationship between the IFT and drug concentration still exists up to concentrations of 1.6 mM.

Importantly the results discussed previously and illustrated in figure 2.16 G, H and I corroborate the trends observed in the leakage data. Firstly, as the CMC for imipramine is the highest of the three drugs examined and has not been reached at the highest concentration employed in these experiments, the presence of the drug will have a minimal effect on the dye. However, chlorpromazine and WAY affect the dye at higher drug concentrations. Discrepancies in the CF efflux data, owing to the presence of these drugs, can be observed in figure 2.16 D and E. Specifically, the percentage of CF released is found to decrease and hence based on the experiments described previously, this phenomenon can be attributed to the presence of drug micelles. Moreover, a greater percentage of CF appears to have been "removed" from the system when 1.6 mM WAY is introduced to CF-containing vesicles c.f. 1.6 mM chlorpromazine. It is thought that this is due to the presence of a greater number of drug micelles comprised of WAY at this concentration, c.f. chlorpromazine, when taking the IFT data for these drugs into consideration. Hence more dye can be sequestered by WAY drug micelles at this concentration. Perhaps therefore the CF assay may also present an interesting way in which to determine the CMC for drugs of interest. As an aside, it was also found that drug-dye controls, performed in the absence of lipid vesicles, mirror the CMC data (Appendix 2 for confirmation of drug-dye interaction).

The degree by which the IFT is reduced by chlorpromazine, WAY and imipramine (figure 2.16 G, H and I) appears to correlate with the initial rate of release (figure 2.16 A, B and C), i.e. chlorpromazine molecules seem to cause a larger drop in the IFT compared to WAY, with WAY resulting in a larger change in the IFT than impramine, for a set concentration. A larger decrease in the IFT reveals that the drug molecules interact more favourably with the air-

water interface. Hence, these data appear to reflect the drugs' abilities to bind to and consequently disrupt the membrane (i.e. their amphiphilicity).

Additionally, the data presented in figure 2.16 A and B, indicate that the initial rate of CF release starts to reduce and plateaus as the CMC of the drug is approached. This is an important result as it suggests that increasing the drug concentration above its CMC does not act in a beneficial manner in terms of the rate of CF release. This result can be understood when considering the relative concentrations of drug monomers in solution above and below the CMC. Below the CMC the number drug monomers in solution will increase with concentration, hence higher drug monomer concentrations will result in a higher degree of membrane perturbation. Above the CMC, however, the drug monomer concentration in solution will plateau, as the additional drug monomers participate in forming micelles; this therefore explains why increasing the drug concentration above its CMC does not further increase the rate of CF release.

2.4.3 Dependency of efflux rate on DOPE content

In order to demonstrate the flexibility of the CF assay and to provide an example of the type of biophysical measurements that can be conducted, the effect of increasing the level of DOPE in a DOPC bilayer on drug-induced CF leakage was monitored. This has not knowingly been investigated or published to date for chlorpromazine, WAY and imipramine.

The reason for considering PC bilayers, doped with different amounts of PE, is that these lipids are both predominant in mammalian membranes, both in the plasma membrane and membranes of cell organelles.[37] Biophysical studies aim to understand how incremental changes in one parameter at a time effect the overall system, thus building a picture containing increasing levels of complexity (i.e. using a bottom up approach).

It was hypothesised that the rate of CF release would increase, upon increasing the mole percent of DOPE in a DOPC bilayer. DOPE is a non-bilayer forming lipid, classed as Type II (see chapter 1, section 1.2.2.3) and as such DOPC bilayers containing DOPE possess higher levels of curvature elastic stress (as discussed in chapter 1, section 1.2.2.4). Hence, one would expect CADs to bind more avidly to such membranes in order to release this stress.[243]

2.4.3.1 Calibration of column using vesicles comprised of DOPC : DOPE

The first step involved calibrating the Sephadex™ column to ensure that vesicles comprised of DOPC : DOPE are eluted into the same fractions. Figure 2.17 A illustrates that the majority of vesicles were eluted into fractions 6-9, which is consistent with the results gained previously; the lipid concentration of the combined eluted fractions (6-9) for a 12.5 mM DOPC : DOPE : RhPE (79.5 : 20 : 0.5 mol % respectively) sample was found to be 2.1 ± 0.3 mM (see Appendix 3). Note that it was also possible to easily check which fractions the lipid sample was eluted into by visually inspecting the fractions. Specifically, the fractions containing the eluted vesicle suspension (i.e. 6-9) appeared red/orange in colour. No discrepancies were found with respect to the fractions into which the various DOPC : DOPE vesicle samples used in this investigation were eluted.

Experiments were performed as described previously (section 2.3.2.3) in order to determine the lipid concentration after dilution. Figure 2.17 B illustrates that the concentration of the collated fractions when diluted (DOPC : DOPE : RhPE column; 79.5 : 20 : 0.5 mol % respectively): (i) is consistent with the measured external standard (DOPC : DOPE : RhPE no column), (ii) is consistent with the DOPC measurements acquired previously (DOPC : RhPE column and DOPC : RhPE no column) and (iii) successfully yields a lipid concentration of 0.2 mM, within error, upon diluting the combined fractions by a factor of ten ("diluted by a factor of 10", figure 2.17 B), as is performed during each experiment.

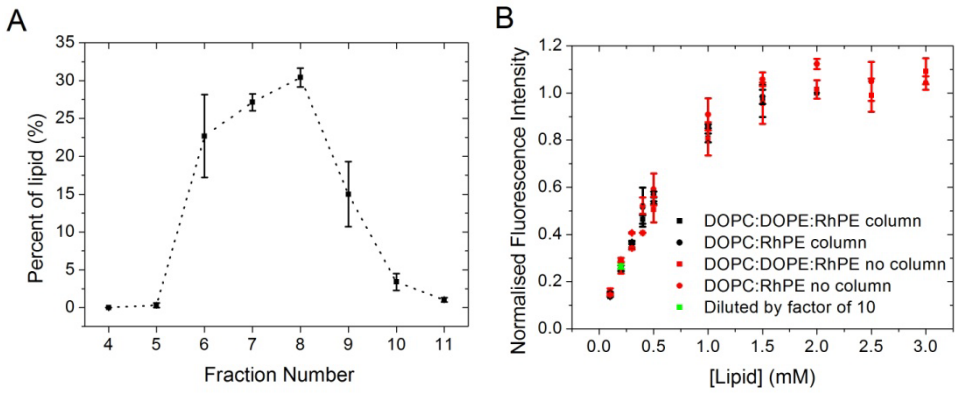


Figure 2.17: Calibration of column 2. (A) Graph indicating the fractions into which the lipid, i.e. DOPC doped with DOPE and Rh PE (79.5 : 20 : 0.5 mol % respectively), is eluted. The fluorescence intensities of each fraction at 591 nm were measured and the percentage of lipid in each calculated accordingly. Fractions 6-9 were combined and used to perform efflux measurements. (B) The lipid concentration of the elutant (combined fractions 6-9) was thought to be ca. 2 mM. In order to confirm this, the sample was diluted to form numerous solutions of different lipid concentration (DOPC : DOPE : RhPE column), and the fluorescence intensities of each compared to a vesicle sample prepared in an analogous manner, which had not been eluted through a Sephadex™ column prior to dilution (DOPC : DOPE : RhPE no column). The data gained after having calibrated the column with solely DOPC : RhPE has been included for comparison (DOPC : RhPE column and DOPC : RhPE no column). Additionally it can be observed that a 10 fold dilution of the combined vesicle fractions, as is performed during each experiment, successfully yields a lipid concentration of 0.2 mM within error ("diluted by a factor of 10"). Errors represent ± 1 s.d. (n > 3).

2.4.3.2 Control for CF vs DOPC : DOPE samples

A further control involved investigating the effect of introducing DOPE into a DOPC bilayer upon the final fluorescence intensity, gained after adding Triton-X 100. For example, it is important to determine whether there may be any substantial effects due to the introduction of differing amounts of a second lipid into the system. Upon the addition of Triton-X 100 (1 % v/v) to 0.1 mM vesicle suspensions, comprised of varying amounts of DOPE in a DOPC bilayer (specifically 0, 20, 40 and 60 mol % DOPE), it was determined that there is very little effect on the final fluorescence intensity after disruption when 20 and 40 mol percent of DOPE is included (compared to the pure

DOPC sample). There does appear, however, to be a slight reduction in the final fluorescence intensity as the percentage of DOPE is increased to high levels, i.e. 60 mol %, although this does not greatly affect the line of best fit (linear regression, gradient equal to -0.2 ± 0.3 fluorescence units / DOPE mol %). The results of this experiment can be viewed in figure 2.18.

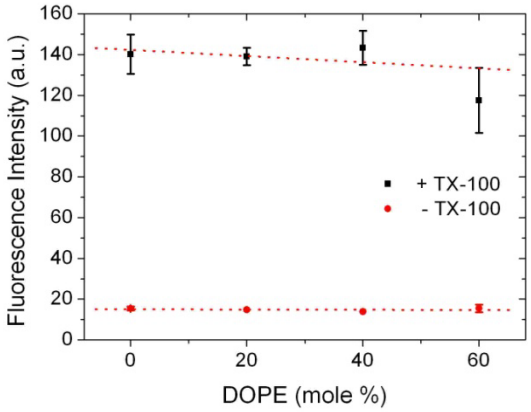


Figure 2.18: **Control investigating the effect of introducing DOPE into a DOPC bilayer upon the final fluorescence intensity.** The final fluorescence intensity has been measured (■) for a series of CF-containing vesicle suspensions upon the introduction of Triton-X 100 (1 % v/v). Specifically, the lipid systems investigated involve using DOPC : DOPE with the respective mol % equal to 100 : 0, 80 : 20, 60 : 40 or 40 : 60. The fluorescence intensity of the vesicle suspensions prior to the addition of Triton-X 100 has also been included (●). Errors represent ± 1 s.d. (n > 3).

2.4.3.3 Results for DOPC : DOPE samples

Figure 2.19 illustrates the results of experiments conducted with chlorpromazine, WAY and imipramine, to determine the effect on the rate of CF leakage upon introducing varying amounts of DOPE into the lipid system. The dependence of both the initial rate of CF release and the percentage of CF released after 50 minutes upon drug concentration was investigated and compared to the results gained in section 2.4.2.

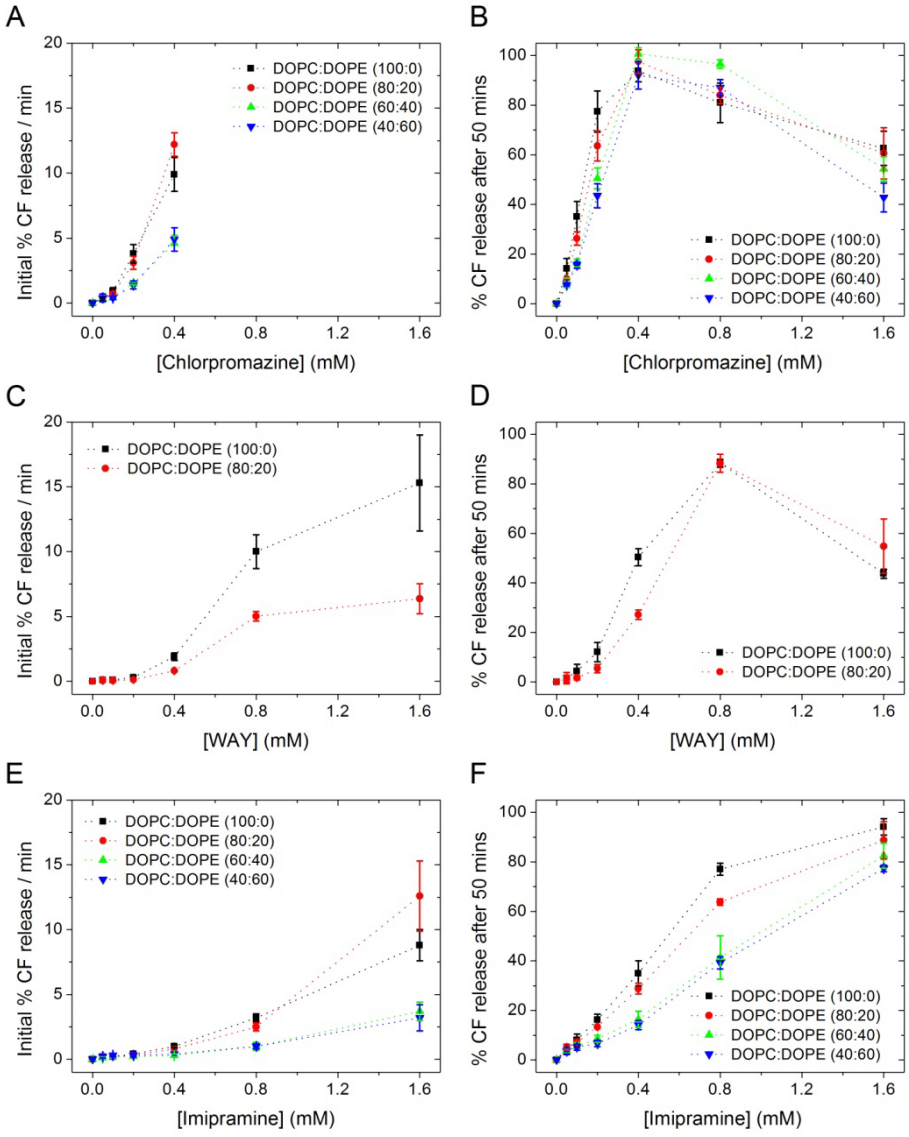


Figure 2.19: **Effect of introducing DOPE, into DOPC bilayers, upon the rate of carboxyfluorescein leakage.** (A), (C) and (E) illustrate the dependence of the initial percentage of CF release per minute upon the introduction of varying mol percents of DOPE within a DOPC bilayer, as well as different concentrations of chlorpromazine, WAY and imipramine respectively. (B), (D) and (F) illustrate the dependence of the percentage of CF released after 50 minutes upon the introduction of varying mol percents of DOPE within a DOPC bilayer, as well as different concentrations of chlorpromazine, WAY and imipramine respectively. Errors represent ± 1 s.d. (n > 3).

The results displayed in figure 2.19 A, C and E (also consult Appendices 4, 5 and 6) indicate that the initial rate of CF release *is* dependent upon the mole percent of DOPE incorporated into a DOPC bilayer (as well as the drug concentration, as previously established). It can be observed that the initial rate of CF release in fact decreases as the DOPE content increases, which opposes the original hypothesis; there exists a consistent decrease in the initial rate of CF release for each of the three drugs.

It is thought that a decrease in the initial rate of CF release with increasing DOPE content prevails due to the presence of hydrogen bonding between the DOPE head groups and drug molecules. In contrast to DOPC, the head group of DOPE consists of an $-NH_3^+$ group (for DOPC, the head group is $-NMe_3^+$). Figure 2.20 illustrates the chemical nature of DOPC and DOPE. The formation of hydrogen bonds between drug and lipid head groups will therefore prevent drug molecules from intercalating at the polar / apolar interface, thus essentially being sequestered at a position farther away from this interface and reducing membrane disruption and the extent of CF leakage. It therefore follows that the greater the DOPE content, the more pronounced the observed effect, which can be observed in the graphs presented in figure 2.19 A, C and E. One point to note is that the fits to the 100 % DOPC efflux curves, used to gain the initial rate of CF release, yield less satisfactory results when the highest measureable drug concentrations are used (0.4 mM for chlorpromazine and 1.6 mM for WAY and imipramine). Essentially an underestimate of the initial rate of CF release is afforded due to the fact that these experimental conditions yield very fast rates of CF efflux. Consequently, it is very difficult to capture the first few data points using this experimental format making it difficult to realise a true representation.

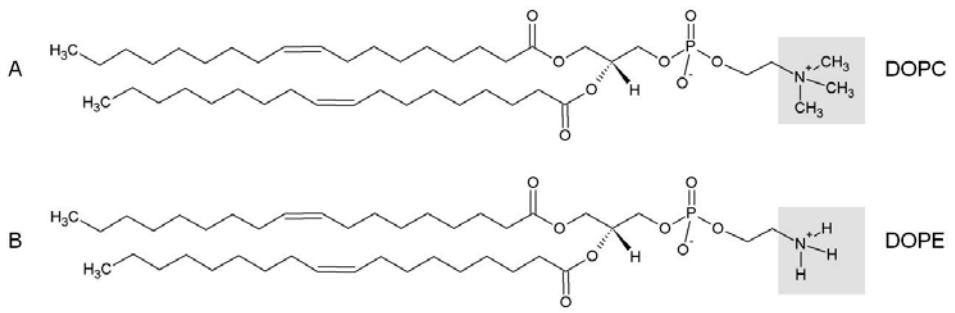


Figure 2.20: **Chemical motifs of DOPC and DOPE.** The chemistry of the head groups for DOPC and DOPE are displayed in (A) and (B) respectively (grey boxes).

The data presented in figure 2.19 B, D, and F again mirror the information gained in figure 2.19 A, C and E. Generally speaking, the data indicate that the percent of CF released at a specific point in time, i.e. 50 minutes after having introduced the drug to the dye loaded vesicles, is very much dependent on the mole percent of DOPE present. This is true for chlorpromazine, WAY and imipramine up to concentrations of 0.4, 0.8 and 1.6 mM respectively. However above a drug concentration of 0.4 and 0.8 mM, for chlorpromazine and WAY respectively, the percent of CF released after 50 mins is approximately equal, suggesting that virtually all of CF has been released.

Additionally, the inclusion of only 20 mol % DOPE appears to have a bigger effect on the initial rate of the release for WAY, in comparison to chlorpromazine and imipramine. This suggests that WAY molecules are sequestered more avidly by the lipid membrane. Upon examining the chemical motif of WAY, it can be observed that the number of potential regions where hydrogen bonding can occur is greater than for chlorpromazine and imipramine (see figure 2.14, section 2.4.2 for chemical motifs). Hence it is postulated that WAY can participate in more hydrogen bonding events with the lipid membrane, or more specifically with DOPE. This explains the reduction in the initial rate of release. Furthermore, this observation provides more evidence to support the aforementioned rationale: that it is the presence of DOPE which leads to the reduction in the initial rate of CF release.

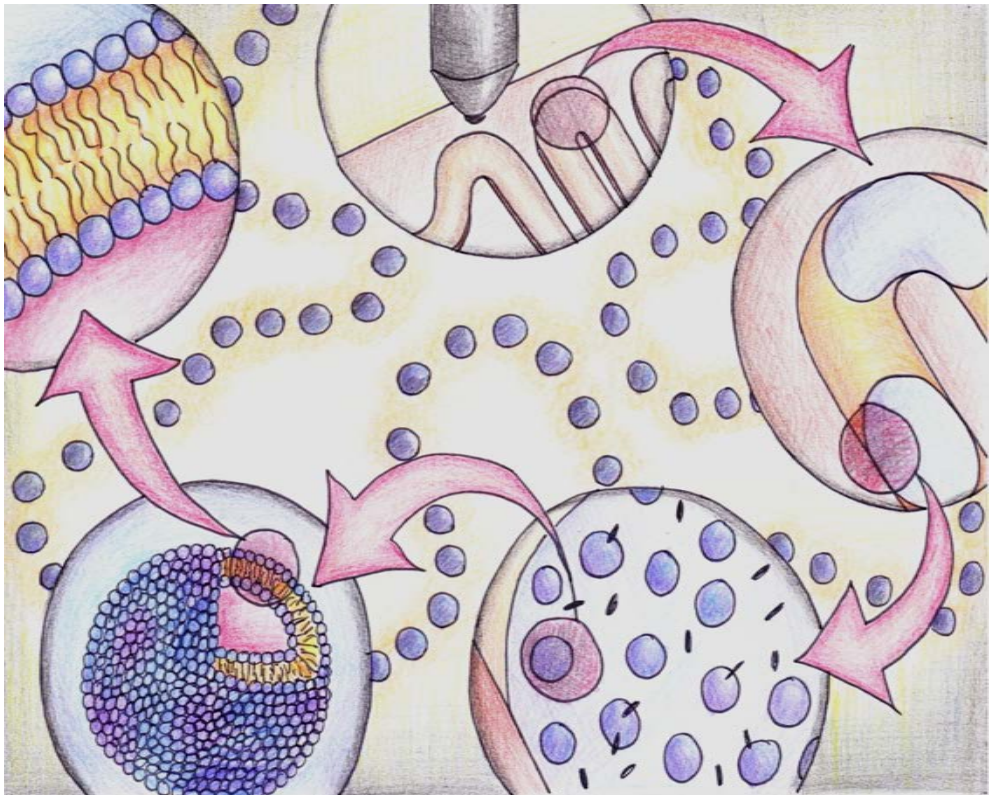
2.5 CHAPTER SUMMARY

The studies presented demonstrate that the CF leakage assay has been successfully set up, affording reproducible data comparable with trends observed in the literature. Additionally, studies highlight the fact that this methodology is able to afford important information about the interaction of drug molecules with model lipid membranes. For example, the influence of increasing the mole percent of DOPE in a DOPC bilayer has been investigated, which was found to reduce the rate of leakage. Hence this assay provides the means to gain further insight into the interaction of drug molecules with lipid membranes at the molecular level.

However, in order to elucidate the effects of different drug compounds on many lipid compositions, where changes in lipid head and tail groups can be investigated, substantial data sets need to be gained – not only in terms of probing different parameters that affect drug-membrane interactions, but also with respect to affording reliability in the data from numerous repeat measurements. In turn this will require significant amounts of reagents, as well as time. Accordingly, the use of microfluidic technologies offers a solution to this problem, where the opportunity to perform numerous experiments in quick succession is possible. Additionally, microfluidic technologies only require very small amounts of reagent, i.e. drug, which will also result in these experiments becoming more economically viable. Chapter 3 details the steps taken in order to translate the CF leakage assay into a high-throughput format using microfluidic technologies.

Chapter 3

Translation of carboxyfluorescein leakage assay into a microfluidic format



"Anybody who has been seriously engaged in scientific work of any kind realizes that over the entrance to the gates of the temple of science are written the words: 'Ye must have faith.'"

Max Planck

3.1 OVERVIEW

Chapter 3 builds on the work detailed in chapter 2, demonstrating that the carboxyfluorescein (CF) leakage assay can be performed in a microfluidic format and hence offers the possibility to rapidly screen drug- and protein-membrane interactions in high-throughput.

Initial attempts involved using fluorescence intensity measurements to perform the leakage assay in a microfluidic format. Unfortunately, calibration of experiments proved problematic and it was therefore decided to utilise time-resolved fluorescence measurements. Preliminary results suggest that this technique offers a potential solution to the problems encountered with the fluorescence intensity measurements.

3.2 INTRODUCTION

3.2.1 Droplet microfluidics

As detailed in chapter 1, section 1.4.1, microfluidic droplet technologies are emerging as a real alternative for use in high-throughput screening. Segmented flow in microchannels, i.e. the formation of water-in-oil droplets via the T-junction or flow-focusing methods (section 1.4.1.3), is highly advantageous. Not only does this technology enable rapid, efficient and reproducible mixing to occur inside each microdroplet,[111] segmented flow also ensures that uniform mixing is achieved. As thousands of droplets may be produced per second using this technique, acting as individual experimental vessels, it also means that large data sets can be collected therefore enabling more sophisticated statistical analyses to be performed. Hence it can be observed that droplet microfluidics offers many advantages over conventional technologies for performing assays, such as 96-well plate assays in fluorescence spectrophotometers.

The work described in this chapter utilises droplet-based microfluidics, owing to the format of the experiment being conducted. Specifically, the drug-dependent leakage of CF, from phospholipid vesicle lumens, is monitored over time. Such an assay, able to probe the interactions of drug molecules with a specific membrane of choice, has not previously been performed in a microfluidic device. The major technique used in the experiments described in this chapter was time-resolved fluorescence spectroscopy. Fluorescence lifetime imaging microscopy (FLIM) was also employed. Hence an introduction to the topic of the fluorescence lifetime has been afforded for the reader.

3.2.2 Fluorescence lifetime measurements

The fluorescence lifetime, denoted by τ, describes the average time that an fluorophore remains in its excited state before emitting a photon and hence returning to its ground state.[244] This emission is not fixed and occurs randomly; hence the fluorescence lifetime is a statistical average, described by the time constant in an exponential decay function such as that detailed in figure 3.1. A typical intensity versus time plot that one would collect during a lifetime experiment is illustrated in figure 3.1.

The lifetime, which can be gained by measuring the gradient of a plot of ln I(t) versus t for fits to single exponential decays, is equivalent to the inverse of the total decay rate (i.e. the sum of the emissive rate, k, and the non-radiative decay rate, k_{nr}) and is often ascertained using specialist software packages. The fluorescence lifetime of a fluorophore can range from the order of a few picoseconds to the microsecond regime.

There are several measurements that can be utilised to determine the fluorescence lifetime. These involve using time- or frequency-domain measurements.[244] Time-domain measurements have been used in the

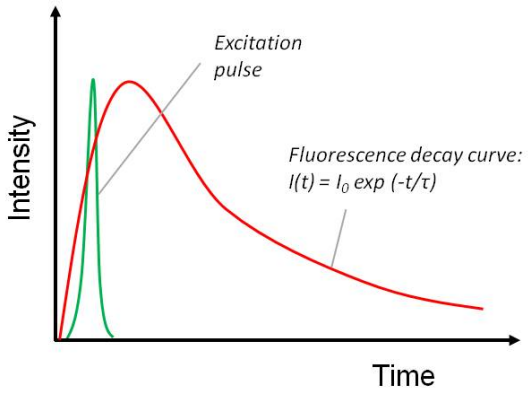


Figure 3.1: **A typical plot of intensity versus time gained during a fluorescence lifetime experiment.** The short excitation pulse and subsequent fluorescence decay are represented by the green and red traces respectively. The exponential decay function used for a single exponential fit is included and the time constant, i.e. the fluorescence lifetime (τ) can be extracted.

experiments described within this chapter, specifically time-correlated single-photon counting (TCSPC), as this was the technique available.

The basic principle of TCSPC is demonstrated in figure 3.2 A-C. A laser pulse of light is used to excite the sample of interest, which results in a photon being emitted at a specific time after excitation. Figure 3.2 A illustrates this principle, where three excitation pulses result in the emission of three photons, but with each photon emitted at a different time after excitation. The use of a pulsed laser, having a pulse repetition rate of 80 MHz, means that 80E-06 pulses occur per second. Hence a large number of photons can be sampled, if a data collection window of 5 minutes is used for example. A histogram of their respective times can be collated and the data then fit to an exponential decay. Figure 3.2 B illustrates how the time for photon emission to occur can vary for a hypothetical sample of eight photons, after having excited the sample with

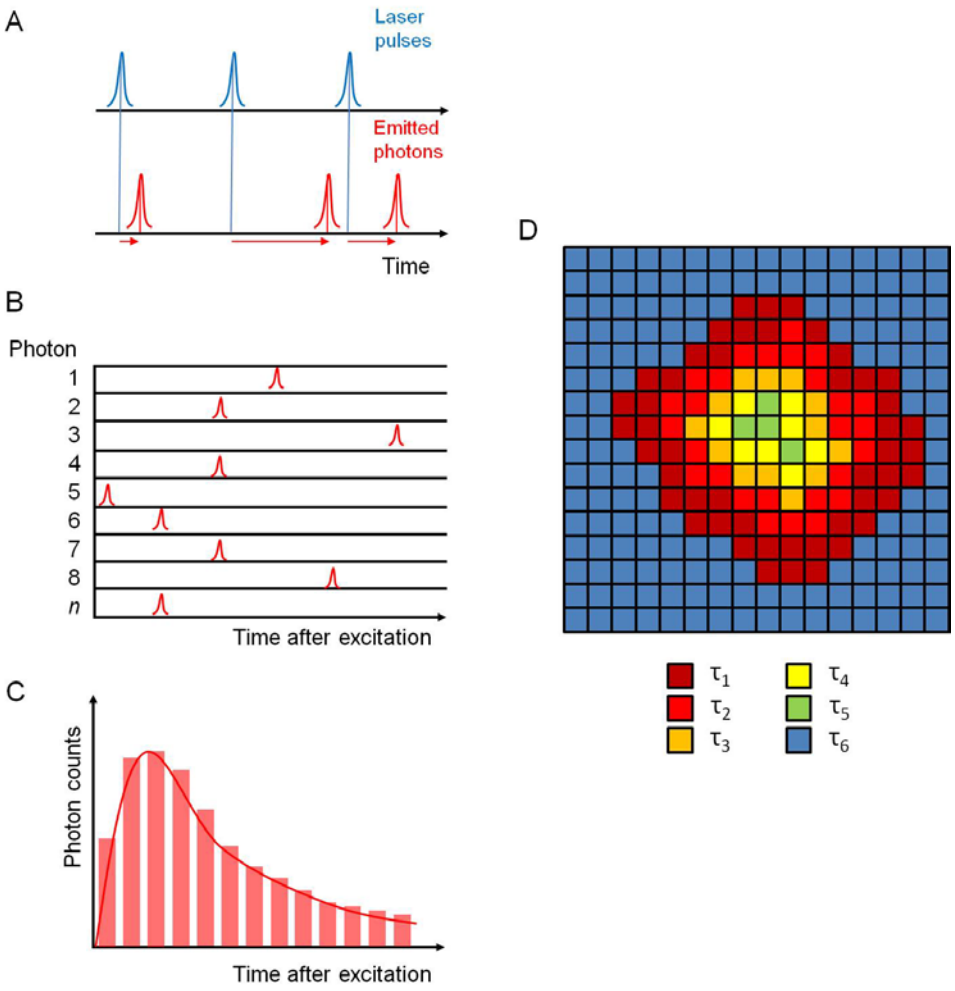


Figure 3.2: **Principle of time-correlated single-photon counting (TCSPC) used to extract information about the fluorescence lifetime.** (A) This image illustrates how the time taken for an excited sample to emit a photon can vary, hence being a random process. The blue waveforms represent the laser pulse used to excite the sample and the red waveforms the emitted photons. (B) If one excites the sample several times, one can begin to build up a 'picture' of how many photons correlate to a specific emission time, as shown in this image. (C) After collecting a sufficient amount of data, a histogram can therefore be constructed and an exponential decay curved fitted in order to extract the fluorescence lifetime. (D) This image illustrates the data one may gain if using fluorescence lifetime microscopy. Each pixel gives a value of the fluorescence lifetime, meaning that information about the lifetime in a specific environment can be gained. The six colours each represent a different value of the fluorescence lifetime (τ_1 - τ_6). Images revised from Lakowicz[244] and Leica website.[245]

eight pulses of light. Subsequently, the registered number of photons that possess specific emission times are collated, after which a histogram can be constructed, such as that illustrated in Figure 3.2 C, and a decay curve fitted.

Fluorescence lifetime measurements can also be conducted using microscopy, where an image can be constructed that describes the change in the fluorescence lifetime of a region of interest. This method is known as fluorescence lifetime microscopy (FLIM) and has been used to conduct the microfluidic experiments described in this chapter. Figure 3.2 D illustrates an example of an image that one might expect to gain using FLIM. Importantly, the image reports any changes in the fluorescence lifetime observed in the environment probed.

3.2.3 Summary and chapter aims

Microfluidic droplet technologies offer many advantages over conventional assay formats. Therefore, the ability to translate the CF assay, detailed in chapter 2, into a high-throughput, microfluidic format is highly desirable. In summary, the experiments detailed in this chapter aim to:

1. Demonstrate that it is feasible to translate the CF leakage assay into a microfluidic format, using microfluidic droplet technologies.
2. Indicate that fluorescence intensity measurements are not suitable for assaying leakage in a quantitative manner.
3. Demonstrate that fluorescence lifetime measurements allow the leakage assay to be performed in a quantitative fashion and in high-throughput.
4. Demonstrate the potential for translating other assays into a high-throughput format, which involves performing fluorescence measurements on bulk vesicle populations.

3.3 MATERIALS AND METHODS

3.3.1 Materials

3.3.1.1 Dye and buffer solutions

The dye solutions and buffers required in order to conduct the experiments detailed in this chapter incorporated the following: Trizma® hydrochloride (TRIS-HCl), sodium chloride (NaCl), sodium hydroxide (NaOH) and CF, all of which were purchased from Sigma-Aldrich®.

3.3.1.2 Photomasks

Photomasks, required for the production of photolithographical features, were designed using the design software package AutoCAD 2005. The masks were sent to and generated by JD Photo-Tools (Photodata Test Services Ltd, Oldham). Specifications are as detailed herein:

- Mask type: emulsion on polyester film
- Size: 10" x 12"
- Polarity: darkfield
- View side: design is viewed from chrome/emulsion side
- Resolution: high

3.3.1.3 Soft-lithography and substrate materials

Materials required for production of microfabricated structures via soft-lithography include the following: 100 mm silicon-wafers (thickness 525 ± 25 μm & single sided polish, IDB Technologies UK Ltd.), Su-8 50 photoresist (Chestech Ltd.), Microposit EC-Solvent (Chestech Ltd.) and Sylguard 184 Elastomer Kit (VWR). A UV lamp was used to irradiate the exposed photoresist. Silicon wafers and glass slides (VWR) were cleaned prior to use

with a 1:2 mixture of hydrogen peroxide and concentrated sulphuric acid ('piranha' solution) (Sigma-Aldrich). Distilled water and isopropylalcohol (IPA, Sigma-Aldrich) were used for rinsing.

Polytetrafluoroethylene (PTFE) ultramicrobore tubing (0.004" ID, Cole-Parmer Instrument), a hole punch (able to punch holes possessing a diameter slightly smaller than 0.004"), plastic syringes (disposable BD Plastipak Syringes) and needles (BD Microlance 25G 1" – Nr. 18, 0.5 × 25 mm) were used as a means to inject fluid into microfluidic devices.

3.3.1.4 Performing measurements in microfluidic devices

In order to generate water-in-oil droplets and hence perform experiments in microfluidic devices, one requires several syringe pumps in order to control fluid manipulation through microfluidic channels. Specifically, three syringe pumps (PHD 2000, Harvard Apparatus) were required to control the flow of two aqueous solutions and one oil carrier fluid. The surfactant / oil mixture utilised in the experiments detailed in this chapter was 1.8 % E2KO660[126] (a kind gift from Raindance Technologies, USA) in FC40 (Sigma-Aldrich®).

3.3.1.5 Carboxyfluorescein leakage assay

DOPC (Avanti Polar Lipids), was used to form vesicle suspensions for the leakage experiments detailed in this chapter. PD-10 columns containing Sephadex™ G25m media (GE Heathcare) were used to remove external dye from the vesicle suspensions, after which the collated vesicle fractions were diluted to yield a final lipid concentration of 0.2 mM (see chapter 2, section 2.3.2.2 for further information). Imipramine HCl (Sigma-Aldrich®) was chosen to induce CF leakage in the preliminary experiments described within this chapter. Microwell plates (Microplate 96 well, Fisher Scientific Ltd.) and a quartz cuvette (Fisher Scientific Ltd., path length 10 mm) were required to conduct both fluorescence intensity and lifetime measurements in a non-microfluidic format.

3.3.2 Methods

3.3.2.1 Dye and buffer preparation

Solutions 2.1 and 2.2 (as detailed in chapter 2, section 2.3.1.2) were prepared and used in the experiments described in this chapter.

3.3.2.2 Creation of photomask

Photomasks were created using the software package, AutoCAD 2005. A screen shot of the software interface is depicted in figure 3.3 A, where examples of the types of features and designs that can be generated in AutoCAD, to produce a photomask, are displayed. Figure 3.3 B illustrates the actual photomask used to create the devices described in the experiments conducted in this chapter. The document "Design Rules for Photomask Generation",[246] produced by JD Photo-Tools, was consulted for advice with respect to drawing designs in AutoCAD. Note that white features in the computer design correspond to areas of transparency in the resulting photomask film (and thus raised features in the patterned photoresist).

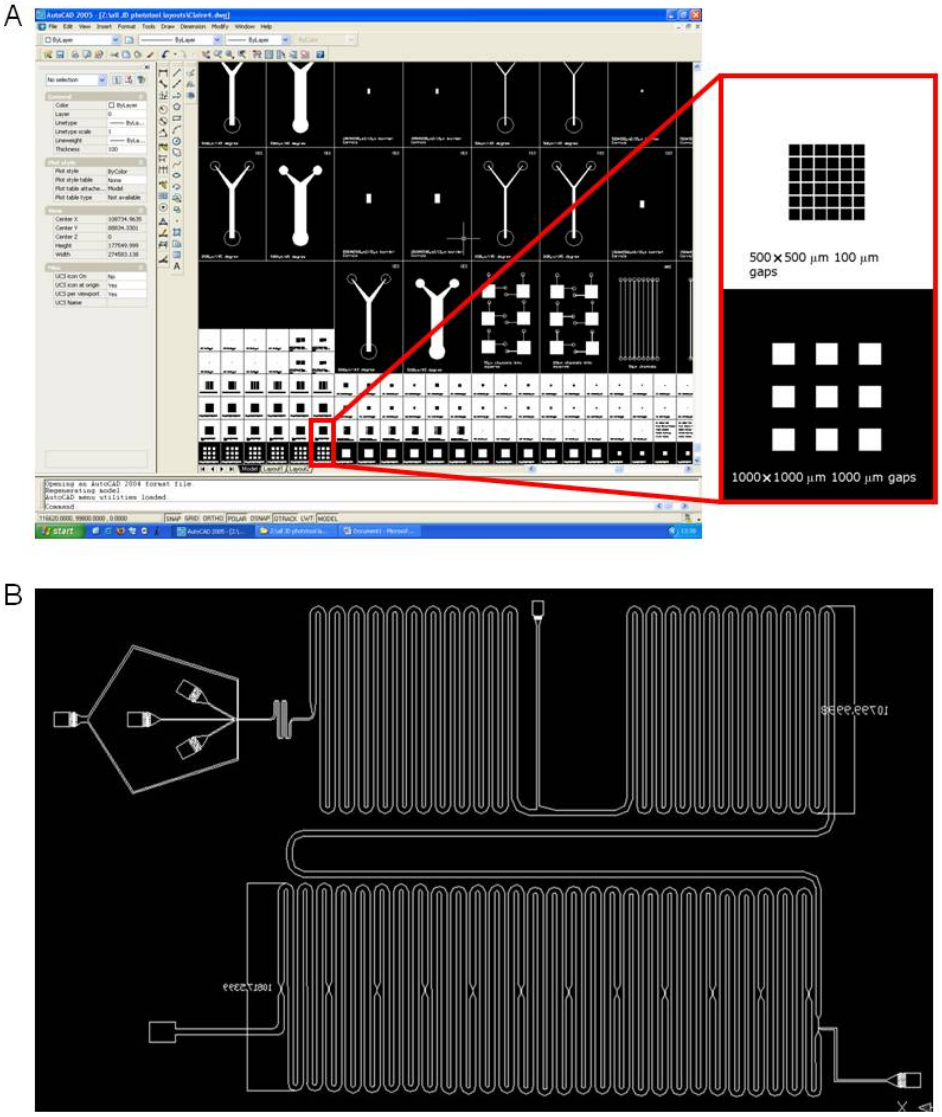


Figure 3.3: **Software used to create photomask designs.** (A) A screenshot of the software package, AutoCAD 2005, used to compose photomask designs; the enlarged area (highlighted by the red boxes) illustrates examples of designs that can be generated. The photomask displayed in (B) represents the design used to create the microfluidic chip detailed in the CF leakage experiments on chip (note that the width of the channels are ca. 300 µm, with a depth of 50 µm).

3.3.2.3 PDMS preparation

Sylguard 184 Elastomer Kit, composed of PDMS (poly(dimethylsiloxane)) elastomer and curing agent, was mixed in a 10:1 ratio respectively to yield a

total weight of ca. 30 g (a suitable volume to cover the 100 mm patterned silicon wafer with ca. 3 mm PDMS). A plastic stirrer was used to mix the two components efficiently. After thorough mixing, the PDMS was degassed to remove remnant air bubbles; the PDMS was placed in a dessicator attached to a vacuum pump for approximately 30 minutes to achieve this.

3.3.2.4 Procedure for microfluidic device assembly

After thorough washing of the silicon wafer(s) in piranha solution (see section 3.3.1.3), rinsing with IPA and then drying with compressed air, the wafer was allowed to dry on a hotplate at 200 °C for 5-10 minutes. SU-8 50 photoresist was then spin coated onto the clean wafer to yield a 50 μm thick layer (single coat) as illustrated in figure 3.4. Coating of the wafer required a spread cycle (ramp to 500 rpm at 100 rpm / s, hold for 10 s) and a spin cycle (ramp to 2000 rpm at 300 rpm / s, hold for 30 s).

Several procedures then follow in order to process the photoresist to form a micropatterned substrate. The spin coated photoresist was subjected to a soft bake, composed of two baking steps: (i) pre-bake at 65 °C for 6 minutes and (ii) soft bake at 95 °C for 20 minutes. The photomask is then placed on top of the soft baked photo resist film and exposed to UV irradiation, as illustrated by step (i) in figure 3.4. MicroChem's processing guidelines should be consulted for further information concerning exposure optimisation / exposure energies etc.).[246] A post exposure bake (PEB) is performed to afford selective cross-linking of the exposed SU-8 film; a two-step increase in heating is required in order to avoid creating unnecessary stresses within the film. Specifically, post exposure bakes at i) 65 °C for 1 minute and ii) 95 °C for 5 minutes were performed. Finally the SU-8 was developed, as shown by step (ii) in figure 3.4, using Microposit EC-Solvent (following optimum developing times), rinsed with IPA and dried in a stream of air after allowing the wafer to cool slowly. Pre-prepared PDMS (see section 3.3.2.3 for PDMS preparation) was then

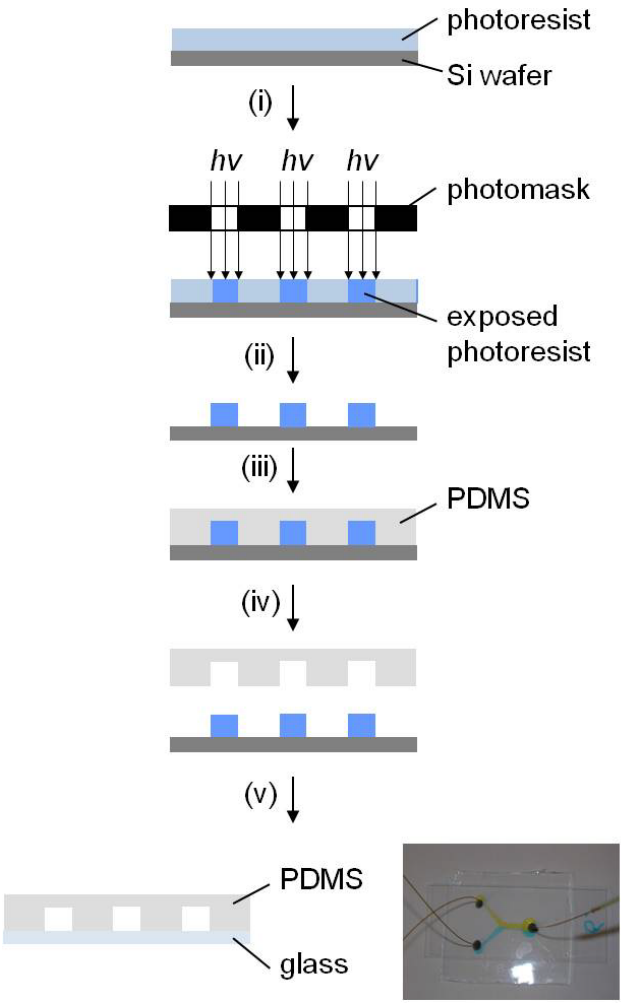


Figure 3.4: **Processes involved in PDMS chip manufacture, using photolithography techniques.** The steps specifically involve: (i) irradiating a thin layer of photoresist (spin coated onto a silicon wafer) with UV light through a photomask, (ii) removing the exposed photoresist with developer, (iii) pouring pre-prepared PDMS over the patterned microstructures in the photoresist and allowing the PDMS to set, (iv) carefully peeling the PDMS off the silicon wafer and (v) assembly of chip by bonding the patterned PDMS to glass slides (the photograph illustrates an example of a microfluidic device).

poured over the patterned SU-8 photoresist and left to set overnight on a level surface (step (iii) in figure 3.4). Note: all chip fabrication was carried out in a specialised clean room.

Once the desired features have been translated to the PDMS substrate via soft-lithography, the microfluidic chip can be assembled. Firstly, the set PDMS is carefully removed from patterned photoresist in order to ensure that the microfabricated features remain intact, as illustrated by step (iv) in figure 3.4. Holes are then punched into the patterned PDMS substrate at the appropriate positions (i.e. where one desires fluid to enter / exit the devices) using a hole punch producing holes with a diameter slightly smaller than that of the PTFE tubing to be inserted (see figure 3.5 A, B, C and figure 3.6 A). The PDMS substrate is then adhered to a clean glass slide (or PDMS) to produce a sealed system (see step (v) in figure 3.4); sonication of the substrates, i.e. both PDMS and glass, prior to device assembly in 0.5 M NaOH, followed by ethanol, distilled water, thorough drying on a hot plate and exposure to an oxygen plasma for 20 seconds (resulting in oxidation of the surfaces) affords good bonding. Note that a microscope slide was placed onto the reverse side of PDMS substrates (i.e. the side containing no microfabricated structures) in order to act as a guide during the bonding process; the microscopy slide is held in place naturally (by suction) and can be removed easily. This is especially important when bonding larger microfabricated PDMS substrates to glass / PDMS substrates in order to ensure that even bonding is gained and the microfabricated structures are conserved.

PTFE tubing (each piece approximately 30 cm in length, or an adequate amount such that your device can be mounted easily onto the microscope stage and connected to the syringe pumps with ease) is carefully inserted into the pre-punched holes in the microfabricated PDMS substrate using a pair of tweezers. Care has to be taken, particularly when thin glass microscopy cover slides are bonded to the microfabricated PDMS substrate, and insertion of the PTFE tubing should be conducted on a flat surface, as otherwise the glass can easily be broken. The PTFE tubing that has been connected to the punched

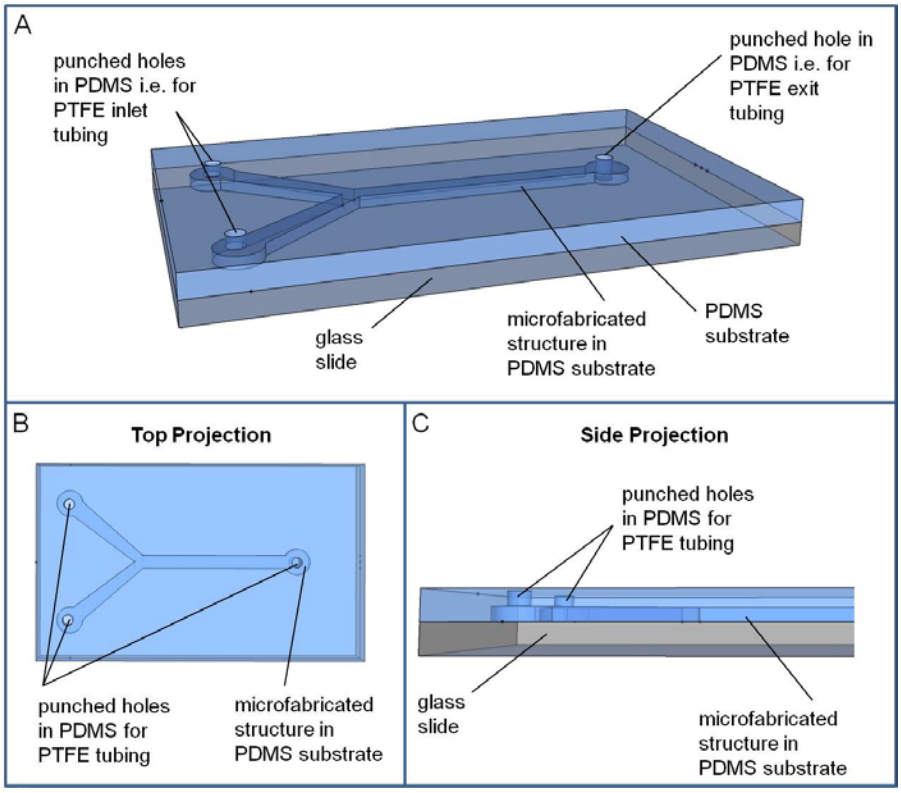


Figure 3.5: **Microfluidic chip assembly 1.** (A) Illustration demonstrating how microfabricated PDMS substrates can be bonded to glass to form microfluidic channels; the top and side projections of an example microfluidic device are shown in (B) and (C) respectively for clarity.

holes in the microfabricated PDMS, now has to be connected to the removable needles attached to the disposable plastic syringes thus enabling fluid to be introduced into the device in a controlled manner. Specifically, disposable needles are inserted into the tubing to afford a pressure-tight system to which plastic syringes are attached (as illustrated in figure 3.6 B). Syringe pumps are used to house the syringes and mechanically drive both aqueous and oil solutions into the devices (see figure 3.6 A). The outlet capillary is connected to a glass vial via PTFE tubing in order to collect waste fluid; this is illustrated in figure 3.6 C for clarity.

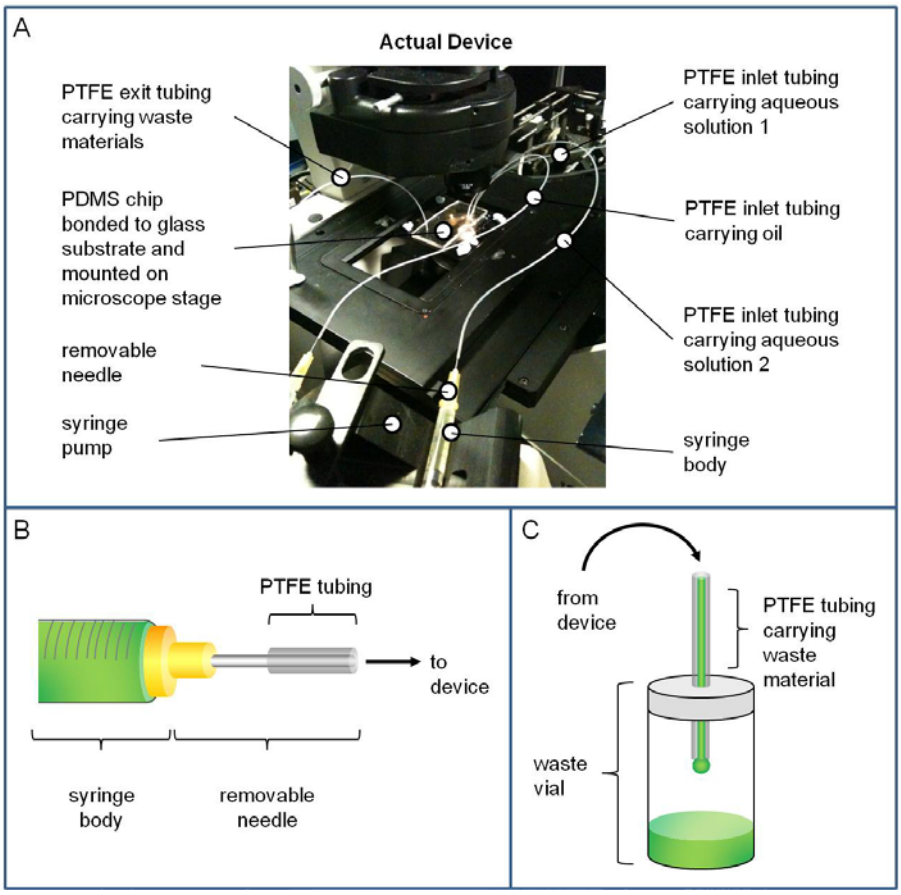


Figure 3.6: **Interfacing of the microfluidic chip with syringes.** (A) Indication of how the PTFE tubing is used to connect the device to syringes housed in syringe pumps; here, an example of the actual device used in the experiments detailed in this chapter is displayed. The illustration in (B) clarifies how the removable needles, which are attached to the syringes, connect to the PTFE tubing thus producing a good seal. Finally, (C) details how the waste material is collected, after having been produced in a microfluidic device during an experiment.

3.3.2.5 Carboxyfluorescein leakage assay

The experimental format detailed in chapter 2, section 2.3.2.3, was used to prepare and perform the CF leakage assays detailed in this chapter. All leakage experiments involved using the drug, impramine HCl, as it is highly water soluble (50 mg / ml)[239] and its effect on CF leakage from DOPC vesicles has been established previously in chapter 2, section 2.4.2. The volumetric ratio of

drug solution introduced to vesicle solution is always 1:1; the final concentration of imipramine in solution was either 1.6 mM or 0.8 mM (specified in the appropriate sections) and the final lipid concentration of DOPC always 0.1 mM. Note that whenever a leakage assay was performed using a different detection system, or in a different experimental environment (i.e. a microfluidic format), an experiment was run in parallel on the fluorescence spectrophotometer (in a well plate format, as described previously in chapter 2, section 2.4.1.1). This was undertaken in order to act as a control for that day's experiments, thus ensuring that the leakage assay was taking place in the expected manner. Additionally, CF-containing vesicles in buffer alone (i.e. in the absence of drug) were monitored over the time course of each kinetic experiment to act as a further control. Fluorescence intensity measurements were conducted using a Cary Eclipse (Varian) Fluorescence Spectrophotometer (Varian, Inc.) with excitation at 490 nm and emission at 516 nm; 96-well plates (Fisher Scientific Ltd.) were employed to contain the sample to be measured.

3.3.2.6 Fluorescence intensity measurements in a microfluidic format

The fluorescence intensity measurements that were conducted in a microfluidic format involved using a confocal fluorescence detection system, specifically an Olympus microscope equipped with a 488 nm diode laser and Avalanche photodiode detector. The samples were excited at 488 nm. A 488 nm dichroic mirror and a 505 nm long pass emission filter were utilised, as well as a second emission filter (500-580 nm bandpass) situated in front of the detector (all Olympus).

3.3.2.7 Fluorescence lifetime measurements in bulk

The fluorescence lifetime measurements conducted in a bulk format were performed using a home-built, time-resolved fluorimeter utilising TCSPC. A quartz cuvette (path length = 1 mm) was used to contain the sample of interest. A pulsed laser was used to excite these samples, namely a titanium

sapphire laser (Mai Tai, Spectra-Physics, Mountain View, CA, USA); an excitation wavelength of 450 nm and a 460 nm long pass emission filter were utilised. Initially, the laser is passed through a piece of quartz which reflects a small portion of the light onto a photodiode. The signal is then amplified and connected to the TCSPC card, informing the card how long it took each photon to arrive at the detector after the excitation pulse. Data acquisition for each data point took ca. 1 s, resulting in just less than 65000 counts / second in the peak decay (with 65000 counts being the maximum that the card can collect).

The fluorescence lifetimes of ten CF samples, the concentrations of which are displayed in table 3.1, were ascertained in order to generate a calibration curve. The results are presented and discussed in the results and discussion section (section 3.4.2.1, also see Appendix 7). Additionally, CF leakage experiments with DOPC vesicles and imipramine HCl were performed using this setup, as described in section 3.4.2.2. Measurements were recorded every two minutes for total period of thirty minutes (see Appendices 8 and 9).

Sample	[CF] (M)	Sample	[CF] (M)
1	5.0E-02	6	1.0E-04
2	2.5E-02	7	2.0E-05
3	6.3E-03	8	6.0E-06
4	1.6E-03	9	2.0E-06
5	3.9E-04	10	4.0E-07

Table 3.1: **The ten samples of carboxyfluorescein used to construct the calibration curves.**

3.3.2.8 Fluorescence lifetime measurements in a microfluidic format

The calibration and fluorescence leakage experiments, performed in a microfluidic format, involved flowing fluids through microfluidic devices. In order to perform the calibration experiment, the ten CF solutions (detailed in

table 3.1), were flowed through the microfluidic channels independently at a total flow rate of 1.6 µl / min.

In order to perform the leakage assay, both the vesicle suspension (loaded with CF, denoted as $Aqueous_1$ or Aq_1) and the imipramine solution ($Aqueous_2$ or Aq_2) were brought into contact with one another using equal flow rates for each aqueous inlet, thus ensuring that 1:1 mixing of the two samples occurred (and hence a 50 % dilution). In order to form oil-in-water droplets, the two aqueous streams (Aq_1 and Aq_2) were brought into contact with an oil stream; droplet formation was achieved using the flow focussing approach (see chapter 1, section 1.4.1.4). Figure 3.7 displays the configuration used. Note that the photograph displayed in figure 3.6 A (section 3.3.2.4) depicts the actual experimental setup, where the device and various aqueous inlets / outlets etc. are highlighted. Figure 3.3 B (section 3.3.2.2) informs one of the device design; the major channels possessed a width and depth of 300 and 50 µm respectively. Experiments were conducted to ascertain the optimum conditions required for stable droplet generation in the device, the results of which are detailed in section 3.4.2.4.

An SP5 confocal microscope (Leica) was used to measure fluorescence lifetimes during experiments performed in a microfluidic format. For FLIM acquisition, a pulsed, titanium sapphire laser (Broadband Mai Tai, Spectra-Physics, Mountain View, CA, USA) was used as the excitation source. An excitation wavelength of 475 nm was utilised and fluorescence emission collected from 490 to 600 nm. The light used to illuminate the sample, as well as the wavelengths of light consequently emitted upon excitation, were distributed and collected respectively through an objective lens via scanning mirrors in the scan head of the microscope.

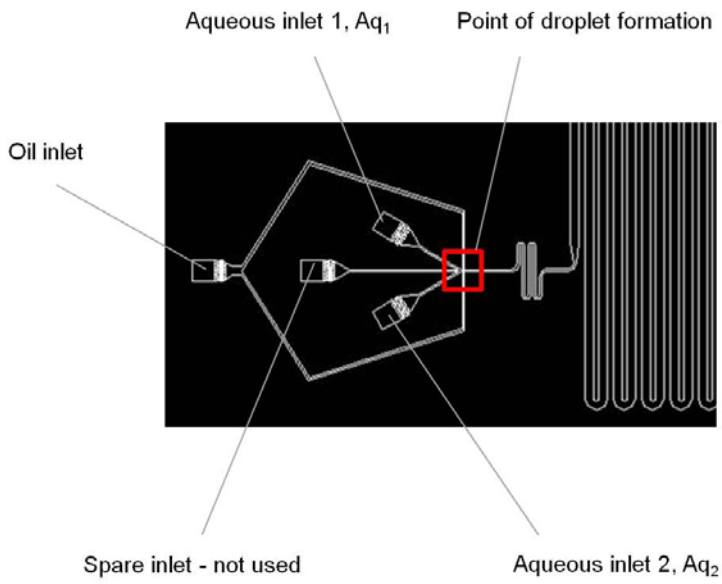


Figure 3.7: **Device configuration for droplet formation.** The flow-focussing approach was utilised for droplet formation – one can see that the two aqueous streams flowing through inlets 1 and 2 (Aq_1 and Aq_2) are focussed onto a 'cross-shaped' junction (indicated by the red box), where they meet the oil carrier fluid. Here droplet generation ensues.

Fluorescence emission was detected using a photomultiplier tube (PMT) and the PMT signal was recorded using TCSPC electronics (SPC-830, Becker & Hickl). Data were acquired at either a single, or various, point(s) along the device in order to construct a calibration curve or kinetic traces for leakage experiments respectively. In the latter case, four channels were analysed per acquisition (i.e. in the field of view), consequently resulting in a value for the average fluorescence lifetime in that region. Data were acquired for a total of 5 minutes for each data point included in the graphs in Appendices 10 and 11.

3.3.2.9 Data analysis of lifetime measurements

The software package, SPC Image, was used to analyse the data and extract values for the fluorescence lifetime. Figure 3.8 displays a screen dump of the main software window.

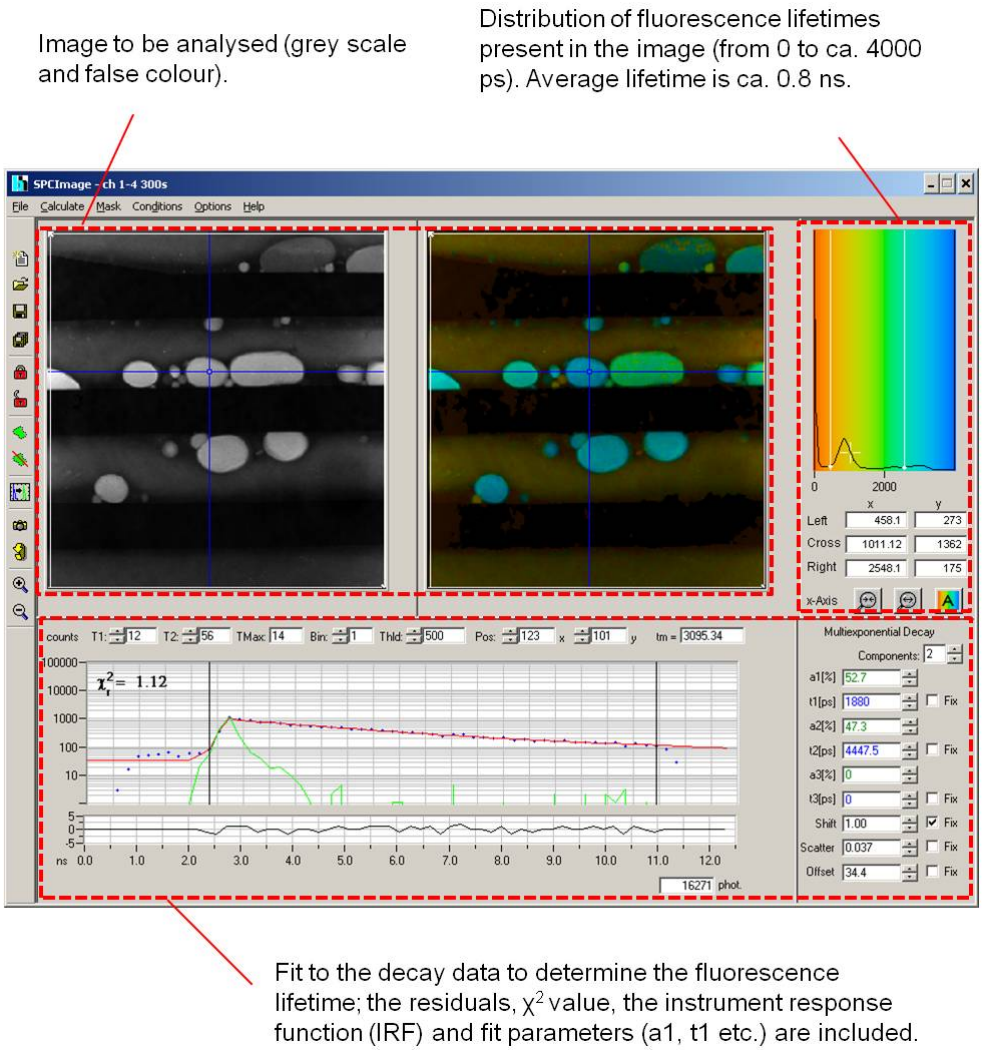


Figure 3.8: **Screen dump of the software package, SPC Image, used to analyse the fluorescence lifetime data.** An example has been included of an image to be analysed. It can be observed that SPC Image enables one to view the distribution of fluorescence lifetimes in the image sampled, by means of a false colour image and histogram. One can also view the fit to the decay data for a specific pixel, as well as the residuals, χ^2 value and fit parameters associated with that fit.

3.4 RESULTS AND DISCUSSION

3.4.1 Fluorescence intensity measurements

The initial step taken in order to translate the bulk assay into a high-throughput droplet format involved measuring the fluorescence response of CF at different concentrations using a microfluidic format. Ten samples, spanning the concentration range of interest (50 mM - 1 μM, see section 3.3.2.7) were prepared in order to ascertain if the output concurs with what was observed for the experiments conducted on the fluorescence spectrophotometer. Several experiments have been conducted, where the fluorescence response for each of the ten CF samples has been measured and assembled into a calibration graph. These are described as follows.

The first experiment involved flowing the ten samples through a microfluidic device in a droplet format (each sample separately). The fluorescence intensity of each sample was then measured at a specific point in the channel. Surprisingly, it was found that the calibration curve was shifted to higher concentration when compared to the results gained using the fluorescence spectrophotometer, as illustrated in figure 3.9 below.

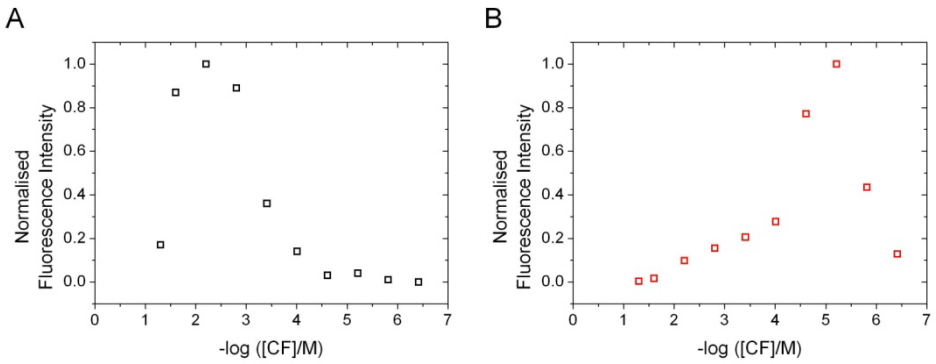


Figure 3.9: **Carboxyfluorescein calibration curve gained using intensity measurements in a microfluidic format.** (A) Calibration curve gained using droplets formed in a microfluidic device (each sample tested separately) and (B) calibration curve gained using fluorescence intensity measurements in the fluorescence spectrophotometer.

It was thought that the observed shift in the calibration curve may be due to loss of CF molecules to the oil-aqueous interface. A loss of dye in this manner would therefore result in an effective decrease in the concentration, thus resulting in an increase in the observed fluorescence intensity. However, each solution was also assessed using a bulk measurement on the same experimental set up, where an oil-aqueous interface is *excluded*. An aliquot of each CF solution was pipetted onto a glass side and the relevant fluorescence intensities of the ten CF samples were measured. The results of this experiment are illustrated in figure 3.10 A. However, a shifted calibration curve still persisted. The same measurement was also conducted using a flow format, where the samples are flowed solely through the microfluidic channels and are thus in the absence of droplets and of an oil-aqueous interface, as the use of a flow format reduces any effects that may have affected the static samples due to photobleaching. Again the calibration curve was still shifted with respect to that observed using intensity measurements on the fluorescence spectrophotometer (data displayed in figure 3.10 B). Hence this indicates that the primary cause of the shift in the calibration curve is not due to a loss of CF molecules to the oil-aqueous interface. Additionally there is no reason why CF would wish to reside at this interface, as its structure possesses two hydroxyl groups and an acid group that are all deprotonated at the pH used in these experiments (pH 7.4), and hence is content residing in an aqueous environment.

For completion, controls were also performed whereby the effect of changing the oil and the total flow rate of the aqueous / oil streams used during droplet generation were investigated. The results of these experiments are illustrated in figure 3.10 B and C respectively, where it is apparent that the same feature persists. Figure 3.10 D provides a summary of the results displayed in figure 3.10 A-C.

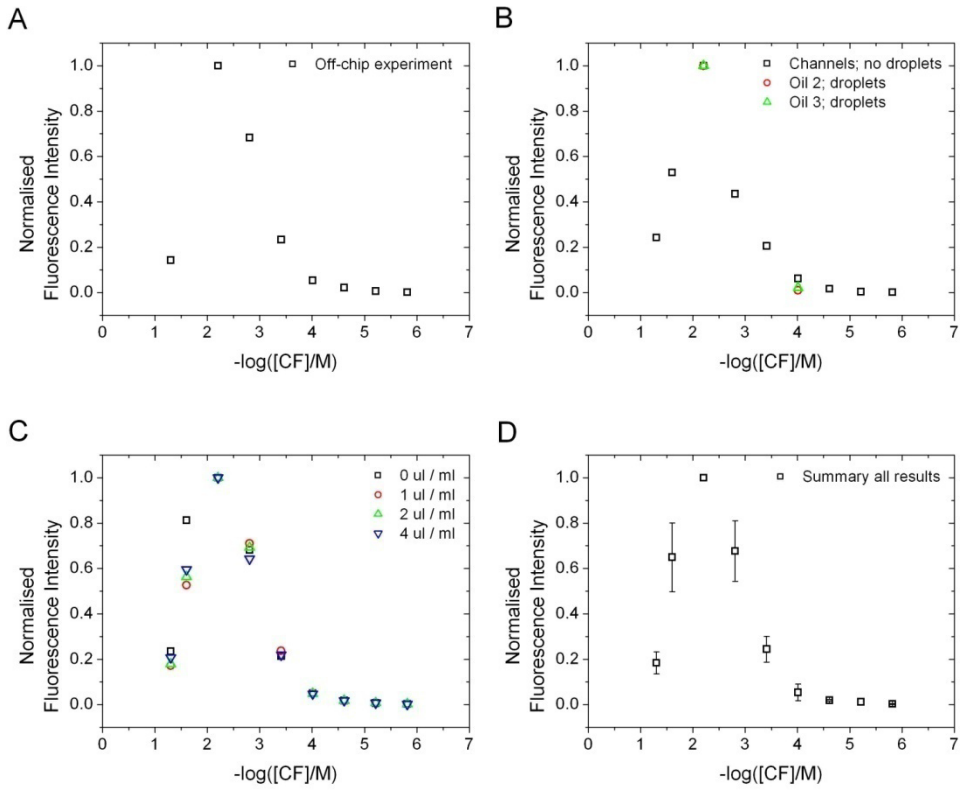


Figure 3.10: **The various control measurements conducted to ascertain which parameters, if any, may explain the shifted calibration curve.** (A) Results of the calibration conducted off-chip, i.e. the ten samples measured using the same set up but aliquots of each are pipetted onto a microscopy slide. (B) Results of the calibration, conducted by flowing each sample through the microfluidic channels, i.e. in the absence of droplets. The results of experiments conducted with two different oils are also included (in the presence of droplets), where oil 2 = FC3283 and oil 3 = oleic acid; note that only two measurements were made, i.e. where the maximum and minimum points were expected to be gained, due to time restraints. (C) This graph indicates the effect of the calibration curve on the total flow rate of the aqueous / oil streams used. (D) Summary of the results displayed in A-C; the indicated errors represent ± 1 s.d ($n \geq 6$).

To conclude, the experiments detailed in this section reveal that the calibration curve is shifted to higher concentrations, when compared to the calibration curve gained using the fluorescence spectrophotometer. A summary of the overall result that these findings portray is detailed in figure 3.11.

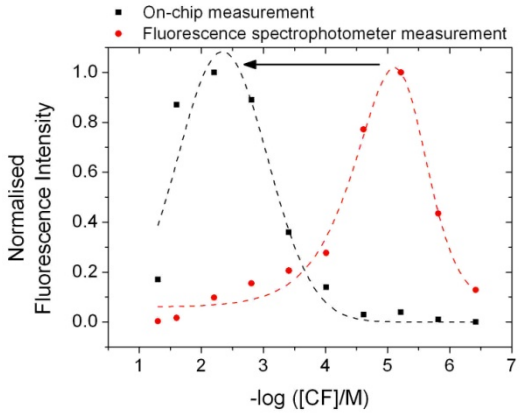


Figure 3.11: **Summary of findings conducted using intensity measurements in a microfluidic format ("on-chip") and compared to the measurements conducted on the fluorescence spectrophotometer.**

Although several controls have been performed, these do not help to explain the origins of the observed differences. It is expected that this feature is due to inherent artefacts associated with intensity based measurements. Additionally, it would not have been feasible to conduct the leakage experiment in a microfluidic format, using the calibration curve gained for this set up. As a result of a shift in the curve to higher concentrations, the sensitivity of the leakage assay is reduced, i.e. a far greater number of vesicles containing CF per set volume are required in order to reach this maximum (or, to afford a smaller dilution). However, it is not sensible to use lipid concentrations above 1 mM, i.e. increasing the vesicle density per droplet, which would be required to use the assay in this format. Nor is it practical to encapsulate higher concentrations of CF within vesicle lumens, in attempt to increase the sensitivity of the leakage assay. Therefore it was decided to move away from intensity measurements and attempt to use fluorescence lifetime measurements.

3.4.2 Fluorescence lifetime experiments

It was expected that solutions of CF present at high concentrations, for example at concentrations corresponding to approximately 50 mM (where the dye participates in concentration-quenching events, as described previously in

chapter 2, section 2.2.1), would yield substantially different fluorescence lifetimes compared to solutions containing CF present at much lower concentrations (approximately 1E-05 M). Therefore it was proposed that this particular property, exhibited by CF solutions, could be exploited and in turn used as an alternative means to investigate the leakage of CF from liposomes upon the addition of drug molecules, for example.

3.4.2.1 Carboxyfluorescein calibration experiment performed in a cuvette format

The first experiments to be conducted involved determining the fluorescence lifetime of ten different CF solutions, each of which is present at a different concentration, thus creating a calibration graph indicating the dependency of the fluorescence lifetime on concentration. The results of the calibration experiment are displayed in figure 3.12 A, where data for two experimental repeats are provided (see Appendix 7 for tabulated data with χ^2 values).

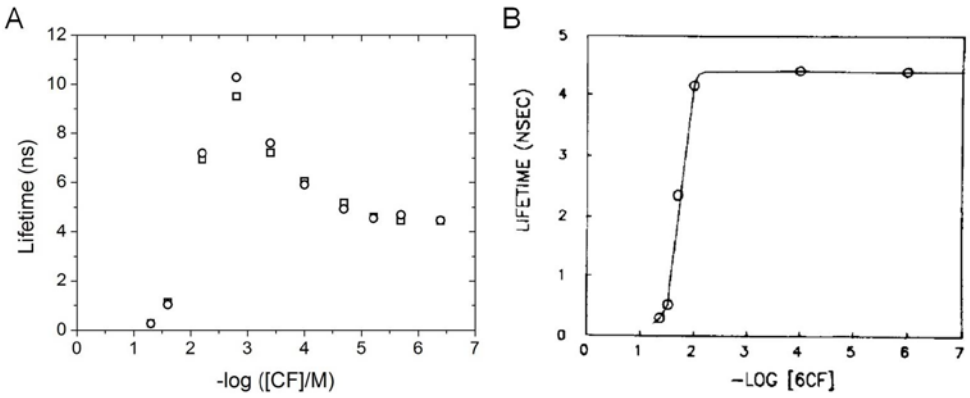


Figure 3.12: **Carboxyfluorescein calibration experiment performed in a cuvette format (fluorescence lifetime).** (A) The fluorescence lifetime gained for each of the ten solutions of CF, present at different concentrations, performed in a cuvette format. Two repeats are displayed and indicated by the symbols □ and ○. (B) Literature data for CF, which indicates the relationship between the concentration of the dye in solution and its fluorescence lifetime. Image reproduced from Chen *et al.*[218]

It is apparent that the data gained experimentally agrees in part with that detailed in the literature (see figure 3.12 B for literature data), particularly in the regions where the concentration of CF in solution is greater than ca. 1E-02 M and less than ca. 1E-05 M. The fluorescence lifetime gained experimentally for CF-containing solutions, possessing a concentration of less than 1E-05 M, is in the region of 4.5 ± 0.1 ns (n = 6), agrees well with the literature value of approximately 4.5 ns (see figure 3.12 B and Appendix 7).[218] The fluorescence lifetime of more concentrated CF samples, e.g. 50 mM, are noticeably shorter – a value of ca. 0.3 ns was gained experimentally (see figure 3.12 A and Appendix 7) and is in agreement with the value presented in figure 3.12 B.[218]

As Chen *et al.* describe,[218] the decrease in the fluorescence lifetime (associated with an increase in the concentration of CF in solution) is unexpected if dimerisation of CF molecules is the only factor contributing to quenching events, as usually the fluorescence lifetime is not found to decrease in static quenching. However, they state that dimerisation is crucial for the observed decrease in the fluorescence lifetime, based on experiments conducted with propylene glycol and highly concentrated solutions of CF. The addition of propylene glycol essentially removes the potential for CF molecules to dimerise. Hence, as the percentage by volume of propylene glycol is increased, in concentrated CF solutions of a fixed concentration (i.e. 0.04 M), the lifetime increases due to the effective increase in the monomer-monomer spacing. Additionally, if the concentration of propylene glycol in solution is kept constant and the CF concentration is altered, the values for the fluorescence lifetime are longer than for the equivalent CF solution in buffer alone. Table 3.2 displays the results of the experiments conducted with propylene glycol.

% (v/v) propylene glycol	[CF] (M)	τ (ns)
0	0.04	0.43
20	0.04	0.92
40	0.04	1.71
60	0.04	2.13
40	0.01	5.23
40	0.02	3.85
40	0.06	0.80

Table 3.2: **The effect of propylene glycol on lifetimes of concentrated carboxyfluorescein.** The data is reproduced from the paper published by Chen *et al.*[218]

It is believed that the observed shortening of the fluorescence lifetime, upon increasing the dye concentration in solution, is due to energy transfer from monomers to non-fluorescent dimers. The dimers are able to act as energy sinks, and the phenomenon arises due to a large overlap in the excitation and emission spectra. For a detailed discussion of the evidence to support this theory, one should consult the paper by Chen *et al.*[218]

Discrepancies between the fluorescence lifetime data gained experimentally and that described in the literature, illustrated previously in figure 3.12 A, do exist. Notably, it can be observed that significant differences reside in the region between 1E-02 to 1E-04 M CF. As the concentration of CF in solution is increased, from approximately 1E-04 M to 1E-03 M, a significant increase in the fluorescence lifetime was observed (compared to the literature data). It is thought that this may be due to reabsorption of the emitted fluorescence intensity, as this phenomenon is known to cause increases the fluorescence lifetime.[247,248] A cuvette possessing a pathlength of 1 cm was used to conduct these experiments, therefore it is possible that this may afford an environment whereby emitted light maybe reabsorbed and emitted in a cyclic manner, within this particular concentration range, hence lengthening the value of the fluorescence lifetime. It is thought that the optimum conditions for this

phenomenon occur at ca. 1E-03 M, where the maximum lifetime value is reached (ca. 10 ns), after which the lifetime decreases rapidly. Interestingly, the concentration at which this decrease in the fluorescence lifetime commences coincides with that of the literature data, i.e. at ca. 3E-03 M CF, suggesting that the same mechanism is responsible for the decrease in the fluorescence lifetime. Note that Chen *et al.* do not disclose the nature of the cells used to conduct the fluorescence lifetime measurements described in their paper.

3.4.2.2 Carboxyfluorescein leakage assay performed using imipramine in a cuvette format

Having determined the dependency of the fluorescence lifetime on the concentration of CF in solution for the cuvette based system, a leakage assay was performed using the drug, imipramine, in the same system. Imipramine was chosen as the drug of choice, for use in the fluorescence lifetime experiments described in this chapter, as it is readily soluble in aqueous solutions and very economical.

The results of the leakage assay are present in figure 3.13. Specifically, the lifetime results for the addition of imipramine to a vesicle suspension loaded with CF in the interior of the vesicles are displayed in figure 3.13 A (yielding final concentrations of imipramine and DOPC equal to 1.6 and 0.1 mM respectively), as well as the data for the control experiment (figure 3.13 B), where the lifetime of the vesicular solution alone, i.e. with no addition of drug, is measured concurrently. Experiments were also conducted on the fluorescence spectrophotometer in parallel with the fluorescence lifetime experiments, in order to ensure that the vesicle leakage experiment occurred as anticipated and thus acted as a further control (see figure 3.13 C).

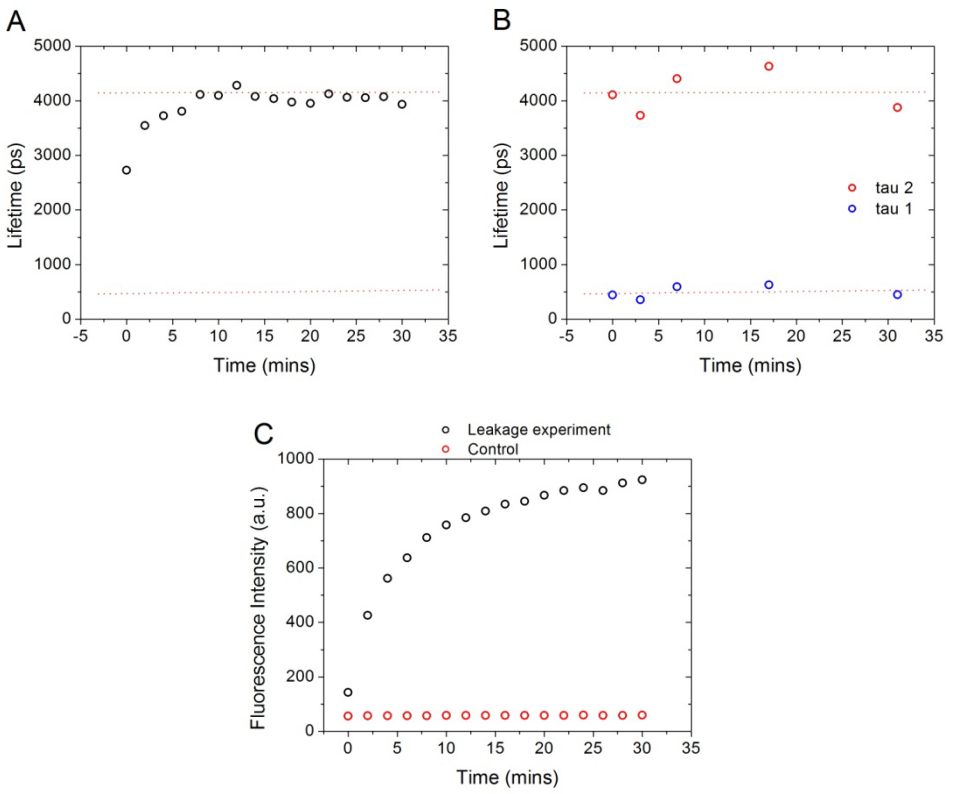


Figure 3.13: **Carboxyfluorescein leakage assay performed using imipramine in a cuvette format (fluorescence lifetime data).** (A) A graph illustrating the results gained for a fluorescence lifetime leakage experiment, upon introducing imipramine to vesicles loaded with CF (final concentrations of imipramine and DOPC equal to 1.6 and 0.1 mM respectively). The dotted red lines are included to indicate where the control measurement lies on this graph. (B) A graph illustrating the fluorescence lifetime results gained for the control experiment, i.e. where no drug has been introduced to the vesicle suspension. Data were fitted to a bi-exponential model, $I(t)=I_0(A_1e(-(t/\tau_1))+A_2e(-(t/\tau_1)))$,[249] where A_1 and A_2 are pre-exponentials factors associated with lifetime components τ_1 and τ_2 respectively. (C) Graph illustrating the fluorescence intensity measurement gained using the same vesicle and drug sample, thus acting as a additional control.

The most important conclusion that one can draw from these initial data is that the fluorescence lifetime is found to increase with time *only* after imipramine is introduced to the vesicle suspension, where a 50 mM CF solution has been incorporated into the vesicle lumens. This increase in lifetime infers a decrease in the dye concentration, which in turn can be attributed to the induction of leakage from the vesicles upon introducing imipramine molecules into the

vesicular solution. Figure 3.13 C further supports that dye leakage occurs as expected: the kinetic measurement, using fluorescence intensities, was gained in an analogous manner to previous experiments (as detailed in section 3.3.2.5). Note that the same vesicle and drug samples were used for both this measurement and the lifetime measurement detailed in figure 3.13 A.

The control experiment for the lifetime data, displayed in figure 3.13 B, illustrates that the lifetime remains constant over the course of the kinetic experiment (as indicated by the linear fits of the data, whose gradients are approximately zero). It can be observed that the fluorescence lifetime is comprised of a short (ca. 500 ps) and a long (ca. 4000 ps) component. The former relates to the quenched CF solution residing within the internal volume of the vesicles, with the latter component most probably due to a small amount of the dye present in the vesicular solution. This may be due to dye that has either leached out of the vesicle interiors or has not been fully excluded during a single passage through the Sephadex column. Interestingly, Chen *et al.* report that the long component may be due to molecules of CF associated with the lipid.[218] Although the experiments were conducted as soon as possible after having removed the free dye present in the external regions of the vesicular suspension, the sample had to be taken to a different laboratory in a different department to conduct the lifetime measurements, and as such the experiments could not be conducted immediately. The control measurement recorded during the fluorescence intensity leakage experiment (see figure 3.13 B) indicates that there is virtually no leakage of dye; however, the fluorescence intensity measurement will not be sensitive to the presence of such low dye concentrations.

In summary, it has been demonstrated that the fluorescence lifetime only deviates from the 500 ps baseline when imipramine molecules are introduced into the vesicle suspension, therefore inducing leakage of the dye. These data suggest that fluorescence lifetime measurements may provide an alternative way in which to perform the CF leakage assay.

3.4.2.3 Carboxyfluorescein calibration experiment performed using a microfluidic format

The ultimate aim of this chapter is to demonstrate that it is feasible to translate a bulk vesicular leakage assay into a microfluidic format, thus opening avenues for one to conduct future investigations that may involve understanding the interaction of drugs or proteins, for example, with vesicle populations. In order to achieve this goal, the first step involved establishing the fluorescence lifetime for a variety of different CF samples, present at different concentrations in solution, when using a *flow* format. In this instance measurements are conducted using a microscope, as opposed to a fluorimeter. These experiments were conducted in an analogous manner to the calibration experiments described previously in section 3.4.2.1, with the main difference being that each solution was flowed through a microfluidic device (see section 3.3.2.8 for details). The results are displayed in figure 3.14 A (see also Appendix 10).

As one can see from figure 3.14 A and B, the calibration curve agrees well with the literature data. Specifically, both sets of data yield a fluorescence lifetime of approximately 300 ps for a 50 mM CF solution, which increases in a linear manner upon dilution to yield a lifetime of approximately 4000 ps at ca. 1E-02 M. Upon further dilution, the lifetime of these solutions remains constant at approximately 4000 ps. However, these data contrast with the calibration data gained, using the cuvette set up (discussed in section 3.4.2.1). Figure 3.14 C illustrates both sets of calibration data plotted on one graph, i.e. the data gained in both the cuvette and microfluidic formats. Here, one can observe that data collected when using the microfluidic format do not show the prominent increase in the fluorescence lifetime between 1E-02 and 1E-04 M.

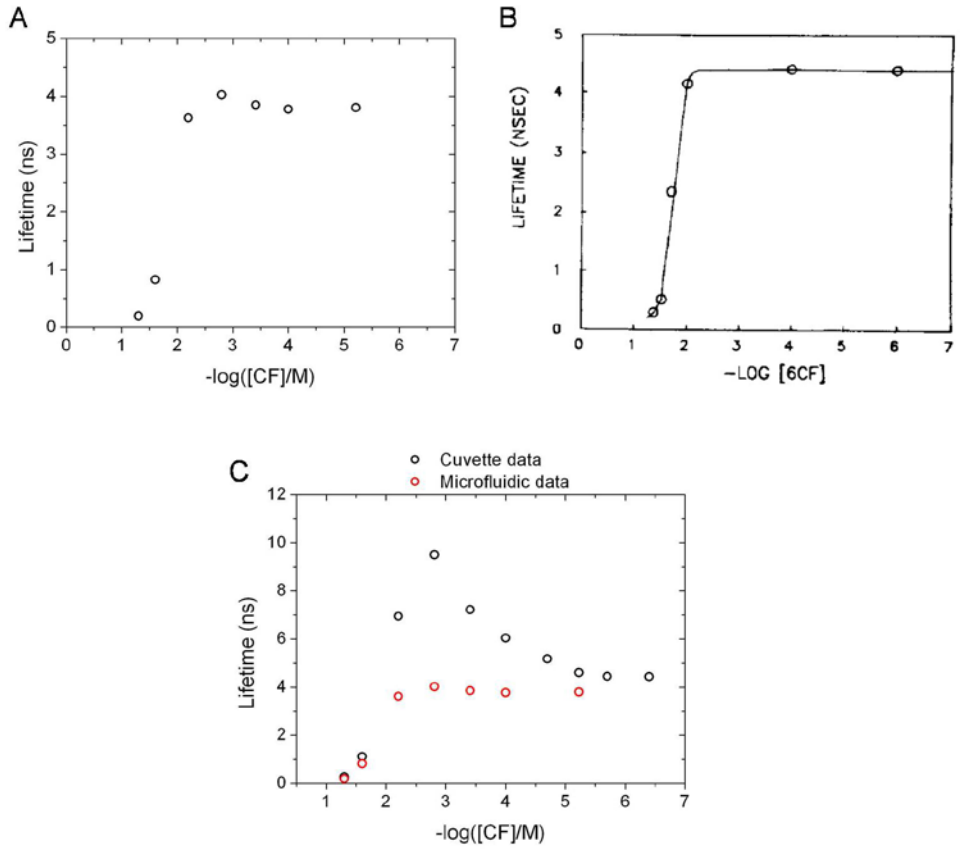


Figure 3.14: **Fluorescence lifetime calibration measurements conducted in a microfluidic format and compared to experiments conducted in a bulk format / literature values.** (A) Graph representing the results of the fluorescence lifetime calibration experiment, performed with the ten different solutions of CF in a microfluidic format. (B) Graph illustrating the literature data for CF, included to provide a means for comparison. Reproduced from the paper by Chen *et al.*[218] (C) Here, the data for the calibration experiments, conducted first in a cuvette (section 3.4.2.1) and then in a microfluidic format, are included on the same graph to enable comparisons to be made between the two.

It is thought personally that this difference may originate from differences in the experimental techniques employed. As alluded to previously, in section 3.4.2.1, it is thought that the prominent increase present in the data measured using the fluorimeter, in a cuvette-based system, was due to reabsorption of the fluorescence emission, due to the use of a longer path length. In the

microfluidic format the path length is much smaller, therefore less reabsorption occurs; there does appear to be a slight increase in the fluorescence lifetime in the region of interest. However, it is thought that the relationship between the fluorescence lifetime and dye concentration, ascertained during the calibration step for the microfluidic set up, will be more advantageous with respect to interpreting the leakage data. The fluorescence lifetime of the dye in solution increases upon dilution, which plateaus at approximately 3.2E-03 M and does not exceed ca. 4 ns upon further dilution (as seen in figure 3.14 A).

3.4.2.4 Carboxyfluorescein leakage assay, performed using imipramine in a microfluidic format

The final challenge involved conducting the leakage assay in a microfluidic device. First of all, the microfluidic device had to be optimised, in order to determine which flow rates would be suitable to yield stable droplet formation using the flow focussing approach. Figure 3.7 (section 3.3.2.8) details the arrangement of the aqueous and oil streams used for droplet formation in this particular set of experiments. Importantly, the microfluidic device was designed such that it would enable kinetic experiments to be monitored over longer timescales, on the order of minutes, thus yielding a suitable time period for monitoring the leakage of encapsulated CF by imipramine, for example. However, a compromise has to be made in order to maximise the experimental time window in order to generate ca. 5-10 minutes of data. Ideally, one requires as low a total flow rate as possible in order to achieve this. However, it is not always possible to gain stable droplet generation at very low total flow rates. This therefore had to be investigated and the results for such experiments are displayed in figure 3.15 and table 3.3.

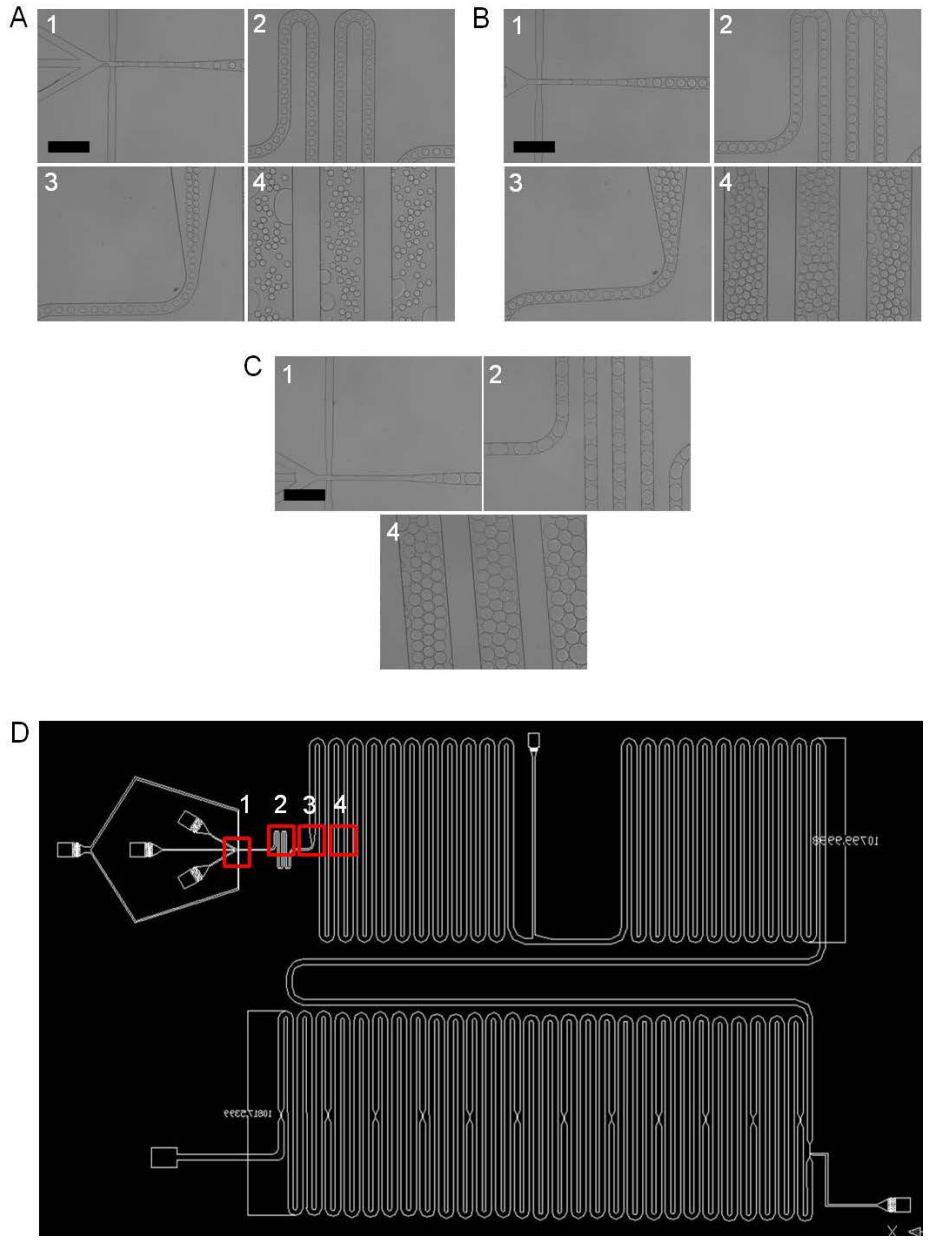


Figure 3.15: **Optimisation of the flow conditions in a microfluidic device for performing the carboxyfluorescein leakage assay.** (A), (B) and (C) illustrate how the droplet volume and density changed upon altering the flow rates of the oil and aqueous streams (Aq_1 and Aq_2). Images 1-4 in (A) were gained using the following flow regimes: oil = 3 µl / min, Aq_1 = Aq_2 = 0.3 µl / min (total flow rate = 3.6 µl / min). Images 1-4 in (B) were gained using the following flow regimes: oil = 1 µl / min, Aq_1 = Aq_2 = 0.3 µl / min (total flow rate = 1.6 µl / min). Images 1, 2 & 4 in (C) were gained using the following flow regimes: oil = 0.4 µl / min, Aq_1 = Aq_2 = 0.3 µl / min (total flow rate = 1.0 µl / min). (B) The red boxes indicate where the four images (1-4) were taken in (A), (B) and (C). Scale bar is equal to 300 µm. Channel depth is 50 µm.

It can be observed from figure 3.15 A, B and C that droplet formation could be successfully attained. Although the images in figure 3.15 C illustrate that droplet formation was possible for this set up, under the conditions employed (oil flow rate = 0.4 µl / min, $Aqueous_{1,2}$ = 0.3 µl / min, total flow rate = 1.0 µl / min; see figure 3.15 C and table 3.3), these conditions did not always yield stable droplet formation. The relationship between the oil and aqueous flow rates was not ideal and therefore droplet formation was not always efficient. As a result, these conditions were not suitable and were excluded from further use. The flow conditions employed in figure 3.15 A (oil flow rate = 3.0 µl / min, $Aqueous_{1,2}$ = 0.3 µl / min, total flow rate = 3.6 µl / min; see table 3.3) and B (oil flow rate = 1.0 µl / min, $Aqueous_{1,2}$ = 1.6 µl / min, total flow rate = 1.0 µl / min; see table 3.3), however, were sufficient to afford stable droplet formation. These data are summarised in table 3.3.

	Flow rate (µl / min)			Total flow rate (µl / min)	Droplet Volume (nl)	Stable flow?
Experiment	**Oil**	**Aq_1**	**Aq_2**			
A	3	0.3	0.3	3.6	~ 0.5	Yes
B	1	0.3	0.3	1.6	~ 1.4	Yes
C	0.4	0.3	0.3	1.0	~ 4.2	No

Table 3.3: **Summary of results regarding the optimisation of the aqueous (Aq_1 and Aq_2) and oil flow rates in the microfluidic device, used to perform the carboxyfluorescein leakage assay.** The images in A, B, and C in figure 3.15 refer to experiments A, B and C described in this table.

In addition to achieving stable droplet generation and maximising the amount of kinetic data that may be gained, one wants to ensure that there are a sufficient number of droplets passing through the microfluidic channels. This is particularly important in order to ensure that the number of photons reaching the detector is maximised, hence improving the signal-to-noise ratio.

It was found that a higher packing density of droplets (per set volume in the channel) is observed, upon decreasing the flow rate of the oil fraction and maintaining the flow rate of $Aqueous_{1,2}$ constant at 0.3 µl / min. This is illustrated in images A3, A4 and B3, B4, in figure 3.15, where the droplet packing density in the channels is greater in B.

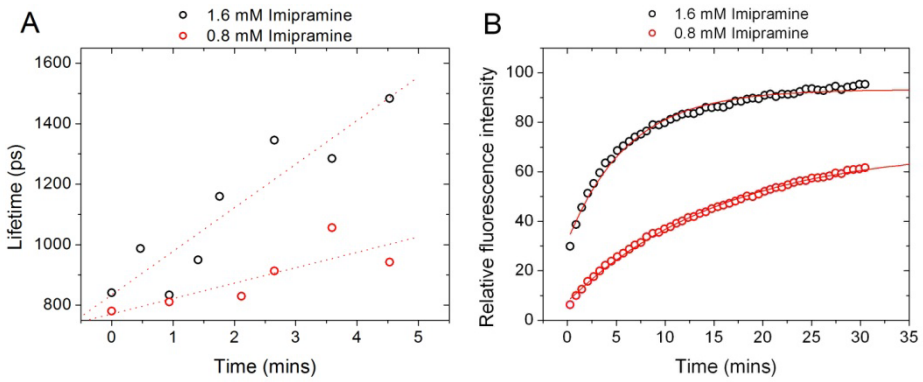
Moreover, it was found that decreasing the flow rate of the oil fraction, whilst maintaining both aqueous flow rates at 0.3 µl / min ($Aqueous_{1,2}$), resulted in an increase in the droplet volume, as well as an increase in the droplet packing density per unit volume. This can be observed when comparing images A2, B2 and C2, and images A4, B4 and C4 in figure 3.15, where the flow rate of the oil fraction is reduced from 3 µl / min, to 1 µl / min, to 0.4 µl / min in A, B, and C respectively; this corresponds to an increase in the droplet volume from ca. 0.5 nl, to ca. 1.4 nl, to ca. 4.2 nl respectively. The data are tabulated in table 3.3.

In summary, the conditions described in experiment B (see table 3.3) were employed to perform the CF leakage assay in a microfluidic format. Firstly, these conditions afford stable droplet generation, where the total flow rate is low enough to allow a sufficient amount of kinetic data to be collected. Moreover, the density of droplet packing per unit channel volume and droplet volume are sufficient in order to maximise the signal-to-noise ratio.

Having optimised the flow conditions for the device, the next step involved attempting to perform the CF leakage assay in a microfluidic format. Imipramine was again used to induce leakage, for reasons explained previously (see section 3.4.2.2), and the experiment was conducted as described in section 3.3.2.5. Figure 3.16 A (and appendix 11) displays the analysed kinetic data for the leakage assay performed with two different concentrations of imipramine, specifically 1.6 and 0.8 mM (final concentration).

It can be observed that upon introducing imipramine to CF-containing vesicles the fluorescence lifetime increases with time, as indicated by the results illustrated in figure 3.16 A, thus indicating that dye is released from the interior

regions of the vesicles to the exterior solution. Moreover it can be observed that the rate of change in the lifetime is dependent upon the number of imipramine molecules introduced into the system, i.e. the final drug concentration. As expected, the more highly concentrated imipramine sample (1.6 mM final concentration) affords a greater rate of CF release compared to the imipramine sample possessing fewer imipramine molecules (0.8 mM final concentration).



C

	Rate$_{1.6\ mM}$ / Rate$_{0.8\ mM}$	**Error**
Intensity Measurement	2.3	± 0.3
Lifetime Measurement	2.8	± 1.6

Figure 3.16: **Comparison of the relative initial rates of change in the fluorescence lifetime and intensity measurements when 0.8 and 1.6 mM imipramine is introduced to carboxyfluorescein-containing vesicles.** (A) Graph illustrating the change in the fluorescence lifetime upon introducing different amounts of imipramine to the CF-containing DOPC vesicles (concentration of DOPC = 0.1 mM). (B) An analogous experiment to that described in A, except graph B monitors the change in the fluorescence *intensity* over time. (C) Tabulated data describing the relative relationship between the initial rates of reaction for both the intensity and lifetime experiments conducted in the presence of 0.8 and 1.6 mM imipramine. The associated errors are included. Further information can be gained by consulting Appendices 11 and 12.

When considering the relative initial rate of change in the fluorescence lifetime of the two samples, which one can assume relates directly to the initial rate of CF leakage, the 1.6 mM sample yields an initial rate that is faster by a factor of 2.8 ± 1.6 in comparison to the 0.8 mM sample (see figure 3.16 C and appendix 12). This agrees with the data gained using an intensity measurement on the fluorescence spectrophotometer (in an analogous experiment), where it was found that the initial rate of CF release for the 1.6 mM sample was greater by a factor of 2.3 ± 0.3 compared to the 0.8 mM sample (see figure 3.16 C and appendix 12). Although the error associated with the lifetime measurements conducted in a microfluidic chip is large, compared to the intensity measurement, if even a small error, for example, of ± 0.3 was applied (if the spread of data about the fit was reduced) then the two values would still be comparable within error. It is apparent that this large error is associated with the greater spread of data about the fit in the lifetime measurements; such an error is not atypical of experiments conducted in a microfluidic environment and is most likely to originate from the averaging of the fluorescence lifetime over the equivalent of three portions of the winding microfluidic channel for each data point. Repeats of the entire experiment should be conducted, as well as averaging the fluorescence lifetime over smaller time increments, in order to reduce this error, but unfortunately it was not possible to do this due to time constraints.

According to the leakage data conducted in the fluorescence spectrophotometer, using fluorescence intensity measurements, approximately 30 and 60 % of CF leakage was observed, after ca. 5 minutes, in the presence of 0.8 and 1.6 mM imipramine respectively (see figure 3.16 B). However, how does the lifetime data compare with this absolute percentage release? Table 3.4 indicates the theoretical concentration of CF present in the vesicle lumens and regions exterior to the vesicle after varying degrees of leakage have occurred. However, this assumes that leakage of the dye from each vesicle lumen occurs at an equivalent rate and from the exact same number of vesicles. In reality,

this scenario will not occur and hence the theoretical calculation can only be used as a guide.

Figure 3.17 illustrates an enlarged section of the calibration curve gained using a microfluidic format – the original graph is depicted in figure 3.14, section 3.4.2.3. Specifically, the first three data points in the region between 1E-01 M and 1E-2.5 M CF are displayed, and a line of best fit indicated. This graph can be used to ascertain a predicted value for the fluorescence lifetime after a certain percentage of dye has been released from the vesicle lumens.

As stated previously, the presence of 0.8 mM imipramine induces ca. 30 % CF leakage after ca. 5 minutes, as determined using fluorescence intensity measurements. Hence according to the data presented in table 3.4, a 30 % release of the dye will yield an internal concentration in the vesicle lumens of ca. 0.035 M (or a value of ca. 1.5 if one takes the negative log of the concentration), which corresponds to a predicted lifetime value of just less than 1 ns as indicated by figure 3.17. This predicted value agrees well with that determined experimentally, specifically ca. 1 ns, as illustrated in figure 3.16 A. Similarly, if ca. 60 % of the internalised CF is released, which was found to occur in the presence of 1.6 mM imipramine during fluorescence intensity measurements, the internal dye concentration will be ca. 0.020 M (or a value of ca. 1.7 if one takes the negative log of the concentration) thus affording a predicted lifetime value of ca. 1.5 ns (see table 3.4 and figure 3.17). This again concurs with the data gained experimentally in a microfluidic format, where the value of the lifetime was c.a 1.5 ns after having left the mixed drug and vesicle solution for 5 minutes (see figure 3.16). Hence the absolute values of CF release for the intensity and lifetime data are comparable, which certainly suggests that this method is exploitable.

	Interior of vesicles			Exterior of vesicles		
CF release (%)	**Amount of CF (moles)**	**Amount of CF (mol / L)**	**-log ([CF]/M)**	**Amount of CF (moles)**	**Amount of CF (mol / L)**	**-log ([CF]/M)**
0	6.00E-09	0.050	1.30	0.00E+00	0.00E+00	0.00
10	5.40E-09	0.045	1.35	6.00E-10	1.00E-06	6.00
20	4.80E-09	0.040	1.40	1.20E-09	2.00E-06	5.70
30	4.20E-09	0.035	1.46	1.80E-09	3.00E-06	5.52
40	3.60E-09	0.030	1.52	2.40E-09	4.00E-06	5.40
50	3.00E-09	0.025	1.60	3.00E-09	5.00E-06	5.30
60	2.40E-09	0.020	1.70	3.60E-09	6.00E-06	5.22
70	1.80E-09	0.015	1.82	4.20E-09	7.00E-06	5.15
80	1.20E-09	0.010	2.00	4.80E-09	8.00E-06	5.10
90	6.00E-10	0.005	2.30	5.40E-09	9.00E-06	5.05
100	0.00E+00	0.000	0.00	6.00E-09	1.00E-05	5.00

Table 3.4: **Theoretical concentration of carboxyfluorescein present in the interior and exterior regions of the vesicles after varying amounts of leakage.** Hence the theoretical position on the calibration curve can be predicted (indicated by the values in the column labelled –log([CF]/M).

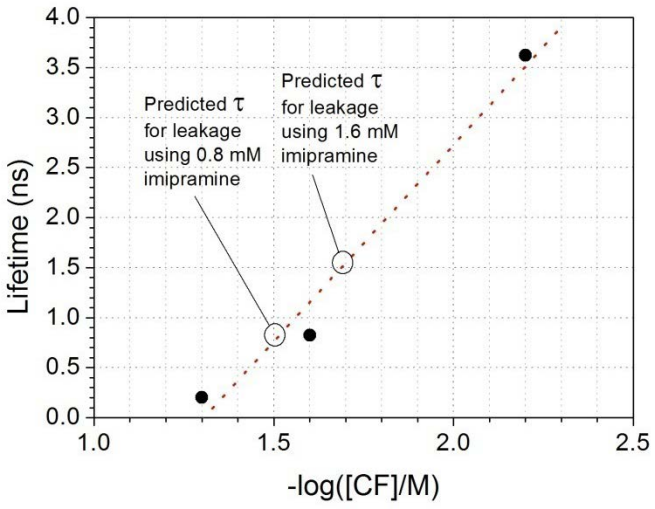


Figure 3.17: **Predicted lifetime values based on the theoretical concentration of carboxyfluorescein present in the interior regions of the vesicles after leakage induced by the presence of 0.8 and 1.6 mM imipramine.** This results in approximately 30 and 60 % CF release after ca. 5 minutes respectively. The former situation yields a lifetime value of just less 1 ns, with the latter resulting in a lifetime value of ca. 1.5 ns.

3.4.2.5 Comparison of the leakage data gained in the cuvette and microfluidic formats

The leakage data gained using the two experimental formats described in this chapter, i.e. the cuvette and microfluidic formats, are illustrated collectively in figure 3.18 A and B.

It has been determined that the introduction of imiprimine affords a change in the fluorescence lifetime, which corresponds to CF leakage, but the absolute change is not consistent between the two experimental formats. The main difference between the two formats is that the fluorescence lifetime appears to increase at a 'faster' rate initially (i.e. during the first 5 minutes) for the leakage assay performed in the cuvette system, when compared to the assay performed in the microfluidic format (for 1.6 mM imipramine data). However, it is thought that this occurrence persists due to the nature of the calibration curve gained using the cuvette format, where a bigger change in the fluorescence lifetime with concentration is observed.

After 10 minutes, ca. 80 % leakage of the dye is observed when 1.6 mM imipramine is introduced (figure 3.16 B), which according to table 3.4 corresponds to an average CF concentration of ca. 0.010 M (or a value of ca. 2.0 if one takes the negative log of the concentration) retained within the liposomes. As illustrated by the enlarged calibration graph displayed in figure 3.18 C, this degree of leakage corresponds to an approximate fluorescence lifetime of 4 ns. This concurs with the experimental data gained, displayed in figure 3.18 A.

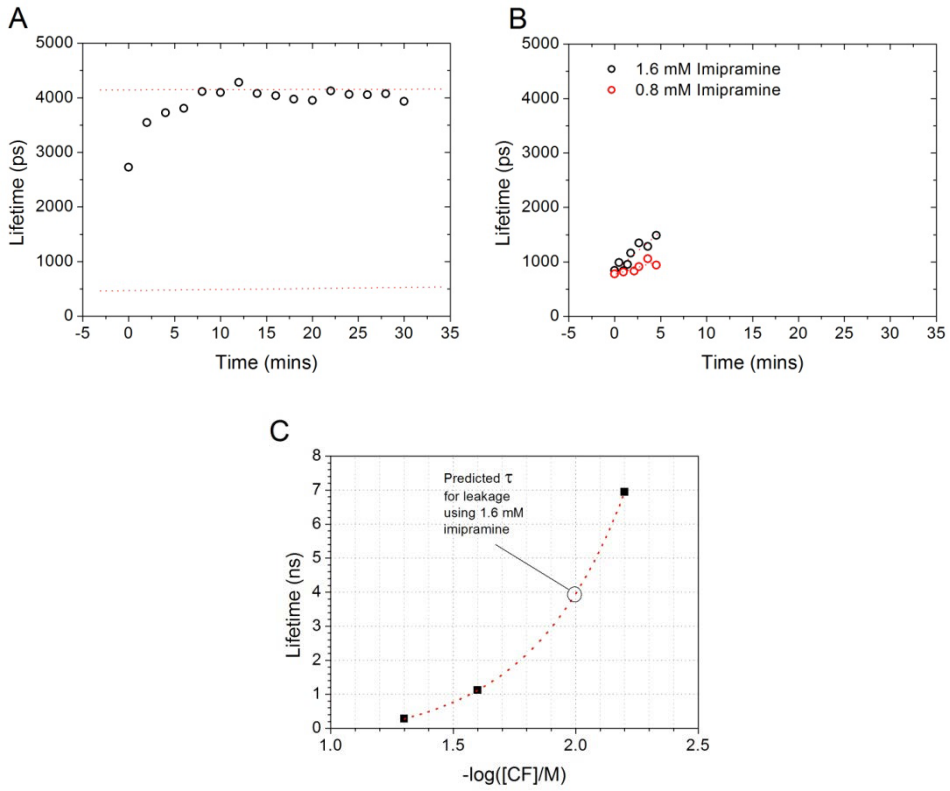


Figure 3.18: **Comparison of leakage data gained in the cuvette and microfluidic formats.** (A) Graph showing the change in the fluorescence lifetime upon introducing 1.6 mM imipramine to CF-containing vesicles using a cuvette format. (B) Graph showing the change in the fluorescence lifetime upon introducing 0.8 and 1.6 mM imipramine to CF-containing vesicles using a microfluidic format. (C) Enlarged region of the calibration curved gained using a cuvette format.

It is also important to appreciate that differences in fluidic mixing between the two experimental formats may have had a small affect the observed kinetics. For example, the samples used in the cuvette format are mixed together by inverting the cuvette, whereas the microfluidic device relies on the weaving of the microfluidic channel to mix the droplets' contents. As the total flow rate used during these experiments was particularly low (1.6 μl / min) and the number of 'weaves' in the channel for mixing also low, the microfluidic format

perhaps did not afford conditions for mixing that were as efficient as in the cuvette system. The cuvette system, however, lacks the ability to collect good kinetic data within the first minute of the experimental window, owing to mixing having to occur offline before data collection can occur.

However, despite these differences, the microfluidic format offers a suitable system in which to work and one where the data are easy to manipulate/interpret (c.f. the cuvette system); namely, it affords calibration data, which agree well with that present in the literature and the dependence of the lifetime is less complicated in the region of interest (from 1E-01 to just below ca. 1E-02 M).

3.4.2.6 Problems associated with the microfluidic format

Although the data gained using the microfluidic format are promising, this experimental format can be challenging to work with. One particular problem that persisted (in virtually 100 % of devices that were assembled) involved dust becoming trapped in the devices, thus resulting in the majority of devices being rendered unusable. In those that were suitable to use, the presence of dust particles lying across the winding microfluidic channel at several points resulted in some of the droplets merging and splitting in these regions. This problem originates from the particularly large size of the microfluidic devices, where the probability of gaining dust particles in the devices is increased (even though the greatest of care was taken in order to avoid this problem). Hence, the merging / splitting events may have had an effect on the quality of the kinetics gained. However, these experiments are monitoring the effect of drugs on bulk vesicle populations and droplet merging / splitting does not appear to have been detrimental, when comparing the lifetime data to the intensity data collected in the fluorescence spectrophotometer (discussed previously in sections 3.4.2.4 and 3.4.2.5). Additionally, only half the length of the microfluidic channel in the devices was used during these experiments, thus offering the potential to gain up to 10 minutes' worth of data in future experiments.

Another problem that persisted during these experiments involved the presence of static droplets adsorbed to the channel at numerous points, as is illustrated in figure 3.19. Although initially quite annoying, these droplets do provide some interesting information. It can be observed that the fluorescence lifetime of the static droplets is much longer than the lifetime of the main channel: the blue and green droplets in figure 3.19 C possess fluorescence lifetimes of approximately 3.1 ns and 2.3 ns respectively, whist the droplets flowing in the main channel have an associated lifetime of 0.8 ns. Note that the droplets flowing in the main channel cannot be resolved as their speed is too fast, compared to the refresh rate of the camera. As these droplets are static, the presence of longer lifetimes (c.f. the droplets flowing in the main channel) can only be due to the continual leakage of CF from the interior of the vesicles into the exterior regions. Hence, this provides further evidence in support of the method and also indicates that such an assay could be performed in a different format, using static droplets as opposed to flow measurements to gain kinetic information.

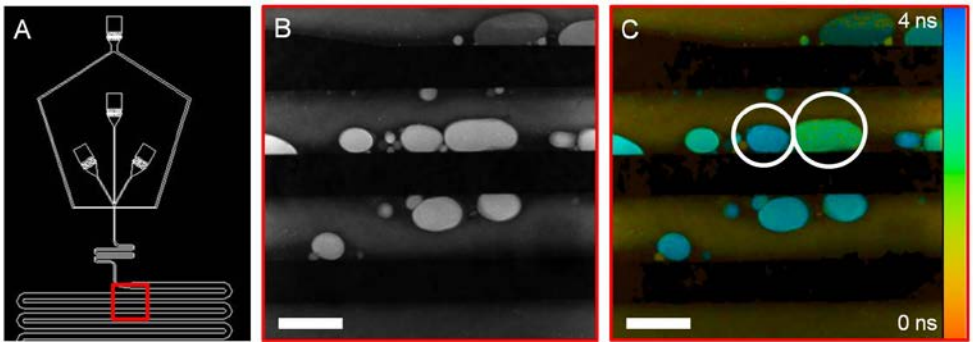


Figure 3.19: **Static droplets adsorbed to the channel in a microfluidic device.** (A) The red box illustrates where the images in B and C were attained in the microfluidic device, i.e. over 3 channels. (B) Grayscale image of the fluorescence lifetime data and (C) a false colour image with colour scale (ranging from red = 0 ns to blue = 4 ns). The two white circles in C illustrate two droplets that are adsorbed to the channel; the blue droplet (left hand side) has a lifetime of 3.1 ns, whilst the green droplet (right hand side) possesses a lifetime of 2.3 ns. The lifetime of the droplets flowing in the main channel is 0.8 ns Scale bar represents 300 μm.

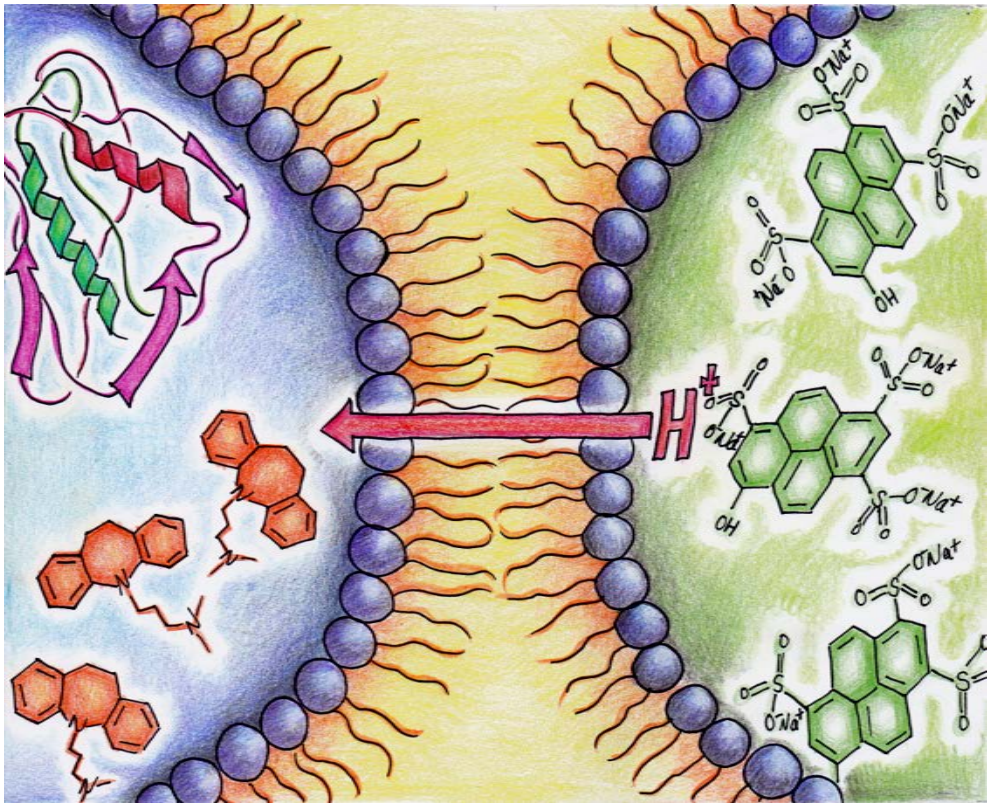
Nevertheless, although there are some problems associated with the method, and hence improvements that can be made, these experiments have shown that it possible to translate bulk vesicle assays into a microfluidic format, with fluorescence lifetime imaging offering a solution to the original problem at hand.

3.5 CHAPTER SUMMARY

In summary, chapter 3 has demonstrated that it is feasible to translate the CF leakage assay into a microfluidic format, using microfluidic droplet technologies. Importantly, this chapter has revealed that fluorescence lifetime measurements are suitable for measuring the rate of CF leakage, and therefore assessing the leakage properties that drug molecules of interest portray, overcoming problems associated with fluorescence intensity measurements. Hence the results described in chapter 3 demonstrate the potential for translating other assays into a microfluidic format, which involve performing fluorescence measurements on bulk vesicle populations, as well as the potential for screening drug-membrane interactions in high-throughput.

Chapter 4

Droplet interface bilayers (DIBs) for probing drug-membrane interactions



"Science never solves a problem without creating ten more."

George Bernard Shaw

4.1 OVERVIEW

Chapter 4 is concerned with using artificial planar lipid bilayers, as a potential means for investigating the interaction of drug molecules upon a single lipid bilayer. This contrasts with the approaches described in chapters 2 and 3, where measurements of bulk vesicle systems have been considered. Droplet interface bilayers, or DIBs, have been chosen as the method of choice for artificial planar bilayer formation, offering many advantages over traditional methods and opening avenues for their formation and screening in high-throughput.

Specifically, this chapter demonstrates that the formation of DIBs can be reproduced easily using the lipid 1,2-diphytanoyl-sn-glycero-3-phosphocholine DPhPC, cited in all literature associated with DIBs. Additionally, the successful formation of DIBs comprised of the more biologically relevant lipid, DOPC, has been achieved for the first time. Finally, the approaches taken to build a proof-of-concept leakage assay across DIBs using pH gradients, for assessing drug-membrane interactions, have been detailed. The problems associated with the manual manipulation of droplets have also been highlighted, hence justifying the need for an approach able to form DIBs reliably and in a uniform manner.

4.2 INTRODUCTION

4.2.1 Liposomes versus artificial planar bilayers

As we have seen previously, the development of assays for the study of drug- and protein-membrane interactions is extremely important. The work detailed in chapters two and three has employed an experimental format where bulk measurements, i.e. the effect of exogenous species on vesicle populations, are predominant. In this instance the average effect of the overall system is

monitored, where noise (with respect to both vesicle size and lipid composition for example) ensues. Although such a format is important, it is also desirable to understand how drug molecules and proteins behave when they are subjected to a single lipid bilayer.

Artificial planar bilayers and vesicle assays each have their own merits. However, the former experimental format is attractive as it enables the researcher to alternate the compositions of the aqueous compartments on either side of the membrane, which is small and inaccessible in vesicular formats. Additionally the use of planar bilayers enables: (i) events taking place in the aqueous compartments to be measured independently and (ii) asymmetric membranes to be formed.

4.2.2 Traditional methods for forming artificial planar bilayers

Artificial planar bilayers have been utilised for many years, most notably as a tool for probing the functional properties of pore forming proteins, such as alamethicin and gramicidin.[250] "Black lipid membranes" (or BLMs) were the first artificially produced planar membranes, developed in the early 1960s. Their formation involves carefully spreading a solvent containing lipid across an aperture, ranging typically from 0.1 to 1 mm in diameter, and waiting for the onset of black spots to form. These black spots then grow to yield a completely 'black' membrane, which corresponds to the solvent being removed from the membrane towards the annulus and its appearance as visualised in reflected light. Such membranes are often referred to in the literature as 'painted' membranes, an expression originating from the technique itself. However, this terminology could equally refer to the care required in mastering this tricky technique.

Advancements were made on the first approaches for artificial planar bilayer formation and include the Montal-Mueller method,[251] a method pioneered in the early 1970's and classed as a "folded membrane" technique.[250] In brief, this technique involves forming artificial lipid membranes by displacing a septum,

armed with a thin Teflon® film (ca. 25 μm in thickness) containing a small aperture, vertically through a Langmuir-Blodgett lipid film.[252] Consequently, the two lipid monolayers formed at the air-water interface are drawn in a downwards direction, where they meet to form a lipid bilayer at the point when the aperture is lowered beneath the water level. A typical experimental setup and illustration of the mechanism of bilayer formation across the aperture is displayed in figure 4.1. Other folded membrane approaches include raising the water levels above the aperture, either independently or simultaneously.[250] Additionally, it can be observed from figure 4.1 that the folded membrane method enables the formation of the asymmetric bilayers, as there are two distinct aqueous environments.

Folded membranes arose due to the need to reduce the amount of solvent residing in the membrane, typical of the painted membrane method. However, membranes formed in this manner are still not completely solvent-free, due to the use of highly volatile solvents (i.e. hexane / pentane) for depositing the lipid at the air-water interface. As these molecules are small, they are therefore more soluble in the membrane. Additionally, the aperture is pre-treated with a much less membrane-soluble organic solvent, such as hexadecane, to aid the tethering of the bilayer to the aperture in the region of the annulus. In spite of this, bilayers exhibiting specific capacitances comparable to those calculated for true bilayers (0.8 μF / cm^2) have been produced using folded membrane methods, as compared to values of 0.4 μF / cm^2 for membranes formed via painted methods.[250]

One way of eliminating the need for lipid soluble solvents, and hence create effectively solvent-free bilayers, is to incorporate vesicle suspensions into the aqueous compartments for the formation of lipid monolayers at the air-water interface.[253] Note that pre-treatment of the aperture with hexadecane is still required, even if the aperture is very small, as otherwise the membranes are too unstable.

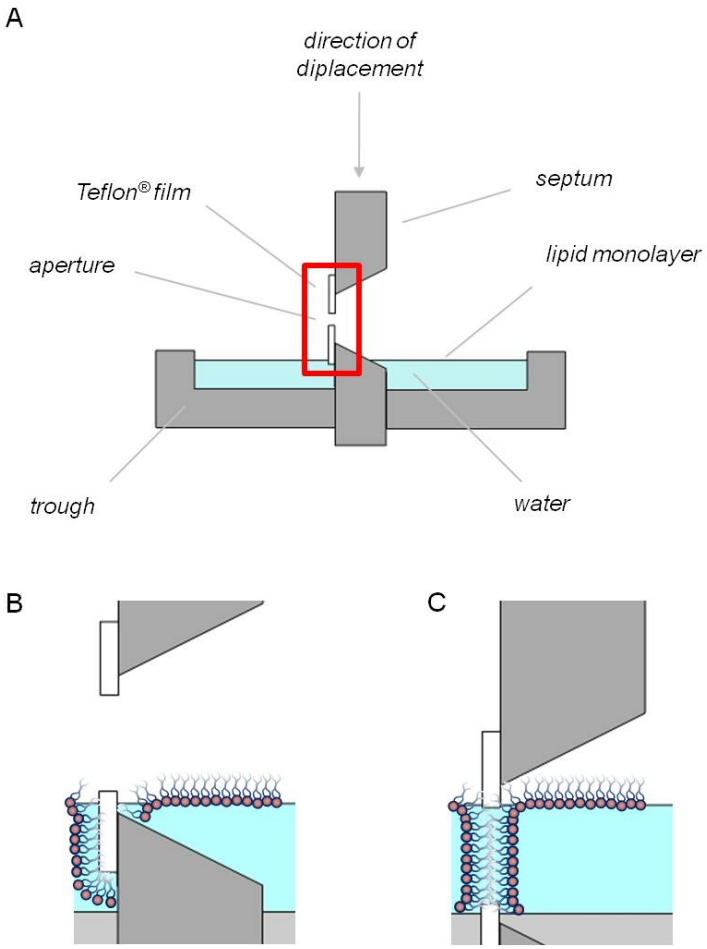


Figure 4.1: **Montal-Mueller method for the formation of artificial planar membranes.** (A) Illustration demonstrating the experimental set-up (figure adapted from Montal and Mueller).[251] A Teflon® film, containing a small aperture, is attached to a septum (highlighted by the red box). The septum is displaced vertically through a Langmuir-Blodgett lipid monolayer in order to form the artificial lipid membrane. (B) and (C) further illustrates this process (prior to and after displacement of the aperture beneath the water level respectively). Note that the diagram is not to scale and no attempt has been made to describe the orientation of the lipid monolayer upon contact to the trough / septum.

4.2.3 Droplet interface bilayers (DIBs)

"Droplet Interface Bilayers" (or "DIBs"), a term coined in recent years, are a modern advancement on the original concept of artificial bilayer formation. A

DIB corresponds to the act of forming a lipid bilayer as a result of bringing together two aqueous droplets that are submersed in an oil environment and in the presence of lipid molecules. Lipids, being amphiphilic in nature, act as surfactant molecules and partition at the aqueous-oil interface, reducing the interfacial surface tension and preventing the aqueous droplets from merging instantaneously upon contact. Consequently, a lipid bilayer is formed as a result of two monolayer leaflets coming into contact with one another. Figure 4.2 illustrates the nature of a DIB. Importantly, specific capacitances of ca. 0.7 μF / cm^2 have been gained for DIBs comprised of DPhPC,[204] which are comparable to theoretical calculations of specific capacitance gained for a lipid bilayer (ca. 0.8 μF / cm^2, as discussed in section 4.2.2).[254]

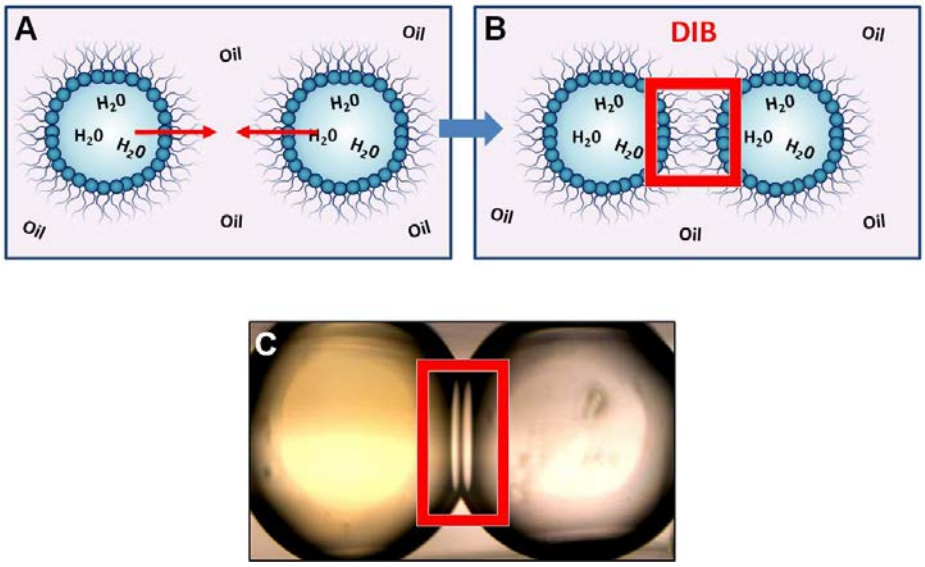


Figure 4.2: **Droplet Interface Bilayer (DIB) formation.** (A) If two aqueous droplets are submersed in an oil environment, their interfacial surface tension is reduced upon the introduction of surfactant molecules, i.e. lipids. As these molecules are characteristically amphiphillic in nature, they will reside at the aqueous-oil interface and form lipid monolayers. (B) Formation of a droplet interface bilayer proceeds after the two lipid monolayers are brought into contact with one another. (C) This image is an example of a DIB gained experimentally.

The concept of DIBs, as they exist in their current form, was first pioneered by Funakoshi *et al.*[202] and Holden *et al.*[203] However, one of the first recorded methods of DIB formation was published by Tsofina *et al.* in 1966, as noted by Bayley *et al.* in their review on DIBs.[204] The major advantages of employing DIBs over traditional methods for planar bilayer formation are summarised in table 4.1.

Advantage	Practicality	Consequence
Ease of formation	no specialist equipment required	quick to master
Stability	lifetime of days to weeks c.f. hours	larger experimental window
Smaller aqueous compartments	setup transportable & more economical	e.g. can be visualised under a microscope
Ability to form >1 bilayer	formation of DIB networks	larger experimental window

Table 4.1: **Summary of the advantages that the DIB system has over conventional methods for artificial planar bilayer formation.**

Importantly, the Bayley laboratory has made several advances in recent years with regard to the way in which DIBs are formed, subsequently classifying two different approaches. Lipids may be doped into the oil phase (termed the "lipid-out" approach) or conversely into the aqueous phase in the form of vesicles (termed the "lipid-in" approach),[204] as illustrated in Figure 4.3 A and B respectively. The lipid-in approach is advantageous, not only because the time taken to achieve monolayer formation is greatly reduced and also more economical, but because asymmetric bilayer formation can be realised by incorporating different vesicle populations into different droplets. Figure 4.3 C

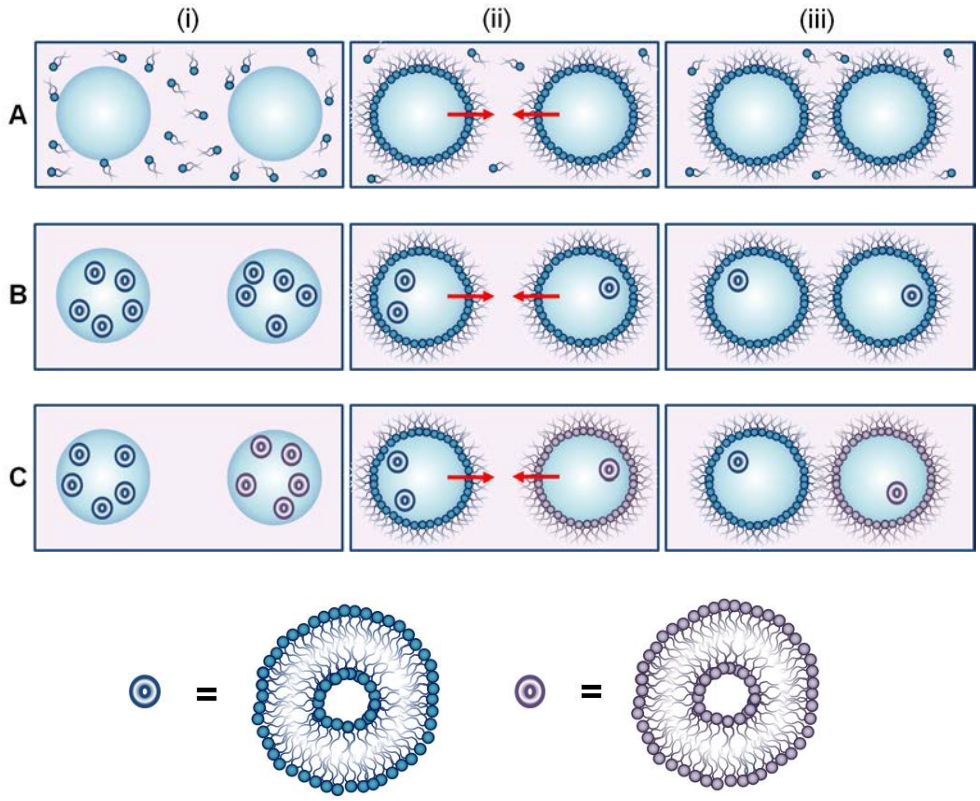


Figure 4.3: **Methods for forming DIBs, including asymmetric DIBs.** (A) The "lipid-out" approach. (B) The "lipid-in" approach. (C) asymmetric DIB (aDIB) formation. The three steps detailed in A, B and C relate to: (i) submersing two aqueous droplets into oil (either containing or not containing lipids), (ii) movement of the two droplets towards one another (denoted by red arrows) after sufficient time has been given for monolayer formation to occur at the aqueous-oil interface and (iii) DIB formation. The small circular entities represent vesicles. Note, diagram not to scale.

demonstrates how asymmetric bilayer formation is achieved using the DIB format.

4.2.4 Summary and chapter aims

For the aforementioned reasons, DIBs present an excellent means by which to interrogate the interaction of molecular species upon model membranes, particularly in relation to the specific influence that a membrane may have upon the interacting species. For example, the membrane composition of each leaflet may or may not be altered by the same degree, thus either maintaining

or destroying lipid symmetry across the two monolayers respectively. The specific interaction of drug molecules upon a lipid membrane, using a DIB format, has not been investigated previously in this manner. This chapter therefore aims to:

1. Demonstrate that DIB formation with DPhPC is reproducible, as detailed by Funakoshi *et al.* and Holden *et al.* (discussed previously in section 4.2.3).
2. Demonstrate that the DIB technique is amenable for use with lipids other than DPhPC, such as the more biologically relevant lipid DOPC.
3. Detail the various steps involved in the development of a proof-of-concept leakage assay, which employs pH gradients and could monitor indirectly the extent to which the membrane is perturbed by exogenous species.
4. Demonstrate an appreciation for the limitations surrounding the practical approach used in this chapter to achieve DIB formation, i.e. manual manipulation. A solution to this problem is offered, providing the rationale for chapter 5.

4.3 MATERIALS AND METHODS

The following section details the materials required and methods employed in performing each of the experiments described in this chapter.

4.3.1 Materials

4.3.1.1 Lipids

The following lipids were used in the experiments detailed in this chapter: 1,2-diphytanoyl-sn-glycero-3-phosphocholine (DPhPC, Avanti Polar Lipids) and 1,2-dioleoyl-sn-glycero-3-phosphocholine (DOPC, Avanti Polar Lipids).

4.3.1.2 Dye and buffer solutions

The following components, all of which were purchased from Sigma-Aldrich®, were used to make the dye and buffer solutions for the experiments described in this chapter, namely 4-(2-hydroxyethyl)piperazine-1-ethanesulfonic acid (HEPES), potassium chloride (KCl), sodium hydroxide (NaOH), 5(6)-carboxyfluorescein (CF) and 8-hydroxypyrene-1,3,6-trisulfonic acid trisodium salt (pyranine). Hereafter, the specific aqueous solutions will be referred to as follows:

Solution 4.1:	10 mM HEPES, 200 mM KCl, pH 7.07
Solution 4.2:	1.3 μM CF, 1 mM HEPES , 200 mM KCl pH 4.6
Solution 4.3:	10 mM HEPES , 200 mM KCl pH 8
Solution 4.4:	1.3 μM CF, 1 mM HEPES , 200 mM KCl pH 8
Solution 4.5:	1 mM pyranine, 10 mM HEPES, 200 mM KCl pH 4
Solutions 4.6-4.9:	As solution 4.5, but instead adjusted to pH 6, 7, 8 and 10 respectively.
Solution 4.10:	1 mM pyranine
Solution 4.11:	60 μM pyranine, pH 5.5

Solution 4.12:	60 μM pyranine, 1 mM HEPES, 200 mM KCl, pH 5.5
Solutions 4.13-4.16:	As solution 4.12, but instead adjusted to 6.4, 6.7, 6.9 and 8 respectively.

4.3.1.3 DIB formation

Hexadecane oil (99%, Sigma-Aldrich®) was used as the oil of choice to aid the formation of DIBs. Glass chambers, having an open channel configuration to enable droplet dispensing and manipulation, were constructed from standard microscopy slides (VWR), Araldite® and silicone rubber compound (both RS Components Ltd.). The basic chamber design can be viewed in figure 4.4. Metal needles (BD Microlance 25G 1" – Nr. 18, 0.5 × 25 mm) were used to move the droplets in the chamber and create DIBs. Their tips were cut, flattened and shaped in order to form suitable metal prongs.

4.3.1.4 IFT measurements

IFT measurements were conducted using an Easy Drop tensiometer (Krüss). A 0.5 ml glass syringe (Hamiliton, bore inner diameter = 3.256 mm), equipped with a disposable needle (Krüss, diameter = 1.830 mm), was used to dose and hence interrogate the solution of interest (see figure 2.6 in chapter 2, section 2.3.2.4 for further details regarding equipment set up). A glass cuvette (Starna Scientific Ltd., Type 3 (2 cm x 1 cm x 5 cm) and cover plate (Krüss) were also required to conduct these measurements.

4.3.2 Methods

4.3.2.1 Vesicle preparation

Vesicle suspensions were comprised of either DPhPC or DOPC and prepared as described previously (chapter 2, section 2.3.2.1). Thin lipid films were prepared with 2 mg of lipid and hydrated with 1 ml of an aqueous solution to yield a concentration of 2 mg / ml. Note that films composed of DOPC were

hydrated with 0.5 ml of an aqueous solution to afford a 4 mg / ml lipid concentration. The various solutions used to hydrate lipid films and form vesicle suspensions for DIB formation are specified in section 4.3.1.2, specifically solutions 4.1, 4.2, 4.3, 4.11 and 4.12. Hydrated lipid films were freeze-thawed five times and subsequently extruded 20 times through 100 nm polycarbonate membranes (Avanti Polar Lipids) and wrapped in foil and stored in the dark when not in use.

4.3.2.2 DIB formation

DIB formation was achieved using the 'lipid-in' approach, as detailed previously in section 4.2.3. Approximately 0.2 μl aliquots of aqueous vesicle suspension were pipetted into hexadecane: the hexadecane and aqueous droplets were contained within glass chambers (see figure 4.4 for design). After having been left in the oil for a period of time, to enable monolayer formation at the oil-water interface, two droplets were brought into contact with one another to form a DIB.

4.3.2.3 Leakage experiments

For each leakage experiment two vesicle populations were prepared; one using a solution of low pH and containing a fluorescent dye (either solutions 4.2, 4.11 or 4.12 as detailed in section 4.3.1.2), the other at higher pH (solution 4.3, see section 4.3.1.2). The standard protocol for the production of small unilamellar vesicles (SUVs) was adopted (see section 4.3.2.1 for details). Note that special care was taken when extruding the two vesicle populations. Each was extruded using a separate extruder, which was freshly cleaned and rinsed with the solution of interest prior to use. This was particularly important in order to maintain the true pH of each vesicle population.

4.3.2.4 Control experiments

Control experiments involved testing whether aqueous solutions, containing either CF or pyranine, leak from the aqueous phase into the oil phase. Equal

volumes of the aqueous fluorescent solution (either solution 4.2, 4.4, 4.12 and 4.15, as described in section 4.3.1.2) and hexadecane oil were placed in the same glass vial, thus forming an aqueous-oil interface, and left for one week in a concealed and dark environment. Aliquots of each phase were then transferred into a 96 well-plate (Fisher Scientific Ltd) and fluorescence measurements carried out on a Cary Eclipse fluorescence spectrophotometer (Varian Inc.). Emission scans, with excitation at 490 or 475 nm (for CF- and pyranine-containing solutions respectively) and emission collected from 500 to 600 nm, were then performed on each of the samples. Both the excitation and emission slits were set to 5 nm, and a medium scan rate and photomultiplier tube detector voltage (PMT) of 500 V employed. Comparisons were then made with fresh samples of hexadecane and original fluorescent solutions (where no aqueous-oil interface was allowed to form).

4.3.2.5 Pyranine fluorescence spectra

All fluorescence spectra conducted for pyranine-containing samples were conducted on a Cary Eclipse fluorescence spectrophotometer (Varian Inc.) using a well-plate reader (96 wells). Excitation spectra, determined in the 300-500 nm range, were attained using a fixed emission wavelength of 510 nm, a PMT of 500 V, a medium scan rate and excitation / emission slits both set to 5 nm. Emission spectra were gained using an excitation wavelength of 460 or 475 nm and emission collected in the region between 500-600 nm. The PMT, scan rate and excitation / emission slits used to gain the emission spectra were identical to those used to gain the excitation spectra.

4.3.2.6 Imaging

All experiments described herein were conducted on a Nikon Eclipse TE 2000-E fluorescence microscope. A QICAM camera (QImaging, Media Cybernetics UK) was used to capture both bright field and fluorescence images. Figure 4.4 illustrates the experimental setup for the experiments

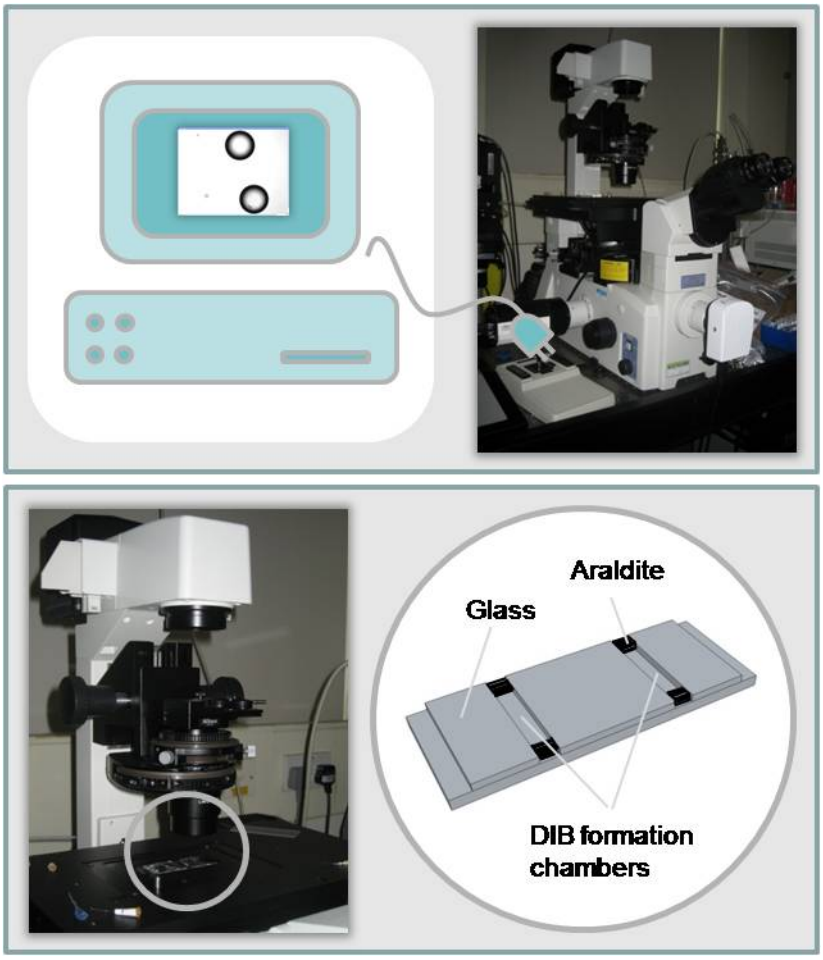


Figure 4.4: **Experimental set-up for DIB experiments using manual manipulation.** The Nikon Eclipse TE 2000-E microscope, used to conduct the experiments described in this chapter, is displayed. A close up view of the microscope indicates where hand-built glass chambers, used for holding droplets and hence viewing DIB formation, are slotted into the microscope stage accordingly.

conducted in this chapter. The software used to drive the equipment was home-built, designed and built by Dr. Nick Brooks in LabView.

The combinations of excitation filters, emission filters and dichroic mirrors used in the filter cubes (Nikon) during the fluorescence experiments detailed in this chapter are specified as follows:

Carboxyfluorescein

Channel 1:	Excitation:	465-495 nm
	Emission:	515-555 nm
	Dichroic:	505 nm

Pyranine

Single channel fluorescence recordings:

Channel 1:	Excitation:	457-487 nm
	Emission:	515-555 nm
	Dichroic:	495 nm

Dual channel fluorescence recordings:

Channel 1:	Excitation:	330-380 nm
	Emission:	515-555 nm
	Dichroic:	505 nm
Channel 2:	Excitation:	457-487 nm
	Emission:	515-555 nm
	Dichroic:	495 nm

The exposure times used during ratiometric experiments when taking bright field, channel 1 and channel 2 recordings were 4 ms, 3000 ms and 1500 ms respectively. Note that the ratio of fluorescence intensities, *r*, is defined as:

$$r = \frac{F_{average}^{460-490nm}}{F_{average}^{330-380nm}} \qquad \text{Equation 4.1}$$

where F = average fluorescence intensity (collected between 515-555 nm) when the sample is excited at either 460-490 nm or 330-380 nm.

4.3.2.7 Image analysis

ImageJ, Image Processing and Analysis in Java (freeware, Wayne Rasband, National Institute of Mental Health USA), was used to analyse and hence gain quantitative information from the microscopy images presented in this chapter. Regions of interest (ROIs) around each fluorescent droplet were defined in order to gain the average fluorescence intensity for the relevant droplet in each image. Note that circular ROIs were used and defined using the bright field images as a guide. The absolute area of the ROI remained constant within each experiment. A screen dump of the graphical user interface is illustrated in figure 4.5.

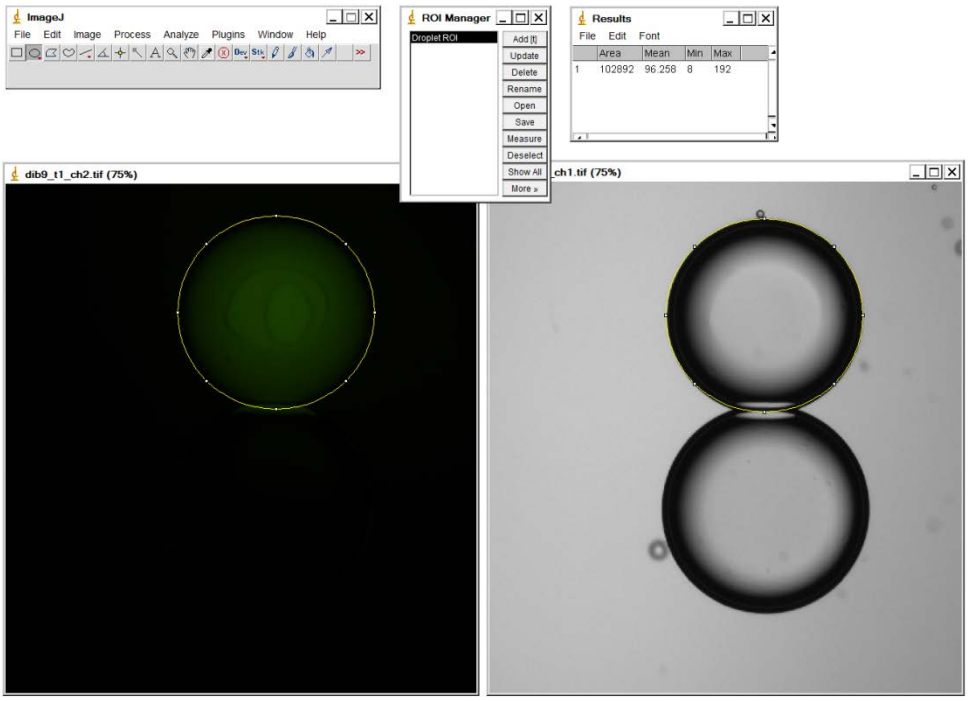


Figure 4.5: **Screen dump of the ImageJ software used for analysing fluorescence microscopy images.** Example images of aqueous, lipid-containing droplets in hexadecane oil are displayed after having been subjected to both fluorescence and bright field illumination. The region of interest (ROI), used to calculate the average fluorescence intensity of a specified region, is highlighted by the yellow circle. The area of the ROI, in addition to the mean, minimum and maximum fluorescence intensity, can be ascertained.

4.3.2.8 IFT measurements

Measurements of IFT at the oil-water interface required the droplets to be suspended in an oil environment, hence a glass cuvette was used to accomodate the embedding phase. As the oil phase is less dense than the aqueous phase ($\varrho_{hexadecane}$ = 0.773 g / ml),[255] the experiments were conducted in the typical manner of water-in-air measurements, where the drop is suspended in a top-down manner. For experiments investigating the surface activity of surfactant molecules at the air-water interface, droplets were suspended in a closed environment containing a few millilitres of aqueous solution in order to maintain a constant drop volume (see figure 2.6 C in chapter 2, section 2.3.2.4 for further information).

All data were collected using the software programme "Drop Shape Analysis". The Trackerman programme was utilised to determine the dependency of a particular surfactant-containing solution on the IFT over time, where the IFT will tend to an equilibrium value (IFT_{eq}) as $t \rightarrow \infty$. This programme was set up to record an IFT measurement at regular time intervals (every 10 s) for a total duration of up to 40 minutes. All experiments were conducted at room temperature and the lights in the vicinity of the tensiometer turned off to ensure that good contrast, between the drop circumference and background, is maintained.

4.3.3 Movie

4.3.3.1 Movie 4.1: 'Formation of droplet interface bilayer (DIB)'

This movie shows DIB formation between a non-fluorescent droplet (2 mg / ml DPhPC) and a fluorescent droplet (2 mg / ml DPhPC with 250 μM fluorescein). The stills from the movie are displayed in figure 4.6; note that the time increment between each image is 1 s and the scale bar represents ca. 400 μm. Please find the movie on the CD accompanying this thesis.

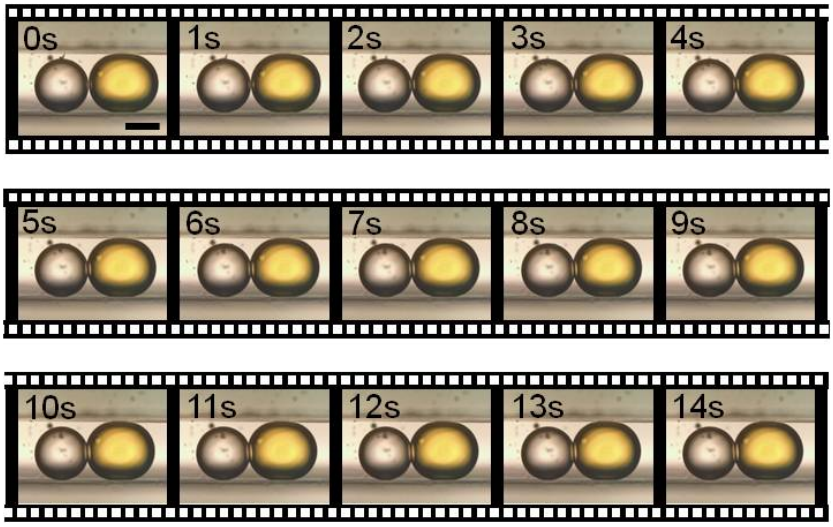


Figure 4.6: **Stills from Movie 4.1: 'Formation of droplet interface bilayer (DIB)'.**

4.4 RESULTS AND DISCUSSION

As described in section 4.2.3, droplet interface bilayers (DIBs) provide an alternative means to probe the effect of exogenous species upon a lipid membrane, offering several advantages over conventional methods for planar bilayer formation. Herein, the following section will discuss the steps taken in achieving successful DIB formation, both with DPhPC and the more biologically relevant lipid DOPC, and detail proof-of-concept experiments, involving the use of pH sensitive dyes, which can be envisaged to offer an indirect means for monitoring the extent to which lipid bilayers are perturbed by drug molecules, or proteins, for example.

4.4.1 Formation of droplet interface bilayers (DIBs)

4.4.1.1 Open channel format for DIB formation

In the first instance it was desirable to reproduce the DIB formation process, reported by the Bayley group. Hand-built chambers were produced for this purpose (see figure 4.4 for chamber design). Open channels thus allowed

droplets to be manually pipetted into the oil and enabled the DIB formation process to be performed in a simple and uncomplicated manner.

Approximately 0.2 μl aliquots of 2 mg / ml DPhPC vesicle suspensions were pipetted into hexadecane, i.e. the same lipid, lipid concentration, aqueous solution (solution 4.1, see section 4.3.1.2) and oil employed by the Bayley group. It is worthy to note that hexadecane is used, as opposed to other members of the decane family, because it is much less soluble in lipid. Lipid bilayers formed in the presence of hexadecane, e.g. using soya bean lecithin, are reported to give higher specific capacities and are more true to native membranes.[250] It would be desirable to use oils possessing longer carbon chains, however this is not possible practically due to their inherent physical properties. Specifically, increasing chain length leads to an increase in the phase transition temperature (see table 4.2, values gained from sigma Aldrich website).

Chemical Name	**Chemical Formula**	**Melting Point (°C)**
Tetradecane	$CH_3(CH_2)_{12}CH_3$	~ 6 °C
Pentadecane	$CH_3(CH_2)_{13}CH_3$	~ 9 °C
Hexadecane	$CH_3(CH_2)_{14}CH_3$	~ 18 °C
Heptadecane	$CH_3(CH_2)_{15}CH_3$	~ 22 °C
Octadecane	$CH_3(CH_2)_{16}CH_3$	~ 28 °C

Table 4.2: **Melting points of different solvents, including hexadecane.**[255-259]

Upon submersing two droplets in hexadecane, they were then manually brought together using a small metal prong. Notably, as soon as droplets came into contact with one another an initiation point was obvious, from which the 'zipping up' of two monolayers in opposing directions to form a droplet interface bilayer (DIB) could clearly be monitored. The images in figure 4.7 illustrate DIB formation between two droplets containing DPhPC vesicle solutions. A movie of this event was captured and can be viewed using the CD accompanying this thesis (Movie 4.1, see section 4.3.3). Characteristic shadowing present on either side of the DIB was observed in every system described herein and is akin to observations made by others previously.[204] As reported by Funakoshi *et al.*, this phenomenon is thought to be due to refraction associated with differing membrane thicknesses in the vicinity of the DIB (i.e. monolayer vs. bilayer).[202] Hence, it was apparent that DIBs could be formed successfully, as determined using optical methods (electrical methods for assessing the formation of DIBs are not currently available in our laboratory).

As these experiments were performed by hand, it was found that the droplets required: (i) enough time for monolayer formation to occur and hence were left in the oil for 5-10 minutes prior to DIB formation and (ii) to be brought

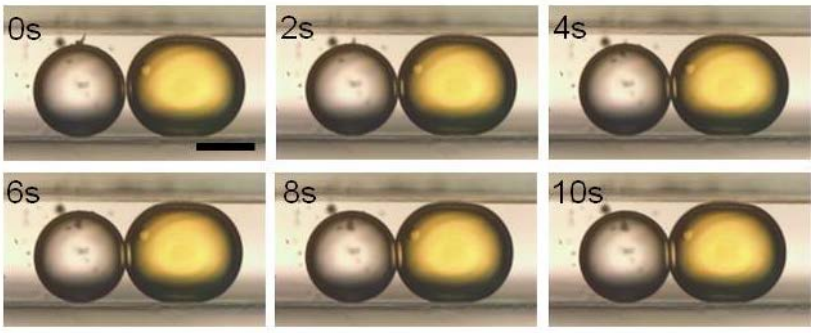


Figure 4.7: **Experimental evidence for the formation of droplet interface bilayers (DIBs).** The sequence of images displayed show two droplets participating in DIB formation. The scale bars represent 400 μm.

together with care (i.e. gently/slowly). Small droplets appeared to stick together very easily, most probably due to the heightened probability of lipid exchange with the interface and thus resulting in more rapid monolayer formation.

It was also confirmed that monolayers participating in DIB formation can be separated once formed, as has been reported elsewhere.[203] The reversibility of DIB formation is therefore of particular use as a mechanism for controlling a system, where commands of a "stop / start" nature may be employed.

4.4.1.2 DIB formation with different lipids: DPhPC versus DOPC

In addition to forming DIBs comprised solely of DPhPC, which has been the only lipid used in DIB production to date, it would be desirable to create DIBs that contain more biologically relevant lipids (or indeed mixtures of lipids) in order to expand their utility. For example, the use of DOPC would be highly relevant since this lipid has been the major lipid of choice in the biophysical assays described previously (in chapters 2 and 3). The chemical structures of DPhPC and DOPC can be viewed in figure 4.8, as well as an example of their ability to participate in DIB formation.

Inspection of figure 4.8 shows that DIBs formed using DOPC display comparable characteristics to DIBs comprised of DPhPC, as assessed using optical measurements. The characteristic shadowing effects reside in both

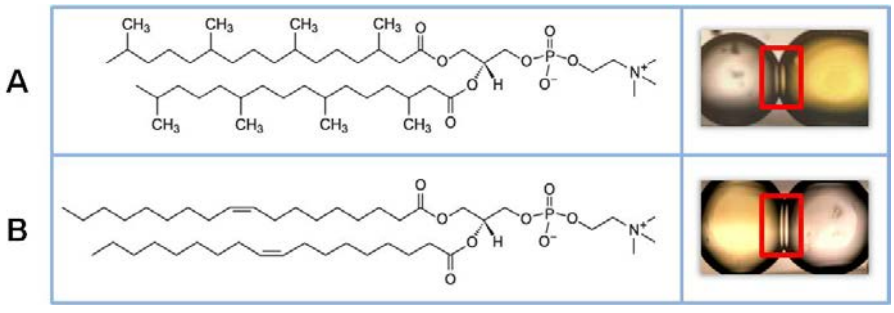


Figure 4.8: **DPhPC and DOPC for DIB formation.** (A) and (B) represent DPhPC and DOPC respectively. An exemplar image of DIB formation for each lipid type has also been included; red boxes indicate DIBs.

cases, indicating that DIB formation has been achieved (highlighted by the red boxes in figure 4.8). That is to say, droplets containing DOPC also form a 'seed' point upon initial contact of the two lipid monolayers, in an analogous manner to that of DPhPC, from which they proceed to zip up to form a droplet interface bilayer. The only experimental observations that were notably different when using DOPC included: (i) the time required to gain sufficient monolayer formation at the aqueous-oil interface and (ii) the lipid concentration used. Subsequently, droplets containing DOPC vesicle suspensions were left in the oil for a minimum of 15 minutes before any attempt was made to form a DIB, as otherwise the droplets simply merged, and a higher DOPC concentration was used to form DOPC DIBs.

Interfacial surface tension measurements were conducted as a means to understand these observations, providing a more quantitative indication of the extent of DPhPC / DOPC interaction at the aqueous-oil interface. Figure 4.9 summarises the interfacial surface tension measurements conducted with DOPC and DPhPC. One major observation that was made from these experiments included realising the extent to which DPhPC lowers the interfacial surface tension, as compared to DOPC, for vesicle suspensions composed from a solution with a lipid concentration equal to 0.2 mM. It was found that the presence of DPhPC results in a greater decrease in the interfacial surface tension, as illustrated by figure 4.9 A, therefore suggesting that DPhPC stabilises the interface more quickly than that of DOPC at this concentration. This concurs with experimental observations i.e. that for a fixed lipid concentration, it is not possible to form DOPC DIBs after only leaving the lipid-containing droplets in the oil for a few minutes.

It would have been interesting to have left the droplets for extended periods of time, to see if both vesicles samples reached the same interfacial surface tension values at equilibrium. However, the droplets were found to fall off after ca. 10 minutes (in the case of the buffer droplets / DOPC containing droplets) and 20 minutes (for the DPhPC containing droplets). As observed in

figure 4.9 A, the interfacial tension of the buffer drop alone decreases with time. This suggests that the gravitational pull on the droplet is far greater than that of the opposing interfacial tension (restorative force) and as such the droplets fall off the needle. It is possible to circumvent such a problem, which is typical of systems possessing lower surface tensions, by using larger needle diameters to support the required drop size. However the needle diameter used in this instance was already very large, and correspondingly could not be increased due to the limitation imposed by the camera's field of view. Nevertheless, these data do support and help explain the observations made experimentally.

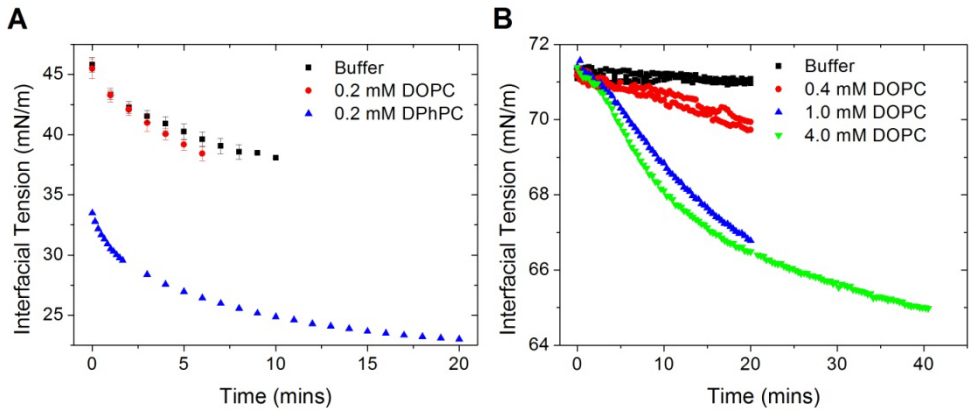


***Figure 4.9*: IFT measurements of DOPC and DPhPC.** Graph A demonstrates how IFT is affected upon introducing aqueous droplets of 0.2 mM DOPC and 0.2 mM DPhPC into hexadecane. Graph B demonstrates the effect of various concentrations of DOPC on the IFT in air.

Another experimental observation that has been made is that an increase in the concentration of lipid used per set volume appears to increase the propensity for DOPC DIB formation. It is therefore proposed that the lipid concentration used to form the DOPC vesicle suspension (0.2 mM) may not be high enough for the particular system measured on the drop tensiometer, displayed in figure 4.9 A. Perhaps the energetic requirement for DOPC

molecules in vesicles to convert to DOPC molecules residing at the interface is less favourable c.f. DPhPC molecules? Hence a higher concentration may be required in order to increase the chance of DOPC monolayer formation at the interface. DPhPC has been found to possess a negative spontaneous curvature (a numeric value could not be found in the literature),[260,261] owing to the presence of bulky acyl chains,[262] and is therefore a Type II lipid (see chapter 1, section 1.2.2.3). DOPC has a spontaneous curvature of approximately zero and is a Type 0 lipid. Therefore this suggests that vesicles comprised of DOPC will be less frustrated (i.e. possess lower levels of curvature elastic stress), c.f. vesicles comprised of DPhPC, and so do not have the same desire to depart from their vesicular form.

Surface tension measurements that were conducted with DOPC at the air-aqueous interface, thus omitting problems associated with taking interfacial surface tension measurements in hexadecane (see figure 4.9 B), support this hypothesis. In this instance it can be observed that a DOPC concentration of 0.4 mM reduces the IFT by only a few mN / m, whereas a 2.5-10 fold increase in the concentration results in a larger reduction in the surface tension. In fact, it appears that total surface coverage has been achieved with only a 2.5 fold increase in lipid concentration (i.e. 1.0 mM). Although this measurement has been taken at the air-aqueous interface it is feasible to extrapolate such results to the liquid-liquid system, where interactions between DOPC acyl tails and hexadecane are more favourable.

4.4.2 Proof-of-concept DIB-leakage experiments

As section 5.4.1 details, successful DIB formation can be attained both with DOPC and DPhPC. Therefore, it is desirable to use this system to further our understanding of the interaction of both synthetic and biological species upon lipid membranes. As such, it was thought interesting to develop a leakage assay for use across DIBs, which in turn can act as a measure of the extent of such

interactions. Here, proof-of-concept experiments are detailed, the principle idea for which involves developing an assay able to monitor proton leakage across a bilayer using a pH sensitive dye as a reporter. The illustrations presented in figure 4.10 demonstrate the principle behind this idea.

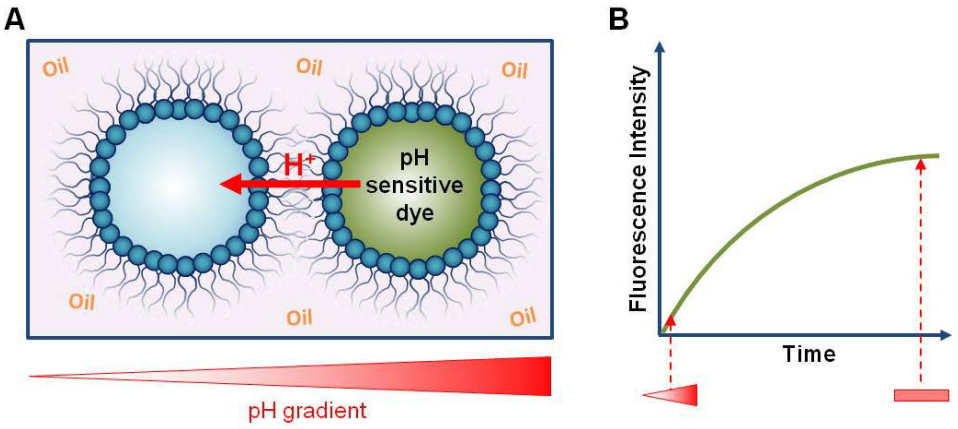


Figure 4.10: **Principle of DIB-leakage experiments.** (A) Diagram illustrating the theoretical set-up; two lipid-containing droplets in oil are brought together to form a DIB, one containing a pH sensitive dye at low pH and the other a buffer at high pH (thus creating a pH gradient across the bilayer). (B) An increase in the fluorescence intensity with time would occur if proton transport across the bilayer takes place, as illustrated by the graph, levelling off when the pH gradient diminishes.

4.4.2.1 Carboxyfluorescein

Initial experiments involved using the pH sensitive dye, CF (experimental information provided in section 4.3.2.3). Chapter 2, section 2.2.1 has discussed the properties of CF in detail, including specific details of self-quenching at high concentrations (millimolar regime). In this instance, the dye concentration is fixed and it is the change in environmental pH that is of interest.

The general format of these experiments involved bringing together two droplets containing DOPC, with the aqueous component of one droplet being at a higher pH than the other, in order to create a pH gradient across the DIB. It was decided to look for an increase in the fluorescence intensity, as opposed

to a decrease. Hence the dye was incorporated into the low pH droplet, as the fluorescence intensity of CF increases with decreasing proton concentration.[218] Figure 4.11 demonstrates the change in the average fluorescence intensity of the fluorescent droplets upon DIB formation (A) and alone (B).

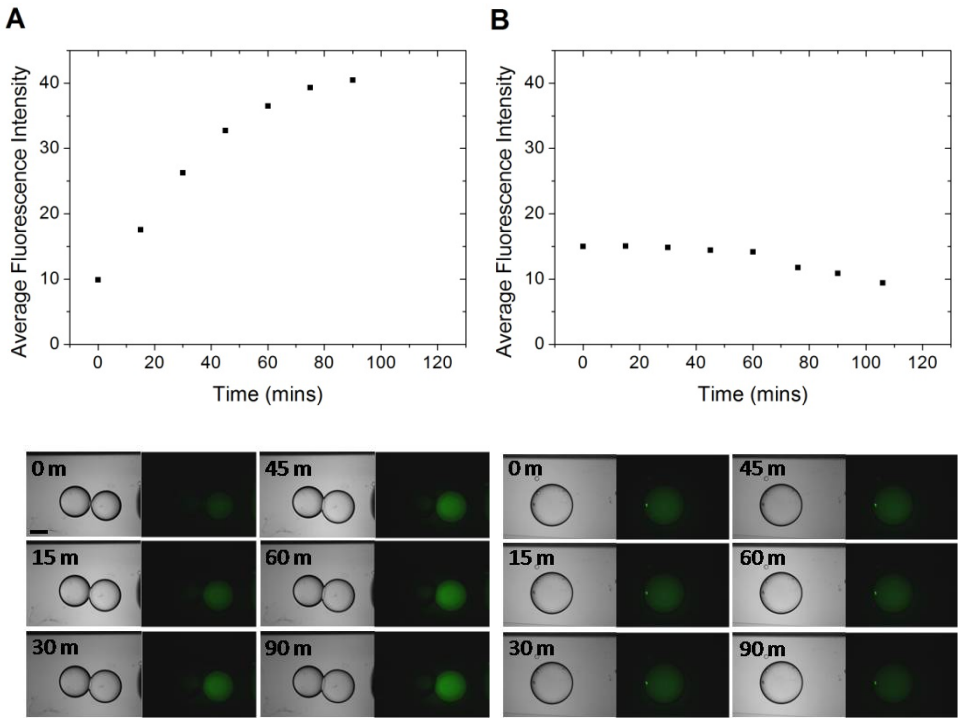


Figure 4.11: **Carboxyfluorescein as a pH sensor for use in leakage experiments across DIBs.** (A) Graph showing the change in the average fluorescence intensity of a CF-containing droplet (droplet on the right, made using solution 4.2, pH 4.6) after having formed a DIB with a non-fluorescent droplet (droplet on the left, made using solution 4.3 pH 8). The corresponding bright field and fluorescence microscopy images are displayed below the graph. (B) Graph and images illustrating that the average fluorescence intensity of a CF-containing droplet in oil alone (i.e. not participating in DIB formation) does not increase. Scale bar represents 400 μm. See section 4.3.1.2 details about the nature of the solutions used.

Note that the average fluorescence intensity of the control droplet initially is higher than that of the fluorescent droplet participating in DIB formation as it is larger in volume.

The decision to monitor an increase in the fluorescence intensity was taken as a means to act as an internal control. If proton loss to the oil is occurring, then an increase in the fluorescence intensity of lone droplets present in the oil

environment would be observed. It is important to note here that for all control experiments associated with the experiments presented in this chapter, there were no instances where the fluorescence intensity of a dye-containing droplet increased when present in the oil alone (i.e. if not participating in DIB formation with another droplet). The fact that an increase in the fluorescence intensity is only observed when a DIB is formed informs one that the setup is effective in measuring proton transport.

However, the average fluorescence intensity of a CF-containing droplet was found to diminish alone, having not been illuminated with the relevant excitation wavelengths previously (see figure 4.12 A & B). Therefore it was concluded that it must be the dye that is leaching out of the droplet and into the oil, due to the protonation and neutralisation of CF, therefore making it more hydrophobic so it can cross the membrane. This observation was supplemented by control data measured using the spectrophotometer (two experimental repeats were conducted). Specifically, aliquots of the CF-containing aqueous solution at pH 4.6 (solution 4.2, see section 4.3.1.2), and also an analogous solution at pH 8 (solution 4.4, see section 4.3.1.2), were placed in contact with the oil and left for one week. The results indicate that the fluorescence intensity of the aqueous fraction at pH 4.6 was greatly diminished when compared to the original aqueous sample, whereas the fluorescence intensity of the aqueous fraction at pH 8 did not differ to the control (see figure 4.12 C and D). Furthermore, when the two droplets displayed in figure 4.12 A and B were brought into contact with one another to form a DIB the average fluorescence intensity started to increase, but subsequently proceeded to diminish shortly afterwards at approximately 50 minutes (see figure 4.12 E, F and G). These results suggest that CF may not be the most suitable dye for use in this application, and as such the decision was taken to use another dye, specifically pyranine.

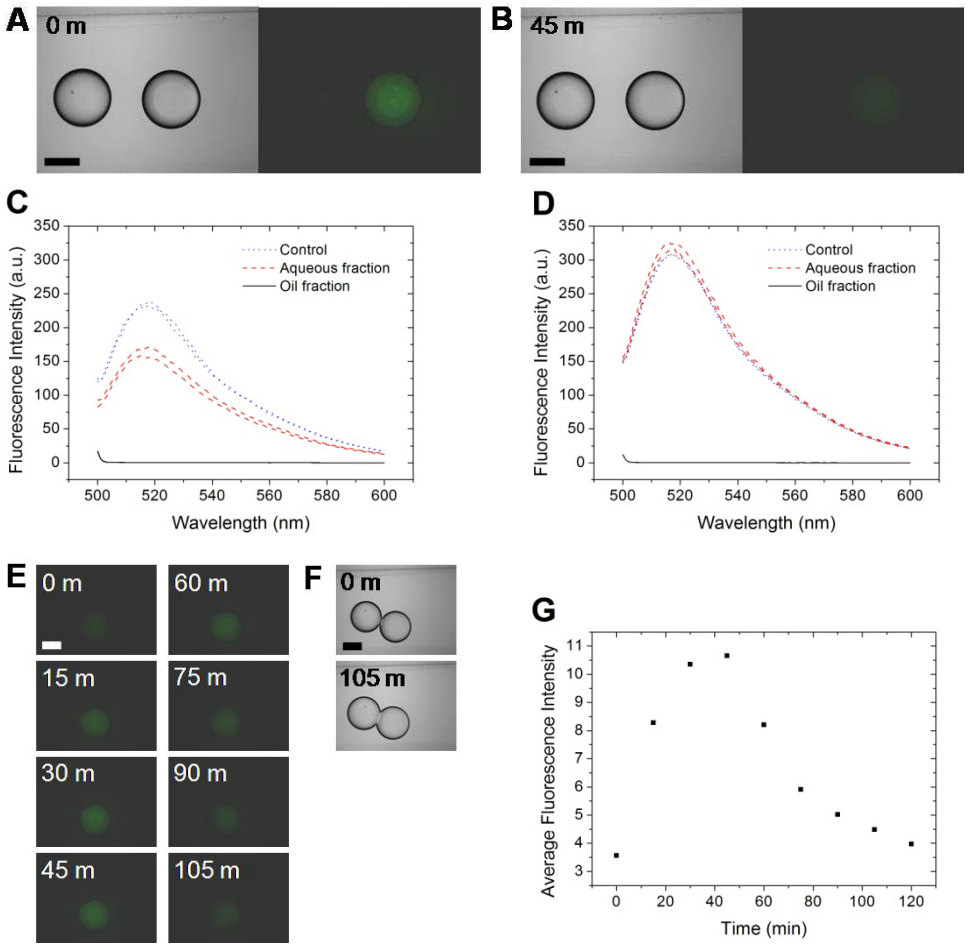


Figure 4.12: **Evidence for carboxyfluorescein leakage into the oil phase.** The average fluorescence intensity of a CF-containing aqueous droplet (solution, 4.2, pH 4.6) in oil diminished after having been left in the dark for ca. 45 minutes; the images in (A) and (B) show the fluorescent droplet at 0 m and 45 m respectively. This data was substantiated with control experiments conducted on the fluorimeter. Aliquots of CF-containing solutions at pH 4.6 (solution 4.2) and pH 8 (solution 4.4) were left in contact with oil for one week; the emission spectra (excitation at 490 nm) for the aqueous and oil fractions (denoted by "Aqueous fraction" and "Oil fraction" respectively) are displayed in (C) and (D) for the pH 4.6 and pH 8 tests respectively. The aqueous fractions were compared to the original solutions, i.e. those that had not been left in contact with oil (denoted "Control"), as illustrated in C and D. Additionally, upon bringing the CF-containing droplet (right-hand droplet, pH 4.6) into contact with the non-fluorescent droplet (left-hand droplet, made using solution 4.3, pH 8) to form a DIB ((E) represents the fluorescence microscopy images and (F) the brightfield images at various time points), the average fluorescence intensity increased initially but shortly arrested, as illustrated quantitatively in graph (G). Scale bars represent 400 μm. See section 4.3.1.2 details about the nature of the solutions used.

4.4.2.2 Properties of pyranine

Pyranine, 8-hydroxypyrene-1,3,6-trisulphonic acid, is a pH sensitive fluorophore that has the advantage of being very economical, extremely water soluble and membrane-impermeable. The latter two points are highly desirable and are predominantly due to the presence of three strongly acidic sulfonate groups, ensuring that the molecule remains ionised over an extended range of pH values.[263] Figure 4.13 illustrates the chemical structure of this dye.

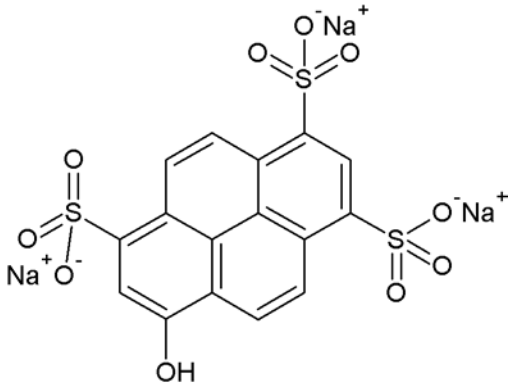


Figure 4.13: **Chemical structure of pyranine, 8-hydroxypyrene-1,3,6-trisulphonic acid (trisodium salt).**

As an initial starting point, aqueous, pyranine-containing samples (solutions 4.5-4.9, see section 4.3.1.2) were prepared and their fluorescence properties explored at a variety of different pH values. After exciting the samples at 460 nm, an unexpected relationship between the observed fluorescence intensity and pH was found to exist, when compared to the published Invitrogen™ literature (see figure 4.14 A and B respectively).[264] Specifically, the emission maximum at 510 nm first increased with pH (from pH 4 to 6), after which a decrease in the fluorescence intensity was observed (most prominently from pH 6 to pH 7). Upon viewing the excitation spectra (fixed emission at 510 nm) it was found that the nature of the spectra, both above and below the

isosbestic point at 405 nm, differed quite substantially to the published literature. For example, it was found that the main peak present within the 400-500 nm region is actually comprised of two peaks, whose intensities change in an opposing manner to one another upon changing the pH. Consequently, it was decided that a system comprised solely of pyranine in water should be investigated.

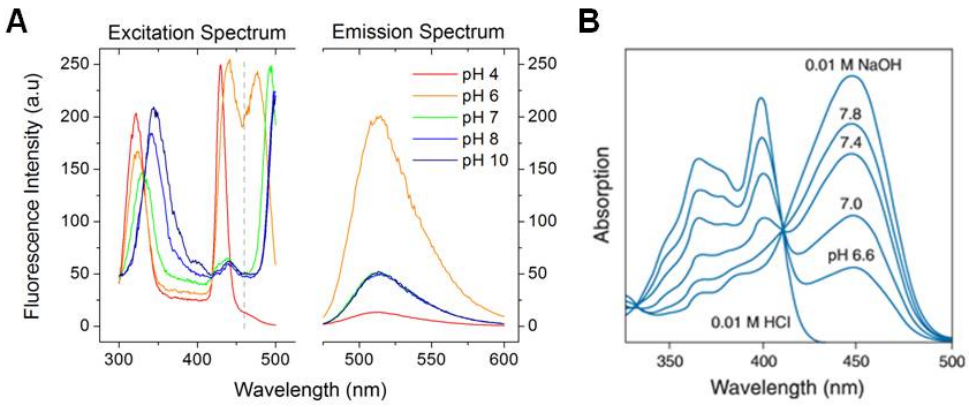


Figure 4.14: **Fluorescence properties of pyranine solutions.** (A) Excitation and emission spectra for a 1 mM pyranine solution measured at different pH values (solutions 4.5-4.9, see section 4.3.1.2) are displayed. An emission wavelength of 510 nm was used to generate the excitation spectrum. An excitation wavelength of 460 nm was employed to gain the emission spectrum, as indicated by the dotted line on the excitation spectrum. (B) Absorption spectra for a variety of pyranine solutions, as published on the Invitrogen™ website.[264]

Upon diluting a 1 mM stock solution of pyranine in water (solution 4.10), it was found that the excitation spectrum (gained using a fixed emission wavelength of 510 nm) was strongly dependent upon the concentration of pyranine in solution, the results of which are displayed in figure 4.15 (green curves). The most notable features present in these graphs is the change in the nature of the peaks(s) present in the 350-400 nm region upon dilution, where an inversion occurs at approximately 125 μM. This effect can be observed more clearly in figure 4.15 A and B (two repeat experiments), where the spectra have been collated and the regions of interest highlighted with circles.

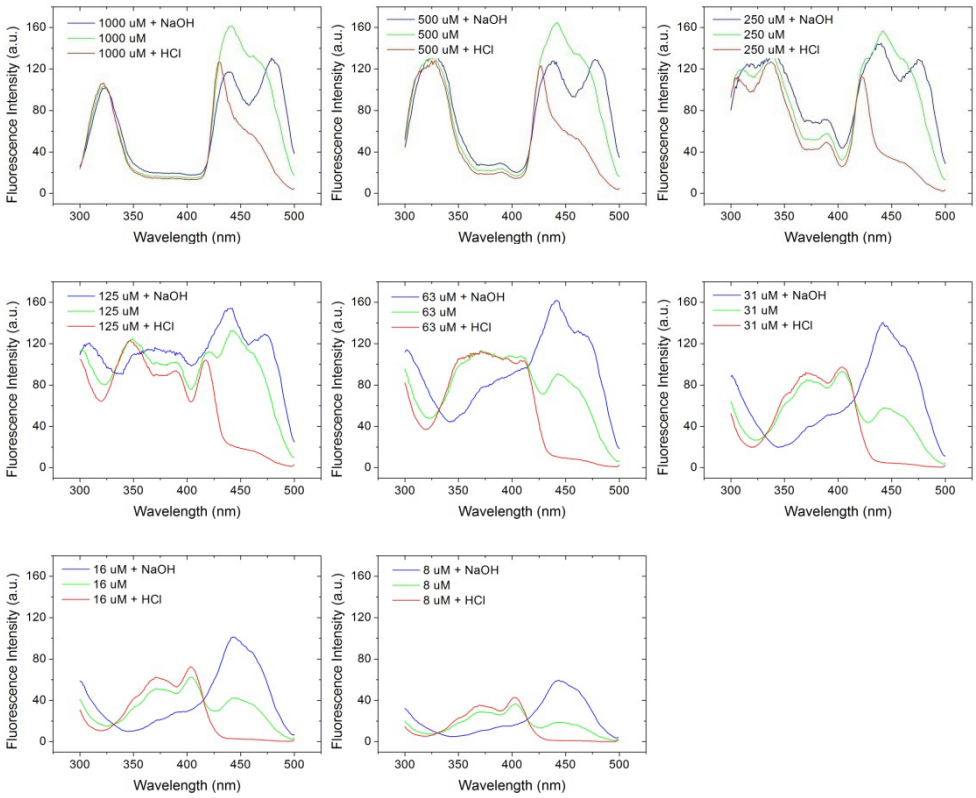


Figure 4.15: **The dependence of pyranine's excitation spectrum upon its concentration and pH in water.** The excitation spectra displayed in this figure, attained using a fixed emission wavelength of 510 nm, illustrate how the nature of pyranine's excitation spectrum is influenced by the concentration of pyranine in water, as well as the presence of both acid and alkali.

The effect of adding both acid and alkali to the system was also monitored for each concentration, as illustrated in figure 4.15. Upon adding acid, the peak present in the 425-500 nm region of the excitation spectrum subsides relative to the original trace (see also the collated spectra in figure 4.16 C). When the pH is raised, this peak increases in intensity with respect to the original trace, for samples below 125 μM, and interestingly splits into two (see figure 4.16 D for collated spectra). This was observed previously in figure 4.14 and is particularly important for choosing suitable excitation filters in fluorescence microscopy.

Additionally, the increase in the peak intensity in the 425-500 nm region observed under alkaline environments (relative to the original trace) is coupled

with a concomitant decrease in the peak intensity in the 350-400 nm region (relative to the original trace). This phenomenon is *only* observed at dye concentrations below 100 μm. The reverse situation (i.e. a decrease occurring concomitantly with an increase of the peak intensities) is observed under acidic environments and again is also only true for this concentration range, though the effect is less prominent. Hence it appears that the typical behaviour of pyranine, where the peak intensities above and below the isosbestic point exist as part of a symbiotic relationship, is only valid for systems within a certain concentration range. Therefore pyranine concentrations less than 100 μM have been employed in all current experiments.

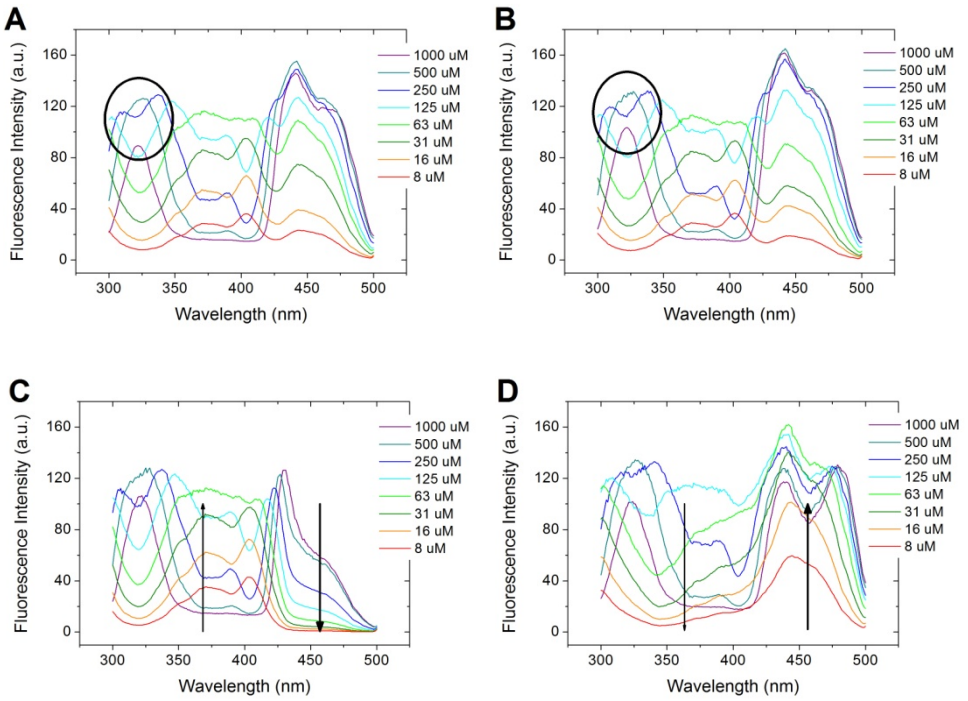


Figure 4.16: **Collated excitation spectra for serially diluted 1 mM pyranine stocks (in water) and in the presence of acidic and alkaline conditions.** (A) and (B) Graphs representing the excitation spectra (gained using a fixed emission wavelength of 510 nm) of 1 mM pyranine stock solutions serially diluted in water (two experimental repeats). The highlighted regions (circles) indicate the point at which the peak in the 350-400 nm region inverts. (C) and (D) Graphs illustrating the effect of introducing both acid and alkali solutions to each pyranine concentration respectively, in order to monitor the changes in fluorescence properties (excitation spectra, gained using 510 nm fixed emission). The arrows indicate the general direction of peak movement upon addition of acid or alkali, when compared to the original traces.

4.4.2.3 DIB leakage assay with pyranine

The first attempt at performing the leakage assay with pyranine as the fluorescent pH indicator involved using an 60 μM aqueous pyranine solution (solution 4.11, pH 5.5, see section 4.3.1.2) to form the 'fluorescent droplet'. As expected, an increase in the average fluorescence intensity was obtained, after having formed a DIB with another droplet containing an aqueous compartment at pH 8 (solution 4.3, see section 4.3.1.2), therefore indicating that the pH of the pyranine-containing droplet is changing with time.

In this instance, however, the DIB collapsed after approximately one hour (see figure 4.17 A and B), which in retrospect can be attributed to an imbalance in osmolarity across the membrane; the non-fluorescent droplet (pH 8) contains 200 mM KCl, which the fluorescent droplet does not. This always occurred when repeat experiments were attempted. Further evidence to support this includes the observation that the pyranine-containing droplet was found to decrease in size (by approximately 36 %) after 35 minutes (see figure 4.17 B). A decrease in the droplet volume is not normally observed as the droplets reside on the bottom of the device, owing to the aqueous phase being more dense than the oil phase. Hence a net movement of water across the DOPC bilayer is taking place due the high concentration of potassium chloride present on the opposite side of the membrane. This concurs with the deviation away from linearity, observed and indicated in the graph presented in figure 4.17 A, where the concentration of pyranine effectively increases with time. As previously determined (see figure 4.16 A and B), an increase in pyranine concentration leads to an increase in fluorescence intensity in the region that is being monitored here (460-490 nm). Note that the fluorescence intensity remains constant after the two droplets have merged and is lower than may be expected due to the dilution of pyranine.

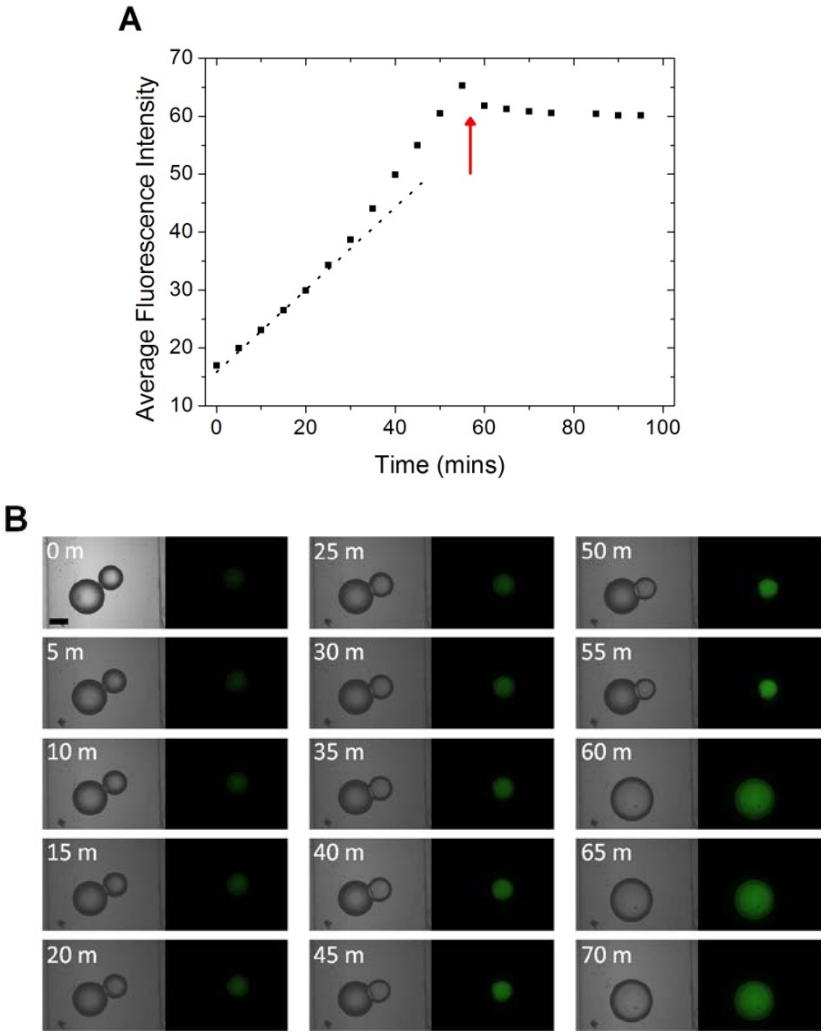


Figure 4.17: **First attempt at performing a DIB leakage assay, using a 60 μM aqueous pyranine solution (solution 4.11, pH 5.5, section 4.3.1.2).** (A) Graph representing the average fluorescence intensity of each pyranine-containing droplet displayed in (B) (right-hand droplets). Note that the bright field and fluorescence microscopy images at t > 70 m are not displayed. The droplets merged after ca. 60 m due to a difference in osmolarity across the bilayer, as indicated by the red arrow in (A), and the average fluorescence intensity found to deviate away from linearity (indicated by the dotted line in (A)) at t ~ 35 m. Scale bar represents 400 μm.

The aforementioned merging event is an important observation, providing further evidence to support the presence of a lipid bilayer between the two droplets, and moreover, that transport across the bilayer is achievable and can be monitored. However in order to make the system more robust and prevent

droplet merging, the presence of salt is required on both sides of the membrane.

Consequently an aqueous solution was prepared, incorporating an analogous concentration of salt to that of the high pH droplet (200 mM KCl, solutions 4.12 and 4.3 respectively, see section 4.3.1.2), to ensure that the osmolarity across the membrane is balanced. Figure 4.18 A illustrates that the properties of this fluorescent solution behave as expected when the pH of the solution is changed. Additionally a linear relationship exists between the observed fluorescence intensity and pH, as illustrated by the graph in Figure 4.18 B.

Control experiments, assessing the tendency of pyranine to leak into the oil phase, were also performed with this solution (see figure 4.18) and conducted in the same format as described previously for CF-containing solutions (see figure 4.12 and section 4.3.2.4). Both the pH 5.5 and pH 8 analogues of the pyranine-containing aqueous solution were tested over a period of a week, the results of which are displayed in figure 4.18 C and D respectively. These results indicate that no discernable leakage of the dye from the aqueous phase and into the oil phase is observed.

A major problem associated with past experiments conducted within this chapter concerns the ability to compare results from one experiment to the next. This problem arises from the variability in droplet size gained when they are pipetted into the oil. Therefore it is proposed that the use of ratiometric measurements can offer a potential solution to this problem, where the results should be independent of droplet size. Note that this statement assumes that the system is identical in every other manner during each experiment, such as the ratio between droplet volumes on either side of the DIB and DIB contact area for example. Hence, a second reason for choosing pyranine is that it also offers the opportunity to conduct ratiometric fluorescence measurements. Excitation of the dye in the regions between 330-380 nm and 460-490 nm

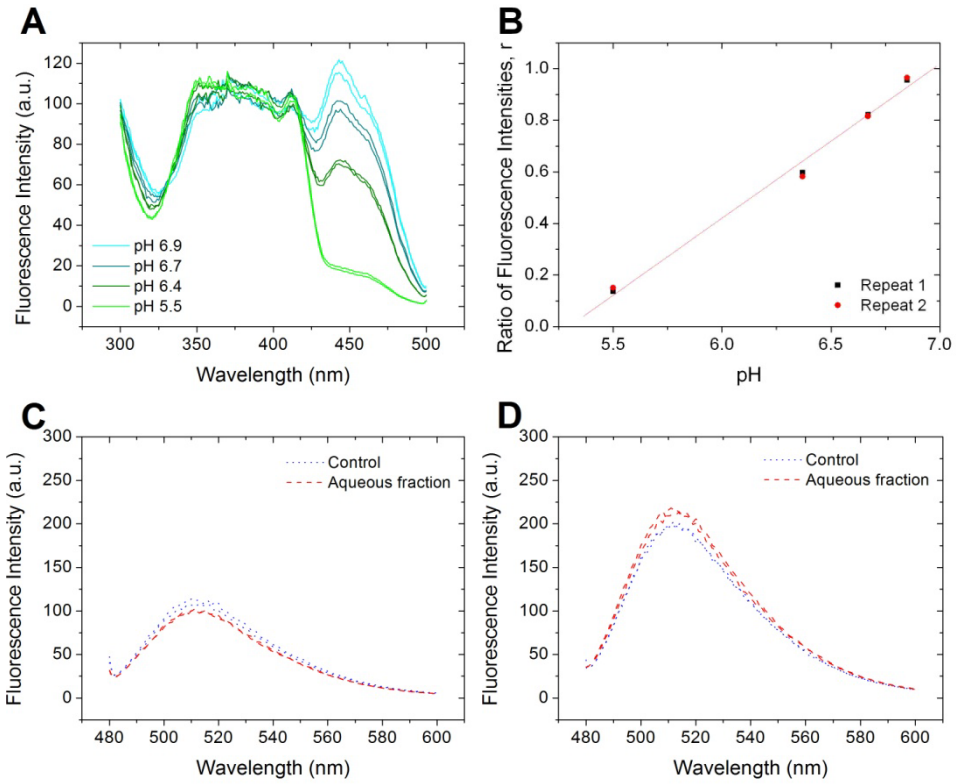


Figure 4.18: **Dependency of excitation spectra on sample pH for 60 µM pyranine-containing solutions, plus control experiment.** (A) Graph representing the excitation spectra (gained using a fixed emission wavelength of 510 nm) of a pyranine-containing solution at different pH values (solutions 4.12-4.15), with graph (B) indicating that a linear relationship exists between the ratio of fluorescence intensities, r, (see equation 4.1, section 4.3.2.6) and pH (conducted on a spectrophotometer). Graphs (C) and (D) represent control experiments conducted on the fluorimeter to test for loss of pyranine to the oil at pH 5.5 and 8 respectively. Aliquots of pyranine-containing solutions at pH 5.5 (solution 4.12) and pH 8 (solution 4.16) were left in contact with oil for one week. The aqueous fractions that had been left in contact with the oil (denoted "Aqueous fraction") were compared to the original solutions (denoted "Control" – these had not been left in contact with oil). These emission spectra were collected using an excitation wavelength of 475 nm. See section 4.3.1.2 details about the nature of the solutions used.

results in a change in the fluorescence emission at 510 nm, with the fluorescence change of the former being very subtle compared to the latter (figure 4.18 A).

Figure 4.19 represents the analysed data for three DIB leakage experiments, using ratiometric fluorescence measurements, as well as the control experiments (seven repeats, taken on at least three different days, with three

different sample populations and at different times of the day). Appendix 13 provides specific information about each of the droplets participating in DIB formation, displayed in figure 4.19 (numbered 1-6, the fluorescent droplet is represented by even numbers); droplet diameter, volume and DIB contact area are included. Appendix 14 contains each of the bright field and fluorescence microscopy images of the droplets participating in DIB leakage experiments plus one control experiment.

It can be observed that three distinct relationships, between the ratio of fluorescence intensities and time, are represented by the data presented in figure 4.19. The first relates to the control system, represented by the black data in figure 4.19.

The control experiments yield a flat base line; hence it is apparent that the ratio between each of the average fluorescence intensities does not change within the population sampled (over a period of nearly three hours). Upon forming a DIB between two aqueous droplets, one of which contains pyranine (the even numbered droplets in figure 4.19), the ratio of fluorescence intensities deviates from the control. Three DIB experiments are detailed, though two different relationships, between the ratio of fluorescence intensities and time, can be identified in these data. These are the second and third relationships alluded to previously, and are represented by: (i) the red and orange curves and (ii) the blue curve displayed in figure 4.19 respectively.

Upon analysing the droplet properties, it can be observed that the volumes of droplets 1 and 3 (0.17 and 0.18 μl respectively, see Appendix 13) are approximately the same, as are the volumes of droplets 2 and 4 (0.11 and 0.09 μl respectively). Furthermore, the DIBs formed between each of these pairs of droplets are approximately equal in area (ca. 1 E-04 cm^2). Hence, they should portray the same leakage characteristics; this is certainly apparent when viewing the relevant curves in figure 4.19 (the red data points relate to droplet 2, with

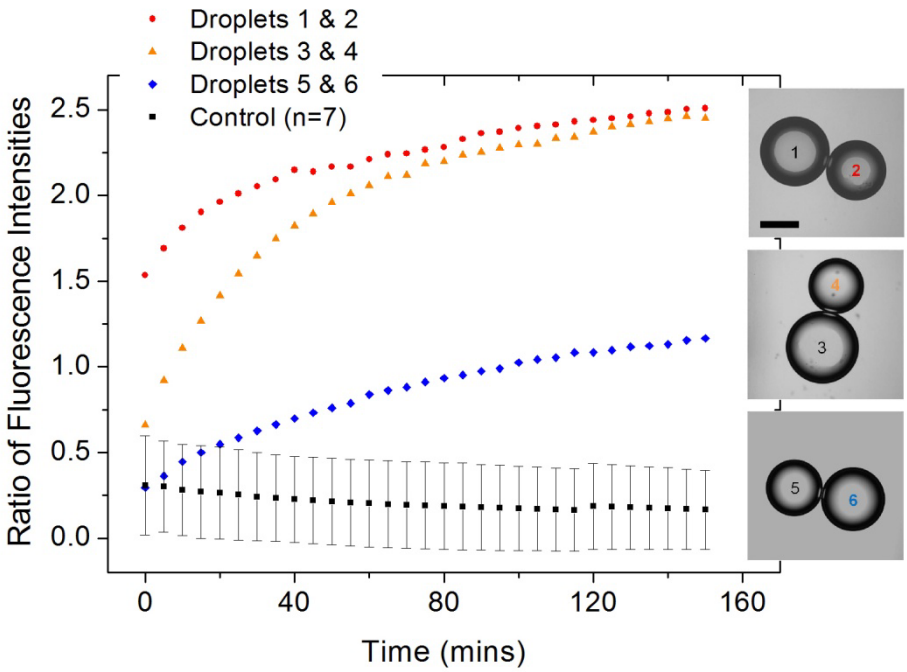


Figure 4.19: **Observed relationships between the ratio of pyranine fluorescence intensity and time for different DIB systems (including control).** The control experiment (black data points) represents the first relationship observed, i.e. a flat baseline, thus indicating that there is no proton leakage throughout the duration of the experiment. Droplets 1 and 2 (red data points) and droplets 3 and 4 (orange data points) represent the second observed relationship, where the fluorescent droplet is always smaller than the non-fluorescent droplet. Droplets 5 and 6 (blue data points) represent the third observed relationship, where the fluorescent droplet is larger than the non-fluorescent droplet. Specific information about the droplet properties (droplet diameter, DIB contact area and droplet volume) is afforded in Appendix 13. Scale bar represent 400 μm.

the orange data points relating to droplet 4). Although there are differences in the initial rate of change, where ambiguities may be introduced due to uncontrollable factors, such as the time taken to complete DIB formation, the curves ultimately tend towards the same value as the system reaches equilibrium.

The third relationship can be identified by the blue data points in figure 4.19 and refers to the situation represented by droplets 5 and 6 in figure 4.19. In this instance, it is the larger droplet of the two which contains fluorescent

pyranine (droplet 6). The response attained for this situation reflects the nature of the DIB system. Note that the DIB contact area formed between droplets 5 and 6 is approximately the same as those formed between droplets 1 and 2, and 3 and 4.

The variation in the observed trends for proton leakage between droplets 5 and 6, and 1 and 2, for example (blue and red data points respectively, illustrated in figure 4.19), arises due to differences in the relative volumes of the fluorescent and non-fluorescent droplets present on either side of the DIB. The non-fluorescent droplet is only 62 % of the volume of the pyranine-containing droplet, if you consider droplets 5 and 6 respectively (0.08 μl and 0.13 μl, see Appendix 13). Conversely, droplet 1 (non-fluorescent, 0.17 μl) is ca. 160 % of the volume of droplet 2 (pyranine containing, 0.11 μl). Hence the kinetics associated with proton transfer across each DIB, and thus pH, will differ. Although initially this observation could be seen as a disadvantage, the observation could actually be used to one's advantage, providing the ability to tune the system to suit a specific need. Two factors that could easily be manipulated include: (i) droplet volume and (ii) the size of the DIB contact area.

If, for example, the volume of the non-fluorescent droplet and DIB contact area are fixed, and only the volume of the fluorescent droplet is altered, two important factors will change: (i) the time taken to reach equilibrium (where the proton concentration on either side of the DIB is equal) and (ii) the magnitude of that equilibrium value. If the volume of the fluorescent droplet is smaller than the volume of the non-fluorescent droplet, the time taken to reach equilibrium will be reduced, compared to the reverse situation (where the volume of the non-fluorescent droplet is larger than the fluorescent droplet). Furthermore, the magnitude of the equilibrium value will be greater for the former situation (where the volume of the fluorescent droplet is smaller than the volume of the non-fluorescent droplet). The same number of protons will transport across the DIB contact area per unit time in both situations, however

this will translate to a bigger change in the pH with time for the fluorescent droplet that is of a *smaller* volume and equilibrium will be reached more quickly. Hence, changes in the relative droplet volumes (for a set DIB contact area) can lead to subtle differences in the kinetic properties of these systems.

The other factor that can be altered in order to manipulate the rate of proton leakage involves changing the area of the droplet interface bilayer. An increase in the area of the droplet-droplet contact area (i.e. DIB), where the droplet volume on either side of the DIB remains constant, will result in an increase in the rate of change of proton transfer. The converse situation also holds. Note that the same equilibrium pH value will be afforded as an analogous system containing a smaller contact area.

It is also important to note that the rate of proton transfer observed in the experiments detailed in figure 4.19 is slow, in comparison to vesicular systems detailed in the literature.[265] However, this is unsurprising, when considering the extremely small area (ca. 1 E-04 cm^2) through which proton permeation is occurring in these DIB systems, compared to the combined surface area of a suspension of vesicles (> 2600 cm^2).[265] It would be interesting to determine whether flux is comparable between DIBs and vesicles. However, owing to the variety in experimental conditions employed in the literature (lipid type, pH gradient etc.), the best way in which to determine this would be to conduct a vesicle leakage assay using analogous experimental conditions c.f. the DIB assay.

4.4.2.4 Limitations of method

Sections 4.4.2.1, 4.4.2.2, 4.4.2.3 and 4.4.2.4 have detailed the various steps involved in setting up a proton leakage assay for monitoring small molecule-membrane interactions. However, it is important to stress that there are some key issues that need to be addressed before further work is attempted.

The first issue that needs to be tackled involves the control of droplet size. The ability to control droplet size using this system, and hence the droplet interface

bilayer area, is a major issue. As discussed previously, and demonstrated by the last set of experimental results in figure 4.19 (section 4.4.2.3), the size of the droplets taking part in DIB formation will ultimately affect the kinetics of the system (i.e. the rate of proton transfer). Therefore in order to ensure that comparable, reproducible data is collected, a system whereby uniform droplet size can be attained is desirable: it was found extremely hard to maintain a constant droplet size and manoeuvre the droplets using manual manipulation. Implementation of a controlled system for droplet generation would mean that each experiment is performed in an equivalent environment, where the droplet properties can be highly conserved between experiments.

Another issue which is of importance, if this assay is to be implemented in future investigations, includes increasing the experimental throughput. This is paramount, as it currently takes a long time to set up each DIB experiment using manual manipulation. The number of experimental repeats would ideally have to be increased substantially in order to fully characterise the system: the ability to produce and bring droplets together in quick succession would provide a good way in which to increase the number of experimental repeats. In turn this would mean that factors that are difficult to control, such as the droplet size and area of the DIB, could be managed more easily c.f. the manual method. Additionally, if the droplet size can be controlled, then the rate of proton leakage can be reliably tuned by tuning the size of droplets on either side of the DIB. A system that could offer these options would be highly beneficial, opening up various new avenues for experimental design.

One limitation concerned with the leakage aspect of these proof-of-concept experiments involves monitoring the effect of a particular species upon *different* lipid bilayer compositions. Composition will affect bilayer thickness, which in turn will affect the permeability coefficient of H^+.[266] Also, it has been reported that the rate of proton transfer can significantly differ to what would be theoretically expected, upon the incorporation of different lipids: Gensure *et al.*[265] state that the inclusion of cholesterol into a lipid bilayer results in a

significant *increase* in the rate of proton transfer, opposing initial hypotheses. Ultimately, this has to be controlled for when making comparisons between data sets of the same molecular species acting upon different membranes.

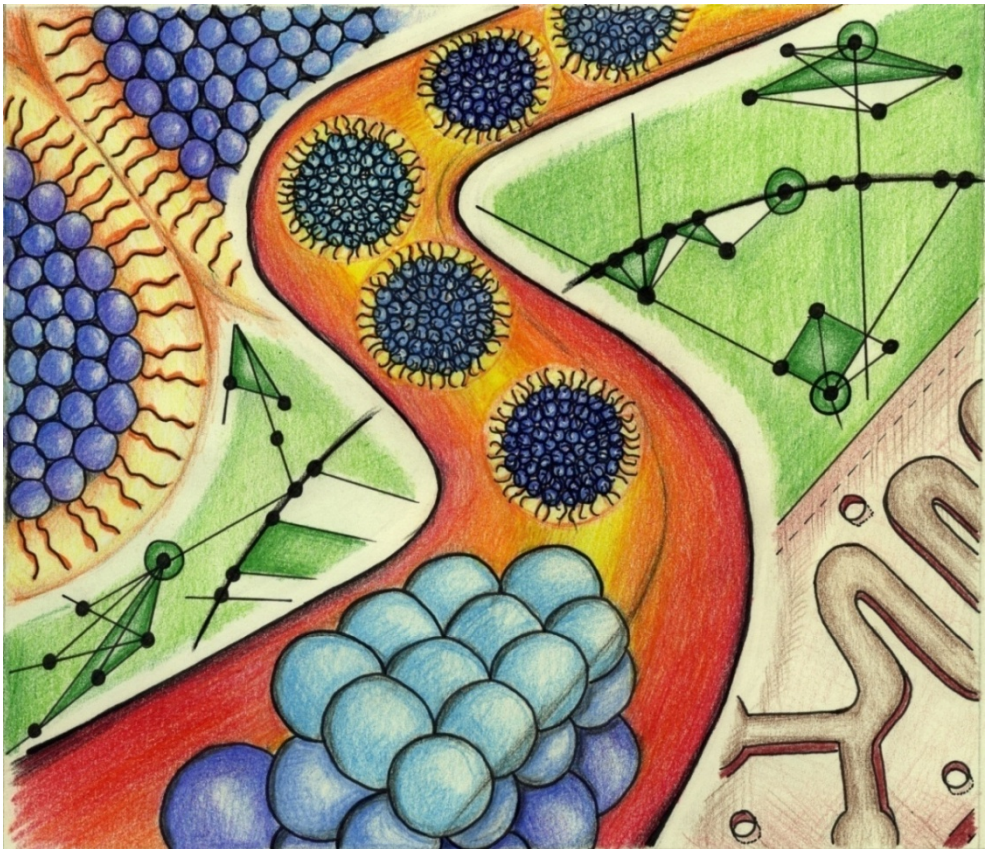
4.5 CHAPTER SUMMARY

In summary, chapter 4 has demonstrated that the formation of DIBs with DPhPC is reproducible. Additionally, it has been demonstrated that DIBs may also be comprised of more biologically relevant lipids, such as DOPC. The inclusion of more biologically relevant lipids in DIB systems is particularly important, with respect to investigating the effects of exogenous species on different lipid combinations.

Chapter 4 has also detailed the various steps involved in the development of a proof-of-concept leakage assay, employing pH gradients, which has the potential to be used to monitor (indirectly) the extent to which the membrane is perturbed by exogenous species. The limitations surrounding the practical approach used to achieve DIB formation in this chapter, i.e. the manual manipulation of droplets, have been discussed. The major issue surrounds the fact that droplet size, and hence the area of the DIB, cannot easily be controlled and ultimately affects the rate of proton leakage. Hence, a technique that can control droplet size, as well as increase the throughput of experiments performed, is highly desirable. The issues discussed in this chapter (section 4.4.2.4 therefore provide the rationale for chapter 5, which details a microfluidic approach for the high-throughput formation of droplet interface bilayers.

Chapter 5

A microfluidic approach for high-throughput droplet interface bilayer (DIB) formation



"Art is science made clear."

Wilson Mizner

Elements of the work contained within this chapter have been published in the journal Chemical Communications. The artwork presented here (designed and drawn by C. E. Stanley) was also accepted and published as the inside cover for the issue in which the aforementioned work was published.[213]

C. E. Stanley *et al.*, *Chem. Commun.*, 2010, **46**, 1620–1622

5.1 OVERVIEW

This chapter presents the development of a microfluidic approach for the formation of droplet interface bilayer (DIB) networks in a high-throughput and controlled manner. Specifically, an automated system has been set-up, where the size of water-in-oil droplets participating in DIB formation is highly uniform and tuneable. Additionally the ability to form three dimensional DIB networks, where droplets are able to fill predefined structures of any desired shape or size, and the possibility for asymmetric DIB formation has been demonstrated. Elements of the work contained within this chapter have been published in the journal Chemical Communications.[213]

5.2 INTRODUCTION

Since the advent of DIB technologies in 2006, several advances have been detailed with respect to enhancing their screening capacity. These have included the use of microfluidic principles, electrical methods for the movement of droplets as well as other, more high-throughput, approaches.

5.2.1 Use of mechanical pumping for bilayer formation

The first systems to use 'microfluidic' concepts, i.e. mechanical pumping of fluids through microchannels, to form lipid bilayers were published in papers by Malmstadt *et al.*[267] and Funakoshi *et al.*[202] in 2006. Although technically DIBs were not formed using these methods (as the fluid either side of the bilayer is not contained within a droplet surrounded by a monolayer of lipid), nevertheless this work instigated the idea to utilise microfluidic tools for DIB formation. Two device set-ups were detailed: both involved pumping two aqueous streams through microchannels in opposing directions, towards one another (see figure 5.1).

The device by Malmstadt *et al.* relies on solvent extraction through PDMS to bring the two lipid-containing interfaces into contact with one another, as illustrated in figure 5.1 A. Although this was a pioneering study, the complicated device set-up only accommodates one lipid bilayer per device and the aqueous chambers are relatively large. Moreover, no comments on the stability of the bilayer were made. The approach described by Funakoshi *et al.* essentially achieves the same goal, but using a far simpler device design. Their device is made out of poly(methyl methacrylate) (PMMA) and so does not rely

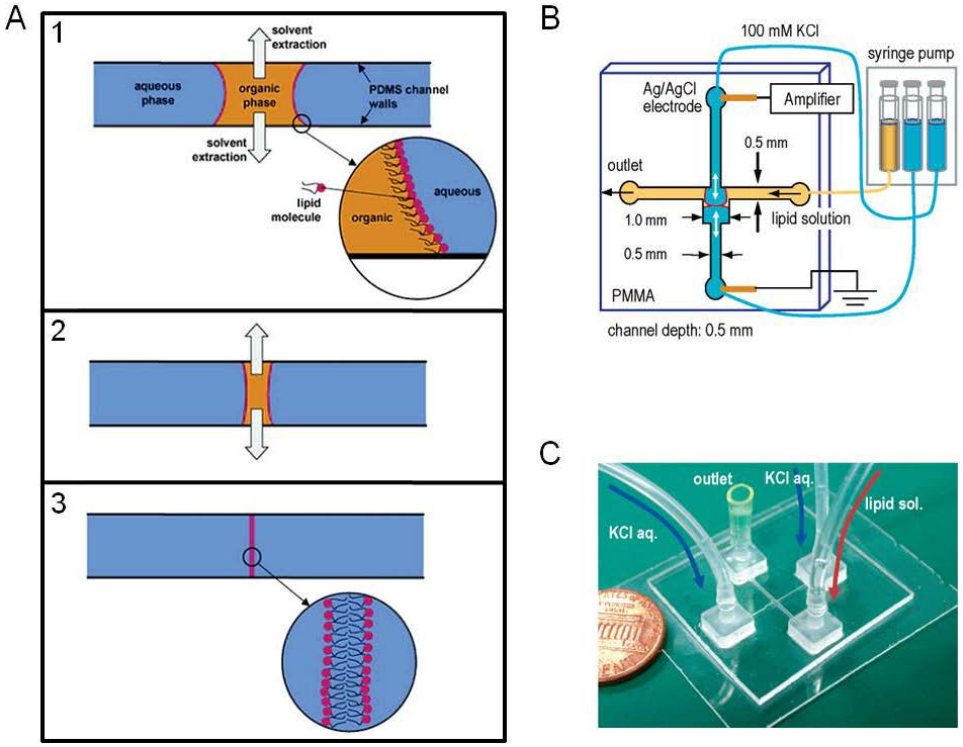


Figure 5.1: **Devices for forming artificial lipid bilayers using microfluidics.** (A) This device relies on solvent extraction through poly(dimethylsulfoxane) (PDMS) for bilayer formation, as illustrated in images 1-3. (B) This device utilises a cross-channel chip made of poly(methyl methacrylate) (PMMA); the process of bilayer formation is illustrated. (C) A photograph of the device displayed in B. Images reproduced from Malmstadt *et al.*[267] and Funakoshi *et al.*[202]

on solvent extraction; rather, it simply pumps two aqueous streams towards one another, in the presence of a lipid-containing oil stream (see figure 5.1 B and C). This system is advantageous as the bilayer interface can quickly be discarded and a fresh bilayer reformed, meaning that successive experiments can be conducted with ease.

5.2.2 Formation of DIB networks

In addition to forming experimental platforms that possess one lipid bilayer for interrogation, of which the first DIB systems were described by Funakoshi *et al.*[202] and Holden *et al.*,[203] the formation of DIB networks has also been achieved.[203,206]

Figure 5.2 A illustrates the concept of a DIB network. Simply, many lipid-containing droplets are submersed in an oil environment and brought into contact with one another. However, a network containing only tens of droplets has been achieved to date. The size of the network created is therefore limited by the manual manipulation of droplets, where typically 100 μm-diameter Ag / AgCl electrodes are employed. Hence, no automation of the process is afforded.

Figure 5.2 B demonstrates how such networks can be utilised to attain higher order systems, comprised of simple components that act in a collective manner. Such a system has been described by Maglia *et al.*,[268] where staphylococcal α-haemolysin pores have been shown to process electrical input signals differently, depending on their orientation in the bilayer.

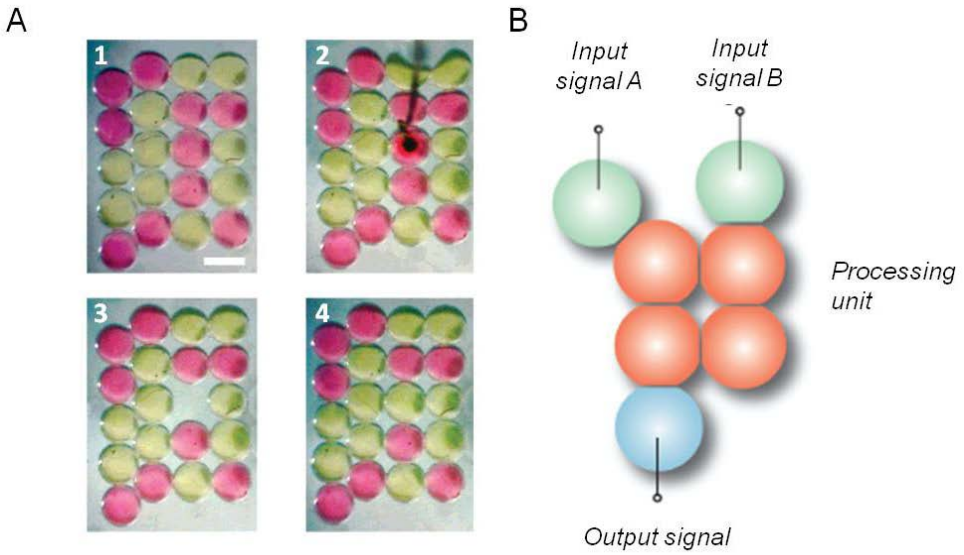


Figure 5.2: **Droplet interface bilayer networks and their application.** (A) The images show a network of DIBs and demonstrate that droplets can be removed from (images 2-3) and replaced (images 3-4) into the network. (B) Illustration of the potential use of such networks, where input signals may be processed. Figures reproduced from Holden *et al.*[203] and Maglia *et al.*[268] The scale bar in A represents 700 μm.

5.2.3 Electrical methods

Electrical methods have also been implemented to manipulate droplets for participation in DIBs. These have included methods that use dielectrophoresis (DEP) and electrowetting on dielectric (EWOD) principles. Such methods provide an alternative to the conventional microfluidic set-up, where electrical signals are used to control the generation and manipulation of aqueous droplets accordingly (as opposed to continuous flow).

The first endeavour to realise DIB formation using digital microfluidics was published by Adhdaei *et al.* in 2008, where a device based on DEP was used.[269] In 2009, Poulos *et al.*[270] demonstrated a more sophisticated approach to DIB formation; here EWOD was used, where essentially only 2-4 electrodes are required to move two droplets together (as opposed to eight in DEP), no Joule heating occurs and Ag / AgCl electrodes are incorporated into the device

design. Figure 5.3 illustrates the EWOD set-up used and the procedure for DIB formation. The application of an electric field across a droplet, which is sandwiched between electrodes covered in a dielectric material, enables it to interact more favourably with the surface i.e. to wet the surface. Activation of specific electrodes can therefore result in the manipulation of droplets.

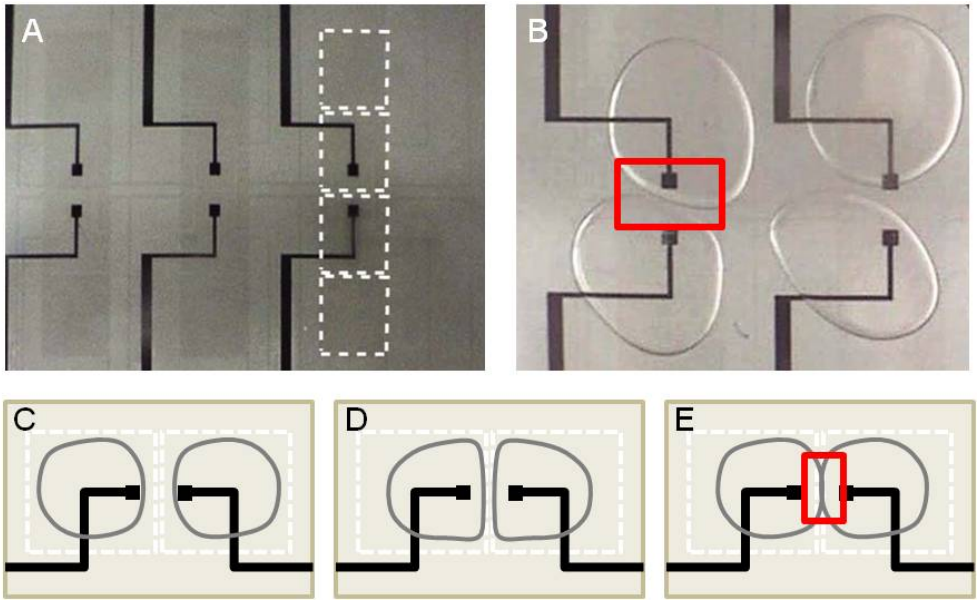


Figure 5.3: **EWOD for DIB formation.** (A) Here the EWOD set-up used can be viewed; indium tin oxide (ITO) electrodes are highlighted with white boxes and the black lines are Ag / AgCl electrodes. (B) The red box highlights successful DIB formation using EWOD (the set of droplets to the right have not been manipulated). (C)-(E) Illustration of the process of DIB formation. The ITO pads are inactive in C, but are activated in D (thus drawing each droplet in the direction of the other). The droplets subsequently relax to form a DIB (highlighted by red box in E) upon deactivation of the pads. Images in A and B have been reproduced from Poulos *et al.*[270]

The use of small sample volumes (2-5 μl) and automation make these devices suitable for lab-on-a-chip processes, where biological assays are easily translatable. However, in terms of their capacity for forming DIB networks, the most advanced set-up that has been published to date is comprised only of a linear sequence of three droplets. One limitation of this work is that droplet

size cannot easily be changed, meaning that the whole device has to be redesigned if this is a requirement. Hence there is a limitation on the size of DIB contact area per device that can be created and so the formation of droplet chains, containing droplets of different size and thus differing in membrane properties, would not be easily achieved.

5.2.4 High-throughput approaches

Several approaches have also been described, which demonstrate the use of high-throughput methods for screening transmembrane ion channel currents. In these systems, bilayers are orientated in a horizontal position and formed either by dispensing aqueous droplets on top of aqueous compartments, both possessing preformed monolayers (in the presence of oil, as illustrated in figure 5.4 A),[207] or using more conventional black lipid membrane (BLM) techniques as demonstrated in figure 5.4 B.[209,271] Syeda *et al.*[212] have used a slightly different type of approach where a suspended droplet, containing protein, is moved across an array of static aqueous compartments and participates in DIB formation at each compartment (figure 5.4 C). Here, staphylococcal α-haemolysin pores are synthesised *in situ* and various ions/drugs screened as potential blockers of this channel.

One disadvantage common to each of these systems, is the ability to form only one bilayer per experimental unit. Hence the creation of multiple drop systems has not been reported and, as such, no method exists for scrutinising events occurring across multiple bilayers. Additionally, devices using more traditional approaches often involve very complex device designs and hence multiple fabrication steps. Syeda's method has only been achieved via manual manipulation to date, though it has been postulated that this approach could be used to screen larger array chips if automated. However, despite there being no reported contamination of the suspended droplet between the nine samples tested, a larger array chip may be more susceptible to spoiling events.

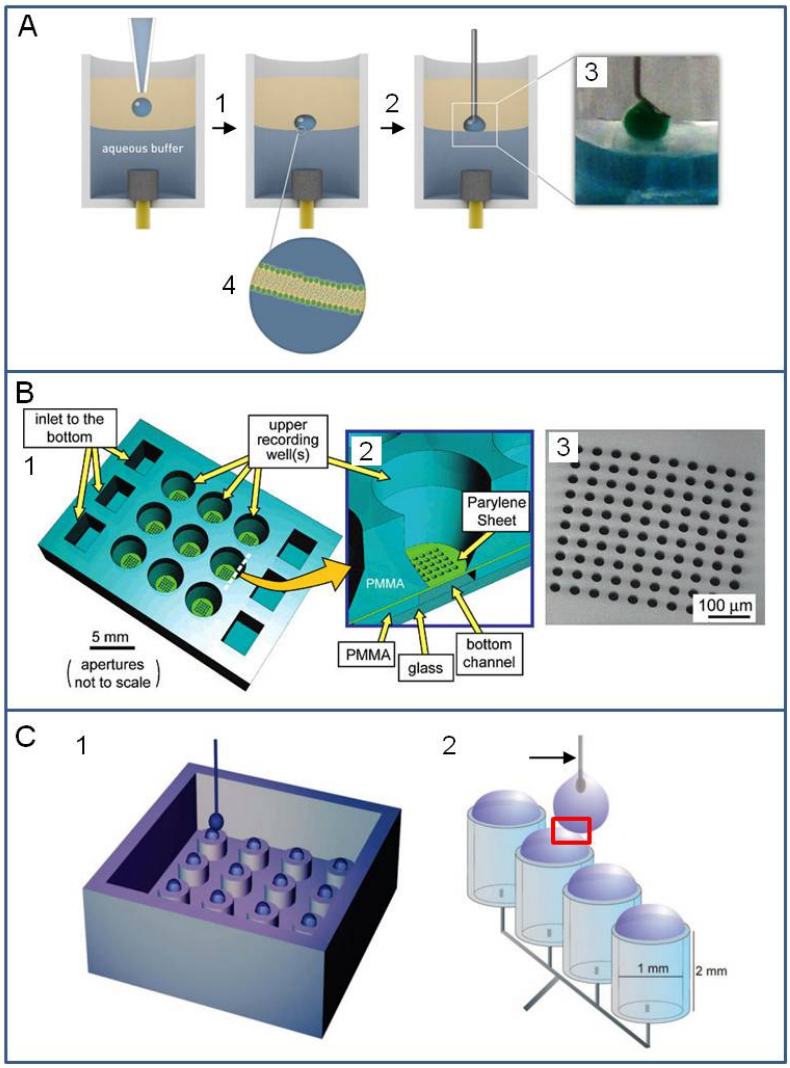


***Figure 5.4*. Current methods for using planar lipid bilayers in high-throughput screens.** (A) The method described by Poulos *et al.* [207] is illustrated. Here, an aqueous lipid-containing droplet (1 µl) is dispensed and falls onto a preformed oil-aqueous interface (see step 1); the aqueous phase also contains lipid molecules and hence a DIB is formed (see step 4). A wire (Ag / AgCl) is inserted into the droplet (step 2) in order to make electrical measurements – an enlarged image of the DIB/droplet/wire is displayed in step 3. (B) Illustration of an example of the use of black lipid membranes (BLMs) in high-throughput screens, specifically by Le Pioufle *et al.*[209,271] The complicated device design is displayed in image 1, with image 2 displaying an enlarged region of an upper recording well. BLMs can be formed across the apertures present in the parylene sheet, pictured in image 3. (C) Illustration of the ion channel screening chip published by Syeda *et al.*[212] A lipid-containing droplet, suspended on a moveable Ag / AgCl electrode, can participate in DIB formation with multiple static aqueous compartments (as shown in step 1). Step 2 illustrates the well and electrode configuration in more detail; the red box indicates DIB formation. Images are adapted from the aforementioned papers.

5.2.5 Summary and chapter aims

As a result of the observations made and experiences gained whilst conducting the experiments detailed in Chapter 4, and upon reviewing the literature, it is evident that the following requirements are desirable for advancing high-throughput DIB systems:

1. The ability to automate droplet manipulation.
2. The ability to control droplet size / DIB contact area with ease.
3. The ability to form extensive networks of DIBs.
4. The ability to form asymmetric DIB systems.
5. The ability to make droplets quickly.

Each of these requirements has been achieved, the details of which are described in the following sections.

5.3 MATERIALS AND METHODS

The following section details the materials required and methods employed in order to perform each of the experiments described in this chapter, specifically relating to the development of a novel microfluidic approach for high-throughput droplet interface bilayer formation.

5.3.1 Materials

5.3.1.1 Lipids

The following lipids were used in the experiments detailed in this chapter: 1,2-diphytanoyl-*sn*-glycero-3-phosphocholine (DPhPC, Avanti Polar Lipids) and 1,2-dioleoyl-*sn*-glycero-3-phosphocholine (DOPC, Avanti Polar Lipids).

5.3.1.2 DIB formation

The buffers used to prepare vesicle suspensions for DIB formation incorporated: 4-(2-hydroxyethyl)piperazine-1-ethanesulfonic acid (HEPES), potassium chloride (KCl), sodium hydroxide (NaOH) and fluorescein, all of which were purchased from Sigma-Aldrich®. Hexadecane oil (99%, Sigma-Aldrich®) was used as the oil of choice to aid the formation of DIBs.

5.3.1.3 Devices

First generation devices ("device 1, 2 and 3")

Materials required for the production of microfabricated structures via soft-lithography included: 100 mm silicon-wafers (thickness 525 ± 25 μm & single sided polish, IDB Technologies UK Ltd), SU-8 50 photoresist (Chestech Ltd), Microposit EC-Solvent (Chestech Ltd), Sylguard 184 Elastomer Kit (VWR) and PTFE (polytetrafluoroethylene) ultramicrobore tubing (0.004" ID, Cole-Parmer Instrument). A UV lamp was used to irradiate the exposed SU-8 50 photoresist. Silicon wafers and glass slides (VWR) were cleaned prior to use with a 1:2 mixture of hydrogen peroxide and concentrated sulfuric acid ('piranha' solution) (Sigma-Aldrich®). Distilled water and isopropylalcohol (IPA, Sigma-Aldrich®) were used for rinsing.

Second generation devices ("device 4")

In order to construct the new devices the following materials were required: hollow square capillaries (borosilicate glass, 1 mm x 1 mm x 50 mm, Composite Metal Services Ltd), 'thin' PTFE ultramicrobore tubing (0.004" ID,

Cole-Parmer Instrument), 'thick' polyethylene (PE) tubing (380 μm ID, Harvard Apparatus UK) and Araldite (RS Components). Plastic syringes (3 ml, disposable BD Plastipak Syringes) and needles (BD Microlance 25G 1" – Nr. 18, 0.5 × 25 mm) were used to collect the carrier fluid and aqueous waste.

5.3.2 Methods

5.3.2.1 Vesicle Preparation

Vesicle suspensions were comprised of either DPhPC or DOPC and prepared as described previously (chapter 2, section 2.3.2.1). Thin lipid films were prepared with 2 mg of lipid and hydrated with 1 ml of buffer to yield a concentration of 2 mg / ml. The two buffer solutions, specifically solution 5.1 (non-fluorescent) or 5.2 (fluorescent), prepared for use in experiments detailed in this chapter, are specified as follows:

Solution 5.1:	10 mM HEPES, 200 mM KCl, pH 7.07
Solution 5.2:	250 μM fluorescein, 10 mM HEPES, 200 mM KCl, pH 7.60

The hydrated lipid films were freeze-thawed five times and subsequently extruded 21 times through 100 nm polycarbonate membranes (Avanti Polar Lipids), wrapped in foil and stored in the dark when not in use.

5.3.2.2 Device fabrication

First generation devices: preliminary investigations ("device 1, 2 and 3")

First generation devices tested in the preliminary investigations were made using traditional photolithographic approaches. The procedures used were detailed explicitly in chapter 3, section 3.3.2.4. To recap, the steps used are shown in figure 5.5. The devices used in the preliminary investigations (devices 1-3) are described in figure 5.6.

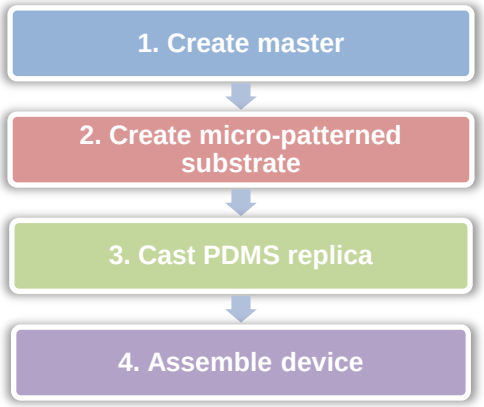


Figure 5.5: **Method of device assembly.** Procedures followed in order to assemble the various microfluidic devices tested in this chapter (in the preliminary experiments).

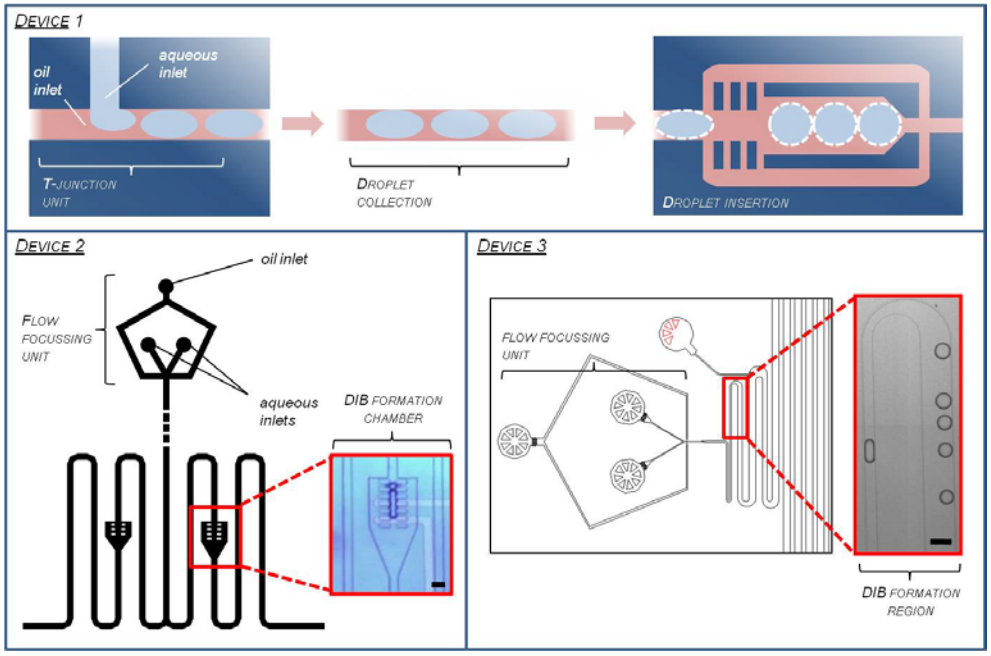


Figure 5.6: **First generation device used during preliminary investigations (devices 1-3).** "Device 1" is comprised of three stages: (i) water-in-oil droplets are generated using the T-junction technique, (ii) the droplets are collected into thin PTFE tubing and (iii) the droplets are then inserted into a chamber for DIB formation. Note that these diagrams are not drawn to scale, however section 5.4.1.1 includes an image of the actual device (to scale). "Device 2" generates droplets using the flow-focusing unit – droplets are then introduced into a chamber for DIB formation. Scale bar represents 50 μm. "Device 3" also generates droplets using the flow-focusing approach – the droplets then pass through a wider microfluidic channel in order to slow down the flow and therefore aid DIB formation (DIB formation region). Scale bar represents 100 μm.

Second generation devices ("device 4")

To assemble second generation devices, 'thin' PTFE tubing was sealed in place at one end of the glass capillary and 'thick' PE tubing to the other (see section 5.3.1.3 for materials); Araldite was used as the sealant. The devices were then carefully placed in an oven (60 °C) and left for 1 hour to allow the Araldite to set. Figure 5.7 details how each of the components are assembled in order to form a new generation device (device 4).

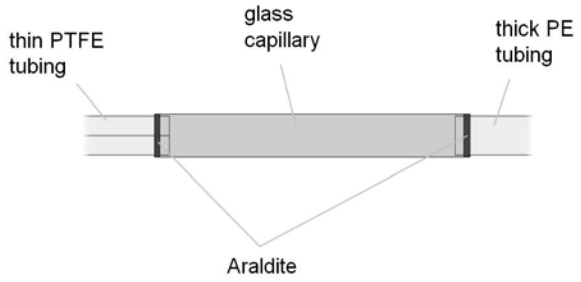


Figure 5.7: **Schematic of the second generation device (device 4).** A projection of the device is displayed (top view) indicating how the PTFE and PE tubings are attached to the glass capillary. Note that the image is not to scale.

5.3.2.3 Water-in-oil droplet formation

Aqueous droplets comprised of vesicle suspensions (detailed in section 5.3.2.1) were created in hexadecane oil. Traditional microfluidic approaches were used to form water-in-oil droplets. Specifically, a syringe pump (PHD 2000, Harvard Apparatus) was used to withdraw oil and aqueous solutions in an alternating manner through the thin PTFE tubing and into the chamber. An auto-sampler was used to manage this process, having the additional benefit of possessing two channels and thus enabling more than one type of aqueous droplet to be introduced into the tubing. Figure 5.8 explains how the auto-sampler generates water-in-oil droplets.

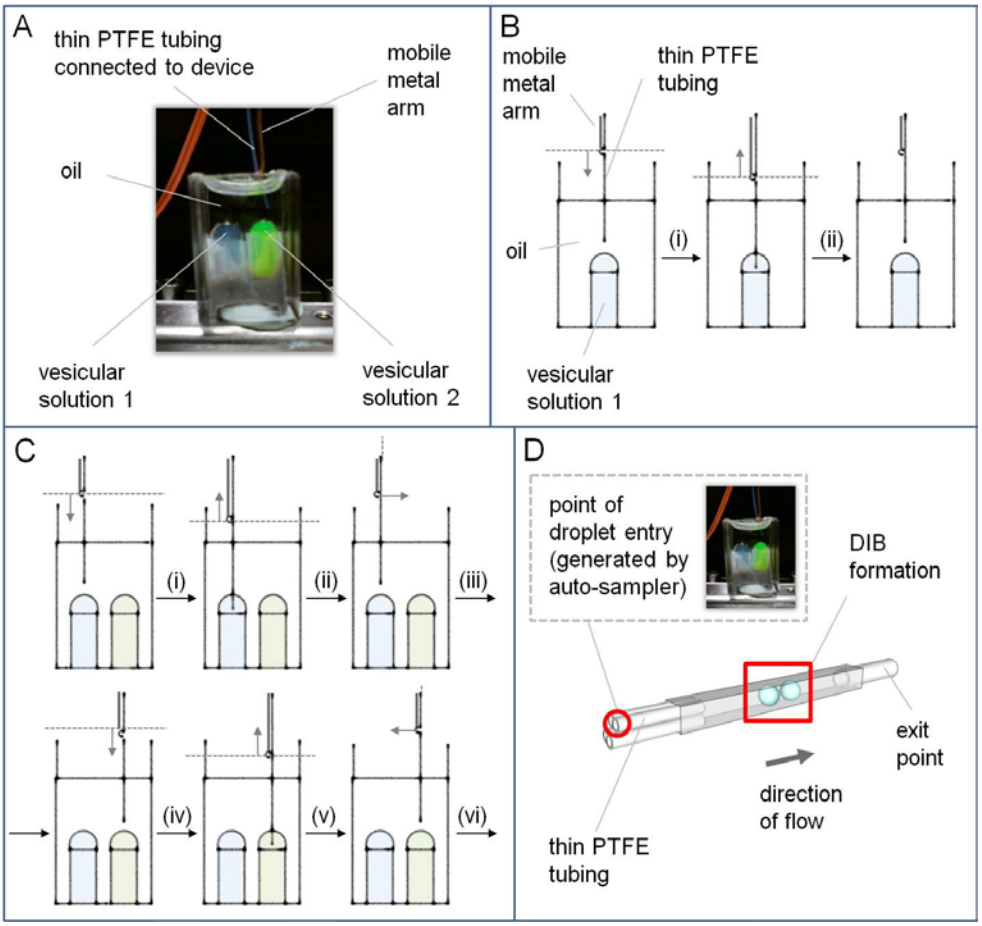


Figure 5.8: **Water-in-oil droplet formation using an auto-sampler.** (A) A cuvette is used to hold the oil and aqueous solutions required to form water-in-oil droplets. Note that a second solution of vesicles may be included to generate more than one type of aqueous droplet in succession (i.e. for asymmetric droplet interface bilayer (aDIB) formation). (B) Thin PTFE tubing, attached to a syringe pump working in refill mode, is held by a mobile metal arm. In order to create water-in-oil droplets, the thin PTFE tubing is: (i) lowered from the oil, into the aqueous solution and (ii) raised from the aqueous solution back into the oil. This process occurs in rapid succession and is repeated constantly in order to generate a series of water-in-oil droplets. The syringe pump operates in refill mode for the duration of this process, i.e. 'withdrawing' oil and aqueous solutions in an alternate fashion. (C) In order to create a series of droplets that alternate in lipid or aqueous composition, two different aqueous droplets can also be formed in succession. The same process occurs as in B, except for the fact that the auto-sampler then moves across to a second channel (containing a second aqueous sample), as detailed in step (iii), before then repeating the sampling process (as illustrated by steps (iv), (v) and (vi)). (D) After droplet generation, the thin PTFE tubing then feeds the droplets into the main channel of the device (device 4, section 5.3.2.2) where DIB formation can proceed.

5.3.2.4 Fluorescence leakage experiments

Fluorescein leakage assays were achieved by forming DOPC DIBs between non-fluorescent and fluoresecent droplets (as detailed in section 5.3.2.1) arranged in an ABAB format, where A and B are fluorescent and non-fluorescent droplets respectively. Such droplet arrangements were achieved using the two channel auto-sampler, as described previously in section 5.3.2.3. Figure 5.9 illustrates the nature of the set-up.

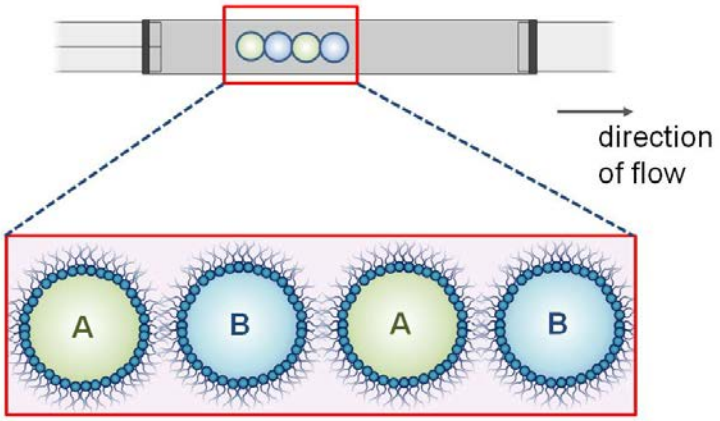


Figure 5.9: **Format of the fluorescein leakage assay.** Both fluorescent and non-fluorescent droplets containing DOPC vesicles (denoted by A and B respectively) are introduced into the device (device 4, section 5.3.2.2) using the two-channel auto-sampler. DIBs are formed downstream upon stopping the flow. Note that the diagram is not to scale.

After introduction of the droplets into the glass capillary and DIB formation, the syringe pump was stopped. Both bright field and fluorescence images were taken using exposures of 20 ms and 2 s respectively and a 5x objective. Fluorescence images were gained via illumination of the fluorescent sample using a mercury lamp (Olympus); a fluorescein filter was employed (480 / 40 nm excitation, 488 nm long pass, Chroma Technology Corp.) as well as two neutral density filters (25ND6 and 25ND25, Olympus) to prevent photo-bleaching. In order to monitor fluorescein leakage, images were taken

every 20 min up to 1 hour, then every 30 min up to 2 hours and finally at 3 hours and 20 hours after the start of the experiment (note that not all images are shown section 5.4.2.4).

5.3.2.5 Control experiments

Two control experiments have been performed. The first simply involved proving that DIB formation only occurs in the presence of lipid molecules, as otherwise droplets merge.

The second involved testing whether fluorescein leaks from the aqueous phase into the oil phase. Equal volumes of fluorescent buffer (solution 5.2, prepared as described in section 5.3.2.1) and hexadecane oil were placed in the same glass vial, thus forming an aqueous-oil interface, and left for five days in a concealed environment. Aliquots of each phase were then transferred into a 96 well-plate and fluorescence measurements carried out on a Cary Eclipse fluorescence spectrophotometer (Varian Inc.). Emission scans, with excitation at 490 nm and emission collected from 500 to 700 nm, were then performed on each of the samples. Both the excitation and emission slits were set to 5 nm, and a medium scan rate and photomultiplier tube detector voltage of 600 V employed. Controls were also conducted with fresh samples of hexadecane and fluorescent buffer (where no aqueous-oil interface was allowed to form) for comparison.

5.3.2.6 Imaging

An Olympus DP71 CCD camera mounted on an Olympus BX51 upright microscope was used to capture all images illustrated in this chapter. Images were acquired using analySIS (Olympus Soft Imaging Solutions GmbH, Version 5.0) and fluorescence images were processed using IrfanView (freeware by Irfan Skiljan, 2009).

5.3.3 Movies

The following movies have been included as supplementary information for the experiments detailed in this chapter:

(i) Movie 5.1: 'Small droplets filling the chamber in device 4'

(ii) Movie 5.2: "Large droplets filling the chamber in device 4'

(iii) Movie 5.3: 'Formation of large droplet DIB network in device 4'

(iv) Movie 5.4: "Formation of DIBs with DOPC in device 4'

The movies were filmed using device 4, as detailed in section 5.3.2.2, as well as the microscope and software detailed in section 5.3.2.6. Stills from each movie have been included for completion as well as a description for the reader to refer to. Please find the movies on the CD accompanying this thesis.

5.3.3.1 Movie 5.1: 'Small droplets filling the chamber in device 4'

This movie shows the successful formation of water-in-oil droplets at the point of entry into the glass chamber of device 4 (section 5.3.2.2). The thin PTFE tubing (inner diameter 102 μm) is present in the lower left hand corner. Here the droplets contain vesicle suspensions comprised of DPhPC (2 mg / ml) and are formed using a volumetric flow rate of 3 μl / min. The stills from the movie are displayed in figure 5.10. Note that the time increment between each image is 1 s and the scale bar represents 200 μm.

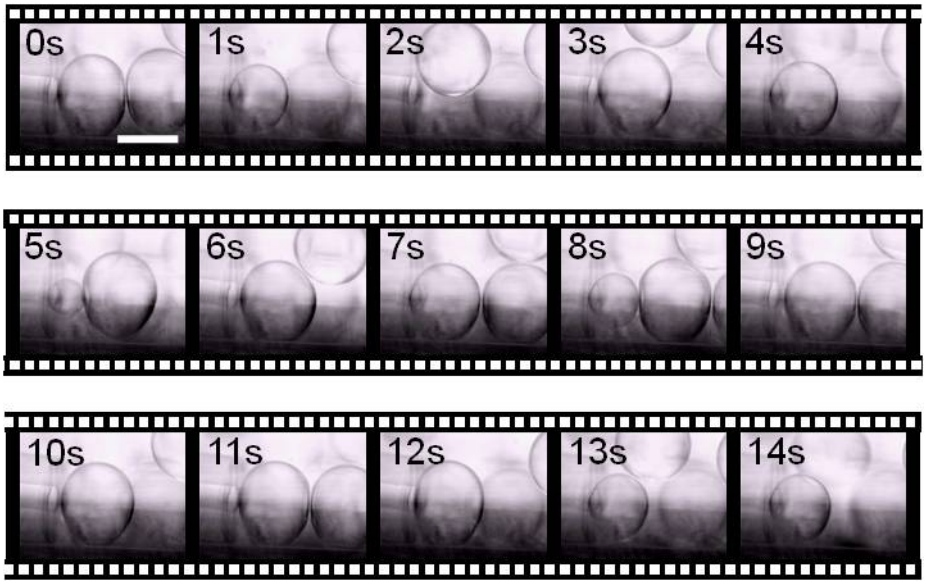


Figure 5.10: **Stills from Movie 5.1: 'Small droplets filling the chamber in device 4'.** The scale bar represents 200 μm.

5.3.3.2 Movie 5.2: 'Large droplets filling the chamber in device 4'

This movie demonstrates that large droplets can be formed and successfully introduced into the chamber in device 4 (section 5.3.2.2), again using DPhPC vesicle suspensions (2 mg / ml). The volumetric flow rate employed is 6 μl / min. The PTFE tubing where droplets are carried can be seen in the lower left hand corner, the interior diameter of which is 102 μm. The stills from the movie are displayed in figure 5.11. Note that the time increment between each image is 3 s and the scale bar represents 400 μm.

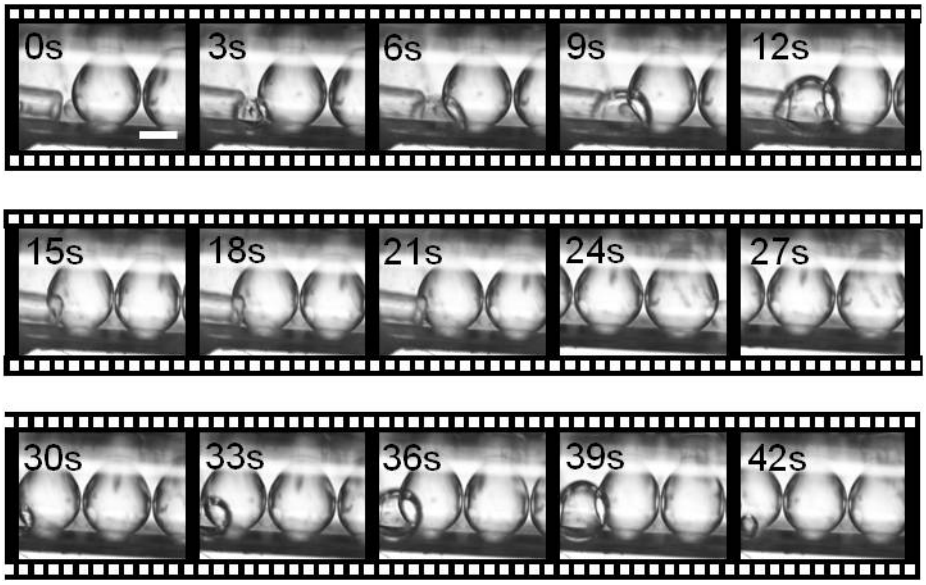


Figure 5.11: **Stills from Movie 5.2: 'Large droplets filling the chamber in device 4'.** The scale bar represents 400 μm.

5.3.3.3 Movie 5.3: 'Formation of large droplet DIB network in device 4'

This movie shows that successful DIB networks can formed with large droplets in two dimensions, again using device 4 (section 5.3.2.2). The conditions used are identical to those stated in section 5.3.3.2. The stills from the movie are displayed in figure 5.12. Note that the time increment between each image is 2 s and the scale bar represents 400 μm.

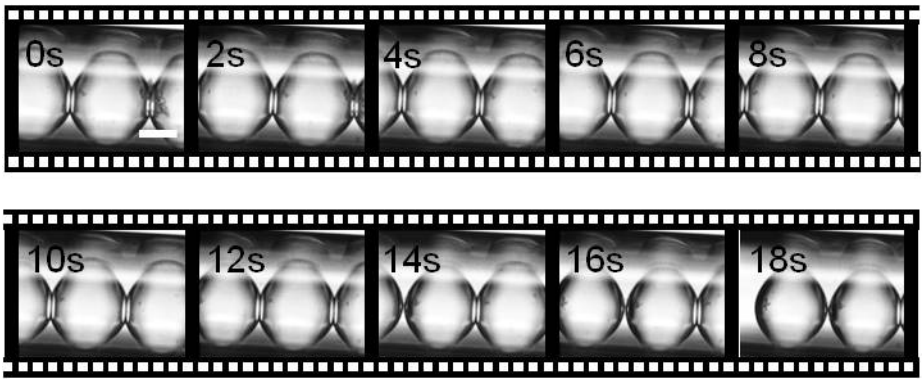


Figure 5.12: **Stills from Movie 5.3: 'Formation of large droplet DIB network in device 4'.** The scale bar represents 400 μm.

5.3.3.4 Movie 5.4: 'Formation of DIBs with DOPC using device 4'

Here, the successful formation of DIBs between multiple droplets containing DOPC vesicle suspensions (2 mg / ml) is demonstrated. Droplets were formed with volumetric flow rates of 12 μl / min using device 4 (section 5.3.2.2). The stills from the movie are displayed in figure 5.13. Note that the time increment between each image is 2 s and the scale bar represents 400 μm.

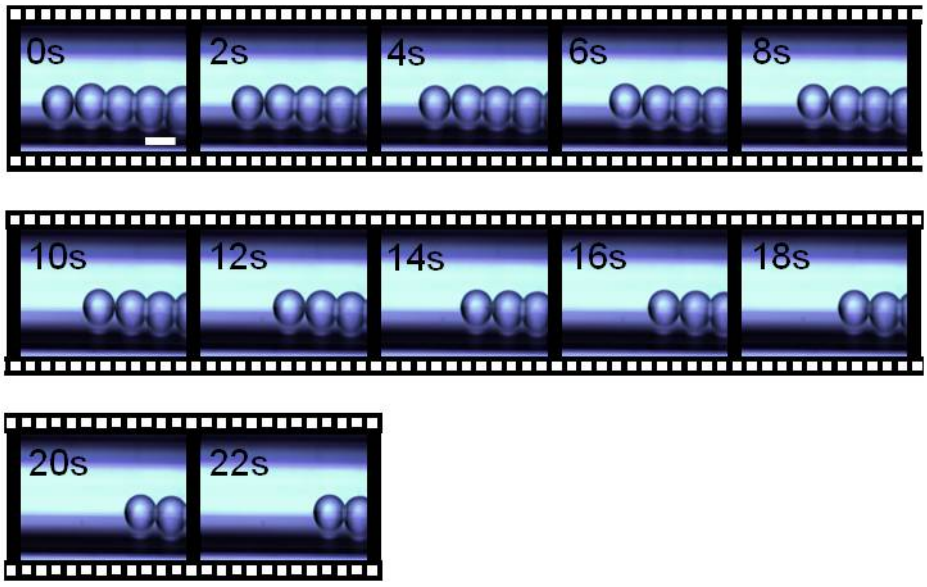


Figure 5.13: **Stills from Movie 5.4: 'Formation of DIBs with DOPC using device 4'.** The scale bar represents 400 μm.

5.4 RESULTS AND DISCUSSION

As the results described in Chapter 4 corroborate, it was found that the movement of the droplets by hand is difficult and that the uniformity of droplet size was poor and uncontrollable. Hence, the idea to generate droplet interface bilayers (DIBs) using a microfluidic approach was thought to be advantageous. Several attempts were made initially to try and achieve this goal using the first generation devices. However, problems were found, which in turn resulted in the development of a simple design (second generation

devices) able to produce DIB networks using microfluidics. The various steps taken in order to achieve these developments are discussed herein.

5.4.1 Preliminary investigations using first generation devices

5.4.1.1 Device designs

Several attempts were made to use a variety of microfluidic devices for DIB formation, specifically using the three devices designs detailed in section 5.3.2.2 (devices 1-3). Initially it was assumed that the droplets would not merge due to the presence of lipid monolayers situated at, and hence stabilising, the droplets' oil-aqueous interfaces. However this was not found to be the case – stable DIB formation could not be gained in any of these devices. The three formats tested, illustrated in figures 5.14, 5.15 and 5.17, are described and discussed below.

The first attempt, which uses "device 1" (see section 5.3.2.2), involved using a T-junction to form aqueous droplets in oil. Chapter 1, section 1.4.1.4 provides an introduction to the traditional microfluidic methods available for water-in-oil droplet formation. After forming water-in-oil droplets (as illustrated in figure 5.14 A) and collecting them in thin PTFE tubing (figure 5.14 B), they were then inserted into a chamber contained within the latter portion of the device (illustrated by figure 5.14 C). It was found that one of the major problems preventing DIB formation was actually associated with the point at which the droplets exited the thin PTFE tubing and entered into the chamber: drops were found to merge, resulting in the formation of very large droplets. This was attributed to the fact that the oil gaps between droplets were not large enough to enable the droplets to enter into the large chamber and move away from the entrance point, a limitation of the of T-junction technique for droplet generation. Additionally, it was not possible to form stable DIBs between the larger droplets, owing to the large interaction between the droplet and PDMS surfaces.

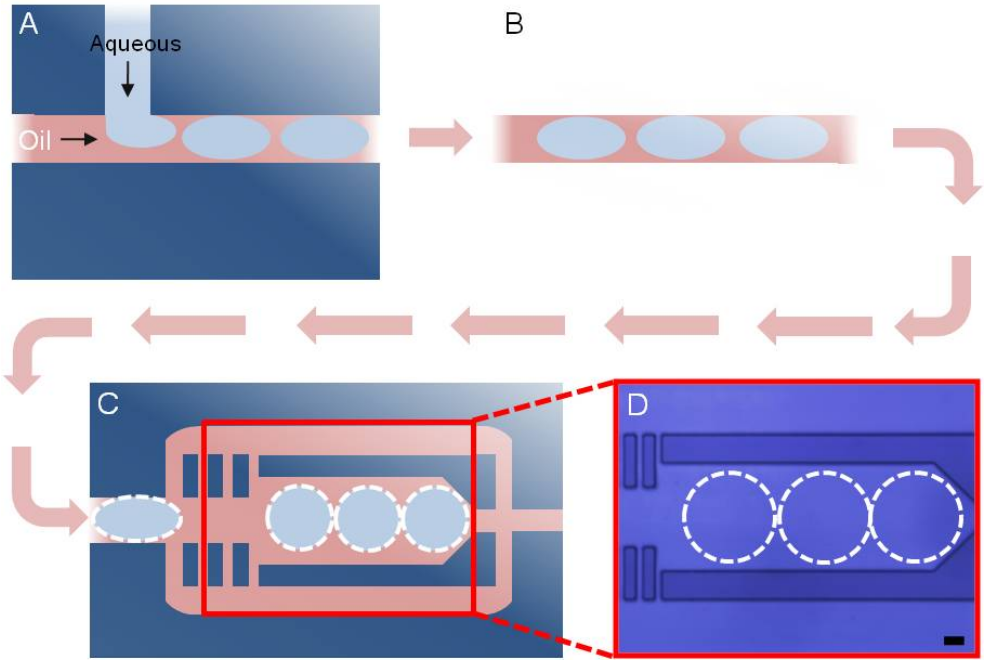


Figure 5.14: **Device 1.** (A) The first device trialled for the formation of DIBs in high-throughput utilised a T-junction technique to form water-in-oil droplets. (B) After formation, the aqueous droplets were then collected into thin PTFE tubing. (C) The final part of the device involved inserting the droplets into a chamber for DIB formation. (D) Bright field image of the area highlighted in C (red box). The dotted circles (white) represent the region where droplets were anticipated to settle and form DIBs. Scale bar represent 100 μm. Note that A-C are not drawn to scale.

Accordingly, a device that could generate droplets and form DIBs concurrently was desired, in order to overcome the problems associated with the first attempt. The second approach therefore utilised a single part device, "device 2" (section 5.3.2.2), whereby droplets could be generated and then held in a chamber downstream for participation in DIB formation. Figure 5.15 illustrates the nature of device 2.

Water-in-oil droplets were created in device 2, as a result of utilising a flow-focusing approach (see chapter 1, section 1.4.1.4 for further information). Figure 5.15 A illustrates the nature of device 2 and the flow-focussing unit employed.

After formation, the aqueous droplets proceed through the microfluidic channels until they reach a pillared section (figure 5.15 B). This pillared section acts in a passive manner and is normally used to reduce the speed of the droplets, holding them in close proximity to one another and thus enabling them to merge in a controlled fashion.[121] It was hypothesised that by performing the same process, but in the presence of lipid molecules (especially DPhPC, see chapter 4, section 4.4.1.2), DIB formation would ensue. However, the droplets were found to merge when they came into contact with one another.

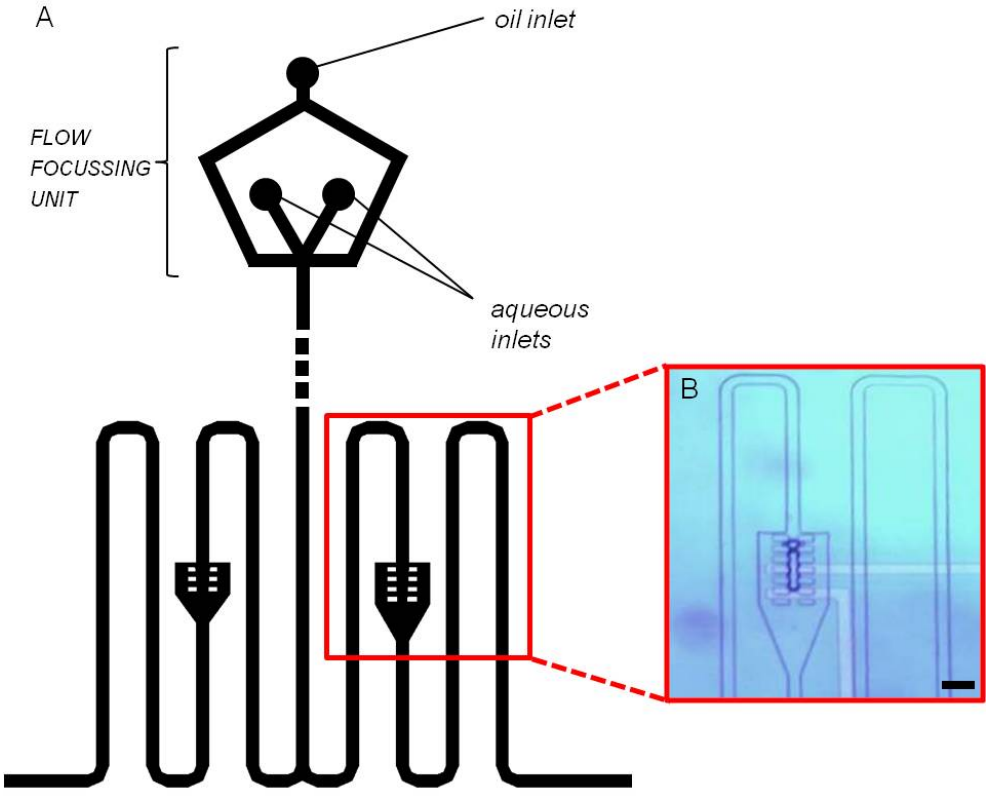


Figure 5.15: **Device 2.** (A) The second device possesses a flow focussing unit to form water-in-oil droplets followed by a pillared section, where it was anticipated that droplets could participate in DIB formation. (B) A bright field image illustrating the region in A highlighted by a red box (pillared section). Scale bar represents 100 μm.

It is believed that the droplet merging events are associated with the pressures exerted upon the droplets being held in the pillared chamber area. That is to say that the pressure exerted upon the droplets, by the flow of oil running through the microfluidic channels in the device dominates monolayer-monolayer interactions. Hence droplet merging occurs as a result. Additionally the pillared structures probably do not assist DIB formation, due to the interaction of the droplet area with the PDMS substrate (even though the PDMS area in close proximity to the droplets is reduced when compared to droplets filling a single channel). An observation made in a microfluidic channel supports this hypothesis, i.e. that the extensive interaction of lipid-containing, aqueous droplets with a PDMS substrate lessens the chances of DIB formation, and is illustrated in figure 5.16. These results indicate that DIB formation does occur, but that it is not stable: the DIB is present for approximately 16 s, after which it ceases to exist (figure 5.16 A).

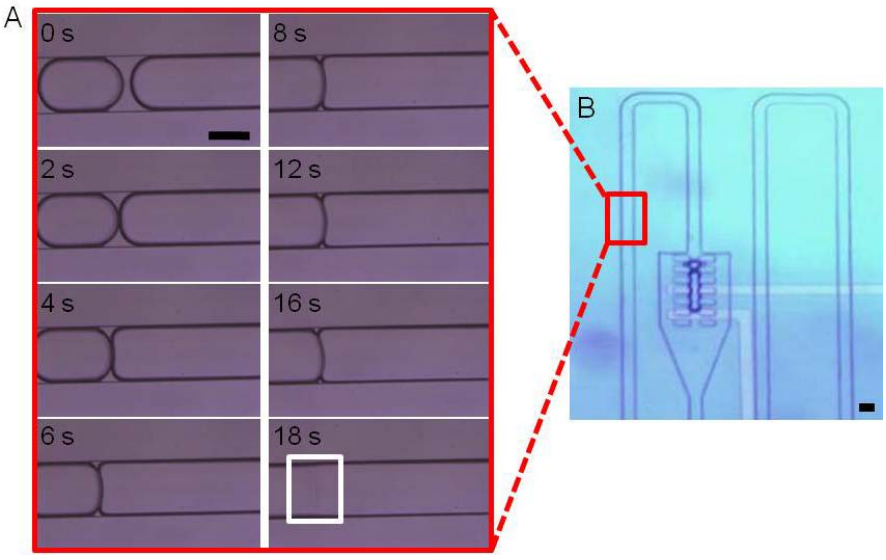


Figure 5.16: **Observations of potential on-chip DIB formation.** (A) DIBs were found to occur in PDMS channels, though their lifetimes are short. DIB formation can be observed, however the DIB ruptures after ca. 16 s (highlighted by the white box) due to the excessive interaction of the droplet with the PDMS substrate. (B) A bright field image which indicates where this observation was made, i.e. in a microfluidic channel. Scale bars represent 50 μm.

Finally, it was decided to try using a device that would enable droplet generation and DIB formation to occur concurrently on-chip, but without a holding chamber. The key aspect of the device design is illustrated in figure 5.17 A and B, where the droplets travel from a narrow channel into a wider channel, hence slowing their rate of movement. Droplets in these devices do form DIBs, but only momentarily: DIB formation and merging events are

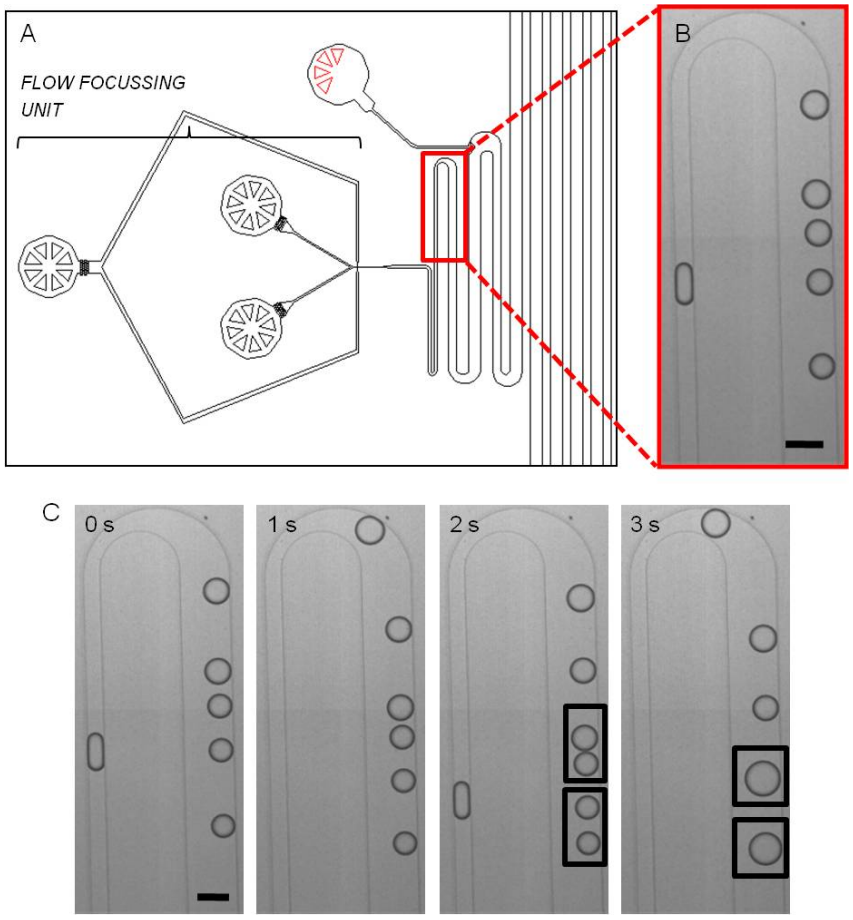


Figure 5.17: **Device 3.** (A) The device design is illustrated, where a flow focusing unit is again utilised for water-in-oil droplet generation. The aim of the experiment was to bring droplets together in an environment where unfavourable interactions with the PDMS substrate are reduced. (B) A bright field image of the highlighted region in A (red box). (C) Here DIB formation can be observed, where contact with the substrate is minimised (indicated by the black boxes in the image taken at 2 s). However, the speed at which the droplets come together in this type of device is too fast, resulting in droplet merging (indicated by black boxes in the image captured at 3 s). Scale bars represent 100 μm.

highlighted in the images captured at 2 s and 3 s respectively (presented in figure 5.17 C). Although substrate-monolayer interactions were minimised in this device, the speed at which the droplets approach one another is thought to be the most significant factor contributing to the merging events.

5.4.1.2 First observation of stable DIB formation on-chip

In summary, it was observed that there was a problem associated with the channel dimensions used in these PDMS microfluidic devices. When using the regimes outlined in section 5.4.1.1, the aqueous droplets tend to fill the entire channel, possessing a cigar-like structure, or at the very least significantly interact with the PDMS substrate. However it was observed, in one of the side channels adjacent to the chamber in device 1, that it would be possible to form stable DIBs using a microdroplet approach. Figure 5.18 illustrates this observation.

In this instance a larger droplet (indicated in figure 5.18 A, but out of the frame of view in figure 5.18 B) was slowly being squeezed through the pillars of the chamber to yield smaller droplets that are stored in the peripheral space. This larger droplet formed as a result of the small droplets merging instantly in the chamber. The first DIB (present in the first image of figure 5.18 B, captured at 0 s) is present for the entire 15 s of video footage, and is able to withstand the introduction of three droplets in succession. It was therefore concluded that one of the important factors for stable DIB formation is the introduction of one drop to another in a controlled and 'gentle' manner so as to not disrupt the DIB. Additionally, it is also important to ensure that substrate-monolayer interactions are minimised, by allowing droplets to adopt a spontaneous, spherical shape.

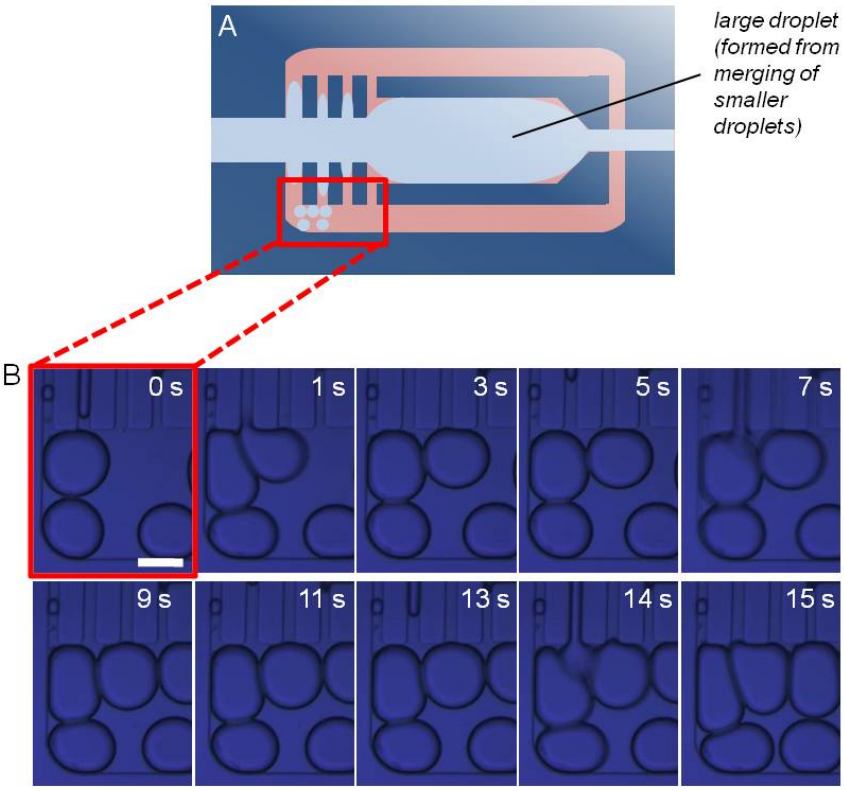


Figure 5.18: **First observation of stable DIB formation on-chip.** (A) Schematic of the device in which this event was observed (device 1, section 5.3.2.2). The formation of a large droplet in the main chamber resulted, due to each of the smaller droplets merging, and is indicated on the diagram. Note that the diagram is not to scale. This large droplet was unintentionally squeezed through the pillars of the chamber to yield smaller droplets that formed DIBs. (B) A series of images demonstrating that DIBs are able to withstand the introduction of successive droplets into the region of interest (red box highlighted in A). This demonstrates that stable DIB formation can occur in a microfluidic device, under suitable conditions. Scale bars represent 100 μm.

5.4.2 Second generation of devices

5.4.2.1 Device design

As a result of the observations detailed in section 5.4.1, a new device was designed and implemented. A major problem associated with using PDMS in device fabrication, for this specific set-up, is the fact that hexadecane: i) 'leaches' out of the PDMS and ii) causes the PDMS to swell.[272,273] Therefore it was desirable in the first instance to move to a system that employed glass.

The device that was therefore designed, "device 4" (see section 5.3.2.2), consisted predominantly of a glass capillary with thin polytetrafluoroethylene (PTFE) tubing (inner diameter = 100 μm) assembled at the entrance point and thick polyethylene (PE) tubing at the exit. A diagram of the device can be viewed in figure 5.19 A. Four lengths of thin PTFE tubing were inserted and secured at the entrance, one of which was used to introduce droplets into the device using a two-channel auto-sampler (see section 5.3.2.3 for information on how the auto-sampler is used to generate water-in-oil droplets) and the remainder used to maintain a uniform flow of oil along the channel. As a result

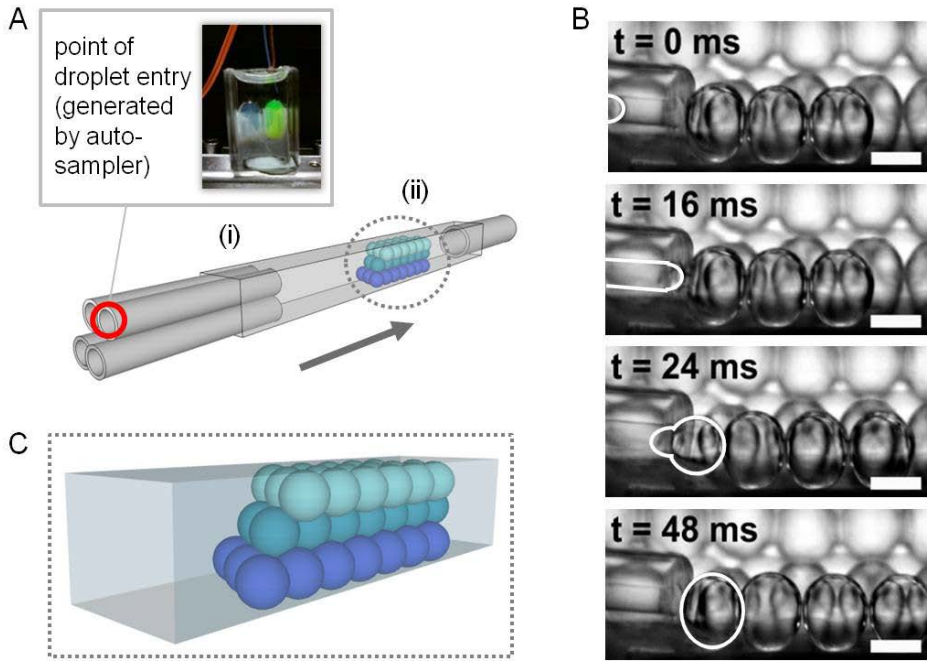


Figure 5.19: **Device 4 for high-throughput droplet interface bilayer (DIB) formation.** (A) The device is comprised of a square glass capillary with tubing inserted at the entrance and exit. Droplets are formed at point (i) and come together to form DIBs downstream at point (ii). Four pieces of thin PTFE tubing (100 μm inner diameter) are used at the entrance in order to create a uniform flow across the channel (arrow represents direction of flow). (B) Water-in-oil droplets are generated using a two-channel auto-sampler. A time course of their formation at point A (i) is illustrated by the series of images. Scale bar represents 200 μm. (C) Illustration demonstrating how DIB networks can also be formed at point A (ii) using device 4.

of thin input tubing, having an inner diameter smaller than that of the channel dimensions, droplets do not fill the entire channel and can hence adopt a spherical shape, fulfilling one of the key requirements stated in section 5.4.1.2. The series of images in figure 5.19 B illustrate the nature of droplet formation. Please also consult Movie 5.1, 'Small droplets filling the chamber in device 4' (see section 5.3.3 for further information), to observe the generation of droplets in real time. Movie 5.1 illustrates that stable droplet formation was attained, affording droplets that are highly uniform in size. It was found that the size of droplets produced in this manner (ca. 200 μm in diameter) was very reproducible. Figure 5.20 illustrates the error associated with the cross-sectional area of the droplets, when compared to the mean value for a sample of 13 droplets. In summary, this corresponds to an average size variation of only 3.3 %.

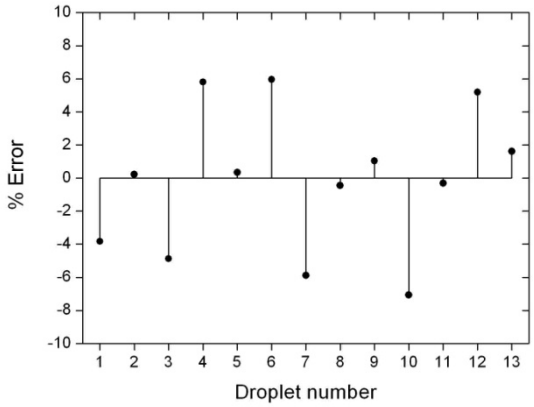


Figure 5.20: **Size variation of water-in-oil droplets.** The graph illustrates how the cross-sectional area of a sample of 13 droplets compares to the mean value gained for the population. Correspondingly, the percentage error for each droplet is indicated, which gives rise to an average size variation of only 3.3 %.

5.4.2.2 High-throughput DIB formation

High-throughput DIB formation was achieved primarily by introducing water-in-oil droplets, containing lipid vesicles comprised of either DPhPC or DOPC, into the device (device 4) and allowing them to form DIBs downstream of the

initial point of entry, as indicated by point (ii) figure 5.19 A and figure 5.19 C. Traditional microfluidic concepts were utilised to introduce water-in-oil droplets into the device. More specifically, a syringe pump, programmed to function in refill mode, was used to withdraw both oil and aqueous vesicle suspensions into the thin PTFE tubing. A two channel autosampler enabled specific volumes of each to be introduced in an alternating fashion, hence affording water-in-oil droplets (as detailed in section 5.3.2.3).

Notably, droplets do not merge at the point at which they enter into the glass channel, rather they travel along the channel forming DIBs downstream. Figure 5.21 illustrates some examples of DIBs formed in this manner.

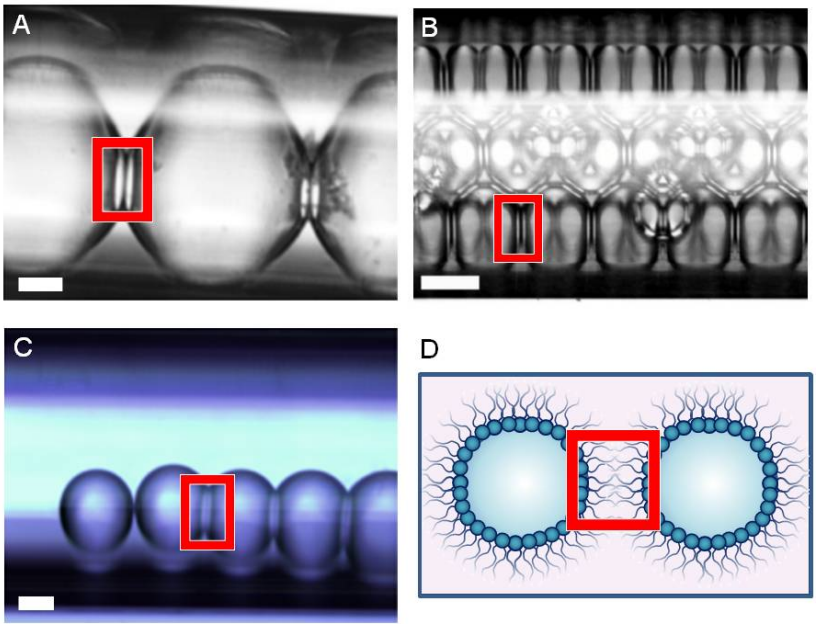


Figure 5.21: **Examples of droplet interface bilayer (DIB) formed in high-throughput.** (A) An example of high-throughput DIB formation using the lipid DPhPC. (B) An example of the formation of three-dimensional DIB networks in high-throughput (also using DPhPC). (C) An example of high-throughput DIB formation using the lipid DOPC. (D) An illustration indicating how DIB formation occurs between two aqueous droplets in an oil environment. The red boxes indicate DIB formation. The scale bars represent 200 μm.

It can be observed from the images displayed in figure 5.21 that the device in question (device 4) provides an ideal environment whereby: (i) successful monolayer formation has ensued, (ii) droplet diameters are not confined to channel dimensions and (iii) droplets are able to approach one another at a suitable rate, thus preventing merging.

5.4.2.3 Control of droplet size

A further benefit of this platform, which cannot be achieved with conventional methods and has not knowingly been described previously in the literature for the production of DIBs, is the ability to tune droplet size in a controlled and automated fashion. The formation of water-in-oil droplets, as described previously, is central to this microfluidic approach; it is therefore perceivable that changes to properties affecting volumetric flows rates can lead to changes in droplet characteristics.

The droplets displayed in figure 5.22 A, which contain DPhPC vesicle suspensions, are approximately 5 nl in volume (200 μm in diameter) and are formed using a relatively low volumetric flow rate of 3 μl / min (see Movie 5.1 and section 5.3.3 for further information). The droplet volume can be increased if the volumetric flow rate is increased and sampling frequencies lowered, as displayed in figure 5.22 B (~ 100 nl volume, 600 μm diameter, 6 μl / min flow rate) and Movies 5.2 and 5.3 (see section 5.3.3 for further information). It was noted that when droplets contained DOPC vesicle suspensions, higher volumetric flow rates (12 μl / min) were required to create droplets of intermediary size (~35 nl, 400 μm diameter, see figure 5.22). It is proposed that these anomalies could be due to differences in the interaction of DPhPC and DOPC with the PTFE tubing or viscosities of the aqueous phase. Note that Movie 5.4 (see section 5.3.3 for further information) illustrates an example of DIB formation with DOPC. Here, the use of a microfluidic approach is particularly valuable. As discussed in

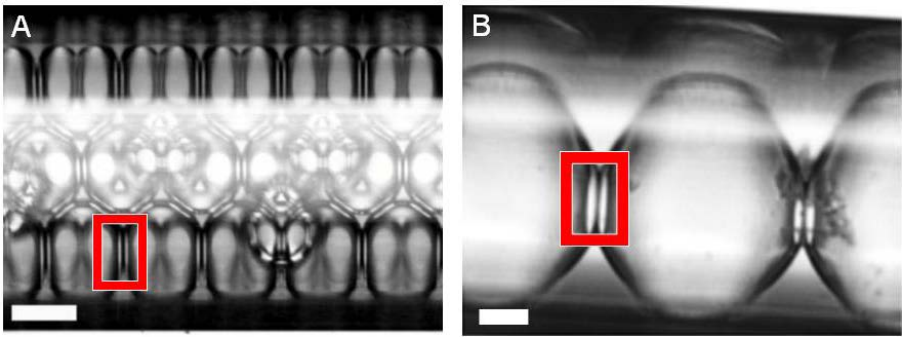


Figure 5.22: **Ability to tune droplet size, hence controlling droplet interface bilayer (DIB) contact area and the number of DIBs each droplet participates in.** (A) The image illustrates small droplets (~5 nl, 200 μm in diameter) that are formed using device 4 (using a volumetric flow rate of 3 μl / min) and pack in three-dimensions, hence forming multiple DIBs per droplet. (B) The image illustrates larger droplets (~ 100 nl, 600 μm in diameter) that are formed using higher volumetric flow rates (6 μl / min), but at a lower frequency, and create a chain of single droplets attached via DIBs stacking in two-dimensions. The scale bars represents 200 μm. DPhPC was used to form DIBs in both A and B. The red boxes indicate DIB formation.

Chapter 4, section 4.4.2.4, forming DOPC DIBs by manual manipulation led to problems in size control. It is observed that the use of microfluidics offers a successful route to forming bilayers that may be more delicate in nature, as well as having the ability to control droplet size.

Furthermore, the ability to control droplet size impacts upon two crucial factors that one may wish to access: (i) the size of the DIB contact area and (ii) the number of contact points, i.e. DIBs, achieved per droplet. The former is a natural consequence of the size of the droplet, with the latter being dependent upon the area available for packing.

Figure 5.22 A illustrates that multiple DIBs per droplet can be attained using this experimental platform due to the formation of 'small' droplets, i.e. droplets possessing cross sectional areas less than half that of the channel. Each droplet has up to twelve nearest neighbours (exceptions being droplets participating in the first and last complete layers, and the incomplete top layer), thus having the potential to pack in either a hexagonal close-packed (HCP) or face-centred

cubic (FCC) manner and forming up to twelve DIBs per droplet. It is difficult to ascertain the exact nature of the packing (i.e. HCP vs FCC) due to optical ambiguities present at the channel edges, caused by the diffraction of light in the square capillary. The presence of an HCP lattice is most probable due to the increased probability in forming an A-type layer as the top layer (if only three complete layers reside in this device); the potential HCP and FCC packing arrangements of droplets in this device are displayed in figure 5.23.

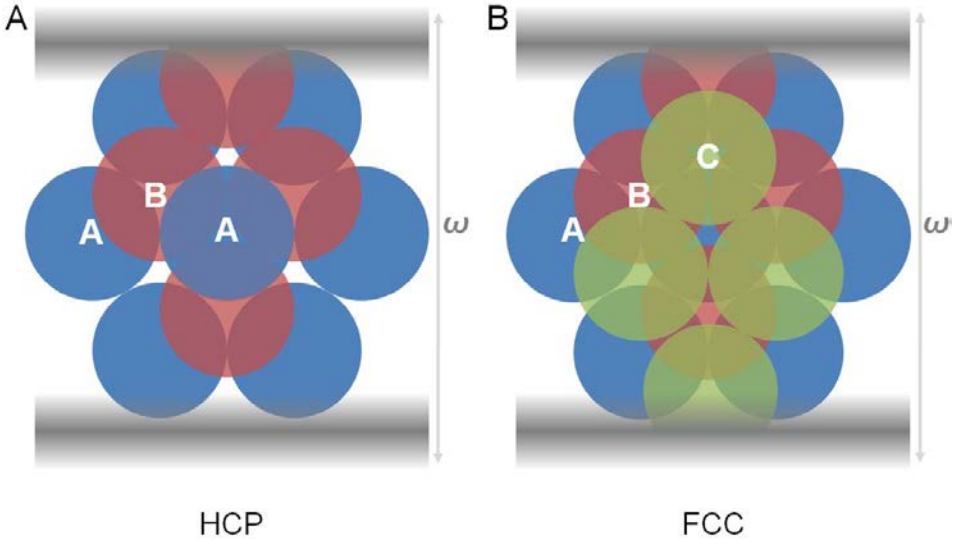


Figure 5.23: **Potential packing arrangements of droplets participating in DIBs.** (A) Schematic demonstrating how small droplets containing lipid vesicles can pack in an hexagonal close-packed (HCP) arrangement. (B) Schematic illustrating the potential for face-centred cubic (FCC) packing. The view depicted here looks down through the channel, from the top to the bottom, with ω indicating the width of the channel.

It suffices to say here that it has been demonstrated that this platform can be utilised to change droplet size, which is attractive due to the ability to produce DIBs that differ in contact area and hence membrane stress. Additionally it is possible to use this system to pack droplets into three-dimensional space, advancing the experimental possibilities for the DIB platform and enabling more sophisticated operations to be probed.

5.4.2.4 Asymmetric droplet systems

As described previously in chapter 4 (section 4.2.3), it is also possible to form asymmetric droplet interface bilayers (aDIBs). This is of key importance as it enables the researcher to create artificial membranes that more accurately mimic those present in the natural world (chapter 1, section 1.2.1.2). However, the ability to produce networks of aDIBs using a microfluidic approach has not been performed previously. This platform therefore lends itself to forming networks of aDIBs in a high-throughput manner, as droplets containing different vesicle compositions may easily be introduced into the thin PTFE tubing in an alternating fashion.

To prove this concept, a linear sequence of ABAB droplets, containing DOPC vesicles in the presence of fluorescent (A) and non-fluorescent (B) buffer (see section 5.3.2.1 for compositions), were introduced into the microfluidic device using a two channel auto-sampler (see sections 5.3.2.3 and 5.3.2.4); the experimental configuration is illustrated in figure 5.24. Specifically this included incorporating a fluorescent dye, in this instance fluorescein, into droplets and monitoring its leakage across a DOPC DIB over time. Fluorescein is well known to leak more readily across DOPC bilayers, in comparison to dyes such as CF, owing to the lack of an additional carboxylic acid group.[216] The first signs of leakage could be observed after approximately 60 minutes, in regions close to the DIBs. Importantly, the droplet sequence presented in figure 5.24 is arranged in an ABABB format, therefore influencing the rate of leakage observed. Upon inspection it is evident that there are two specific environments into which the dye can leak; the first will see leakage from two fluorescent droplets whereas the second will see contributions from just one, therefore leading to an asymmetric rate of leakage. Note that bright field images confirm that the droplet configuration is stable over the time course of the entire experiment and that experimental conditions remained the same throughout.

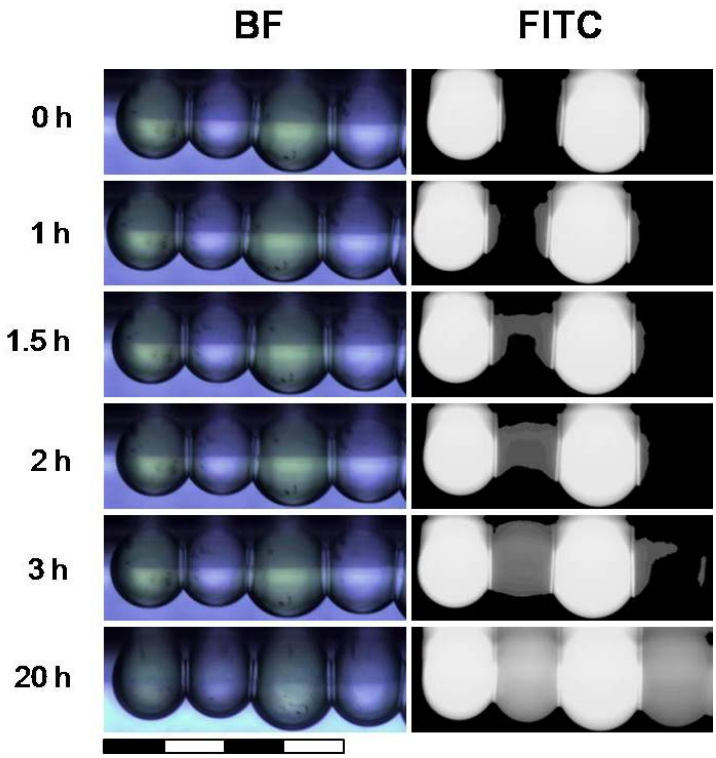


Figure 5.24: **Asymmetric DIB (aDIB) formation and fluorescein leakage assay showing successful DIB formation with DOPC.** The leakage of fluorescein across DOPC bilayers is monitored and both bright field (BF) and fluorescence (FITC, i.e. using a fluorescein isothiocyanate filter) images captured at various time points, specifically 0 h, 1 h, 1.5 h, 2 h, 3 h and 20 h; the first signs of leakage can be observed after 1 h. Note that the rate of leakage is asymmetric due to the ABABB droplet configuration, where A and B denote fluorescent and non-fluorescent droplets respectively (the fifth droplet lies outside the region of interest) and there is a slight variation in droplet size due to an artefact of the tubing at the droplet formation site. Scale bar represents 1600 μm (total length, i.e. 4 × 400 μm).

Control experiments were also performed (see figure 5.25), whereby equal volumes of fluorescein buffer and hexadecane oil were placed in the same vial and left in dark room for five days; no discernable leakage of fluorescein into the oil phase was discovered when compared to the original solutions (which had not been left in direct contact with one another).

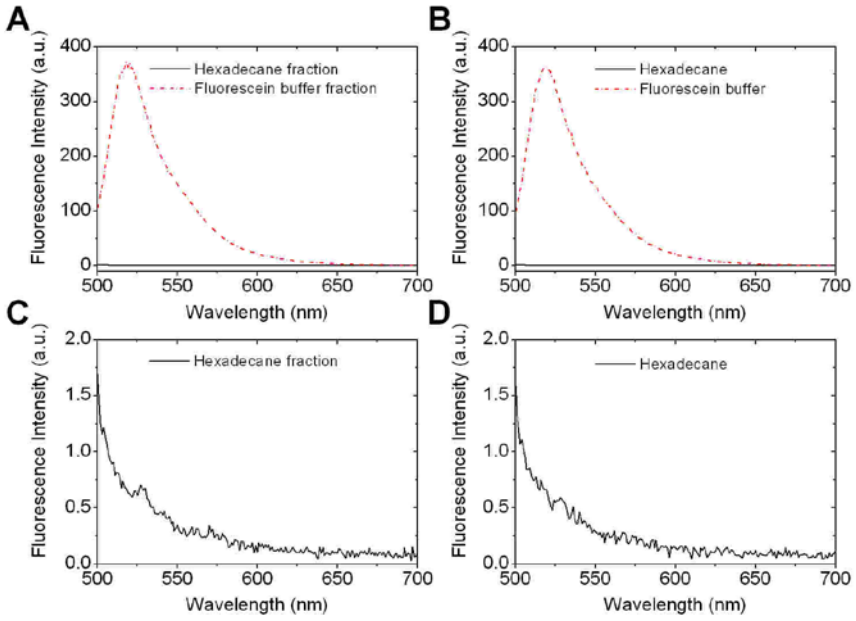


Figure 5.25: **Results of fluorescein control experiments**. (A) Graph showing the fluorescence traces for hexadecane (solid black line) and fluorescein buffer (dashed red line) fractions taken from samples that have been stored in the same glass vial for five days. (B) Graph showing the fluorescence traces for hexadecane and fluorescein buffer samples that have not been kept in contact with one another. (C) and (D) Enlarged regions of the fluorescence traces shown for hexadecane in A and B respectively.

It is apparent that microfluidic approaches will facilitate the formation of highly complex DIB systems. For example, it is clear that in addition to the simple AAAA, BBBB and ABAB systems that have been produced using this set-up, the formation of higher order systems (such as ABCABC droplet formats) are also feasible. ABAB linear arrangements allow one type of a-DIB to reside, whereas ABCABC systems enable the formation of three (between AB, BC and CA), as clarified by figure 5.26. Moreover, this approach can allow the user to tailor the format to their specific need, i.e. by introducing any combination of droplets that they may require, i.e. AABBAA etc. One can envisage future advances to extend the a-DIB linear network into the three-dimensional regime.

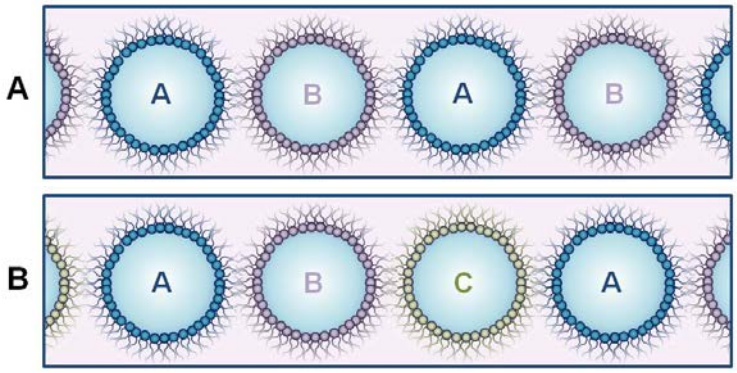


Figure 5.26: **Formation of higher order a-DIBs.** (A) ABAB formats can easily be formed, enabling the user to conduct experiments using one type of aDIB (i.e. comprised of membrane A and B only). (B) The formation of higher order aDIBs, with the inclusion of >2 droplet types can also be envisaged. The schematic illustrates how the incorporation of three types of droplet, arranged in an ABCABC format, can lead to the formation of three different aDIBs (comprised of either AB, BC or CA).

5.5 CHAPTER SUMMARY

In summary, this chapter has investigated the factors affecting successful DIB formation, in the context of a microfluidic environment, and consequently demonstrated the formation of a simple, microfluidic device (device 4, section 5.4.2) able to form DIBs in an automated manner. Moreover, this device creates a suitable environment for bringing droplets together in a controlled manner to form DIBs. This addresses problems associated with the manual manipulation of droplets, where droplets containing lipids such as DOPC are more delicate to handle and, more often than not, simply merge.

This approach enables the researcher to control droplet size with ease and hence the DIB contact area. These factors are extremely important with respect to creating stable platforms for replicating experimental conditions, in order to conduct repeat measurements and standardise assays for example. Additionally, the use of a microfluidic approach further widens the experimental opportunities, enabling the researcher to change the droplet

volume, and hence the size of the DIB contact area, as well as the complexity of the DIB network (i.e. whether the droplets stack in 1-, 2- or 3D). The latter point is dependent upon the relationship between the droplet radius and channel dimensions (height, width and length). The following statements will therefore hold:[274]

(i) For 1D stacking of droplets

$$h < 4r \quad \text{AND} \quad w < 4r \quad \text{AND} \quad l \geq 4r$$

$$\text{Therefore: } 0.25 < r/h \text{ AND } 0.25 < r/w \text{ AND } 0.25 \geq r/l$$

(ii) For 2D stacking of droplets

$$h < 4r \quad \text{AND} \quad w \geq 4r \quad \text{AND} \quad l \geq 4r$$

$$\text{Therefore: } 0.25 < r/h \text{ AND } 0.25 \geq r/w \text{ AND } 0.25 \geq r/l$$

(iii) For 3D stacking of droplets

$$h \geq (2\sqrt{6}/3)r + 2r \text{ AND } w \geq \sqrt{3}r + 2r \text{ AND } l \geq 4r$$

$$\text{i.e. } h \geq 3.63r \text{ AND } w \geq 3.73r \text{ AND } l \geq 4r$$

$$\text{Therefore: } 0.28 < r/h \text{ AND } 0.27 \geq r/w \text{ AND } 0.25 \geq r/l$$

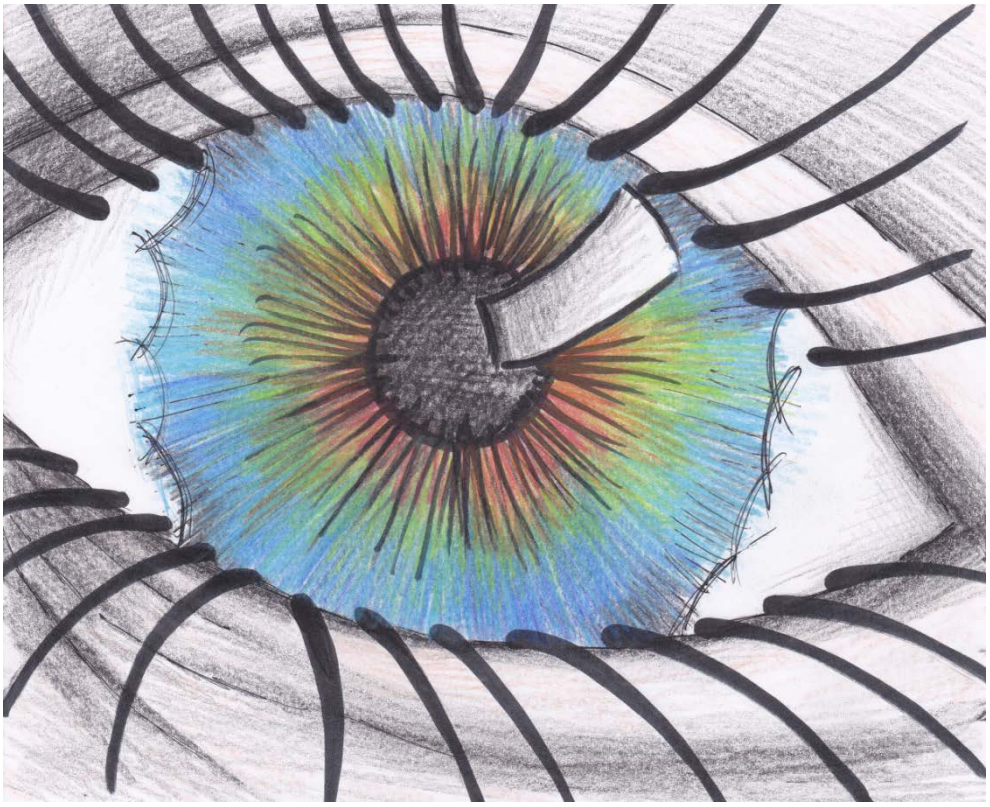
Where: r = radius of droplet

h, w, l = height, width and length of channel respectively

Furthermore, the ability to incorporate more than one type of droplet in an automated manner will open opportunities for forming more complex DIB networks, in terms of being able to alter the lipid composition present with the two monolayers of the DIB, but also in terms of incorporating droplets possessing different aqueous conditions.

Chapter 6

Future directions



"Learn from yesterday, live for today, hope for tomorrow. The important thing is not to stop questioning."

Albert Einstein

6.1 OVERVIEW

This chapter details suggestions for future work, based on the experiments detailed in this thesis.

6.2 CHAPTERS 2 AND 3

6.2.1 Critique of chapters 2 and 3

Chapter 2 has detailed the development of a CF leakage assay, for the study of drug-membrane interactions, where the reproducibility of the assay and the effect of lipid composition on the rate of CF leakage have been investigated. Importantly, chapter 3 has demonstrated the potential for translating vesicle assays, such as the CF leakage assay, into a microfluidic format, hence offering the possibility to rapidly screen drug- (and protein-) membrane interactions in high-throughput. Specifically an increase in the fluorescence lifetime with time was observed, due to the decrease in concentration of CF from the interior of the vesicle. Future work could involve extrapolating more detailed kinetic information from the lifetime data, i.e. by fitting the data to more complex functions. For example, the contribution of the long and short components to the lifetime data over time could be examined, in addition to assessing any changes in the associated amplitudes.

During device fabrication, dust particles were often trapped in the devices and thus blocked the channel. The devices used for these experiments are particularly large, hence there is a heightened probability of the dust becoming trapped, despite great care being taken during device assembly. A thin cover slip was used to seal the microfluidic chamber to meet the requirements imposed by the microscope. In retrospect, a very thin layer of PDMS could have been used instead. After PDMS is poured and allowed to set, it can be bonded immediately to another layer of PDMS without the washing steps detailed in section 3.3.2.4, thus reducing the chances of dust adsorption to the

surface of the substrates. Not only should this help to relieve any problems associated with dust becoming trapped in devices and blocking channels, it should also alleviate problems associated with adsorption of droplets to the glass substrate.

Unfortunately, due to time restrictions, the measurements described in chapter 3 only considered one drug. Ideally we wish to perform high-throughput experiments that survey the effects of many different drugs upon the membrane, such as those described in chapter 2. Therefore a dosing system may be implemented to achieve this, such as the method employed by Ismagalov's group.[275] This dosing system involves drawing a sufficient amount of drug, required for each assay, into a piece of Teflon tubing. Each solution is separated by an air bubble, which is an efficient way to prevent cross contamination between each drug solution.[276,277] Figure 6.1 illustrates the nature of the dosing system. The Teflon tubing, containing the desired drug solutions, can then be connected to the device. In order to perform dose-dependent assays, a third aqueous inlet can easily be introduced into the device design (i.e. the spare inlet, as denoted in figure 3.7, chapter 3). This third inlet would contain solely buffer solution, enabling the drug stream to be diluted by

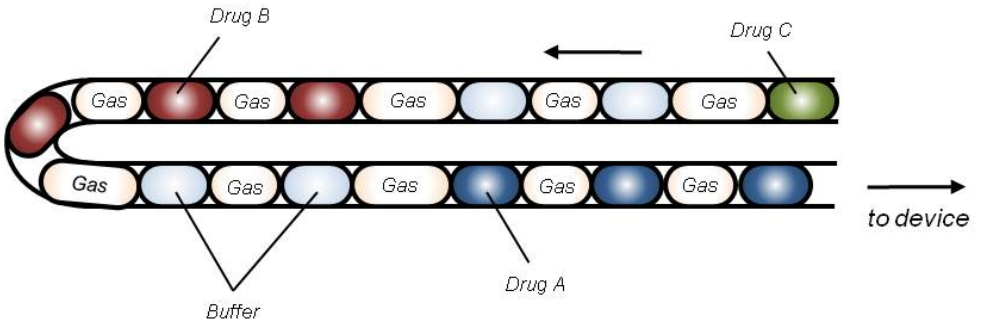


Figure 6.1: **Dosing system.** Example of how a dosing system may be used to introduce several drug samples into a device to enable high-throughput screening assay to be performed. Each sample is separated by a gas droplet, thus eliminating cross contamination between drug samples.

varying the ratio of the drug and buffer flow rates (i.e. $Aqueous_2$ and $Aqueous_3$).

The only major disadvantage of this experimental format is the need to scan across the device constantly to gain the required kinetic information. Perhaps a system whereby pairs of droplets are merged (i.e. one containing the vesicle solution and the other drug solution, thus initiating the reaction) and held in an array format, may serve as an effective way in which to exclude the need to scan constantly. The adsorbed static droplets, observed using the microfluidic format and presented in figure 3.19 (section 3.4.2.6), indicate that fluorescence lifetime imaging microscopy would be a suitable method if this approach was adopted. Additionally, more data points per experiment can easily be gained using this approach, thus enhancing the resolution of the kinetic traces. However, such a method would be limited by the field of view of the microscope and the hence the number of experiments that one can conduct at any one time. One major advantage of the current experimental design, and hence a reason justifying why it was chosen, is the fact that thousands of droplets are sampled for each data point recorded during the kinetic measurement. If the microscope stage and the syringes could be programmed to perform numerous leakage experiments, the potential for using such a technology in automated, high-throughput screens would be enhanced.

6.2.2 Non-specific binding (NSB) in positron emission tomography (PET)

Positron emission tomography (PET) is a non-invasive imaging technique, used to quantitatively measure *in vivo* processes in clinical investigations.[278-280] Compounds of therapeutic interest are labelled with radioisotopes, including ^{11}C, ^{13}N, ^{15}O and ^{18}F ($t_{1/2}$ = 20, 10, 2 and 110 min respectively).[281] Such species decay by positron emission to form a positron (and neutron), which upon collision with an electron annihilates to form two 512 eV gamma rays at 180^o

to one another. Subsequent co-incidence detection of these rays enables 3D image reconstruction.

PET studies are becoming an increasingly popular technique in which to assist the drug development process,[282] in particular CNS drug development.[283] However, non-specific binding (NSB) of radiolabelled drug molecules is often a major problem in PET imaging. High levels of NSB result in a poor signal-to-noise ratio, thus vastly reducing the quality of the PET image.[284] As a result, it is desirable to understand the molecular basis of this phenomenon and how levels of NSB can be reduced by enhancing our understanding of how drugs interact with membranes. The work detailed in chapters 2 and 3 will therefore enable high-throughput investigations to be performed, with the aim of furthering our understanding of drug-membrane interactions in general and the origins of NSB.

6.3 CHAPTERS 4 AND 5

6.3.1 Expansion of droplet interface bilayer (DIB) system for use with additional lipids

It is felt that an important area to investigate further, with respect to expanding the scope of the work described in this thesis, is the compatibility of different lipid types with DIB systems. DPhPC was the major lipid cited in the literature concerning DIBs (other than the small mole percents of fluorescently tagged lipids used to create asymmetric lipid bilayers)[205] until the work detailed in chapter 5 had been published. Such investigations are extremely important if one wishes to consider the effect of different lipid compositions on protein function, for example, hence further characterisation is required.

It is also worthy to note that not all lipids may be suitable for use in DIB formation. Here preliminary observations with 1,2-didodecanoyl-sn-glycero-3-phosphocholine (DLPC) are commented upon, with regards to suggesting

avenues for future exploration, as well as considering the possibility of using cholesterol in such systems.

6.3.1.1 DLPC observations

As a brief aside, droplets containing vesicles comprised of DLPC were administered into hexadecane during a preliminary investigation. Although this lipid can be used to form stable vesicle suspensions, unexpected observations were found to occur upon monolayer formation at the aqueous-oil interface.

Upon depositing the lipid suspension into the oil, the droplets were left as usual in order to allow time for monolayer formation. After having left the droplets for approximately one minute, it was observed that the aqueous-oil interface started to fluctuate. Images A and B in figure 6.2 illustrate this effect, where A shows the droplet after having just been submersed in the oil and B details the development of the effect over time. The red boxes in B highlight the regions where large undulations develop at the aqueous-oil interface with time. The short lipid acyl chains appear to pose a problem in this system, despite being saturated and thus potentially offering stable monolayer formation. The presence of comparatively short chain lengths may enable a degree of flexibility to reside within the system, which would otherwise not occur if, for example, DOPC or DPhPC lipids are used. It appears that the chain-chain interactions are not prevalent enough to prevent the lipid monolayer from bending both towards and away from itself, therefore enabling flexibility in the monolayer.

Interestingly if this system is left in the oil for a matter of minutes, the aqueous phase was found to 'crystallise'. Figure 6.2 C and D show a droplet containing a DLPC vesicle suspension that has been submersed in hexadecane for approximately 1 and 10 minutes respectively. It is quite apparent that the appearance of the droplet has changed dramatically within this period; a fern-like, fingering pattern was found to develop quite rapidly, noticeably growing

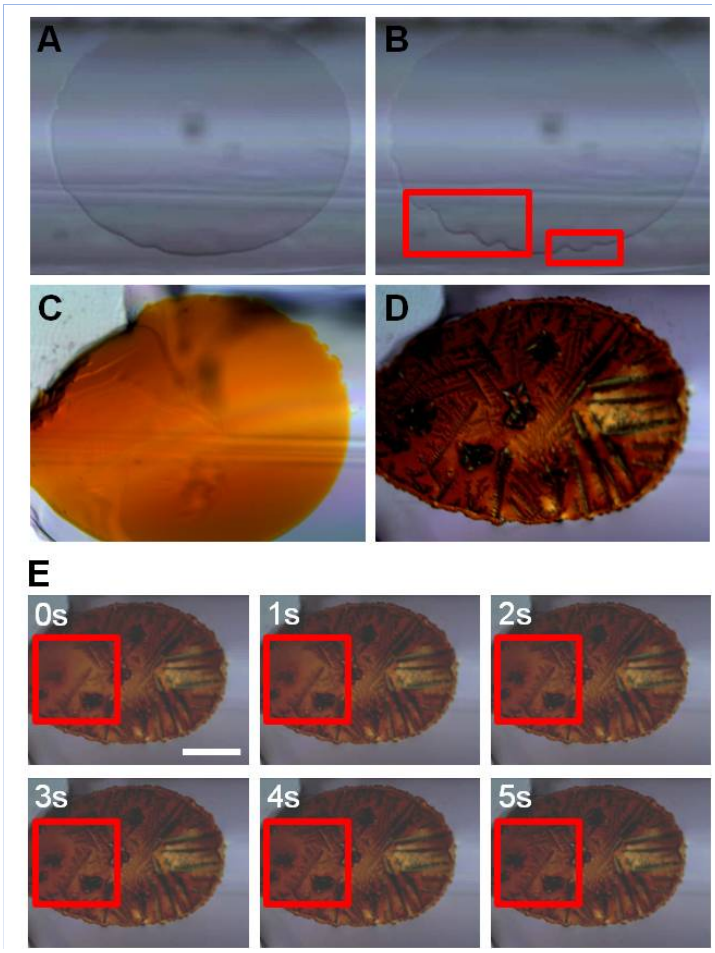


Figure 6.2: **Effects of DLPC in hexadecane.** (A) A droplet pipetted into oil and containing DLPC vesicles. (B) After having left the droplet for approximately one minute, the aqueous-oil interface started to fluctuate. The red boxes highlight the regions where large undulations develop at the aqueous-oil interface with time. (C) and (D) show a droplet containing a DLPC vesicle suspension that has been submersed in hexadecane for approximately 1 and 10 minutes respectively. The appearance of the droplet changes dramatically after 10 minutes (D). (E) Images showing the development of this change in appearance with time.

in a radiative manner. This growth phenomenon is highlighted in the images displayed in figure 6.2 E. Note that although the droplet displayed in these images contained CF-containing aqueous solution, this effect was still observed in the absence of the dye.

Although this effect was repeatable on the same day, it did not appear to be repeatable when attempted on a separate occasion, where a different stock of DLPC was employed. Whether it be that the original lipid stock had degraded, or that a very specific set of conditions are required in order to achieve this effect, it is nevertheless, very interesting. The ability to control a system in a controlled and predictable manner, for instance possessing the ability to instigate a phase change, may be highly desirable for the future development of this technology.

6.3.1.2 Cholesterol

If, for example, one would wish to produce cholesterol-containing DIBs, hence aligning the complexity of the lipid content towards that of more biologically relevant mammalian membranes, potential problems associated with cholesterol demixing into the oil phase may be foreseen. Sterol-modified phospholipids (SMLs),[285] a novel family of synthetic lipids synthesised by the Szoka group, therefore provide an opportunity to interrogate DIBs comprised of cholesterol-containing lipid mixtures in model membrane systems.

Specifically, cholesterol is chemically attached to a glycerophospholipid molecule, i.e. its chemical motif consists of cholesterol substituted at either the sn-1 or -2 positions in place of an aliphatic tail. Interestingly it has been observed that the biophysical properties of the chimeric form of cholesterol behave in a similar manner to that of free cholesterol. Although the immediate application of SMLs by the Szoka group is concerned with enhanced liposomal drug delivery, where SML-doped liposomes are highly resistant to contents leakage due to the enhanced liposome stability associated with a reduction in cholesterol exchange with biomembranes, such lipid molecules are of great interest to anyone conducting studies of a biophysical nature on model membranes. Consequently, SMLs could be of great use in the field of droplet-interface bilayers (DIBs).

6.3.1 Expansion of automated approach for DIB formation

As a result of the experiments conducted in chapter 5, future developments of automated approach for DIB formation may include the following:

1. Searching for different types of oils that are more compatible with PDMS devices.
2. Incorporating electrodes into the device design to enable conductivity measurements to be performed.
3. The ability to enable microinjection into aqueous compartments on either side of the DIB.
4. Fully characterise the effect of changing parameters such as volumetric flow rates and sampling frequencies on droplet characteristics, and also the effects of using different lipid compositions.

APPENDIX 1: Column calibration 1

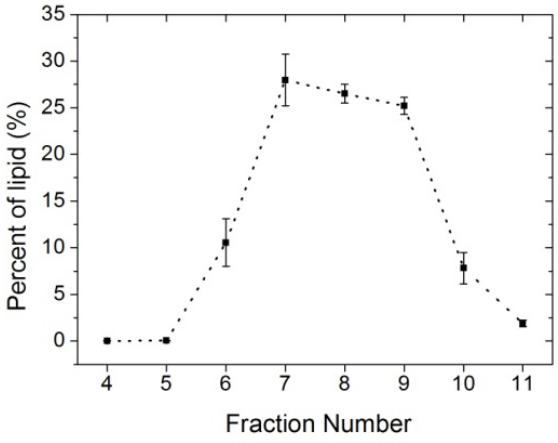


***Figure A1.1*: Column calibration.** Graph indicating the fractions into which the lipid, i.e. DOPC doped with Rh PE (99.5 : 0.5 mol %), is eluted. The fluorescence intensities of each fraction at 591 nm were measured and the percentage of lipid in each calculated accordingly. Fractions 6-9 were collated and used to perform efflux measurements. Errors represent ± 1 s.d. (n > 3). Chapter 2, section 2.4.1.2 should be consulted for further information and for discussions of the data.

Fraction Number	Lipid per fraction (%)	Error (±)	Max lipid per fraction (%)	Min lipid per fraction (%)
6	10.5	2.6	13.1	7.9
7	28.0	2.8	30.8	25.2
8	26.5	1.0	27.5	25.5
9	25.2	0.9	26.1	24.3
Total % lipid =	**90.2**		**97.5**	**82.9**

***Table A1.1:* Column calibration data 1A**. The percentage of lipid, and associated errors, for fractions 6-9 are tabulated (also displayed in the graph in figure A1.1). The total percentage of lipid collected is indicated (90.2 %), as well as the maximum and minimum percentages (within error). Hence 90.2 ± 7.3 % lipid is collected.

$[Lipid]_{(prior\ to\ elution)}$	12.5	mM
$Volume_{(prior\ to\ elution)}$	300	µl
$Moles_{(prior\ to\ elution)}$	3.8E-06	mol
$Moles_{(post\ elution)}$	3.4E-06	mol
$Volume_{(post\ elution)}$	1700	µl
$[Lipid]_{(post\ elution)}$	2.0	mM
Max $moles_{(post\ elution)}$	3.7E-06	mol
Max $volume_{(post\ elution)}$	1700	µl
Max $[lipid]_{(post\ elution)}$	2.2	mM
Min $moles_{(post\ elution)}$	3.1E-06	mol
Min $volume_{(post\ elution)}$	1700	µl
Min $[lipid]_{(post\ elution)}$	1.8	mM
$[Lipid]_{(post\ elution)}$	**2.0 ± 0.2**	**mM**

Table A1.2: **Column calibration data 1B.** The data displayed in this table indicates: i) the number of moles of lipid present prior to elution and ii) the number of moles of lipid collected post elution, and hence the lipid concentration, if 82.9, 90.2 and 97.5 % of the lipid is retrieved. This translates to a post elution lipid concentration of 2.0 ± 0.2 M.

APPENDIX 2: Exponential fit of efflux data and confirmation of drug-dye interaction

Exponential decay model used to fit efflux data:

$$y = Ae^{-\frac{x}{t}} + y_0 \qquad \text{Equation A.1}$$

Upon differentiation with respect to x, the gradient of the fit curve may be gained for any given value of x.:

$$\frac{dy}{dx} = -\frac{A}{t}e^{-\frac{x}{t}} \qquad \text{Equation A.2}$$

When $x = 0$, the following is true:

$$\frac{dy}{dx} = -\frac{A}{t}e^{-\frac{0}{t}} \qquad \text{Equation A.3}$$

$$\frac{dy}{dx} = -\frac{A}{t} \qquad \text{Equation A.4}$$

Also, when $x = 0$, $y = A + y_0$.

The graph illustrated in figure A2.1 illustrates an example of experimental efflux data that is fitted to an exponential decay model. The fitted parameters are illustrated and their use in determining the initial rate of CF efflux indicated.

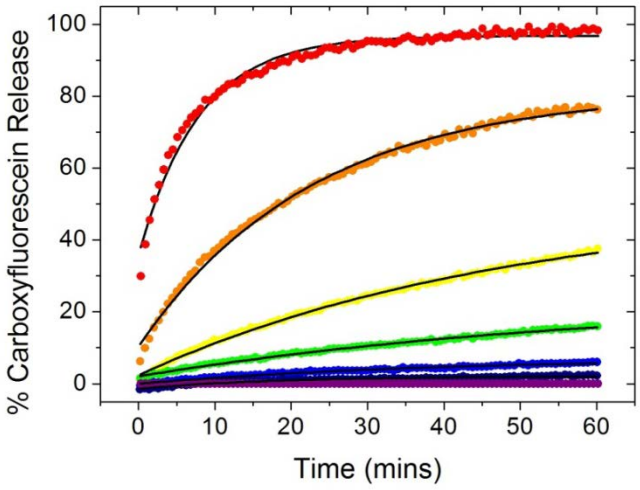


Figure A2.1: **Experimental efflux data fitted to an exponential decay model**. This figure illustrates how the efflux data, induced by the introduction of different concentrations of imipramine to CF-containing vesicles, compares to the fitted data. Drug concentrations employed (final) are represented as follows: 1.6 mM (●), 0.8 mM (●), 0.4 mM (●), 0.2 mM (●), 0.1 mM (●), 0.05 mM (●), 0 mM (●).

[Imi] (mM)	**1.6 mM**		**0.8 mM**		**0.4 mM**		**0.2 mM**		**0.1 mM**		**0.05 mM**	
Parameter	**Value**	**Error**	**Value**	**Error**	**Value**	**Error**	**Value**	**Error**	**Value**	**Error**	**Value**	**Error**
y_0	96.83	0.26	81.40	0.50	50.65	0.82	24.07	0.77	7.32	0.27	2.20	0.07
A	-61.22	0.99	-71.26	0.46	-48.28	0.74	-22.03	0.71	-7.30	0.23	-3.59	0.08
t	7.85	0.22	22.68	0.47	49.12	1.47	61.80	3.39	39.46	2.93	18.53	1.28
Chi^2/DoF	3.15		1.22		0.20		0.07		0.05		0.05	
R^2	0.98		1.00		1.00		1.00		0.98		0.95	
-A/t	7.80		3.14		0.98		0.36		0.19		0.19	

Table A2.1: **Table collating the different parameters associated with an exponential decay fit of the efflux data displayed in figure A2.1.**

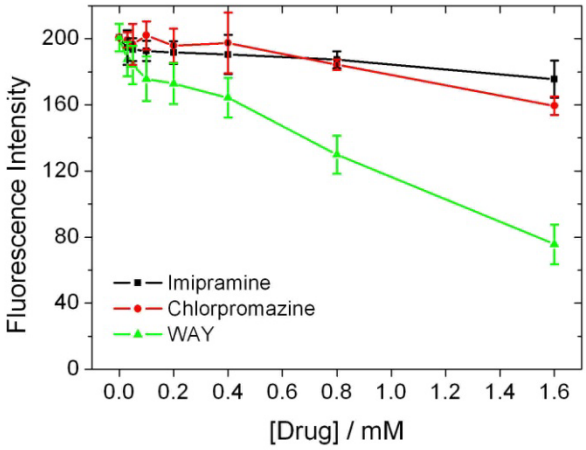


Figure A2.2: **Control data confirming drug-dye interaction.** This graph illustrates the influence of drug concentration (for imipramine, chlorpromazine and WAY) on the fluorescence intensity of CF (concentration of CF = 10 μm), confirming the drug-dye interaction in the absence of lipid vesicles (where the concentration of drug is above the CMC). This data concurs with the trends observed in interfacial surface tension measurements (see section 2.4.2) and mirrors the CMC data. Notably, the CMC of WAY is the lowest, at ca. 0.4 mM (see figure 2.16, section 2.4.2) - dye is therefore sequestered by micelles at drug concentrations greater than the CMC. Chlorpromazine possesses a CMC of 1.4 mM (see figure 2.16, section 2.4.2) and imipramine has not yet reached its CMC at a drug concentration equal to 1.6 mM.

APPENDIX 3: Column calibration 2

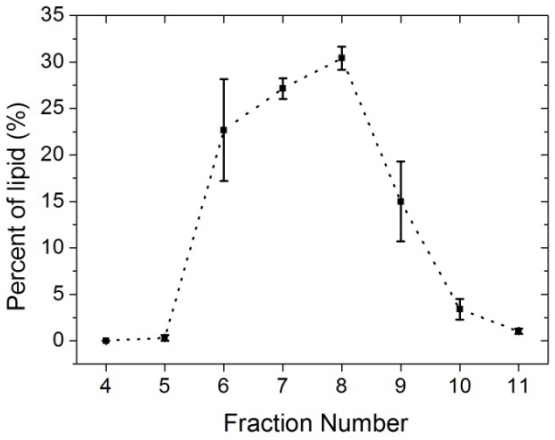


***Figure A3.1*: Column calibration 2.** Graph indicating the fractions into which the lipid, i.e. DOPC:DOPE doped with Rh PE (79.5 : 20 : 0.5 mol %), is eluted. The fluorescence intensities of each fraction at 591 nm were measured and the percentage of lipid in each calculated accordingly. Fractions 6-9 were collated and used to perform efflux measurements. Errors represent ± 1 s.d. (n > 3). Chapter 2, section 2.4.3.1 should be consulted for further information and for discussions of the data.

Fraction Number	Lipid per fraction (%)	Error (±)	Max lipid per fraction (%)	Min lipid per fraction (%)
6	22.7	5.5	28.2	17.2
7	27.1	1.1	28.3	26.0
8	30.4	1.2	31.6	29.2
9	15.0	4.3	19.3	10.7
Total % lipid =	**95.2**		**107.4**	**83.1**

***Table A3.1:* Column calibration data 2A.** The percentage of lipid, and associated errors, for fractions 6-9 are tabulated (also displayed in the graph in figure A3.1). The total percentage of lipid collected is indicated (95.2 %), as well as the maximum and minimum percentages (within error). Hence 95.2 ± 12.2 % lipid is collected.

[Lipid] (prior to elution)	12.5	mM
Volume (prior to elution)	300	µl
Moles (prior to elution)	3.8E-06	mol
Moles (after elution)	3.6E-06	mol
Volume (after elution)	1700	µl
[Lipid] (after elution)	2.1	mM
Max moles (after elution)	4.0E-06	mol
Max volume (after elution)	1700	µl
Max [Lipid] (after elution)	2.4	mM
Min moles (after elution)	3.1E-06	mol
Min volume (after elution)	1700	µl
Min [Lipid] (after elution)	1.8	mM
[Lipid] (after elution)	**2.1 ± 0.3**	**mM**

Table A3.2: **Column calibration data 2B.** The data displayed in this table indicates: i) the number of moles of lipid present prior to elution and ii) the number of moles of lipid collected post elution, and hence the lipid concentration, if 83.1, 95.2 and 107.4 % of the lipid is retrieved. This translates to a post elution lipid concentration of 2.1 ± 0.3 mM.

APPENDIX 4: CF-encapsulated DOPC : DOPE vesicles and chlorpromazine

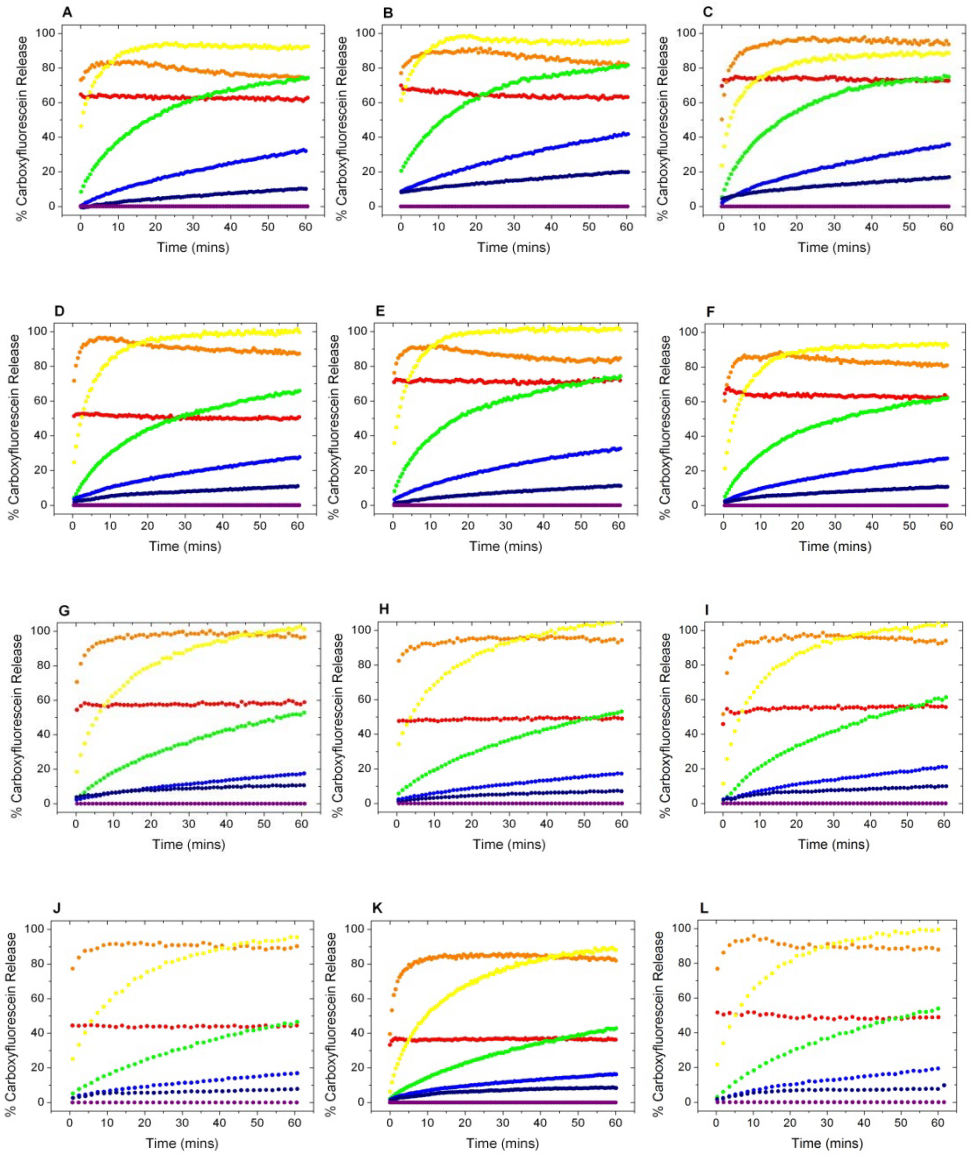


Figure A4.1: **Efflux of carboxyfluorescein from vesicle lumens upon the addition of chlorpromazine; dependence on mole percent of DOPE in a DOPC bilayer.** Three repeats of the data are included. The graphs relate to the following: A-C = DOPC : DOPE (100 : 0), D-F = DOPC : DOPE (80 : 20), G-I = DOPC : DOPE (60 : 40) and J-L = DOPC : DOPE (40 : 60). Chlorpromazine concentrations employed (final) are represented as follows: 1.6 mM (●), 0.8 mM (●), 0.4 mM (●), 0.2 mM (●),0.1 mM (●), 0.05 mM (●), 0 mM (●).

APPENDIX 5: CF-encapsulated DOPC : DOPE vesicles and WAY

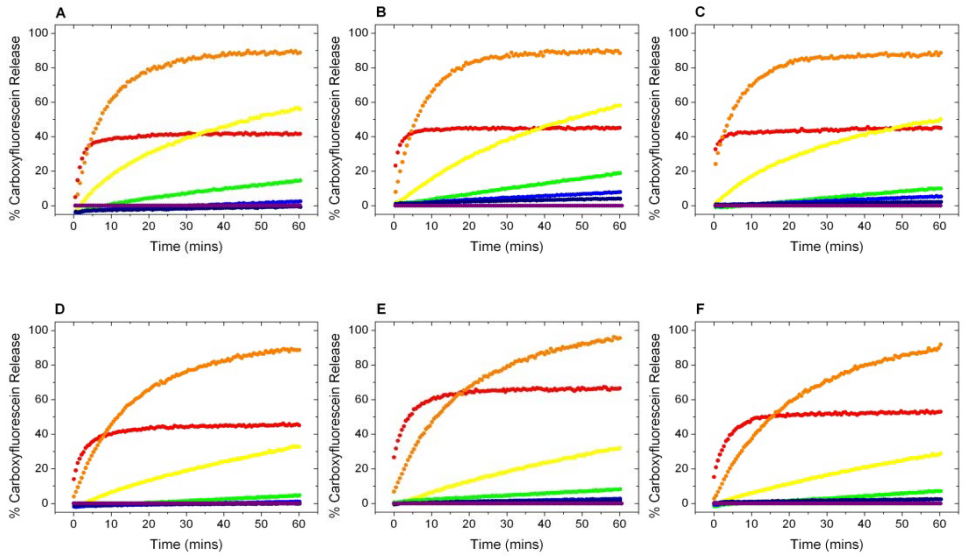


Figure A5.1: **Efflux of carboxyfluorescein from vesicle lumens upon the addition of WAY; dependence on mole percent of DOPE in a DOPC bilayer.** Three repeats of the data are included. The graphs relate to the following: A-C = DOPC : DOPE (100 : 0) and D-F = DOPC : DOPE (80 : 20). WAY concentrations employed (final) are represented as follows: 1.6 mM (●), 0.8 mM (●), 0.4 mM (●), 0.2 mM (●), 0.1 mM (●), 0.05 mM (●), 0 mM (●).

APPENDIX 6: CF-encapsulated DOPC : DOPE vesicles and imipramine

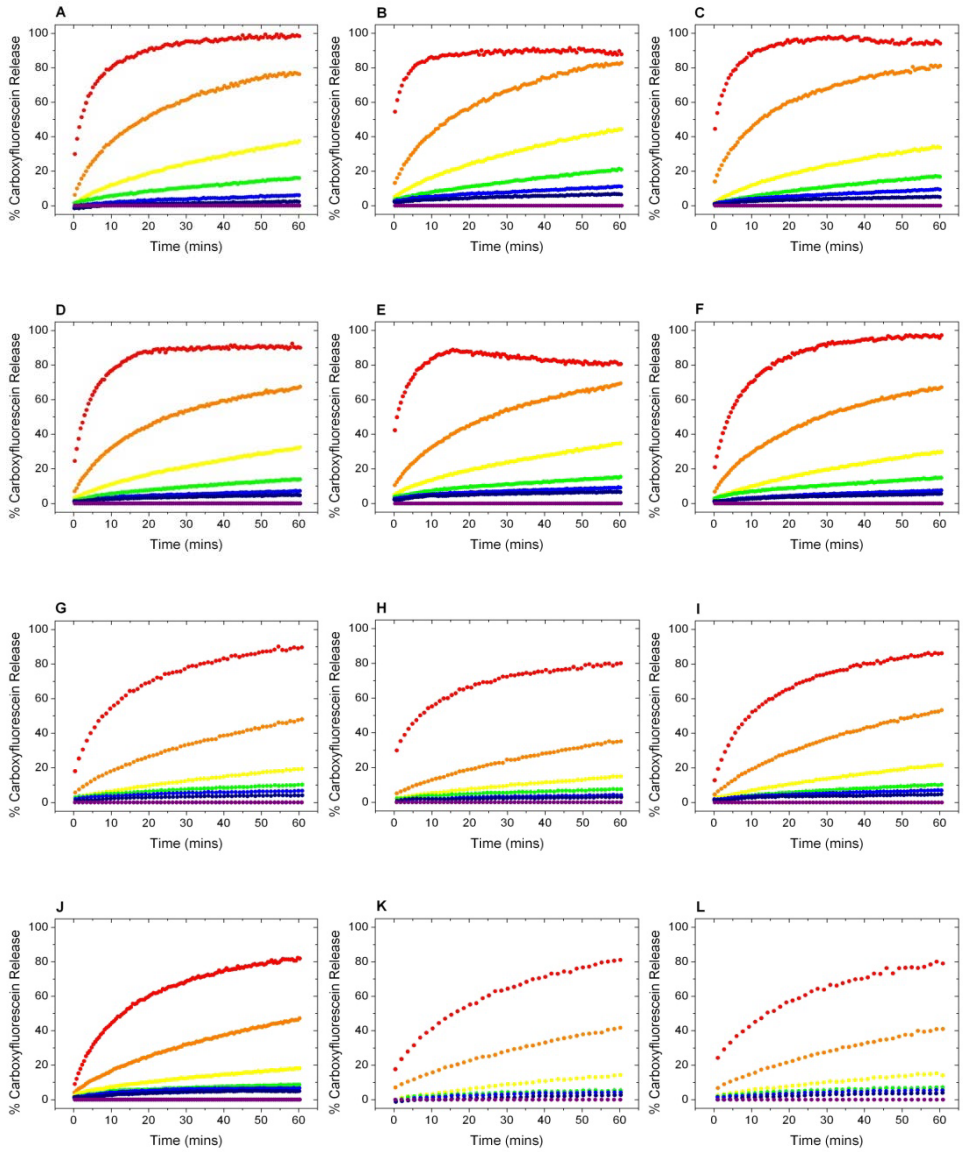


Figure A6.1: **Efflux of carboxyfluorescein from vesicle lumens upon the addition of imipramine; dependence on mole percent of DOPE in a DOPC bilayer.** Three repeats of the data are included. The graphs relate to the following: A-C = DOPC : DOPE (100 : 0), D-F = DOPC : DOPE (80 : 20), G-I = DOPC : DOPE (60 : 40) and J-L = DOPC : DOPE (40 : 60). Imipramine concentrations employed (final) are represented as follows: 1.6 mM (●), 0.8 mM (●), 0.4 mM (●), 0.2 mM (●), 0.1 mM (●), 0.05 mM (●), 0 mM (●).

APPENDIX 7: Fluorescence lifetime data for the carboxyfluorescein calibration experiment performed in a cuvette format

			Repeat 1		Repeat 2	
Sample	**[CF] (M)**	**-log ([CF] (M))**	**τ_1 (ns)**	**χ^2**	**τ_1 (ns)**	**χ^2**
1	5.0E-02	1.30	0.28	1.14	0.27	1.43
2	2.5E-02	1.60	1.12	1.10	1.03	1.26
3	6.3E-03	2.20	6.95	1.74	7.20	1.24
4	1.6E-03	2.80	9.51	1.30	10.3	1.16
5	3.9E-04	3.41	7.22	1.31	7.60	0.95
6	1.0E-04	4.00	6.04	1.30	5.90	1.04
7	2.0E-05	4.70	5.18	1.31	4.93	1.02
8	6.0E-06	5.22	4.61	1.68	4.56	1.03
9	2.0E-06	5.70	4.46	1.69	4.67	1.07
10	4.0E-07	6.40	4.45	1.57	4.47	1.13

Table A7.1: **Single exponential fit to carboxyfluorescein calibration data (in bulk), thus yielding the corresponding fluorescence lifetime (τ_1) and χ^2 values.**

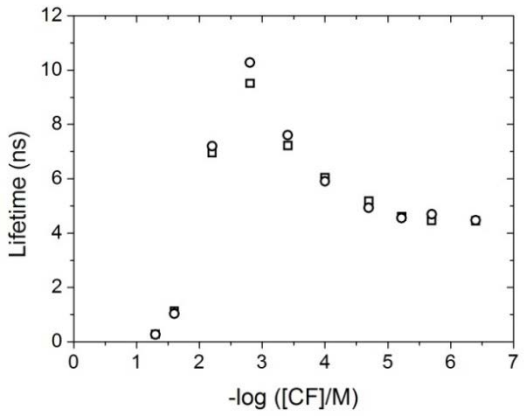


Figure A7.1: **The fluorescence lifetime gained for each of the ten solutions of carboxyfluorescein, present at different concentrations, based on the data provided in table A7.1 (above).** Chapter 3, section 3.4.2.1 should be consulted for further information and for discussions of the data.

APPENDIX 8: Fluorescence lifetime data for the carboxyfluorescein leakage assay performed using imipramine in a cuvette format

Time (mins)	τ_1 (ps)	χ^2
0	2729	1.17
2	3542	1.46
4	3724	1.58
6	3804	1.06
8	4115	1.52
10	4098	1.28
12	4282	1.40
14	4080	1.30
16	4035	1.04
18	3973	1.00
20	3951	1.00
22	4125	1.26
24	4062	1.07
26	4054	1.21
28	4071	1.05
30	3936	1.12

Table A8.1: **Single exponential fit to data gained during the carboxyfluorescein leakage assay, performed using imipramine (in bulk), thus yielding the corresponding fluorescence lifetime (τ_1) and χ^2 values.**

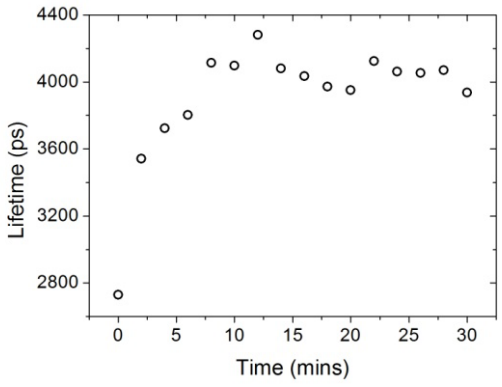


Figure A8.1: **The change in fluorescence lifetime over time upon addition of imipramine to a DOPC vesicular solution (1.6 and 0.1 mM respectively, final concentrations), based on the data provided in table A8.1 (above).** Chapter 3, section 3.4.2.2 should be consulted for further information and for discussions of the data.

APPENDIX 9: Fluorescence lifetime control data performed in a cuvette format and used to accompany the carboxyfluorescein leakage assay

Time (mins)	α_1	τ_1 (ps)	α_2	τ_2 (ps)	χ^2
0	56.4	439	43.6	4107	1.32
3	48.1	354	51.9	3729	1.21
7	51.4	590	48.6	4403	1.37
17	50.7	625	49.3	4630	1.37
31	45.0	447	55.0	3877	1.15

Table A9.1: **Double exponential fit to control data, where the fluorescence lifetime of carboxyfluorescein-containing vesicles (DOPC, 0.1 mM see chapter 3, section 3.3.2.5) in solution is measured at various intervals during the time course of the experiment.** The corresponding fluorescence lifetime (τ_1, τ_2) and χ^2 values are displayed.

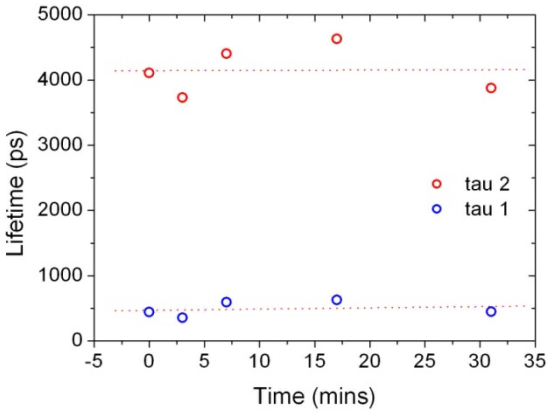


Figure A9.1: **The change in fluorescence lifetime over time, based on the data provided in table A9.1 (above), of carboxyfluorescein-containing vesicles suspended in solution (DOPC, 0.1 mM see chapter 3, section 3.3.2.5) i.e. where no drug, solely buffer has been introduced.** Chapter 3, section 3.4.2.2 should be consulted for further information and for discussions of the data.

APPENDIX 10: Fluorescence lifetime data for the carboxyfluorescein calibration experiment performed in a microfluidic format

Sample	[CF] (M)	-log [CF]	τ_1 (ns)
1	5.0E-02	1.30	0.20021
2	2.5E-02	1.60	0.82257
3	6.3E-03	2.20	3.62383
4	1.6E-03	2.80	4.02521
5	3.9E-04	3.41	3.85486
6	1.0E-04	4.00	3.7749
7	2.0E-05	4.70	-
8	6.0E-06	5.22	3.80569

Table A10.1: **Single exponential fit to carboxyfluorescein calibration data (in a microfluidic format), thus yielding the corresponding fluorescence lifetime (τ_1).**

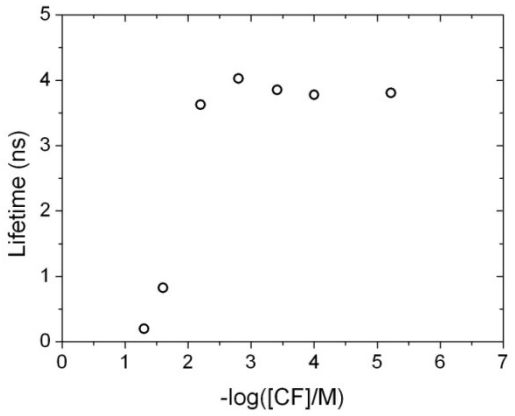


Figure A10.1: **The fluorescence lifetime gained for each of the ten solutions of carboxyfluorescein, present at different concentrations, based on the data provided in table A10.1 (above).** Chapter 3, section 3.4.2.3 should be consulted for further information and for discussions of the data.

APPENDIX 11: Fluorescence lifetime data (and fits to data) for the carboxyfluorescein leakage assay performed using imipramine in a microfluidic format

Time (mins)	1.6 mM Imipramine τ_1 (ps)	0.8 mM Imipramine τ_1 (ps)
0	841	780
0.5	987	-
0.9	834	811
1.4	950	-
2.1	-	829
1.8	1159	-
2.7	1345	913
3.6	1285	1056
4.5	1483	942

Table A11.1: **Single exponential fit to the data gained when carboxyfluorescein leakage is induced by imipramine in a microfluidic format.** Both 1.6 and 0.8 mM imipramine solutions (final concentrations) were employed; the corresponding fluorescence lifetime values (τ_1) are displayed.

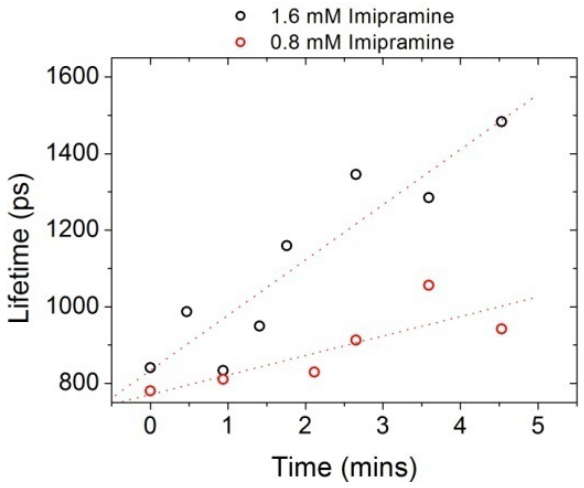


Figure A11.1: **The change in fluorescence lifetime over time upon addition of imipramine solutions (1.6 and 0.8 mM, final concentration) to a DOPC vesicular solution (0.1 mM, final concentration), based on the data provided in table A11.1.** Chapter 3, section 3.4.2.4 should be consulted for further information and for discussions of the data.

Linear Regression for 1.6 mM Imipramine:

Y = A + B * X

Parameter	Value	Error
A	833.79665	57.90412
B	144.13603	23.97019

R	SD	N	P
0.92611	99.413098		9.53528E-4

Table A11.2: **Linear regression associated with the data displayed in figure A11.1.**

Linear Regression for 0.8 mM Imipramine:

Y = A + B * X

Parameter	Value	Error
A	771.09383	47.71553
B	50.92917	17.26231

R	SD	N	P
0.82774	64.490416		0.04196

Table A11.3: **Linear regression associated with the data displayed in figure A11.1.**

APPENDIX 12: Fluorescence intensity data (and fits to data) for the carboxyfluorescein leakage assay performed using imipramine

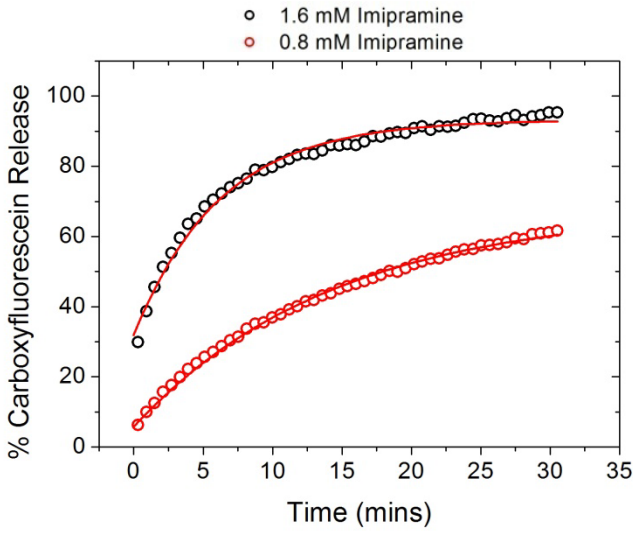


Figure A12.1: **The change in fluorescence intensity over time upon addition of imipramine solutions (1.6 and 0.8 mM, final concentration) to a DOPC vesicular solution (0.1 mM, final concentration).** Chapter 3, section 3.4.2.4 should be consulted for further information and for discussions of the data.

Data: 1.6 mM Imipramine, Model: ExpDec1

Equation: y = A1*exp(-x/t1) + y0

Chi^2/DoF = 2.60918

R^2 = 0.98936

y0	93.29301	0.44732
A1	-61.40944	1.01347
t1	6.2097	0.22224

-A/t = gradient of the tangent at (0, A+y0)

Table A12.1: **Fitted exponential decay associated with the data displayed in figure A12.1.**

Data: 0.8 mM Imipramine, Model: ExpDec1

Equation: y = A1*exp(-x/t1) + y0

Chi^2/DoF = 1.37612

R^2 = 0.99491

y0	67.90723	1.04351
A1	-62.11674	0.89019
t1	14.40883	0.5861

-A/t = gradient of the tangent at (0, A+y0)

Table A12.2: **Fitted exponential decay associated with the data displayed in figure A12.1.**

APPENDIX 13: Properties of droplets 1-6

Drop 1: Non-fluorescent		**Drop 2: Fluorescent Drop**		**DIB Contact area**	
Diameter =	689 μm	Diameter =	587 μm	Diameter =	109 μm
	0.07 cm		0.06 cm		0.01 cm
Radius =	345 μm	Radius =	294 μm	Radius =	55 μm
	0.03 cm		0.03 cm		0.01 cm
Volume =	1.7E-04 ml	**Volume =**	1.1E-04 ml	**Area =**	1.E-04 cm^2
	0.17 μl		0.11 μl		
Drop 3: Non-fluorescent		**Drop 4: Fluorescent Drop**		**DIB Contact area**	
Diameter =	699 μm	Diameter =	547 um	Diameter =	117 μm
	0.07 cm		0.05 cm		0.01 cm
Radius =	349 μm	Radius =	274 μm	Radius =	59 μm
	0.03 cm		0.03 cm		0.01 cm
Volume =	1.8E-04 ml	**Volume =**	8.6E-05 ml	**Area =**	1.E-04 cm^2
	0.18 μl		0.09 μl		
Drop 5: Non-fluorescent		**Drop 6: Fluorescent Drop**		**DIB Contact area**	
Diameter =	539 μm	Diameter =	631 μm	Diameter =	106 μm
	0.05 cm		0.06 cm		0.01 cm
Radius =	270 μm	Radius =	316 μm	Radius =	53 μm
	0.03 cm		0.03 cm		0.01 cm
Volume =	8.2E-05 ml	**Volume =**	1.3E-04 ml	**Area =**	1.E-04 cm^2
	0.08 μl		0.13 μl		

Table A13.1: **Properties of droplets 1-6.** The diameter, radius and volumes of droplets 1-6 are displayed in the table. These properties relate to the experiments discussed in chapter 4, section 4.4.2.3.

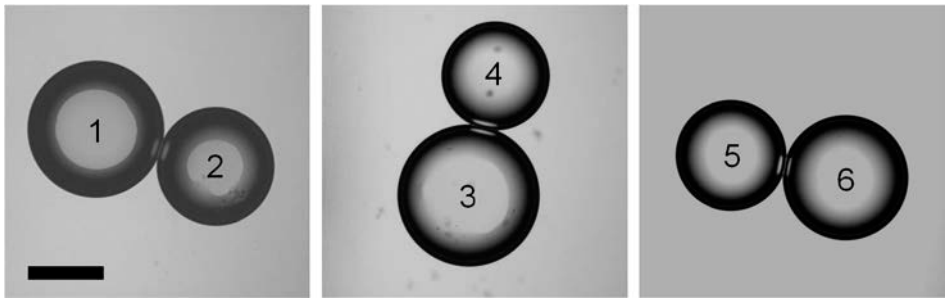


Figure A13.1: **Bright field images of droplets 1-6.** This figure displays the nature of droplets 1-6, which relates to the experiments discussed in chapter 4, section 4.4.2.3. Scale bar represents 400 μm.

APPENDIX 14: Bright field and fluorescence images of droplets participating in DIB leakage experiments.

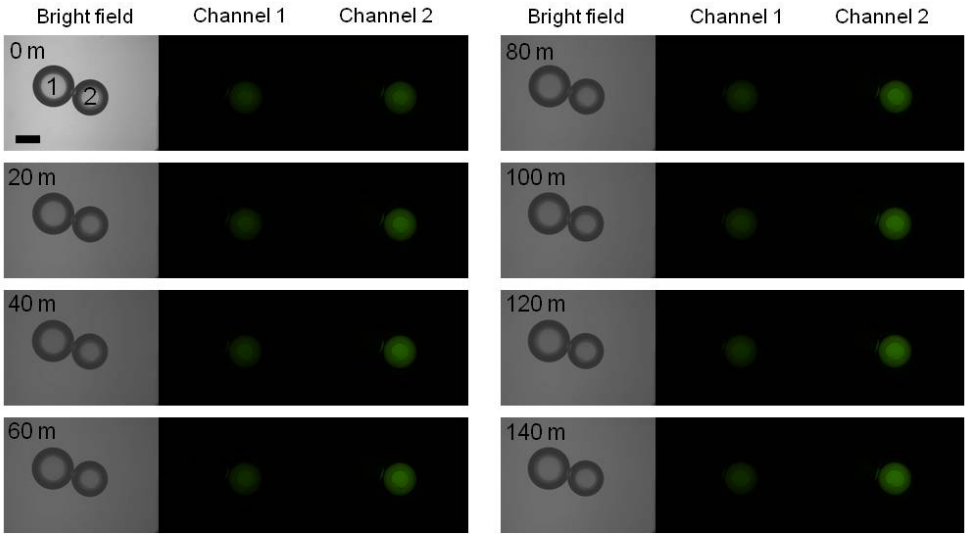


Figure A14.1: **Droplets 1 and 2.** Bright field and fluorescence images (see chapter 4, section 4.3.2.6 for specific details relating to the fluorescence channels 1 and 2) of droplets 1 and 2 participating in DIB leakage experiments described in chapter 4, section 4.4.2.3. Scale bars represent 400 μm.

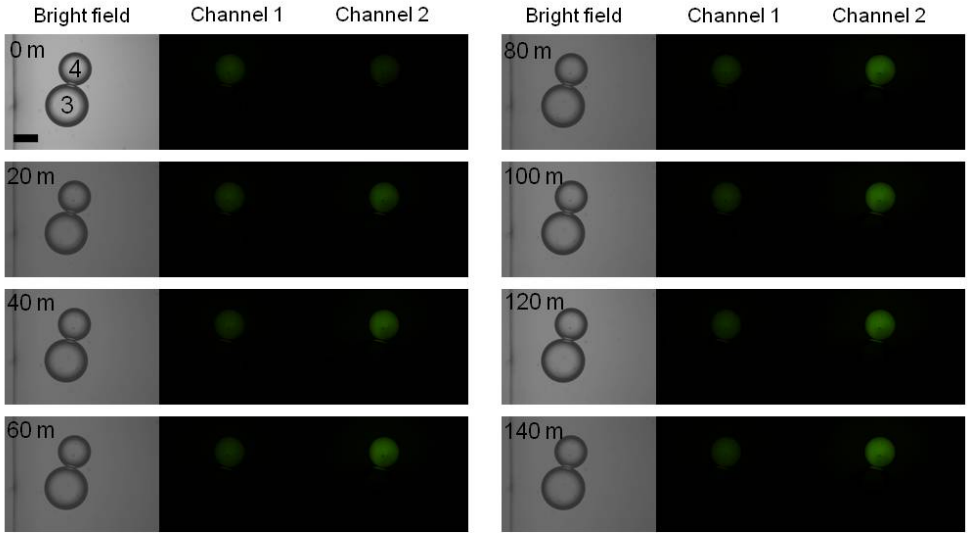


Figure A14.2: **Droplets 3 and 4.** Bright field and fluorescence images (see chapter 4, section 4.3.2.6 for specific details relating to the fluorescence channels 1 and 2) of droplets 3 and 4 participating in DIB leakage experiments described in chapter 4, section 4.4.2.3. Scale bars represent 400 μm.

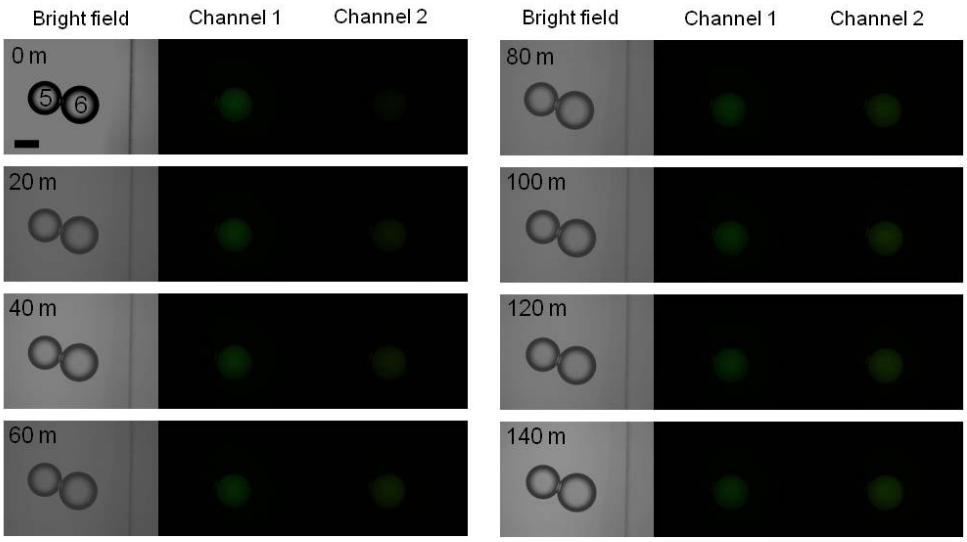


Figure A14.3: **Droplets 5 and 6.** Bright field and fluorescence images (see chapter 4, section 4.3.2.6 for specific details relating to the fluorescence channels 1 and 2) of droplets 5 and 6 participating in DIB leakage experiments described in chapter 4, section 4.4.2.3. Scale bars represent 400 μm.

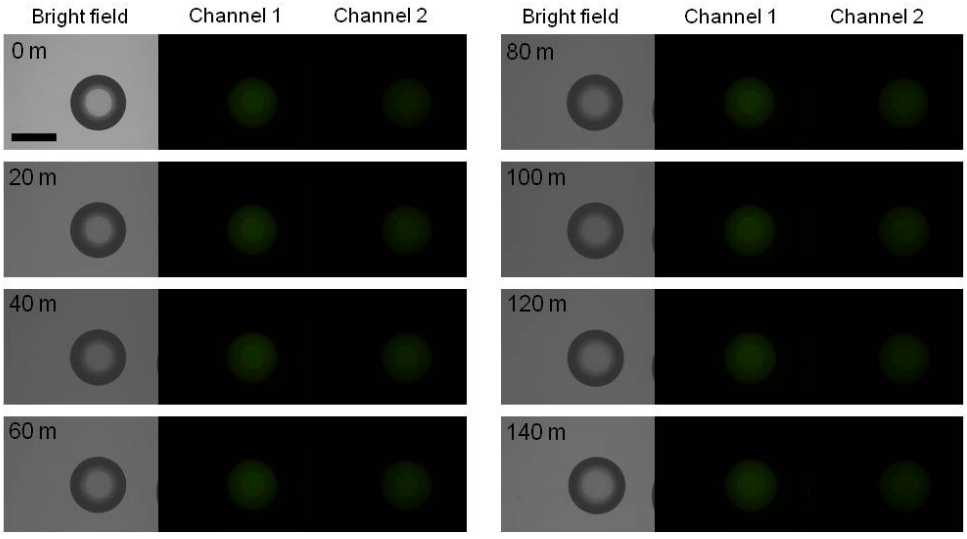


Figure A14.4: **Control droplets.** Bright field and fluorescence images (see chapter 4, section 4.3.2.6 for specific details relating to the fluorescence channels 1 and 2) of an exemplar control droplet, used during experiments described in chapter 4, section 4.4.2.3. Scale bars represent 400 μm.

BIBLIOGRAPHY

1. Attard, G.S., Templer, R.H., Smith, W.S., Hunt, A.N. & Jackowski, S. Modulation of CTP:phosphocholine cytidylyltransferase by membrane curvature elastic stress. *Proc. Natl. Acad. Sci.* **97**, 9032-9036 (2000).
2. Phillips, R., Ursell, T., Wiggins, P. & Sens, P. Emerging roles for lipids in shaping membrane-protein function. *Nature.* **459**, 379-385 (2009).
3. Cevc, C. *Phospholipids Handbook*, (Marcel Deckker, Inc., New York, 1993).
4. Hirschmann, H. The nature of substrate asymmetry in stereoselective reactions. *J. Biol. Chem.* **235**, 2762-2767 (1960).
5. Sprong, H., van der Sluijs, P. & van Meer, G. How proteins move lipids and lipids move proteins. *Nat. Rev. Mol. Cell. Biol.* **2**, 504-513 (2001).
6. van Meer, G. Lipids of the golgi membrane. *Trends Cell Biol.* **8**, 29-33 (1998).
7. Alberts, B. et al. *Molecular Biology of the Cell*, (Garland Science, New York, 2002).
8. Scarlata, S.F. Effects of cholesterol on membrane surfaces as studied by high-pressure fluorescence spectroscopy. *Biophys. Chem.* **69**, 9-21 (1997).
9. Falck, E., Patra, M., Karttunen, M., Hyvönen, M.T. & Vattulainen, I. Impact of cholesterol on voids in phospholipid membranes. *J. Chem. Phys.* **121**, 12676-12689 (2004).
10. Nishizuka, Y. Intracellular signaling by hydrolysis of phospholipids and activation of protein kinase C. *Science.* **258**, 607-614 (1992).
11. O'Shea, P. Physical landscapes in biological membranes: physico-chemical terrains for spatio-temporal control of biomolecular interactions and behaviour. *Philos. T. Roy. Soc. A.* **363**, 575-588 (2005).
12. Ishii, I., Fukushima, N., Ye, X. & Chun, J. Lysophospholipid receptors: signaling and biology. *Annu. Rev. Biochem.* **73**, 321-354 (2004).

13. Berridge, M.J. Inositol trisphosphate and diacylglycerol as second messengers. *Biochem. J.* **220**, 345-360 (1984).
14. Pike, L.J. Lipid rafts: bringing order to chaos. *J. Lipid. Res.* **44**, 655-667 (2003).
15. Binder, W.H., Barragan, V. & Menger, F.M. Domains and rafts in lipid membranes. *Angew. Chem. Int. Ed.* **42**, 5802-5827 (2003).
16. Giocondi, M.-C. et al. Surface topography of membrane domains. *Biochim. Biophys. Acta.* **1798**, 703-718 (2010).
17. Danielsen, E.M. Involvement of detergent-insoluble complexes in the intracellular transport of intestinal brush border enzymes. *Biochemistry.* **34**, 1596-1605 (1995).
18. Sargiacomo, M., Sudol, M., Tang, Z. & Lisanti, M.P. Signal transducing molecules and glycosyl-phosphatidylinositol-linked proteins form a caveolin-rich insoluble complex in MDCK cells. *J. Cell. Biol.* **122**, 789-807 (1993).
19. Skibbens, J.E., Roth, M.G. & Matlin, K.S. Differential extractability of influenza virus hemagglutinin during intracellular transport in polarized epithelial cells and nonpolar fibroblasts. *J. Cell. Biol.* **108**, 821-832 (1989).
20. Simons, K. & Ikonen, E. Functional rafts in cell membranes. *Nature.* **387**, 569-572 (1997).
21. Simons, K. Lipid rafts and signal transduction. *Nat. Rev. Mol. Cell. Biol.* **1**, 31-41 (2000).
22. Singer, S.J. & Nicolson, G.L. The fluid mosaic model of the structure of cell membranes. *Science.* **175**, 720-731 (1972).
23. Saxton, M.J. Lateral diffusion in an archipelago. The effect of mobile obstacles. *Biophys. J.* **52**, 989-997 (1987).
24. Jacobson, K., Sheets, E.D. & Simson, R. Revisiting the fluid mosaic model of membranes. *Science.* **268**, 1441-1442 (1995).

25. Chandler, D. Interfaces and the driving force of hydrophobic assembly. *Nature.* **437**, 640-647 (2005).
26. Branton, D. Membrane structure. *Ann. Rev. Plant. Physio.* **20**, 209-238 (1969).
27. Mathews, C.K., van Holde, K.E. & Ahern, K.G. *Biochemistry*, (Addison Wesley Longman, Inc., San Francisco, 2000).
28. van Meer, G. Cellular lipidomics. *EMBO J.* **24**, 3159-3165 (2005).
29. van Meer, G. Lipid map of the mammalian cell. *J. Cell. Sci.* **124**, 5-8 (2011).
30. Dowhan, W. Molecular basis for membrane phospholipid diversity: why are there so many lipids? *Annu. Rev Biochem.* **66**, 199-232 (1997).
31. Dennis, E.A. Diversity of group types, regulation, and function of phospholipase A2. *J. Biol. Chem.* **269**, 13057-13060 (1994).
32. Callisen, T.H. & Talmon, Y. Direct imaging by cryo-TEM shows membrane break-up by phospholipase A2 enzymatic activity. *Biochemistry.* **37**, 10987-10993 (1998).
33. Balsinde, J., Balboa, M.A., Insel, P.A. & Dennis, E.A. Regulation and inhibition of phospholipase A2. *Annu. Rev. Pharmacol. Toxicol.* **39**, 175-189 (1999).
34. Jones, D., Morgan, C. & Cockcroft, S. Phospholipase D and membrane traffic. Potential roles in regulated exocytosis, membrane delivery and vesicle budding. *Biochim. Biophys. Acta.* **1439**, 229-244 (1999).
35. Morris, A.J., Engebrecht, J. & Frohman, M.A. Structure and regulation of phospholipase D. *Trends Pharmacol. Sci.* **17**, 182-185 (1996).
36. Singer, W.D., Brown, H.A. & Sternweis, P.C. Regulation of eukaryotic phosphatidylinositol-specific phospholipase C and phospholipase D. *Annu. Rev. Biochem.* **66**, 475-509 (1997).
37. van Meer, G., Voelker, D.R. & Feigenson, G.W. Membrane lipids: where they are and how they behave. *Nat. Rev.* **9**, 112-124 (2008).

38. Holthuis, J.C.M., Pomorski, T., Raggers, R.J., Sprong, H. & Van Meer, G. The organizing potential of sphingolipids in intracellular membrane transport. *Physiol. Rev.* **81**, 1689-1723 (2001).

39. Levin, I.W. Two types of hydrocarbon chain interdigitation in sphingomyelin bilayers. *Biochem.* **24**, 6282-6286 (1985).

40. Bretscher, M.S. Membrane structure: some general principles. *Science.* **181**, 622-629 (1973).

41. Boon, J.M. & Smith, B.D. Chemical control of phospholipid distribution across bilayer membranes. *Med. Res. Rev.* **22**, 251-281 (2002).

42. Verkleij, A.J. & Post, J.A. Membrane phospholipid asymmetry and signal transduction. *J. Membrane. Biol.* **178**, 1-10 (2000).

43. Uchida, K., Emoto, K., Daleke, D.L., Inoue, K. & Umeda, M. Induction of apoptosis by phosphatidylserine. *J. Biochem.* **123**, 1073-1078 (1998).

44. Bevers, E.M., Comfurius, P., Dekkers, D.W.C. & Zwaal, R.F.A. Lipid translocation across the plasma membrane of mammalian cells. *Biochim. Biophys. Acta.* **1439**, 317-330 (1999).

45. Rothman, J.E. & Lenard, J. Membrane asymmetry. *Science.* **195**, 743-753 (1977).

46. Pomorski, T., Holthuis, J.C.M., Herrmann, A. & van Meer, G. Tracking dwon lipid flippases and their biological functions. *J. Cell. Sci.* **117**, 805-813 (2004).

47. Martin, O.C. & Pagano, R.E. Transbilayer movement of fluorescent analogs of phosphatidylserine and phosphatidylethanolamine at the plasma membrane of cultured cells. *J. Biol. Chem.* **262**, 5890-5898 (1987).

48. Bitbol, M. & Devaux, P.F. Measurement of outward translocation of phospholipids across human erythrocyte membrane. *Proc. Natl. Acad. Sci.* **85**, 6783-6787 (1988).

49. Basse, F., Stout, J., Sims, P. & Wiedmer, T. Isolation of an erythrocyte membrane protein that mediates Ca^{2+} -dependent transbilayer movement of phospholipid. *J. Biol. Chem.* **271**, 17205-17210 (1996).
50. Lynch, M.L. & Spicer, P.T. (eds.). *Bicontinuous Liquid Crystals*, (Taylor & Francis Group, LLC, Boca Raton, 2005).
51. Bradbury, M. *The Concept of a Blood-Brain Barrier*, (John Wiley & Sons Ltd, Bath, 1979).
52. Suckling, A.J., Rumbsby, M.G. & Bradbury, M.W.B. (eds.). *The Blood-Brain-Barrier in Health and Disease*, (Ellis Horwood Ltd. & VCH Verlagsgesellschaft mbH., Chichester & Weinheim, 1986).
53. Seddon, A.M. et al. Drug interactions with lipid membranes. *Chem. Soc. Rev.* **38**, 2509-2519 (2009).
54. Baciu, M. et al. Degradative transport of cationic amphiphilic drugs across phospholipid bilayers. *Phil. Trans. R. Soc. A.* **364**, 2597-2614 (2006).
55. Sebai, S.C. et al. To lipophilicity and beyond - towards a deeper understanding of radioligand non-specific binding. *Neuroimage.* **31**, T56 (2006).
56. Epand, R.M. Lipid polymorphism and protein-lipid interactions. *Biochim. Biophys. Acta.* **1376**, 353-368 (1998).
57. Shearman, G.C., Ces, O., Templer, R.H. & Seddon, J.M. Inverse lyotropic phases of lipids and membrane curvature. *J. Phys.-Condens. Mat.* **18**, S1105-S1124 (2006).
58. Luzzati, V. & Husson, F. The structure of the liquid-crystalline phases of lipid-water systems. *J. Cell Biol.* **12**, 207-219 (1962).
59. Seddon, J.M. & Templer, R.H. Cubic phases of self-assembled amphiphilic aggregates. *Phil. Trans. R. Soc.* **344**, 377-401 (1993).
60. Cevc, G. & Richardsen, H. Lipid vesicles and membrane fusion. *Adv. Drug. Deliver. Rev.* **38**, 207-232 (1999).

61. Hafez, I.M. & Cullis, P.R. Roles of lipid polymorphism in intracellular delivery. *Adv. Drug. Deliver. Rev.* **47**, 139-148 (2001).

62. Seddon, J.M. & Templer, R.H. Chapter 3: Polymorphism of Lipid-Water Systems. in *Handbook of Biological Physics*, Vol. 1 (eds. Lipowsky, R. & Sackmann, E.) (Elsevier Science., 1995).

63. Bergstrand, N. & Edwards, K. Aggregate structure in dilute aqueous dispersions of phospholipids, fatty acids and lysophospholipids. *Langmuir.* **17**, 3245-3253 (2001).

64. Kirk, G.L., Gruner, S.M. & Stein, D.L. A thermodynamic model of the lamellar to inverse hexagonal phase transition of lipid membrane-water systems. *Biochem.* **23**, 1093-1102 (1984).

65. Zimmerberg, J. & Kozlov, M.M. How proteins produce cellular membrane curvature. *Nat. Rev. Mol. Cell. Biol.* **7**, 9-19 (2006).

66. Helfrich, W.Z. Elastic properties of lipid bilayers: theory and possible experiments. *Z. Naturforsch.* **28C**, 693-703 (1973).

67. Ces, O. & Mulet, X. Physical coupling between lipids and proteins: a paradigm for cellular control. *Signal Transduction.* **6**, 112-132 (2006).

68. Wang, A. & Dennis, E.A. Mammalian lysophospholipases. *Biochim. Biophys. Acta.* **1439**, 1-16 (1999).

69. Israelachvilli, J.N., Marcelja, S. & Horn, R.G. Physical principles of membrane organization. *Q. Rev. Biophys.* **12**, 121-200 (1980).

70. Burger, K.N.J. Greasing membrane fusion and fission machineries. *Traffic.* **1**, 605-613 (2000).

71. Meiberg, W. & Booth, P.J. The activation energy for insertion of transmembrane alpha-helices is dependant on membrane composition. *J. Mol. Biol.* **319**, 839-853 (2002).

72. Lipinski, C.A., Lombardo, F., Dominy, B. & Feeny, W. Experimental and computational approaches to estimate solubility and permeability in drug discovery and development settings. *Adv. Drug Deliver. Rev.* **23**, 3-25 (1997).

73. Sebai, S.C. Studies of cationic amphiphilic drug catalysed membrane degradation. PhD thesis. Imperial College London. (2007).

74. Seeman, P. Brain dopamine receptors. *Pharmacol. Rev.* **32**, 229-313 (1980).

75. Schreier, S., Malheiros, S.V.P. & dd Paula, E. Surface active drugs: self-association and interaction with membranes and surfactants. Physicochemical and biological aspects. *Biochim. Biophys. Acta.* **1508**, 210-234 (2000).

76. Girardin, F. Membrane transporter proteins: a challenge for CNS drug development. *Dialogue. Clin. Neurosci.* **8**, 311-321 (2006).

77. Rubin, L.L. & Staddon, J.M. The cell biology of the blood-brain barrier. *Ann. Rev. Neurosci.* **22**, 11-28 (1999).

78. Wright, E.M., Hirayama, B.A. & Loo, D.F. Active sugar tranport in health and disease. *J. Int. Med.* **261**, 32-43 (2007).

79. Matsuda, T., Takuma, K. & Baba, A. Na^{+}-Ca^{2+} exchanger: physiology and pharmacology. *Jpn. J. Pharmacol.* **74**, 1-20 (1997).

80. Templer, R.H. et al. Inverse bicontinuous cubic phases in 2:1 fatty acid/phosphatidylcholine mixtures. The effects of chain length, hydration, and temperature. *J. Phys. Chem. B.* **102**, 7251-7261 (1998).

81. Weibel, D.B. & Whitesides, G.M. Applications of microfluidics in chemical biology. *Curr. Op. Chem. Biol.* **10**, 584-591 (2006).

82. Devoe, D.L. & Lee, C.S. Microfluidic technologies for MALDI-MS in proteomics. *Electrophoresis.* **27**, 3559-3568 (2006).

83. Fox, M.B. et al. Electroporation of cells in microfluidic devices: a review. *Anal. Bioanal. Chem.* **385**, 474-485 (2006).

84. Andersson, H. & van den Berg, A. Microfluidic devices for cellomics: a review. *Sensor. Actuator.* **92**, 315-325 (2003).

85. de Jong, J., Lammertink, R.G.H. & Wessling, M. Membranes and microfluidics: a review. *Lab Chip.* **6**, 1125-1139 (2006).

86. Horsman, K.M., Bienvenue, J.M., Blasier, K.R. & Landers, J.P. Forensic DNA analysis on microfluidic devices: a review. *J. Forensic. Sci.* **52**, 784-799 (2007).

87. Breslauer, D.N., Lee, P.J. & Lee, L.P. Microfluidics-based systems biology. *Molec. Biosys.* **2**, 97-112 (2006).

88. Whitesides, G.M. The origins and the future of microfluidics. *Nature.* **442**, 368-373 (2006).

89. Hong, J., Edel, J.B. & deMello, A.J. Micro- and nanofluidic systems for high-throughput biological screening. . *Drug Discov. Today.* **14**, 134-146 (2009).

90. Carstens, C., Elbracht, R., Gartner, C. & Becker, H. Opportunities and limits of cell-based assay miniaturisation in drug discovery. *Expert Opin. Drug Discov.* **5**, 673-679 (2010).

91. Shi, W., Qin, J., Ye, N. & Lin, B. Droplet-based microfluidic system for individual Caenorhabditis elegans assay. *Lab Chip.* **8**, 1432-1435 (2008).

92. Blow, N. Microfluidics: in search of a killer application. *Nat. Methods.* **4**, 665-670 (2007).

93. Huebner, A. et al. Microdroplets: a sea of applications? *Lab Chip.* **8**, 1244-1254 (2008).

94. Theberg, A.B. et al. Microdroplets in microfluidics: an evolving platform for discoveries in chemistry and biology. *Angew. Chem. Int. Ed.* **49**, 5846-5868 (2010).

95. Jakeway, S.C., de Mello, A.J. & Russell, E.L. Miniaturized total analysis systems for biological analysis. *Fresenius J. Anal. Chem.* **366**, 525-539 (2000).

96. Situma, C., Hashimoto, M. & Soper, S.A. Merging microfluidics with microarray-based bioassays. *Biomolec. Eng.* **23**, 213-231 (2006).

97. Balagadde, F.K., You, L., Hansen, C.L., Arnold, F.H. & Quake, S.R. Long-term monitoring of bacteria undergoing programmed population control in a microchemostat. *Science.* **309**, 137-140 (2005).

98. Sia, S.K. & Whitesides, G.M. Microfluidic devices fabricated in poly(dimethylsiloxane) for biological studies. *Electrophoresis.* **24**, 3563-3576 (2003).

99. McDonald, J.C. & Whitesides, G.M. Poly(dimethylsiloxane) as a material for fabricating microfluidic devices. *Accounts Chem. Res.* **35**, 491-499 (2002).

100. Takayama, S. et al. Topographical micropatterning of poly(dimethylsiloxane) using laminar flows of liquids in capillaries. *Adv. Mater.* **13**, 570-574 (2001).

101. McDonald, J.C. et al. Fabrication of microfluidic systems in poly(dimethylsiloxane). *Electrophoresis.* **21**, 27-40 (2000).

102. Chaudhury, M.K. & Whitesides, G.M. Direct measurement of interfacial interactions between semispherical lenses and flat sheets of poly(dimethylsiloxane) and their chemical derivatives. *Langmuir.* **7**, 1013-1025 (1991).

103. Bhattacharya, S., Datta, A., Berg, J.M. & Gangopadhyay, S. Studies on surface wettability of poly(dimethylsiloxane) (PDMS) and glass under oxygen-plasma treatment and correlation with bond strength. *J. Microelectromech. S.* **14**, 590-597 (2005).

104. Unger, M.A., Chou, H.-P., Scherer, A. & Quake, S.R. Monolithic microfabricated valves and pumps by multilayer soft lithography. *Science.* **288**, 113-116 (2000).

105. Einav, S. et al. Discovery of a hepatitus C target and its pharmacological inhibitors by microfluidic affinity analysis. *Nat. Biotech.* **26**, 1019-1027 (2008).

106. Beebe, D.J., Mensing, G.A. & Walker, G.M. Physics and applications of microfluidics in biology. *Ann. Rev. Biomed. Eng.* **4**, 261-286 (2002).

107. Hardt, S. & Schonfeld, F. *Microfluidic Technologies for Miniaturized Analysis Systems*, (Springer, New York, 2007).

108. Berg, H.C. *Random Walks in Biology*, (Princeton University Press, 1983).

109. Grigoriev, R.O., Schatz, M.F. & Sharma, V. Chaotic mixing in microdroplets. *Lab Chip.* **6**, 1369-1372 (2006).

110. http://www.media.mit.edu/physics/pedagogy/nmm/student/95/aries/mas864/obstacles.html. (Accessed 30 Nov 2006).

111. deMello, A.J. Control and detection of chemical reactions in microfluidic systems. *Nature.* **442**, 394-402 (2006).

112. Casadevall i Solvas, X. & deMello, A.J. Droplet microfluidics: recent developments and future applications. *Chem. Commun.* **47**, 1936-1942 (2011).

113. Tice, J.D., Song, H., Lyon, A.D. & Ismagilov, R.F. Formation of droplets and mixing in multiphase microfluidics at low values of the Reynolds and the Capillary numbers. *Langmuir.* **19**, 9127-9133 (2003).

114. The, S.-Y., Lin, R., Hung, L.-H. & Lee, A.P. Droplet microfluidics. *Lab Chip.* **8**, 198-220 (2008).

115. Umbanhowar, P.B., Prasad, V. & Wietz, D.A. Monodisperse emulsion generation via drop break off in a coflowing system. *Langmuir.* **16**, 347-351 (2000).

116. Thorsen, T., Roberts, R.W., Arnold, F.H. & Quake, S.R. Dynamic pattern formation in a vesicle-generating microfluidic device. *Phys. Rev. Lett.* **86**, 4163-4166 (2001).

117. Song, H., Tice, J.D. & Ismagilov, R.F. A microfluidic system for controlling reaction networks in time. *Angew. Chem. Int. Ed.* **115**, 791-796 (2003).

118. Anna, S.L. Formation of dispersions using "flow focusing" in microchannels. *Appl. Phys. Lett.* **82**, 364-366 (2003).

119. Bringer, M.R., Gerdts, C.J., Song, H., Tice, J.D. & Ismagilov, R.F. Microfluidic systems for chemical kinetics that rely on chaotic mixing in droplets. *Phil. Trans. R. Soc. Lond. A.* **362**, 1087-1104 (2004).

120. Zagnoni, M., Baroud, C.N. & Cooper, J.M. Electrically initiated upstream coalescence cascade of droplets in a microfluidic flow. *Phys. Rev. E.* **80**, 046303(1)-046303(9) (2009).

121. Niu, X., Gulati, S., Edel, J.B. & DeMello, A.J. Pillar-induced droplet merging in microfluidic circuits. *Lab Chip.* **8**, 1837–1841 (2008).

122. Link, D.R., Anna, S.L., Weitz, D.A. & Stone, H.A. Geometrically mediated breadup of drops in microfluidic devices. *Phys. Rev. Lett.* **92**, 054503(1)-054503(4) (2004).

123. Schaerli, Y. & Hollfelder, F. The potential of microfluidic water-in-oil droplets in experimental biology. *Mol. BioSyst.* **5**, 1392-1404 (2009).

124. Huebner, A. et al. Static microdroplet arrays: a microfluidic device for droplet trapping, incubation and release for enzymatic and cell-based assays. *Lab Chip.* **9**, 692-698 (2009).

125. Schmitz, C.H.J., Rowat, A.C., Koster, S. & Weitz, D.A. Dropspots: a picoliter array in a microfluidic device. *Lab Chip.* **9**, 44-49 (2009).

126. Holtze, C. et al. Biocompatible surfactants for water-in-fluorocarbon emulsions. *Lab Chip.* **8**, 1632-1639 (2008).

127. Ahn, K. et al. Dielectrophoretic manipulation of drops for high-speed microfluidic sorting devices. *Appl. Phys. Lett.* **88**, 024104(1)-024104(3) (2006).

128. Niu, X., Zhang, M., Peng, S., Wen, W. & Sheng, P. Real-time detection, control, and sorting of microfluidic droplets. *Biomicrofluid.* **1**, 044101(1)-044101(12) (2007).

129. Jahn, A., Vreeland, W.N., Gaitan, M. & Locascio, L.E. Controlled vesicle self-assembly in microfluidic channels with hydrodynamic focusing. *J. Am. Chem. Soc.* **126**, 2674-2675 (2004).

130. Jahn, A., Vreeland, W.N., DeVoe, D.L., Locascio, L.E. & Gaitan, M. Microfluidic directed formation of liposomes of controlled size. *Langmuir.* **23**, 6289-6293 (2007).

131. Menger, F.M. & Keiper, J.S. Chemsitry and physical of giant vesicles as biomembrane models. *Curr. Op. Chem. Biol.* **2**, 726-732 (1998).

132. Bagatolli, L.A. To see or not to see: lateral organisation of biological membranes and fluorescence microscopy. *Biochim. Biophys. Acta.* **1758**, 1541-1556 (2006).

133. Reeves, J.P. & Dowben, R.M. Formation and properties of thin-walled phospholipid vesicles. *J. Cell. Physiol.* **73**, 49-60 (1969).

134. Darszon, A. et al. Reassembly of protein-lipid complexes into large bilayer vesicles: perspectives for membrane reconstitution. *Proc. Natl. Acad. Sci.* **77**, 239-243 (1980).

135. Moscho, A., Orwar, O., Chiu, D.T., Modi, B.P. & Zare, R.N. Rapid preparation of giant unilamellar vesicles. *Proc. Natl. Acad. Sci.* **93**, 11443-11447 (1996).

136. Angelova, M.I. & Dimitrov, D.S. Liposome electroformation. *Faraday Discuss. Chem. Soc.* **81**, 303-311 (1986).

137. Estes, D.J. & Mayer, M. Electroformation of giant liposomes from spin-coated films of lipids. *Colloid Surface. B.* **42**, 115-123 (2005).

138. Estes, D.J. & Mayer, M. Giant liposomes in physiological buffer using electroformation in a flow chamber. *Biochim. Biophys. Acta.* **1712**, 152-160 (2005).

139. Estes, D.J., Lopez, S.R., Fuller, A.O. & Mayer, M. Triggering and visualising the aggregation and fusion of lipid membranes in microfluidic chambers. *Biophys. J.* **91**, 233-243 (2006).

140. Sugiura, S. et al. Novel method for obtaining homogeneous giant vesicles from a monodisperse water-in-oil emulsion prepared with a microfluidic device. *Langmuir.* **24**, 4581-4588 (2008).

141. Stachowiak, J.C., Richmond, D.L., Li, T.H., Brochard-Wyart, F. & Fletcher, D.A. Inkjet formation of unilamellar lipid vesicles for cell-like encapsulation. *Lab Chip.* **9**, 2003-2009 (2009).

142. Stachowiak, J.C. et al. Unilamellar vesicle formation and encapsulation by microfluidic jetting. *Proc. Natl. Acad. Sci.* **105**, 4697-4702 (2008).

143. Ota, S., Yoshizawa, S. & Takeuchi, S. Microfluidic formation of monodisperse, cell-sized, and unilamellar vesicles. *Angew. Chem. Int. Ed.* **48**, 6533-6537 (2009).

144. Yeon, J.H. & Park, J.-K. Drug permeability assay using microhole-trapped cells in a microfluidic device. *Anal. Chem.* **81**, 1944-1951 (2009).

145. Young, E.W.K., Watson, M.W.L., Srigunapalan, S., Wheeler, A.R. & Simmons, C.A. Technique for real-time measurements of endothelial permeability in a microfluidic membrane chip using laser-induced fluorescence detection. *Anal. Chem.* **82**, 808-816 (2010).

146. Huh, D. et al. Reconstituting organ-level lung function on a chip. *Science.* **328**, 1662-1668 (2010).

147. Dittrich, P.S. & Manz, A. Lab-on-a-chip: microfluidics in drug discovery. *Nat. Rev. Drug Discov.* **5**, 210-218 (2006).

148. Teh, S.-Y., Lin, R., Hung, L.-H. & Lee, A.P. Droplet microfluidics. *Lab Chip.* **8**, 198-220 (2008).

149. Jung, H., Robison, A.D. & Cremer, P.S. Multivalent ligand-receptor binding on supported lipid bilayers. *J. Struct. Biol.* **168**, 90-94 (2009).

150. Groves, J.T. & Boxer, S.G. Micropattern formation in supported lipid membranes. *Acc. Chem. Res.* **35**, 149-157 (2002).

151. Holden, M.A., Jung, S.-Y., Yang, T., T., C.E. & Cremer, P.S. Creating fluid and air-stable solid supported lipid bilayers. *J. Am. Chem. Soc.* **126**, 6512-6513 (2004).

152. Yee, C.K., Amweg, M.L. & Parikh, A.N. Direct photochemical patterning and refunctionalisation of supported phospholipid bilayers. *J. Am. Chem. Soc.* **126**, 13962-13972 (2004).

153. Kassgaard, T., Leidy, C., Crowe, J.H., Mouritsen, O.G. & Jorgensen, K. Temperature-controlled structure and kinetics of ripple phases in one- and two-component supported bilayers. *Biophys. J.* **85**, 350-360 (2003).

154. Rossetti, F.F., Textor, M. & Reviakine, I. Asymmetric distribution of phosphatidyl serine in supported phospholipid bilayers on titanium dioxide. *Langmuir.* **22**, 3467-3473 (2006).

155. Tsougeni, K., Tserepi, A. & Gogolides, E. Photosensitive poly(dimethylsiloxane) materials for microfluidic applications. *Microelectron. Eng.* **84**, 1104-1108 (2007).

156. de Silva, M.N., Desai, R. & Odde, D.J. Micro-patterning of animal cells on PDMS substrates in the presence of serum without the use of adhesion inhibitors. *Biomed. Microdevices.* **6**, 219-222 (2004).

157. Hillborg, H. & Gedde, U.W. Hydrophobicity changes in silicone rubbers. *IEEE T. Dielect. El. In.* **6**, 703-717 (1999).

158. Duffy, D.C., McDonald, J.C., Schueller, J.A. & Whitesides, G.M. Rapid prototyping of microfluidic systems in poly(dimethylsiloxane). *Anal. Chem.* **70**, 4974-4984 (1998).

159. Phillips, K.S. & Cheng, Q. Microfluidic immunoassay for bacterial toxins with supported phospholipid bilayer membranes on poly(dimethylsiloxane). *Anal. Chem.* **77**, 327-334 (2005).

160. Rossetti, F.F., Bally, M., Michel, R., Textor, M. & Ilya, R. Interactions between titanium dioxide and phosphatidyl serine-containing liposomes: formation and patterning of supported phospholipid bilaters on the surface of a medically relevant material. *Langmuir.* **21**, 6443-6450 (2005).

161. Richter, R.P., Berat, R. & Brisson, A.R. Formation of solid-supported lipid bilayers: an integrated view. *Langmuir.* **22**, 3497-3505 (2006).

162. Janshoff, A. & Steinem, C. Transport across artificial membranes - an analytical perspective. *Anal. Bioanal. Chem.* **385**, 433-451 (2006).

163. Castellana, E.T. & Cremer, P.S. Solid supported bilayers: from biophysical studies to sensor design. *Surf. Sci. Rep.* **61**, 429-444 (2006).

164. Tanaka, M. Polymer-supported membranes: physical models of cell surfaces. *MRS. Bulletin.* **31**, 513-520 (2006).

165. Johnson, B.R.G., Bushby, R.J., Colyer, J. & Evans, S.D. Self-assembly of actin scaffolds at ponticulin-containing supported phospholipid bilayers. *Biophys. J.* **90**, L21-L23 (2006).

166. Majewski, J. et al. Structural studies of polymer-cushioned lipid bilayers. *Biophys. J.* **75**, 2363-2367 (1998).

167. Goksu, E.I. et al. Silica xerogel / aerogel-supported bilayers: consequences of surface corrugation. *Biochim. Biophys. Acta.* **1798**, 719-729 (2010).

168. Tribet, C. & Vial, F. Flexible macromolecules attached to lipid bilayers: impact on fluidity, curvature, permeability and stability of the membranes. *Soft Matter.* **4**, 68-81 (2008).

169. Jenkins, A.T.A. et al. Ion-selective lipid bilayers tethered to microcontact printed self-assembled monolayers containing cholesterol derivatives. *Langmuir.* **14**, 4675 (1998).

170. Jenkins, A.T.A. et al. Microcontact printing of lipophilic self-assembled monolayers for the attachment of biomimetric lipid bilayers to surfaces. *J. Am. Chem. Soc.* **121**, 5274-5280 (1999).

171. Jeuken, L.J.C. et al. Redox enzymes in tethered membranes. *J. Am. Chem. Soc.* **128**, 1711-1716 (2006).

172. Romer, W. et al. *J. Am. Chem. Soc.* **126**, 16267-16274 (2004).

173. Williams, T.L., Vareiro, M.M.L.M. & Jenkins, A.T.A. Fluorophore-encapsulated solid-supported bilayer vesicles: a method for studying membrane permeation processes. *Langmuir.* **22**, 6473-6476 (2006).

174. Yoshina-Ishii, C. et al. Diffusive dynamics of vesicles tethered to a fluid supported bilayer by single particle tracking. *Langmuir.* **22**, 5682-5689 (2006).

175. Sackmann, E. Supported membranes: scientific and practical applications. *Science.* **271**, 43-48 (1996).

176. Koenig, B.W. et al. Neutron reflectivity and atomic force microscopy studies of a lipid bilayer in water adsorbed to the surface of a silicon single crystal. *Langmuir*. **12**, 1343-1350 (1996).

177. Kung, L.I., Kam, L., Hovis, J.S. & Boxer, S.G. Patterning hybrid surfaces of proteins and supported lipid bilayers. *Langmuir*. **16**, 6773-6776 (2000).

178. Brian, A.A. & McConnell, H.M. Allogeneic stimulation of cytotoxic T cells by supported planar membranes. *Proc. Natl. Acad. Sci. USA*. **81**, 6159-6163 (1984).

179. Weirich, K.L., Israelachvili, J.N. & Fygenson, D.K. Bilayer edges catalyze supported lipid bilayer formation. *Biophys. J*. **98**, 85-92 (2010).

180. Stroumpoulis, D., Parra, A. & Tirrell, M. A kinetic study of vesicle fusion on silicon dioxide surfaces by ellipsometry. *AICHE. J*. **52**, 2931-2937 (2006).

181. Cremer, P.S. & Boxer, S.G. Formation and spreading of lipid bilayers on planar glass supports. *J. Phys. Chem. B*. **103**, 2254-2559 (1999).

182. Richter, R.P. & Brisson, A.R. Following the formation fo supported lipid bilayers on mica: a study combining AFM. QCM-D and ellipsometry. *Biophys. J*. **88**, 3422-3433 (2005).

183. Seantier, B. & Kasemo, B. Influence of mono- and divalent ions on the formation of supported phospholipid bilayers via vesicle adsorption. *Langmuir*. **25**, 5767-5772 (2009).

184. Boxer, S.G. Molecular transport and organisation in supported lipid membranes. *Curr. Op. Chem. Biol*. **4**, 704-709 (2000).

185. Groves, J.T. & Boxer, S.G. Electric field-induced concentration gradients in planar supported bilayers. *Biophys. J*. **69**, 1972-1975 (1995).

186. Cremer, P.S., Groves, J.T., Kung, L.I. & Boxer, S.G. Writing and erasing barriers to lateral mobility into fluid phospholipid bilayers. *Langmuir*. **15**, 3893-3896 (1999).

187. Hovis, J.S. & Boxer, S.G. Patterning barriers to lateral diffusion in supported lipid bilayer membranes by blotting and stamping. *Langmuir*. **16**, 894-897 (2000).

188. Groves, J.T., Ulman, N., Cremer, P.S. & Boxer, S.G. Substrate-membrane interactions: mechanisms for imposing patterns on a fluid bilayer membrane. *Langmuir*. **14**, 3347-3350 (1998).

189. Groves, J.T., Ulman, N. & Boxer, S.G. Micropatterning fluid lipid bilayers on solid supports. *Science*. **275**, 651-653 (1997).

190. Hovis, J.S. & Boxer, S.G. Patterning and composition arrays of supported lipid bilayers by microcontact printing. *Langmuir*. **17**, 3400-3405 (2001).

191. Kam, L. & Boxer, S.G. Cell adhesion to protein-micropatterned-supported lipid bilayer membranes. *J. Biomed. Mater. Res.* **55**, 487-495 (2001).

192. Orth, R.N. et al. Creating biological membranes on the micron scale: forming patterned lipid bilayers using a polymer lift-off technique. *Biophys. J.* **85**, 3066-3073 (2003).

193. Jackson, B.L. & Groves, J.T. Hybrid protein-lipid patterns from aluminium templates. *Langmuir*. **23**, 2052-2057 (2007).

194. Okazaki, T., Morigaki, K. & Taguchi, T. Phospholipid vesicle fusion on micropatterned polymeric bilayer substrates. *Biophys. J.* **91**, 1757-1766 (2006).

195. Mayer, M., Yang, J., Gitlin, I., Gracias, D.H. & Whitesides, G. Micropatterned agarose gels for stamping arrays of proteins and gradients of proteins. *Proteomics*. **4**, 2366-2376 (2004).

196. Majd, S. & Mayer, M. Hydrogel stamping of arrays of supported lipid bilayers with various lipid compositions for the screening of drug-membrane and protein-membrane interactions. *Angew. Chem. Int. Ed.* **44**, 6697-6700 (2005).

197. Cremer, P.S. & Yang, T. Creating spatially addressed arrays of planar supported fluid phopholipid membranes. *J. Am. Chem. Soc.* **121**, 8130-8131 (1999).

198. Castellana, E.T. & Cremer, P.S. Imaging large arrays of supported lipid bilayers with a macroscope. *Biointerphases.* **2**, 57-63 (2007).

199. Kam, L. & Boxer, S.G. Formation of supported lipid bilayer cmpostition arrays by controlled mixing and surface capture. *J. Am. Chem. Soc.* **122**, 12901-12902 (2000).

200. Kam, L. & Boxer, S.G. Spatially selective manipulation of supported lipid bilayers by laminar flow: steps toward biomembrane microfluidics. *Langmuir.* **19**, 1624-1631 (2003).

201. Jackson, B.L. & Groves, J.T. Scanning probe lithography on fluid lipid membranes. *J. Am. Chem. Soc.* **126**, 13878-13879 (2004).

202. Funakoshi, K., Suzuki, H. & Takeuchi, S. Lipid bilayer formation by contacting monolayers in a microfluidic device for membrane protein analysis. *Anal. Chem.* **78**, 8169-8174 (2006).

203. Holden, M.A., Needham, D. & Bayley, H. Functional bionetworks from nanoliter water droplets. *J. Am. Chem. Soc.* **129**, 8650-8655 (2007).

204. Bayley, H. et al. Droplet interface bilayers. *Mol. BioSyst.* **4**, 1191-1208 (2008).

205. Hwang, W.L., Chen, M., Cronin, B., Holden, M.A. & Bayley, H. Asymmetric droplet interface bilayers. *J. Am. Chem. Soc.* **130**, 5878-5879 (2008).

206. Hwang, W.L., Holden, M.A., White, S. & Bayley, H. Electrical behaviour of droplet interface bilayer networks: experimental analysis and modelling. *J. Am. Chem. Soc.* **129**, 11854-11864 (2007).

207. Poulos, J.L. et al. Ion channel and toxin measurement using a high throughput lipid membrane platform. *Biosens. Bioelectron.* **24**, 1806-1810 (2009).

208. Zagnoni, M., Sandison, M.E., Marius, P. & Morgan, H. Bilayer lipid membranes from falling droplets. *Anal. Bioanal. Chem.* **393**, 1601-1605 (2009).

209. LePioufle, B., Suzuki, H., Tabata, K.V., Noji, H. & Takeuchi, S. Lipid bilayer microarray for parallel recording of transmembrane ion currents. *Anal. Chem.* **80**, 328-332 (2008).

210. Suzuki, H., Tabata, K.V., Noji, H. & Takeuchi, S. Highly reproducible method of planar lipid bilayer reconstitution in polymethyl methacrylate microfluidic chip. *Langmuir.* **22**, 1937-1942 (2006).

211. Suzuki, H., Tabata, K.V., Kato-Yamada, Y., Noji, H. & Takeuchi, S. Planar lipid bilayer reconstitution with a micro-fluidic system. *Lab Chip.* **4**, 502-505 (2004).

212. Syeda, R., Holden, M.A., Hwang, W.L. & Bayley, H. Screening blockers against a potassium channel with a droplet interface bilayer array. *J. Am. Chem. Soc.* **130**, 15543-15548 (2008).

213. Stanley, C.E. et al. A microfluidic approach for high-throughput droplet interface bilayer (DIB) formation. *Chem. Commun.* **46**, 1620-1622 (2010).

214. Nussio, M.R., Sykes, M.J., Miners, J.O. & Shapter, J.G. Characterisation of the binding of cationic amphiphilic drugs to phospholipid bilayers using surface plasmon resonance. *Chem. Med. Chem.* **2**, 366-373 (2007).

215. Seydel, J.K. & Wiese, M. *Drug-Membrane Interactions*, (Wiley-VCH, Weinheim, 2002).

216. Weinstein, J.N., Blumenthal, R. & Klausner, R.D. Carboxyfluorescein leakage assay for lipoprotein-liposome interaction. *Method. Enzymol.* **128**, 657-668 (1986).

217. Grimes, P.A., Stone, R.A., Laties, A.M. & Li, W. *Arch. Ophthalmol.* **100**, 635 (1982).

218. Chen, R.F. & Knutson, J., R. Mechanism of fluorescence concentration quenching of carboxyfluorescein in liposomes: energy transfer to nonflorescent dimers. *Anal. Biochem.* **172**, 61-77 (1988).

219. Edwards, K.A. & Baeumner, A.J. Liposomes in analyses. *Talanta.* **68**, 1421-1431 (2006).

220. Ladhokhin, A.S., Wimley, W.C. & White, S.H. Leakage of membrane vesicle contents: determination of mechanism using fluorescence requenching. *Biophys. J.* **69**, 1964-1971 (1995).

221. Leidy, C., Linderoth, L., Andresen, T.L., Mouritsen, O.G. & Jorgensen, K. Domain-induced activation of human phospholipase A2 type IIA: local versus global lipid composition. *Biophys. J.* **90**, 3165-3175 (2006).

222. Ladhokhin, A.S., Wimley, W.C., Hristova, K. & White, S.H. Mechanism of leakage of contents of membrane vesicles determined by fluorescence requenching. *Method. Enzymol.* **278**, 474-486 (1997).

223. Yandek, L.E. et al. Mechanism of the cell-penetrating peptide transportan 10 permeation of lipid bilayers. *Biophys. J.* **92**, 2434-2444 (2007).

224. Pokorny, A. & Almeida, F.F. Kinetics of dye efflux and lipid flip-flop induced by d-lysin in phosphatidylcholine vesicle and the mechanism of graded release by amphiphatic, a-helical peptides. *Biochem.* **43**, 8846-8857 (2004).

225. Gregory, S.M., Cavenaugh, A., Journigan, V., Pokorny, A. & Almeida, P.F.F. A quantitative model for the all-or-none permeabilisation of phospholipid vesicles by the antimicrobial peptide cecropin A. *Biophys. J.* **94**, 1667-1680 (2008).

226. Ambroggio, E.E., Separovic, F., Bowie, J.H., Fidelio, G.D. & Bagatolli, L.A. Direct visualisation of membrane leakage induced by the antibiotic peptides: maculatin, citropin and aurein. *Biophys. J.* **89**, 1874-1881 (2005).

227. Weinstein, J.N., Yoshikami, S., Henkart, P., Blumenthal, R. & Hagins, W.A. Liposome-cell interaction: transfer and intracellular release of a trapped fluorescent marker. *Science.* **195**, 489-492 (1977).

228. Mordon, S., Devoisselle, J.M., Begu, S. & Desmettre, T. Laser-induced release of liposome-encapsulated dye: a new diagnostic tool. *Laser. Med. Sci.* **13**, 181-188 (1998).

229. Begu, S., Mordon, S., Desmettre, T. & Devoisselle, J.M. Fluorescence imaging method for in vivo pH monitoring during liposomes uptake in rat liver using a pH-sensitive fluorescent dye. *J. Biomed. Opt.* **10**, 024008 1-6 (2005).

230. http://www.avantilipids.com/PreparationOfLiposomes.html. (Accessed 22 Jul 2007).

231. http://www.gelifesciences.com/aptrix/upp00919.nsf/content/ LD_153206006-R350. (Accessed 15 Aug 2011).

232. GE-Healthcare. Gel Filtration: Principles and Methods (Handbook). (2008).

233. Sun, T. A study of the separation principle in size exclusion chromatography. *Macromolecules.* **37**, 4304-4312 (2004).

234. Israelachvili, J.N. Intermolecular and Surface Forces. (Academic Press Ltd., London, 1991).

235. Chang, H.M., Reitstetter, R. & Gruener, R. Lipid-ion channel interactions: increasing phospholipid headgroup size but not ordering acyl chains alters reconstituted channel behavior. *J. Membrane Biol.* **145**, 13-19 (1995).

236. Rex, S. Pore formation induced by the peptide melittin in different lipid vesicle membranes. *Biophys. Chem.* **58**, 75-85 (1996).

237. Lee, A.G. Local anesthesia: the interaction between phospholipids and chlorpromazine, propranolo, and practolol. *Mol. Pharmacol.* **13**, 474-487 (1977).

238. http://www.sigmaaldrich.com/catalog/ProductDetail.do?lang=en&N4=W108|SIGMA&N5=SEARCH_CONCAT_PNO|BRAND_KEY&F=SPEC. (Accessed 17 Apr 2011).

239. http://www.sigmaaldrich.com/catalog/ProductDetail.do?lang=en&N4=I7379|SIGMA&N5=SEARCH_CONCAT_PNO|BRAND_KEY&F=SPEC. (Accessed 11 Apr 2011).

240. Furton, K.G. & Norelus, A. Determining the critical micelle concentration of aqueous surfactant solutions. *J. Chem. Educ.* **70**, 254-257 (1993).

241. Patist, A., Bhagwat, S.S., Penfield, K.W., Aikens, P. & Shah, D.O. On the measurement of critical micelle concentrations of pure and technical-grade nonionic surfactants. *J. Surfactants Deterg.* **3**, 53-58 (2000).

242. Constantinides, P.P. & Steim, J.M. Physical properties of fatty acyl-CoA: critical micelle concentrations and micellar size and shape. *J. Biol. Chem.* **260**, 7573-7580 (1985).

243. Shearman, G.C. et al. Using membrane stress to our advantage. *Biochem. Soc. T.* **35**, 498-501 (2007).

244. Lakowicz, J.R. *Principles of Fluorescence Spectroscopy*, (Springer Science and Business Media, LLC., New York, 2006).

245. http://www.leica-microsystems.com/products/confocal-microscopes/confocal-methods/flim/. (Accessed 12 Dec 2010).

246. http://www.microchem.com/products/pdf/SU8_50-100.pdf. (Accessed 22 Jul 2007).

247. Kaplanova, M. & Cermak, K. Effect of reabsorption on the concentration dependence of fluorescence lifetimes of chlorophyll a. *J. Photochem.* **15**, 313-319 (1981).

248. Sluch, M.I., Averjushkin, A.S., Tolstikhin, O.I. & Vitukhnovsky, A.G. Influence of reabsorption on fluorescence lifetime of molecular crystals at α-particle excitation. *Phys. Scripta.* **50**, 585-587 (1994).

249. Robinson, T. et al. Removal of background signals from fluorescence thermometry measurements in PDMS microchannels using fluorescence lifetime imaging. *Lab Chip.* **9**, 3437-3441 (2009).

250. Hanke, W. & Schlue, W.-R. *Planar Lipid Bilayers: Methods and Applications*, (Academic Press Ltd., London, 1993).

251. Montal, M. & Mueller, P. Formation of bimolecular membranes from lipid monolayers and a study of their electrical properties. *Proc. Natl. Acad. Sci.* **69**, 3561-3566 (1972).

252. Blodgett, K.B. Films built by depositing successive monomolecular layers on a solid surface. *J. Am. Chem. Soc.* **57**, 1007-1022 (1935).

253. Schlindler, H. Formation of planar bilayers from artificial or native membrane vesicles. *Febs. Letts.* **122**, 77-79 (1980).

254. Punnamaraju, S. & Steckl, A.J. Voltage control of droplet interface bilayer lipid membrane dimensions. *Langmuir.* **27**, 618-626 (2011).

255. http://www.sigmaaldrich.com/catalog/ProductDetail.do?lang=en&N4=H0255|SIGMA&N5=SEARCH_CONCAT_PNO|BRAND_KEY&F=SPEC. (Accessed 10 Dec 10).

256. http://www.sigmaaldrich.com/catalog/ProductDetail.do?lang=en&N4=46180|RIEDEL&N5=SEARCH_CONCAT_PNO|BRAND_KEY&F=SPEC. (Accessed 10 Dec 10).

257. http://www.sigmaaldrich.com/catalog/ProductDetail.do?lang=en&N4=P7385|SIGMA&N5=SEARCH_CONCAT_PNO|BRAND_KEY&F=SPEC. (Accessed 10 Dec 10).

258. http://www.sigmaaldrich.com/catalog/ProductDetail.do?lang=en&N4=51578|FLUKA&N5=SEARCH_CONCAT_PNO|BRAND_KEY&F=SPEC. (Accessed 10 Apr 10).

259. http://www.sigmaaldrich.com/catalog/ProductDetail.do?lang=en&N4=74691|FLUKA&N5=SEARCH_CONCAT_PNO|BRAND_KEY&F=SPEC. (Accessed 10 Dec 10).

260. Yang, L. & Huang, W. A rhombohedral phase of lipid containing a membrane fusion intermediate structure. *Biophys. J.* **84**, 1808-1817 (2003).

261. Yang, L. & Huang, H.W. Observation of a membrane fusion intermediate structure. *Science.* **297**, 1877-1879 (2002).

262. Sakuma, Y., Imai, M., Yanagisawa, M. & Komura, S. Adhesion of binary giant vesicles containing negative spontaneous curvature lipids induced by phase separation. *Eur. Phys. J. E.* **25**, 403-413 (2008).

263. Avnir, Y. & Barenholz, Y. pH determination by pyranine: medium-related artifacts and their correction. *Anal. Biochem.* **347**, 34-41 (2005).

264. http://www.invitrogen.com/site/us/en/home/References/Molecular-Probes-The-Handbook/pH-Indicators/Probes-Useful-at-Near-Neutral-pH.html. (Accessed 19 Apr 10).

265. Gensure, R.H., Zeidel, M.L. & Hill, W.G. Lipid raft components cholesterol and sphingomyelin increase H^+/OH^- permeability of phosphatidylcholine membranes. *Biochem. J.* **398**, 485-495 (2006).

266. Paula, S., Volkov, A.G., Van Hoek, A.N., Haines, T.H. & Deamer, D.W. Permeation of protons, potassium ions, and small polar molecules through phospholipid bilayers as a function of membrane thickness. *Biophys. J.* **70**, 339-348 (1996).

267. Malmstadt, N., Nash, M.A., Purnell, R.F. & Schmidt, J.J. Automated formation of lipid-bilayer membranes in a microfluidic device. *Nano Lett.* **6**, 1961-1965 (2006).

268. Maglia, G. et al. Droplet networks with incorporated protein diodes show collective properties. *Nat. Nanotechnol.* **4**, 437-440 (2009).

269. Aghdaei, S., Sandison, M.E., Zagnoni, M., Green, N.G. & Morgan, H. Formation of artificial lipid bilayers using droplet dielectrophoresis. *Lab Chip.* **8**, 1617-1620 (2008).

270. Poulos, J.L., Nelson, W.C., Jeon, T.-J., Kim, C.-J. & Schmidt, J.J. Electrowetting on dielectric-based microfluidics for integrated lipid

bilayer formation and measurement. *Appl. Phys. Lett.* **95**, 1806-1810 (2009).

271. Zagnoni, M., Sandison, M.E. & Morgan, H. Microfluidic array platform for simultaneous lipid bilayer membrane formation. *Biosens. Bioelectron.* **24**, 1235-1240 (2009).
272. Lee, J.N., Park, C. & Whitesides, G.M. Solvent compatibility of poly(dimethylsiloxane)-based microfluidic devices. *Anal. Chem.* **75**, 6544-6554 (2003).
273. Jiyeon, L., Kim, M.J. & Lee, H.H. Surface modification of poly(dimethylsiloxane) for retarding swelling in organic solvents. *Langmuir.* **22**, 2090-2095 (2006).
274. Krishna, P. & Pandey, D. *Close-packed structures.*, (International union of crystallography by University College Cardiff Press., Cardiff, Wales., 1981).
275. Kline, T.R., Runyon, M.K., Pothiawala, M. & Ismagilov, R.F. ABO, D blood typing and subtyping using plug-based microfluidics. *Anal. Chem.* **80**, 6190-6197 (2008).
276. Sassa, F., Fukuda, J. & Suzuki, H. Microprocessing of liquid plug for bio/chemical analyses. *Anal. Chem.* **80**, 6206-6213 (2008).
277. Zheng, B. & Ismagilov, R.F. A microfluidic approach for screening submicroliter volumes against multiple reagents by using preformed arrays of nanoliter plugs in a three-phase liquid/liquid/gas flow. *Angew. Chem. Int. Ed.* **44**, 2520-2523 (2005).
278. Hoffmann, E.J., Phelps, M.E., Mullani, N.A., Higgins, C.S. & Ter-Pogossian, M.M. Design and performance characteristics of a whole-body positron transaxial tomograph. *J. Nuc. Med.* **17**, 493-502 (1976).
279. Passchier, J., Gee, A., Willemsen, A., Vaalburg, W. & van Waarde, A. Measuring drug-related receptor occupancy with positron emission tomography. *Methods.* **27**, 278-286 (2002).

280. Phelps, M.E. Positron emission tomography provides molecular imaging of biological processes. *Proc. Natl. Acad. Sci.* **97**, 9226-9233 (2000).

281. Elsinga, P.H. Radiopharmaceutical chemistry for positron emission tomography. *Methods.* **27**, 208-217 (2002).

282. Cunningham, V.J., Parker, C.A., Rabiner, E.A., Gee, A.D. & Gunn, R.N. PET studies in drug development: methodological considerations. *Drug Discov. Today.* **2**, 311-315 (2005).

283. Lee, C.-M. & Farde, L. Using positron emission tomography to facilitate CNS drug development. *Trends Pharmacol. Sci.* **27**, 310-316 (2006).

284. Laruelle, M., Slifstein, M. & Huang, Y. Relationships between radiotracer properties and image quality in molecular imaging of the brain with positron emission tomography. *Mol. Imaging Biol.* **5**, 363-375 (2003).

285. Huang, Z. & Szoka Jr., F.C. Sterol-modified phospholipids: cholesterol and phospholipid chimeras with improved biomembrane properties. *J. Am. Chem. Soc.* **130**, 15702-15712 (2008).